Photophysics of Doped Semiconductor Quantum Dots: A Path Towards New Optoelectronic Materials

A Thesis

Submitted for the Degree of

Doctor of Philosophy

In the faculty of Science

by

Payel Mondal

New Chemistry Unit

Jawaharlal Nehru Centre for Advanced Scientific Research

(A Deemed University)

Bangalore – 560064

June 2022

Dedicated to

The Almighty God

&

My Parents

DECLARATION

I hereby declare that the matter embodied in this thesis entitled **"*Photophysics of Doped Semiconductor Quantum Dots: A Path Towards New Optoelectronic Materials*"** is the result of the research carried out by me at the New Chemistry Unit, Jawaharlal Nehru Centre for Advanced Scientific Research, Bangalore, India, under the supervision of Prof. Ranjani Viswanatha and it has not been submitted elsewhere for the award of any degree or diploma.

In keeping with the general practices of reporting scientific observation, due acknowledgements have been made whenever the work described is based on the findings of other investigators. Any omission which might have occurred by oversight or error in judgement is regretted.

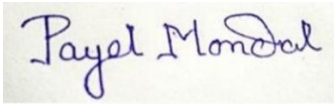

Bangalore

……..
Payel Mondal

CERTIFICATE

I hereby certify that the matter embodied in this thesis entitled **"*Photophysics of Doped Semiconductor Quantum Dots: A Path Towards New Optoelectronic Materials*"** has been carried out by Ms. Payel Mondal at the New Chemistry Unit, Jawaharlal Nehru Centre for Advanced Scientific Research, Bangalore, India, under my supervision and has not been submitted elsewhere for the award of any degree or diploma.

Bangalore

Prof. Ranjani Viswanatha

(Research Supervisor)

Acknowledgements

At the end of my Ph.D. journey, I am so glad that I survived while I enjoyed the journey. I owe a big thanks to all the wonderful people around me whose guidance, support, and companionship have helped me finish this journey on a high note. *This Ph.D. thesis is the culmination of the efforts of all the people who have contributed in making this research journey successful in so many ways.*

First and foremost, I would like to express my heartfelt gratitude to my research supervisor **Prof. Ranjani Viswanatha** *for providing me home away from my home*. Her excellent guidance, constant motivation, and invaluable suggestions during the entire course of my Ph.D have helped me grow each day. I am extremely fortunate to have her as my supervisor who gave me unfaltering support throughout in academics and beyond, who gave me enough freedom to work on the topics of my choice, and monitored my progress patiently. I will be forever thankful to her for making my research journey an enjoyable learning experience for me.

My heartfelt gratitude to **Prof. C. N. R. Rao**, F.R.S., for being the inspirational epitome who kept motivating me throughout my journey. I would also like to convey my sincere thanks to the Chairman of the New Chemistry Unit, Prof. Subi J. George for providing the excellent infrastructure and necessary facilities to conduct the thesis work smoothly.

I would like to thank all my **Collaborators**. My special thanks to Prof. Guilio Cerullo, and Luca Moretti from Politecnico di Milano, Italy for the TA measurements, Prof. Arindam Chowdhury, Deepshikha Arora, Somnath Kashid from IIT Bombay for the single-particle fluorescence measurements. My sincere thanks to Prof. DD Sarma and Prof. Anshu Pandey for the engrossing scientific discussion regarding the single-molecule fluorescence measurements and the instrumentation. I owe my thanks to Prof. Wolfgang A. Caliebe, and Dr. Akhil Tayal for the assistance in EXAFS measurements in PETRA III (P64) DESY, Germany. *I have been greatly benefitted from their expertise and the insightful discussion we had.*

I would like to thank my I would like to thank all my Ph.D. course instructors, Prof. Umesh V. Waghmare, Prof. Ranjani Viswanatha, Prof. A. Sundaresan, and Prof. K. S. Narayan for their instructive and enjoyable courses, and stimulating scientific interactions.

My sincere thanks to all the technical staff in JNCASR especially Mr. Kannan, Mr. Rahul, Dr. Jay, Mr. Vasu, Mrs. Gayathri, Mr. Shiva Kumar, Mr. Anil for their help with various characterization techniques, and Mr. Mune Gowda, Mr. Dileep, Mr. Peer for all the audio/visual help. I also would like to thank Ms. Mellisa and Mr. Naveen in the NCU office, academic staff, administrative staff, library, complab, hostel office, and JNCASR security for providing me with various facilities and a peaceful stay in JNCASR.

I thank CSIR for providing me with the Ph.D. fellowship. I would also like to thank Department of Science and Technology (DST), and JNCASR for providing the funding for different scientific affairs.

I wish to thank all my school and college teachers and everyone who have helped me be enriched with knowledge. My sincere thanks to ***Mr. Subrata Roy***, ***Mr. Shyamal Das***, ***Late Prof. Dinabandhu Kundu***, and ***Prof. Ch. Subrahmanyam***. *Thank you so much for shaping me into who I am today.*

I am ever grateful to my wonderful lab family. I owe my sincere thanks to my present and past lab mates Dr. Murthy, Dr. Avijit, Kushagra, Dr. Mahima, Dr. Pradeep, Saptarshi, Prasenjit, Gauttam, Suhas, Subham, Soumya, Subhashri, Adarsh, Gautam P, Angira, Sowmeya, for their wonderful companionship and scientific discussions. I also thank all the visiting students and visiting faculty who worked with me. *A special thanks to Murthy bhaiya who treated me as his younger sister and guided me in the initial days of my Ph. D.*

My heartfelt thanks to all my friends, especially those who made Bangalore home for me. I thank Brinta, Soumita, Shakil, Tanmay, Swarna, Abhishek, Vinita, Parul for making my Bangalore days enjoyable and memorable. I would also like to thank Indrani di, a sister from another mother, for all the love and support throughout. A big thanks to Priyanka, Poulomy, Miki, Arpan, and Ayan for being there always.

Lastly, ***Maa*** and ***Baba***, I can't thank you enough. You have made me believe in myself and guided me to the right path always. You have been a constant source of inspiration and energy that kept me going forward each and every day. Without your love and support, it would never have been possible to finish this journey. **Bhai**, thank you so much for loving me and being there with me always. My heartfelt thanks to a very special person **Avisek** who has been a pillar for me throughout my journey. *Thank you so much for being there through all my thick and thin, for your unfailing love, support, and understanding that made me finish this long*

journey with ease. Also, Mrs. Nilima Dutta, my another mother, thank you so much for understanding me and loving me. Also, I wish to thank all my family members and relatives for all the love and support.

Finally, I would like to thank each and every one who has helped me directly and indirectly in finishing this journey.

Payel

June 2022

Preface

Controlled incorporation of a few impurity atoms/ions, especially transition metal ions into semiconductor quantum dots (QDs) impart many interesting properties that play a major role in making the semiconductor industry more versatile. The effect of doping becomes further pronounced due to the strong quantum confinement effect and high surface-to-volume ratio in QD materials. However, the lack of a few fundamental yet very significant aspects has been the major bottleneck in the development of these materials for practical applications. In this thesis, we studied various singly doped QDs to elucidate the unresolved problems related to their fundamental photo-physics. We also synthetically engineered a few dual-doped QD systems and studied their interesting photo-physics. The thesis is divided into seven chapters:

Chapter 1 The first chapter provides a brief overview of the existing literature describing numerous interesting properties of semiconductor quantum dots, including the opportunities related to doping as well as challenges that are faced in synthesizing good quality doped nanocrystals. Specially, doping of various transition metal ions largely functionalizes new optical properties in QDs. However, understanding their emission mechanism from a fundamental viewpoint is lacking and much debated in the literature. Here, we discuss various anomalous properties of these doped QD systems. Further, we discuss about designing various dual-doped nanocrystals with many desirable interesting properties as well as several challenges related to it.

Chapter 2 In this chapter we briefly describe several synthetic methodologies to obtain transition metal-doped semiconductor quantum dots that were used in this thesis. This chapter also discusses the advanced techniques that have been employed to study different QD systems reported in this thesis, like single-particle fluorescence spectroscopy, transient absorption spectroscopy, extended x-ray absorption fine structure followed by a discussion on various characterization techniques used to study the doped QDs.

The rest of the thesis is largely divided into two parts based on the research findings of the work. **Part I** discusses the fundamental emission mechanism of Cu and Mn-doped nanocrystals as well as the excited state carrier dynamics of various singly doped nanocrystals. This part is further divided into three subsequent chapters.

Chapter 3 is divided into 2 parts. **Chapter 3A** first discusses the fundamental quantum mechanical phenomenon explaining the optical properties of the monovalent and divalent Cu dopants acquired from the reported literature, and then describes the lack of unanimity regarding the Cu oxidation state and hence their emission mechanism due to the spatial clutter that arises from the existing ensemble measurements. Following this debate, **Chapter 3B** involves determining the dopant oxidation state by employing a fluorescence microscopic technique specifically probing individual Cu-doped nanocrystals to eliminate the uncertainty arising from ensemble behavior. This chapter provides more conclusive evidence to the long-lasting debate on the dopant emission mechanism even though the system was studied extensively.

Chapter 4 again consists of 2 parts. **Chapter 4A** involves the study of bandgap-dependent energy/charge transfer in Mn-doped II-VI semiconductor nanocrystals and the burial of signature yellow-orange Mn emission when the host bandgap approaches the Mn excitation energy. Based on the optical studies like temperature-dependent as well as gated PL we study the nature of tunable higher energy emission in Mn-doped nanocrystals which in literature was wrongly attributed to the excitonic emission. In **Chapter 4B** we further study the origin of the tunable higher energy emission as well as the broad emission width of Mn in Mn-doped CdZnSe alloy nanocrystals using single-particle fluorescence spectroscopy to have a comprehensive understanding of the Mn emission mechanism that was elusive for past several decades.

Chapter 5 introduces various transition metal-doped CdS nanocrystals, especially studies the carrier dynamics involving the vibrational states in CdS nanocrystals as well as host-dopant interactions using the ultrafast pump-probe technique. Transient absorption analysis of these doped nanocrystals gives a quantitative measure of the excitation and decay processes that occur within the vibrational levels after non-resonant excitation of such doped systems. In addition to that, the oxidation state of dopants is studied which is further corroborated by EXAFS.

Further, **Section II** talks about dual doping in semiconductor nanocrystals where dual doping can induce synergistic properties that are otherwise negligible or absent in the individually doped systems. Here, we have discussed the challenges associated with dual doping in quantum dots as it has not been very trivial to incorporate two different dopants at the same time in a host lattice with good reproducibility. In the subsequent chapters, we have addressed various

synthetic aspects of dual doping followed by their optical and optoelectronic properties. This section is divided into chapters 6 and 7 respectively.

In **Chapter 6** we designed and synthetically engineered Cu, Mn dual-doped II-VI semiconductor quantum dots in search of an efficient single-source white light emitter. In the process, we have discussed various challenges involved in administering multiple dopants within the constraint of one host due to the factors like differential bonding strength, diffusivity, etc and keeping that in mind, in this chapter we adopted two distinct doping strategies, namely nucleation doping, and growth doping to ensure the incorporation of both the dopants within the same host lattice. Dual doping of Cu and Mn in a large bandgap material like ZnSe brings in the blue-green emission related to Cu and yellow-orange emission related to Mn dopants, giving rise to a synergy of bright white light emission in dual-doped nanocrystals. Here, we have engineered the nanocrystals in such a way that their core and surface electronic structures can be manipulated by various factors so that one can customize the type of white light emission from warm white to cool white from the single-source dual-doped emitters.

Chapter 7 focuses on the study of host-dopant as well as dopant-dopant interactions in dual-doped semiconductor nanocrystals. Herein, Mn, Fe dual-doped CdS nanocrystals have been synthesized. Fe is known as an efficient fluorescence quencher due to the presence of acceptor states induced by Fe doping. However, the administration of Fe into Mn-doped CdS behaves differently without much alteration in photoluminescence perhaps due to the interactions between the electronic states of the host and two dopants. We study these interactions as well as the excited state charge carrier dynamics using the ultrafast pump-probe technique as well as EXAFS.

Abbreviations

QDs	Quantum dots
NCs	Nanocrystals
VB	Valence band
VBM	Valence band maximum
CB	Conduction band
CBM	Conduction band maximum
PL	Photoluminescence
PLQY	Photoluminescence quantum yield
DMS	Dilute magnetic semiconductor
FEG	Field emission gun
LED	Light-emitting device
TEM	Transmission electron microscopy
XRD	X-ray diffraction
ICP-OES	Inductively coupled plasma-optical emission spectroscopy
EXAFS	Extended x-ray absorption fine structure
XANES	X-ray absorption near edge structure
ICSD	Inorganic crystal structure database
MCD	Magnetic circular dichroism
EPR	Electron paramagnetic resonance
TA	Transient absorption
TM	Transition metal
ODE	1-octadecene
OA	Oleic acid
OLAm	Oleylamin
TOP	Trioctylphosphine
PMMA	polymethyl methacrylate
SILAR	successive ionic layer adsorption and reaction
PB	Photobleaching
MBE	Molecular beam epitaxy
MOCVD	Metal organic chemical vapor deposition

Table of Contents

Declaration……iii

Certificate……...v

Acknowledgments……vii

Preface……...xi

Abbreviations……...xv

Chapter 1. Introduction……...1

1.1. Overview……3

1.2. Synthesis of quantum dots……...4

1.3. Doping in II-VI semiconductor QDs……5

1.3.1. Nucleation and growth doping……7

1.3.2. Diffusion doping……10

1.4. Dual doping in QDs……...12

1.5. Properties of transition metal-doped QDs……14

1.5.1. Optical properties……..14

1.5.2. Magnetic properties……...15

1.5.3. Magneto-optical properties……16

1.5.4. Electrical properties……...16

1.6. Open challenges……17

1.7. Present study……..18

Bibliography……22

Chapter 2. Methodology……..……...31

2.1. UV-visible absorption spectroscopy……..31

2.2. Photoluminescence (PL) spectroscopy……..…34

2.3. X-ray diffraction (XRD)……39

2.4. Transmission electron microscopy (TEM)……40

2.5. Inductively coupled plasma-optical emission spectroscopy……...41

2.6. Single-particle fluorescence spectroscopy…….41

2.6.1. Standardization of the instrument……42

2.7. Transient absorption (TA) spectroscopy……....51

2.8. Extended X-ray absorption fine structure spectroscopy (EXAFS)…….52

Bibliography…….54

Part 1. Fundamental photophysics of transition metal-doped II-VI semiconductor quantum dots

Chapter 3. Part A. Oxidation State of Cu: Photophysics and the Debate…….57

3.1. Abstract……..59

3.2. Introduction……...59

3.3. Discussions……61

3.3.1. Mechanism of Cu emission…….……..…61

3.3.2. Ensemble studies and the debate……..62

3.3.3. Summary……..72

Bibliography…….73

Chapter 3. Part B. Probing Copper Oxidation State Using Single-Particle Fluorescence Spectroscopy……...……79

3.4. Previous part……..81

3.5. Abstract…...……...81

3.6. Introduction……...81

3.7. Experimental section…….83

3.8. Results and discussion……...85

3.9. Conclusion…….95

Bibliography…….97

Chapter 4. Part A. Study of Mn-Doped II-VI Semiconductor Quantum Dots as a Function of Bandgap and Composition……..103

4.1. Abstract…...…….105

4.2. Introduction…….105

4.3. Experimental section……106

4.4. Results and discussion…….108

4.5. Conclusion……...119

Bibliography……...121

Chapter 4. Part B. Study of the Origin of Tunable Higher Energy Emission in Mn-Doped II-VI Semiconductor Quantum Dots……...125

4.6. Introduction…….127

4.3. Experimental section……128

4.4. Results and discussion…….128

4.5. Conclusion……...133

Bibliography……...134

Chapter 5. Ultrafast Carrier Dynamics in Transition Metal-Doped CdS Quantum Dots……137

5.1. Abstract…...…….139

5.2. Introduction…….139

5.3. Experimental section……140

5.4. Results and discussion…….141

5.5. Conclusion……...148

Bibliography……...149

Part 2. Study of Optoelectronic Properties of Dual-Doped II-VI Semiconductor Quantum Dots

Chapter 6. Electronic Structure Study of Dual Doped II-VI Semiconductor Quantum Dots Towards Single-Source White Light Emission……..155

6.1. Abstract…...…….157

6.2. Introduction…….157

6.3. Experimental section……159

6.4. Results and discussion…….162

6.5. Conclusion……...177

Bibliography……...178

Chapter 7. Synthesis and Study of Ultrafast Carrier Dynamics in Mn, Fe Dual-Doped CdS Quantum Dots……...181

7.1. Abstract…...…….183

7.2. Introduction…….183

7.3. Experimental section……184

7.4. Results and discussion…….187

7.5. Conclusion……...194

Bibliography……...196

List of publications……..…….199

Chapter 1

Introduction

1.1. Overview

Quantum dots (QDs) are nanocrystals (NCs) of semiconducting materials, characterized by a 3D confinement potential for carriers resulting in a discrete energy spectrum.[1-3] Due to the spatial confinement resulting from their extremely small size (2-20 nm), QDs exhibit size, shape, and composition-dependent properties enabling multiple applications in various fields, especially in optoelectronics, photovoltaics, etc.[4-10] The properties of intrinsic QDs are further altered by introducing impurities into the crystal lattice.[11-12] Thus, the ability to precisely, uniformly, and stably incorporate impurities/dopants into the semiconductor NCs enables a thorough and systematic study of their electronic structures and the fundamental photophysics. In this thesis, we primarily worked on the transition metal ion-doped QDs where we discussed the challenges and advantages associated with doping followed by various doping techniques that are suitable to achieve the stable and uniformly doped QDs. Our study also involves the modification of the surface electronic structure in QDs as it plays a major role in determining the associated photophysics.[13-18] Further, we discuss the recent advances in physical aspects of transition metal-doped QDs and the enigma related to their fundamental photophysics that are unresolved for decades now.

Although doping enables a vast domain of research to modulate the properties of II-VI semiconductors, the studies are largely restricted to one type of impurity ions doped in QDs.[19-26] However, doping two types of impurities simultaneously in a single QD system is interesting where synergistic properties can be attained from the same material that are otherwise not present in the individually doped systems.[27] However, dual-doping has rarely been explored in II-VI semiconductor QDs because it is associated with various practical challenges like different bonding strengths and diffusivity within the host lattice that integrates with the host in different ways and this, in turn, lacks in controlling the dopant concentration and hence the stability of dual-doped QDs. Few attempts have been made to study the optical properties in dual-doped II-VI semiconductor QDs.[28-31] However, finding the right doping method, stability, modulation of QD surfaces, detailed carrier dynamics in dual-doped QD systems are not well explored. Our work emphasizes on engineering the dual-doped QDs by judiciously choosing the right doping methods in order to achieve unprecedented control over the dopant concentration as well as the surface electronic structure so that the process of dual-doping could be unified across the QD systems. This thesis is majorly focused on studying the underlying photophysics of both singly-doped and dual-doped II-VI semiconductor QDs from a very fundamental perspective using various advanced probes.

1.2. Synthesis of quantum dots

The synthesis methodologies of semiconductor quantum dots (QDs) have shown remarkable progress in the past two decades, and various synthetic approaches have been developed to synthesize the QDs, ranging from vapor phase epitaxial growth like molecular beam epitaxy (MBE), metal-organic chemical vapor deposition (MOCVD) to various liquid-phase methods.[32-36] Although the vapor phase epitaxial growth methods have been successfully employed in the preparation of size-tunable QDs, there exist a few inherent drawbacks such as the use of expensive experimental setups, lesser control over the surface chemistry, and difficulty in the separation of products from the substrates.[37-38] Contrary to that, the liquid-phase synthetic methods are less energy-demanding processes that have shown the potential to produce highly crystalline and monodispersed QDs in various solutions with narrow size distribution and better surface processibility. The liquid-phase synthesis routes largely involve the preparation of colloidal QDs via hot-injection organometallic synthesis, non-injection organometallic synthesis, aqueous synthesis, etc.[39-41]

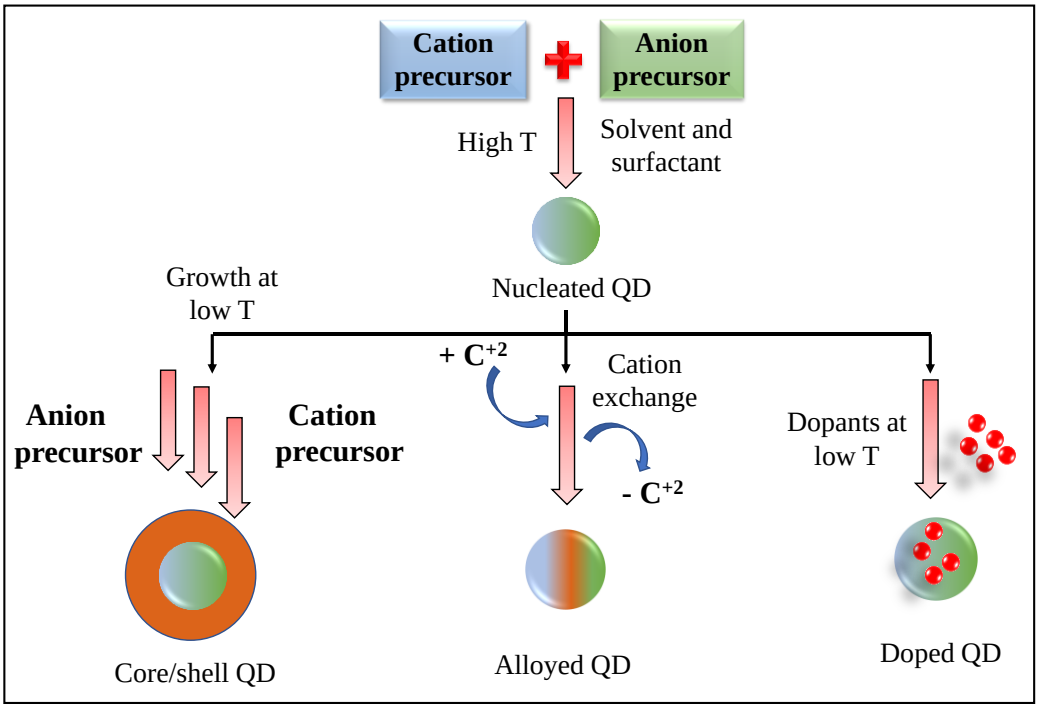

Figure 1.1. *General schematic showing the synthesis of the quantum dots in colloidal method starting from various precursors leading to the formation of complex QD structures as well as doped QDs.*

The colloidal method was first reported by Murray, Norris, and Bawendi for the synthesis of CdS, CdSe, and CdTe QDs.[42] Typically, in the colloidal method, QDs are synthesized by mixing the molecular precursors containing the constituent elements. Thermal decomposition of the precursors leads to the nucleation of the nanocrystals which are then annealed under high temperature causing the growth of the nanocrystals and the decoupling between nucleation and growth during the synthesis of QDs leads to the development of high-quality defect-free dots.[43] The best feasible way to achieve high-quality QDs involves the rapid injection of anion precursors into the cation precursors at very high temperatures in presence of surfactants.[44] Surfactants are usually the long-chain organic ligands that are used to control the growth of the QDs, passivate dangling bonds present at the QD surfaces, and maintain the overall stability of the QDs both in the solid and solution phase.[45-46] A schematic is shown in Figure 1.1 describing the general scheme of colloidal synthesis of II-VI semiconductor QDs.

1.3. Doping in II-VI semiconductor QDs

Deliberate insertion of impurities into the semiconductor QDs has garnered a lot of attention as the dopants within the QD host lattice functionalize the semiconductor nanocrystals (NCs) yielding numerous interesting properties like optical,[47-50] magnetic,[51-53] electronic,[54-55] and magneto-optical[56-57] properties which are otherwise absent or not very prominent in their undoped counterparts. Although undoped QDs show good size and composition-dependent emission tunability as shown in Figure 1.2, their applicability in fabricating devices is restricted due to the problem of self-quenching arising from small Stokes shift. However, doping increases the Stokes shift substantially which helps in overcoming the issue of self-quenching which make these doped QDs suitable candidates for solution-processed photovoltaics[58-59], light-emitting diodes (LEDs),[60-61] photodetectors,[62-63] and spintronic applications,[64] especially in this era of miniaturization of devices. However, it is not a trivial process to incorporate dopants into the host matrix since it depends upon a number of factors such as the nature of the dopant, the temperature at which dopants are incorporated, size and crystal structure of the host, surface ligands and so on which make the process complicated. Although a lot of attempts have been made to dope transition metals into semiconductor QDs during the past,[47, 49, 65-66] the mechanism of doping was not well understood. The major problem associated with the stability of doped nanocrystals is the self-purification[67] process where the dopant atoms are expelled out of the host lattice due to the incompatibility of dopants with the intrinsic host lattice.

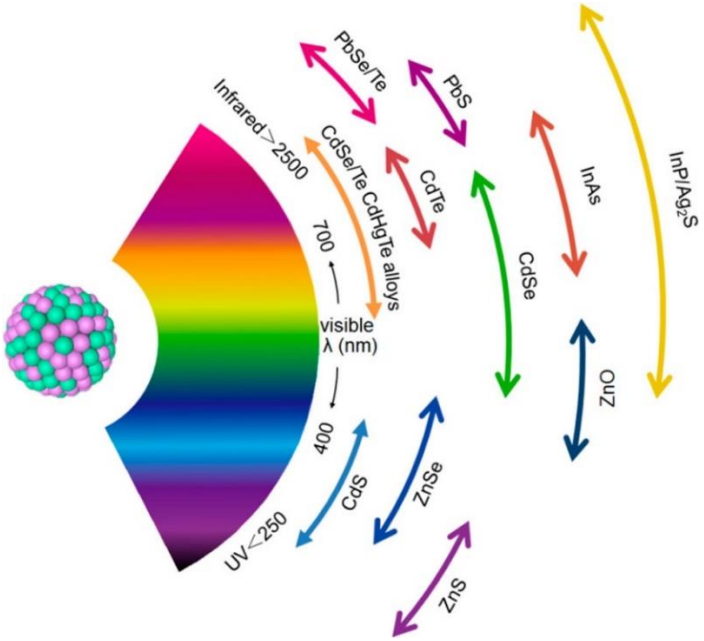

Figure 1.2. *A series of undoped quantum dots showing size and composition dependent emission tunabilty. Adopted with permission from ref 46. Copyright 2018 American Chemical Society.*

Also, the inefficient adsorption of certain impurities onto the nanocrystal surface[68] makes the doping process difficult in certain host lattices. For instance, it was observed from theoretical binding energy calculations that the CdSe QDs would be efficiently doped if the host crystallizes in a zinc-blende structure.[68] The same report showed that the organic ligands at the surface themselves can also bind the dopant ions, competing with the surface adsorption leading to a decrease in the doping efficiency. Thus, the researchers were keen to understand the various steps involved in the dopant incorporation to achieve efficient doping in terms of concentration and location of the dopants in the host matrix as well as greater stability of dopants within the host lattice.

Recently, Chen et al.[69] studied several elementary processes involved in the synthesis of doped quantum dots using solution-phase synthetic routes. Four distinct kinetic processes were identified, namely surface adsorption, lattice incorporation, lattice diffusion, and lattice ejection with the critical reaction temperatures associated with each of the processes as shown in Figure 1.3. They further stated that the lattice ejection and surface desorption processes can occur at a relatively lower temperature as compared to the process of lattice diffusion. Thus,

the nucleation-doping strategy involving the lattice diffusion process is much more temperature tolerant than that of the growth-doping method.

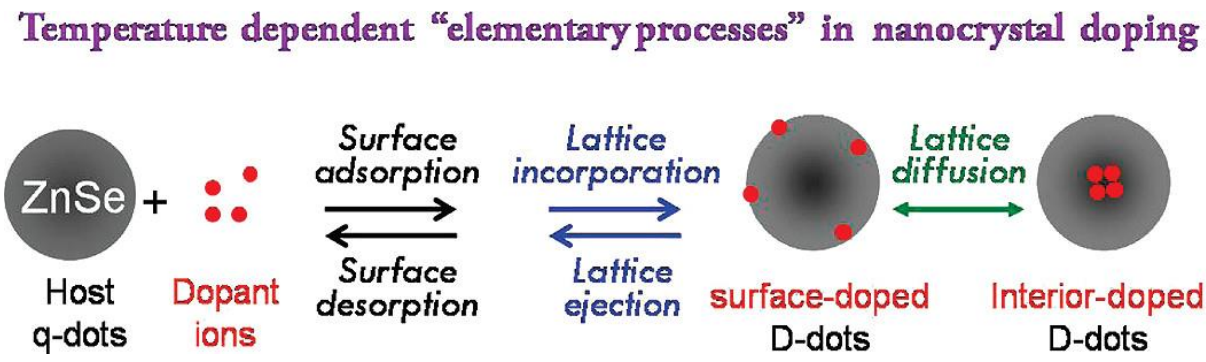

Figure 1.3. *Different elementary processes involved in the synthesis of doped quantum dots namely (1) surface adsorption, (2) lattice incorporation, (3) lattice diffusion, and (4) lattice ejection leading to surface desorption. Adopted with permission from ref 69. Copyright 2009 American Chemical Society.*

1.3.1. Nucleation and growth-doping

Nucleation-doping and growth-doping are the two mechanistically important doping methods that are the most widely used methods to dope transition metal ions into II-VI semiconductor QDs, were first proposed by Pradhan et el.[43] for the doping of Mn and Cu into ZnSe QDs. To deal with the differential reactivities of the dopants, the two processes were decoupled, and effective doping could be achieved. A simple synthetic scheme is shown in Figure 1.4 describing the two doping methods. Nucleation-doping involves the formation of dopant-anion clusters by injecting the host anionic precursor into the dopant precursor at a high temperature followed by overcoating of the host material. After the nucleation of QDs, the reaction conditions were modified in such a way that the growth of the host material becomes the only dominant process which, in turn, results in the uniform diffusion of the dopants into the host matrix. On the other hand, the growth-doping strategy involves the formation of the small host quantum dots under high temperatures followed by quenching of the reaction by lowering the reaction temperature. Active dopant precursors were then introduced at this relatively lower temperature, and doping occurs without the further growth of the host. Further, shells consisting of isocrystalline or hetero-crystalline material could be grown to encapsulate the dopant ions to protect them from surface oxidation.[48, 70] A prototype example for this proposed mechanism is shown in Figure 1.5. where the reactions were carried out to synthesize

Mn and Cu-doped ZnSe NCs. As is observed in Figure 1.5, manganese is best doped following the nucleation-doping method whereas, successful incorporation of Cu could be achieved by the growth-doping strategy.

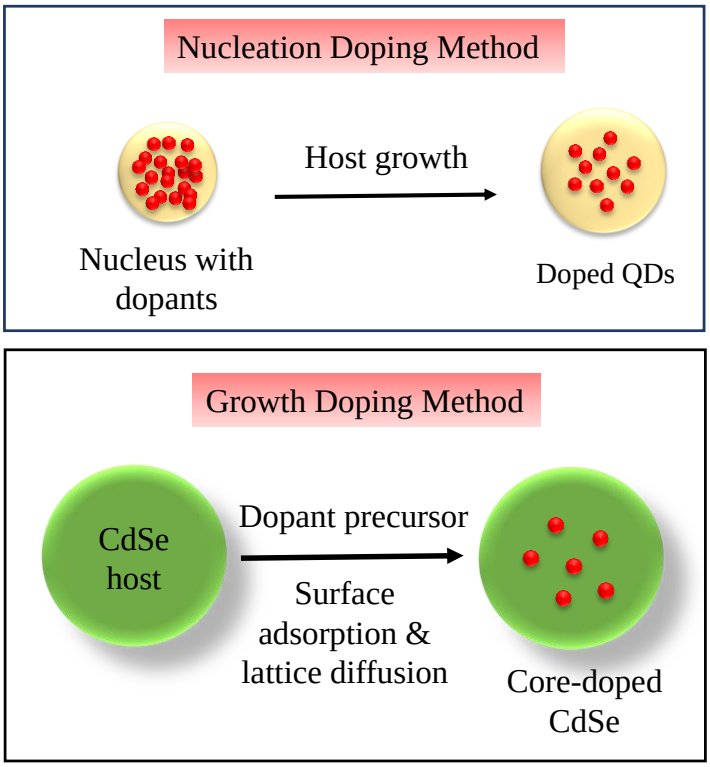

Figure 1.4. *Two important synthetic scheme to achieve efficient stable doping into QDs.*

It has been observed that the intensity of Cu-related photoluminescence (PL) increases and the excitonic emission decreases with the annealing time and further growth of ZnSe leads to the redshift of PL. The above result would have been impossible to attain without the decoupling technique as the maximum dopant intensity can be obtained after a substantially long doping/annealing time. On the other hand, Mn requires a higher reaction temperature to be nucleated and so does the host overcoating and thus, the nucleation-doping favors uniform doping of Mn^{2+} into ZnSe. The major disadvantage of this technique is that the high-temperature annealing during the growth of the host shell causes the expulsion of dopant ions due to the process of self-purification of the NCs. It was observed in the literature[69] that the Cu emission in ZnSe QDs was stable up to the overcoating temperature of 210 ^{o}C or below where the dopant ions were well diffused within the NCs. However, a further increase in overcoating

temperature to 220 °C or higher resulted in a reduction in Cu emission intensity. In fact, when the annealing temperature was 250 °C, the Cu emission completely vanished due to the expulsion of dopants out of the NCs as shown in Figure 1.6(a), (b) and (c).

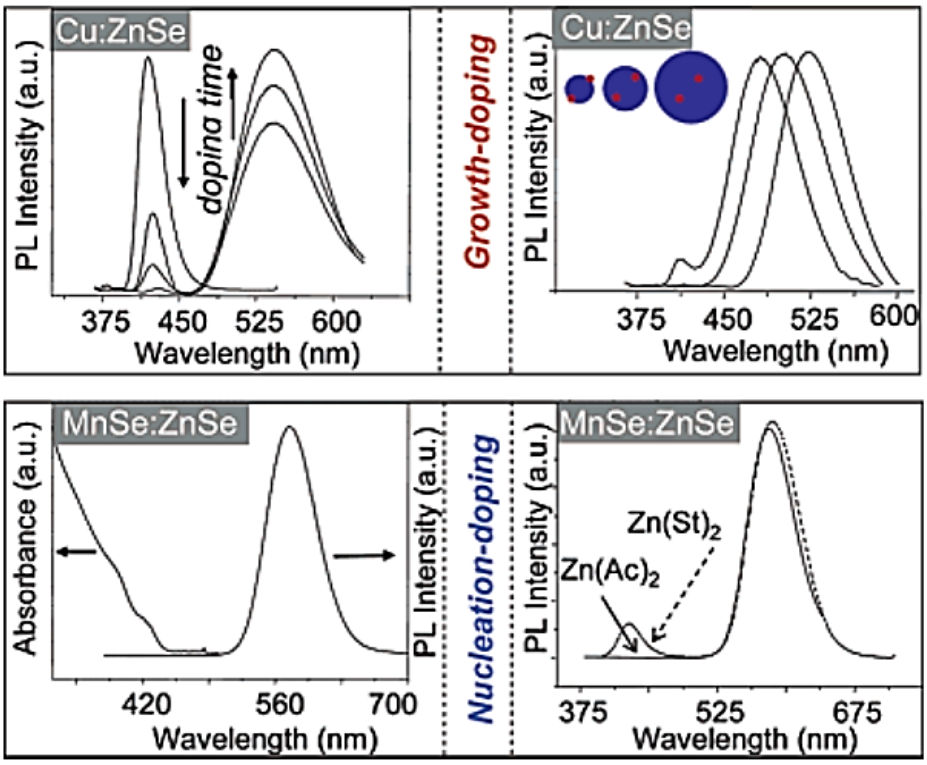

Figure 1.5. *Spectroscopic representation of growth doping (top panel) and nucleation doping (bottom panel). Adopted with permission from ref 43. Copyright 2005 American Chemical Society.*

Thus, it is very important to maintain an optimal temperature for the diffusion of Cu dopants as well as to retain the stability of the doped dots. Along with the temperature, reaction time is another parameter that determines the efficiency of doping which in turn controls the relative intensities of excitonic and dopant emission. The temporal evolution of the PL spectrum of ZnSe QDs in the presence of copper oleate in octadecene at 40 °C was studied.[69] The intensity of excitonic emission reduced and saturated after about 45 min, and no Cu emission was observed at a temperature as low as 40 °C. However, upon raising the temperature to 60 °C and higher, the lower energy Cu emission started appearing and a dominant Cu emission was observed only when the temperature was increased to 100 °C. The concentration of Cu dopants also affects the intensity of Cu emissions. Tananaev et al.[71] studied the emission properties of a series of Cu-doped CdSe nanocrystals by varying the concentration of Cu and with an

increase in the copper stearate, the intensity of Cu emission increases at the expense of band edge emission, suggesting an increased population of Cu doped QDs. Thus, by doping the extensive study of various parameters, researchers were able to achieve stable doped QDs with optimum doping levels following these two methods.

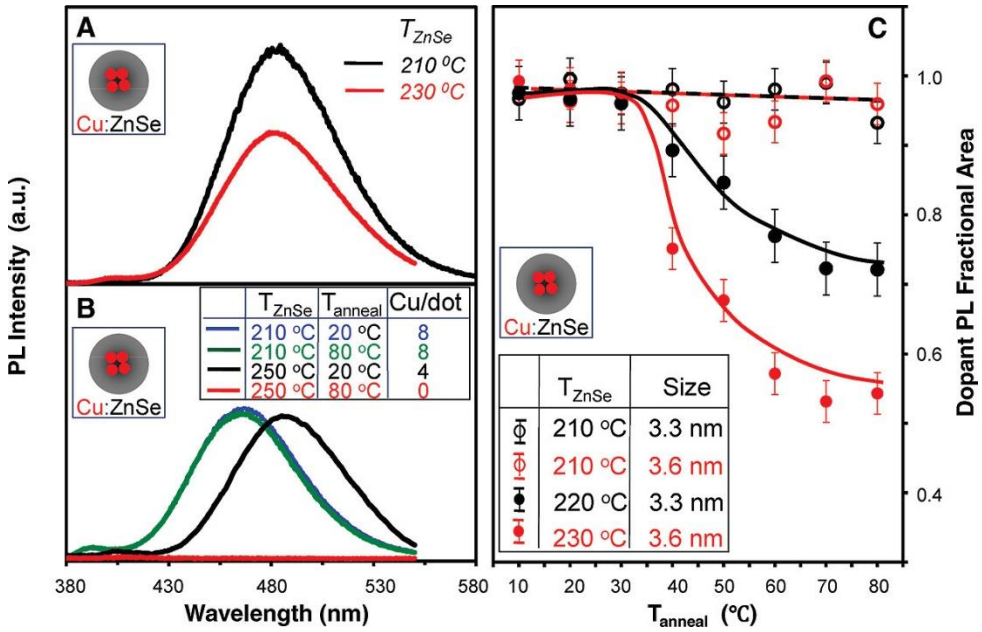

Figure 1.6. *(a) Emission spectra of Cu-doped ZnSe QDs prepared at different ZnSe overcoating temperatures (T_{ZnSe}), 210 and 230 °C. (B) PL spectra of Cu-doped ZnSe QDs with T_{ZnSe} of 250 and 210 °C, and their corresponding spectra after thermal annealing at 80 °C. The inset table shows the number of Cu ions per nanocrystal (Cu/dot) for the four samples. (C) Fractional area of the Cu dopant PL of the Cu-doped ZnSe QDs as a function of thermal annealing temperatures (T_{anneal}) for different overcoating temperatures and different sizes of the nanocrystals. Cu dopant PL at its maximum brightness for each case was set as 1. Adopted with permission from ref 69. Copyright 2009 American Chemical Society.*

1.3.2. Diffusion doping

Another doping method has been adapted to synthesize transition metal-doped semiconductor QDs, first coined by Saha et al.[50] which utilizes the diffusion of the dopants and the self-purification process as an aid instead of battling the same. In the diffusion doping method, a dopant-chalcogenide core was first formed at a very high temperature followed by

growing a thick shell of semiconductor material onto the dopant core using the successive ion layer adsorption and reaction (SILAR) technique as shown in Figure 1.7.

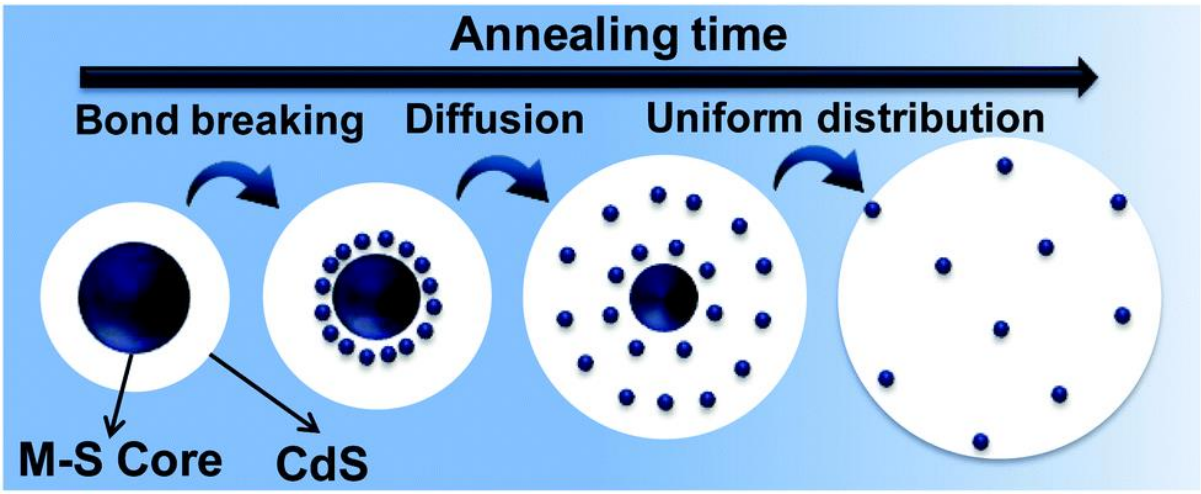

Figure 1.7. *This schematic explains the formation of uniformly doped QDs through dopant-sulfide bond breaking and diffusion of dopant ions into the host. Adopted with permission from ref 50. Copyright 2009 Royal Society of Chemistry.*

Annealing these core/shell nanostructures at high temperatures enables diffusion at the core/shell interface and eventually into the semiconductor shell leading to uniform diffusion of dopants into the crystal lattice. Based on the bond dissociation energy of the dopant-containing core as well as the diffusion coefficient of the dopant ions, the annealing time and temperature can be modified to attain effective doping with great control over dopant concentration, doping uniformity as well as the size of the QDs. For example, uniform doping has been achieved in the case of Fe-doped CdS QDs starting from iron oxide or sulfide core.[72] Elemental mapping through STEM-EDX and study of local structure using extended X-ray absorption fine structure (EXAFS) analysis confirmed the uniform distribution of Fe into CdS matrix without any cluster formation as shown in Figure 1.8. Thus, this diffusion doping technique has been demonstrated to be a great tool to achieve uniformly doped QDs which has also been extended to dope other dopants such as Mn^{2+}, Co^{2+}, Ni^{2+}, etc.,[50] characterized by steady-state as well as time-resolved PL measurements.

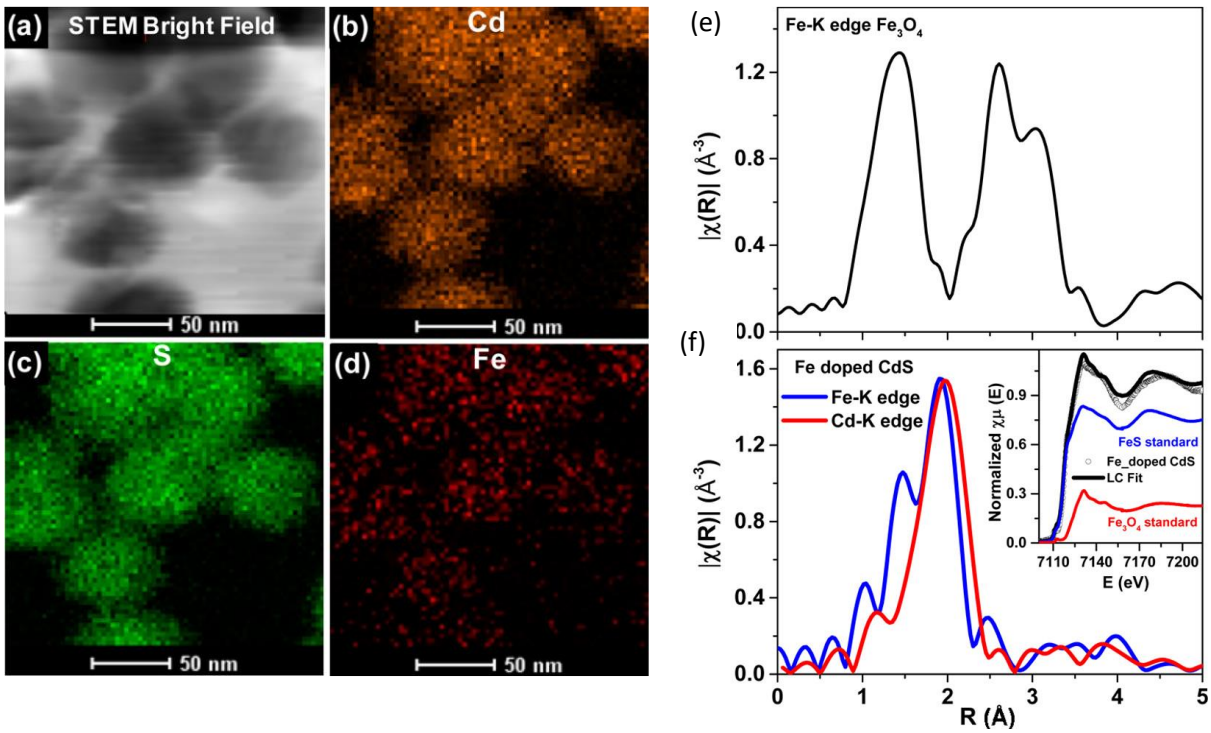

Figure 1.8. *Elemental mapping of through STEM-EDX of Fe-doped CdS shows uniform distribution of the elements suggest uniform doping and study of local structure through EXAFS shows diffusion of Fe ions without formation of any clusters. Adopted with permission from ref 72. Copyright 2016 American Chemical Society.*

1.4. Dual doping in QDs

As already discussed, the precedent doped semiconductor nanocrystals largely rely on the single doping that have emerged as a technologically important tool to introduce numerous interesting properties that are otherwise not present in the intrinsic host and extensive effort has been made to incorporate dopants into QD hosts in a controlled manner. However, a little success has been made to explore the dual-doped QDs. Although, dual doping appears to be a powerful technique to tailor the properties of semiconductor nanocrystals arising due to the host-dopant as well as dopant-dopant interactions, the synthesis, and study of dual-doped QDs are largely limited due to a series of thermodynamic challenges, such as differential bonding strength and diffusivity of dopants, thermodynamics of dopants adsorption onto the surface of QDs, etc. that makes the incorporation of two different dopants simultaneously into the same QD system nontrivial.

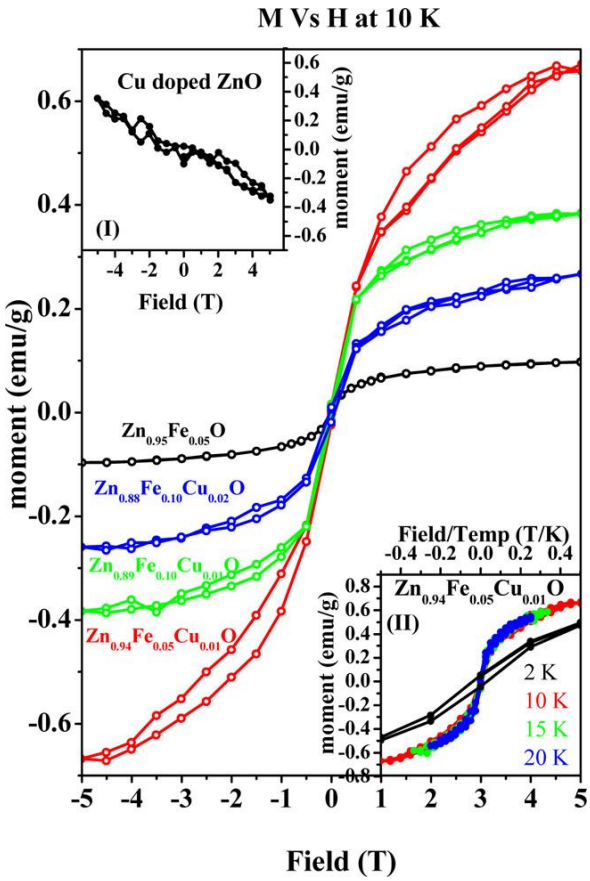

Figure 1.9. *M–H curves of different percentages of Fe/Cu-doped ZnO nanocrystals, measured at 10 K. Inset (I) shows the M–H curve of Cu-doped ZnO, showing diamagnetism. Inset (II) shows M as a function of H/T for the* $Zn_{0.94}Fe_{0.05}Cu_{0.01}O$ *sample at different temperatures, showing that the hysteresis loop at 2 K does not scale with temperature. Adopted with permission from ref and 73. Copyright 2012 American Chemical Society.*

In the recent past, a set of reports on dual-doped QDs have been surfaced where the synergistic properties were perceived that were otherwise not present in the individually doped QDs. Viswanatha et al.[73] studied Fe, Cu co-doping into free-standing ZnO QDs and showed that while individual Cu-doped ZnO was diamagnetic and Fe-doped ZnO was antiferromagnetic in nature due to the interaction between the Fe sites without any magnetic ordering, the dual doping of Cu and Fe into ZnO exhibited ferromagnetic behavior at low temperature as shown in Figure 1.9. Yuan et al.[74] showed that dual doping of Mn and Cu into Zn-In-S QDs resulted in bright white light emission whereas, individual Cu-doped and Mn-doped Zn-In-S were green-emitting and orange-emitting QDs. While optical and magnetic properties arising out of dual doping have also been studied in a few other systems,[75-77] a detailed understanding of the

fundamental photophysics including the charge carrier dynamics, bulk and surface electronic states, and dopant-dopant interactions is lacking.

1.5. Properties of transition metal-doped QDs

It is well known that doping impurity ions, especially transition metal ions, into II-VI semiconductor QDs alters the photophysics of QDs and imparts new functionalities such as optical, magnetic,[78] electrical, magneto-optical properties.

1.5.1. Optical properties

Transition metal ion-doped QDs have been regarded as one of the promising color-converting materials due to their emission tunability ranging from visible to NIR spectrum, large stokes shifted PL, and good chemical and thermal stability. To date, Cu and Mn remained the workhorse out of all the transition metal dopants. Doping Mn^{2+} introduces two atomic-like energy states between the conduction band (CB) and valence band (VB) of the host material and the photo-generated charge carriers undergo the transition through $^4T_1 \rightarrow {}^6A_1$ levels giving rise to Mn^{2+}-related emission.[79] This transition through Mn^{2+} levels is forbidden, and hence, the emission involves a long-lived decay pathway.[64, 80-81] Also, since the transition occurs through two midgap states, the Mn emission is largely characterized by an invariant yellow-orange PL feature when it is doped into substantially wide bandgap material as is shown in Figure 1.10(a). Unlike Mn^{2+}, Cu introduces one midgap state upon doping[82] and Cu emission arises due to the transition from host CB to Cu d-level,[83-84] which in turn, results in bandgap-dependent tunable emission in the quantum-confined regime.[43, 85] For instance, Srivastava et al.[85] showed that Cu doping in ZnS QDs, alloyed with Cd enables tunability of Cu-related emission ranging from ~ 500 nm to ~ 750 nm as shown in Figure 1.10(b). Dopants like Ni^{2+}, Co^{2+} were also found to affect the intrinsic PL properties of host QDs.[86] Both Ni, and Co doping have shown the evolution of a new broad PL peak which is red-shifted from the excitonic emission having a substantially longer lifetime (~300 ns). Also, there are other optically active transition metal dopants such as Cr and Ag which give rise to the new emission properties upon doping.[87]

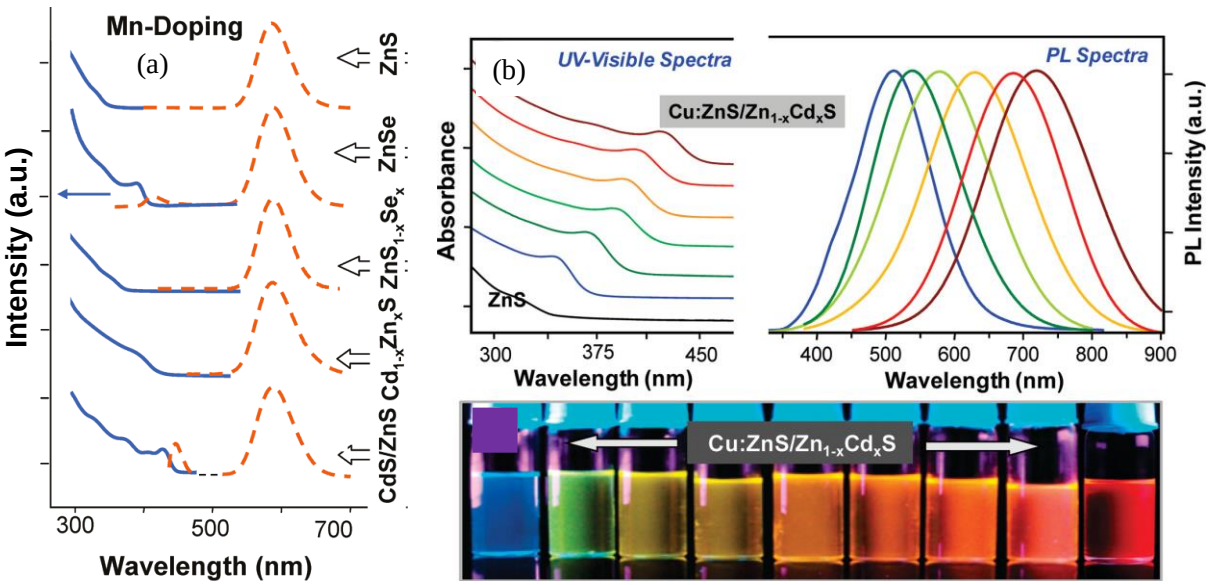

Figure 1.10 *(a) Emission properties of (a) Mn-doped and (b) Cu-doped QDs. Adopted with permission from ref and 84 and 85. Copyright 2010 and 2012 American Chemical Society.*

1.5.2. Magnetic properties

The study of magnetism in the quantum-confined regime has become a subject of interest due to several fundamentally compelling[88-89] and technologically important[90] aspects. When the non-magnetic semiconductor or insulator materials exhibit magnetic ordering due to the incorporation of a very small amount of magnetic dopants, are known as dilute magnetic semiconductors (DMS)[91-92] and are quite different compared to the bulk ferromagnetic materials. By incorporating transition metal dopants into II-VI semiconductors, DMS materials introduce localized unpaired spins that are magnetically coupled to delocalized charge carriers, known as sp-d exchange interaction, leading to an enhancement in magnetism. Schwartz et al. showed that an aggregate of 3.6% Co-doped ZnO DMS-QDs results in ferromagnetic ordering at room temperature (300 K) with the saturation magnetic moment of 2.56×10^{-3} emu/g.[93] Jana et al.[86] showed that doping ZnSe, CdZnS, and $CuInS_2$ nanocrystals with Ni^{2+} having a concentration of as low as 1% induces room temperature ferromagnetism in the QD systems. Due to these interesting magnetic properties, DMS materials are potential candidates for spin-based electronic devices.[94]

1.5.3. Magneto-optical properties

DMS quantum dots are also known to respond to optical perturbations leading to interesting magneto-optical properties. The interplay between localized magnetic dopant ions and the charge carriers of the host semiconductor yields a spin-exchange interaction leading to an enhancement in magneto-optical effects, such as giant Zeeman splitting, large Faraday rotation.[95-96] Further, the quantum confinement effect in semiconductor nanostructures significantly alters the exchange interaction between the magnetic ion spins and charge carriers thus paving the way to control the magneto-optical responses by engineering the size and shapes of the semiconductor nanostructures.[97] Magnetic circular dichroism (MCD) measurements were performed on Mn-doped CdSe nanoribbons with strong quantum and dielectric confinement at temperatures ranging between 4.2 K to room temperature. It showed spectrally separated features of the heavy hole and light hole-exciton transitions indicating confine-dependent s-d exchange constants. The combined giant sp-d exchange interaction and the strong excitonic resonances resulted in a pronounced magneto-optical response up to room temperature with an unusually high effective g-factor of about 13 at 300 K.[98]

1.5.4. Electrical properties

Doping in QDs plays a crucial role in tuning the transport properties of host materials, very similar to their bulk counterparts. Since thin films of QDs are inherently insulating in nature, the introduction of extra carriers can trigger the electrical conduction in them. To achieve electrical conductivity, heterovalent impurities are to be incorporated which induces the generation of additional charge carriers in the systems. Several strategies were employed to introduce extra charge carriers into the QD films. The study includes the placement of electron-donating molecules in close proximity to the QD surfaces[99-100] as well as through electrochemical doping.[101-102] For instance, the introduction of Cd impurities into InAs QDs modulated the conductivity of the QD films.[103] CdSe is one of the most studied QD systems in literature for studying electrical conductivity. Recently, it was shown that doping aliovalent Ag^+ into CdSe QDs alters the electrical properties of the host. Increasing the doping concentration of Ag^+ changes the CdSe QDs from an n-type to a p-type semiconductor. These properties induced by doping enable an opportunity to exploit the doped semiconductor nanostructures for numerous potential applications. However, there are many open challenges associated with these doped systems.

1.6. Open challenges

Despite a lot of progress made in the field of transition metal-doped II-VI semiconductor QDs both from the perspective of good quality doped QD synthesis as well as numerous applications in optoelectronics,[5, 9] spintronics,[64] sensing,[104] etc., the major challenge that remains is the understanding of fundamental photophysics which have been elusive so far in many cases. One such fundamental yet significant drawback is the mechanism of Cu emission in II-VI semiconductor QDs which is debated due to the conflicting reports on the oxidation state of Cu that appeared in the literature. For a given PL spectrum of Cu-doped QDs, usually, two distinct emission bands are observed. While one peak corresponds to excitonic emission, the other one corresponds to Cu-related emission. The distinction between the two oxidation states of Cu has been difficult due to the lack of spatial separation of the emission spectrum obtained from the ensemble measurements which, in turn, leads to many other open questions related to Cu emission such as the origin of excitonic emission, mechanism of Cu emission, etc. A detailed discussion of the Cu emission mechanism is done in Chapter 3 of this thesis.

Another widely studied transition metal dopant is manganese. Doping Mn^{2+} ions into semiconductor QDs introduces two atomic-like midgap states and the photo-excitation results in the sensitization of Mn levels followed by intense photoluminescence (PL) arising due to ligand field transition through $^4T_1 \rightarrow {}^6A_1$ levels in Mn^{2+}.[49, 64, 79, 81] Although spectroscopically well-characterized, the mechanism of sensitization of Mn levels has been debated in the literature whether it is through charge or energy transfer from the host[105-106] For instance, due to the extremely intense PL and the relative insensitivity of Mn emission on the external factors, it is widely accepted in the community that the excitation of Mn levels occurs through energy transfer[107-108] as shown in Figure 1.11(a) and (b). However, the measurement of the rate of exciton-dopant energy transfer by pump-probe transient absorption (TA) spectroscopy revealed a substantially higher timescale than a typical energy transfer rate.[108-109] In addition, the timescale involved in the nonradiative hole trapping process (50-100 ps) suggested a possible charge transfer shown in Figure 1.11(c).

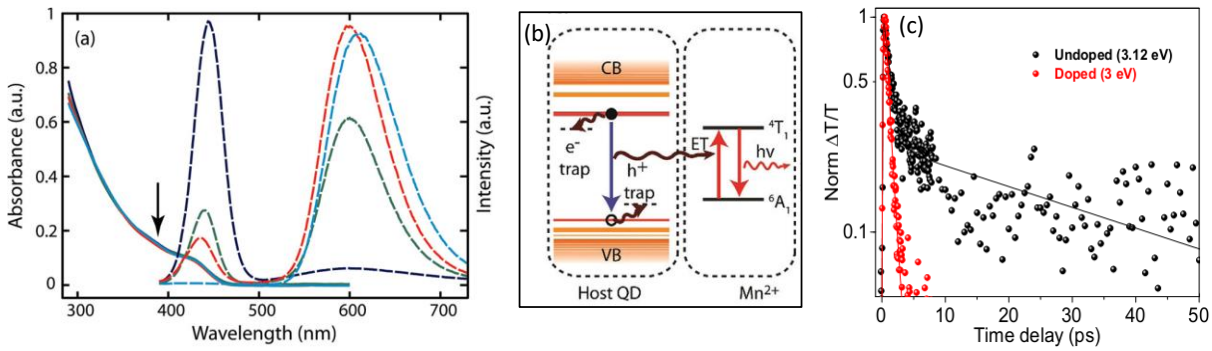

Figure 1.11. *(a) Emission spectra of Mn-doped QDs with different Mn doping levels showing intense Mn emission. (b) Proposed mechanism showing energy transfer. Adopted with permission from ref 109. Copyright 2010 American Chemical Society. (c) differential transmission dynamics of undoped and Mn-doped QDs showing the typical energy transfer time. Adopted with permission from ref 110. Copyright 2019 American Chemical Society.*

In fact, another recent study showed a plausible mechanism of charge transfer and thereby formation of Mn^{3+} transient state.[110] The same study showed a bandgap-dependent evolution in Mn PL. However, the detailed photophysics behind the observation is left unexplored which makes the Mn emission elusive despite an extensive study of the same. Similarly, there are transition metal-doped QDs that remained largely unexplored, especially the photophysics including the carrier dynamics. Additionally, there exist many undiscovered aspects related to dual-doped quantum dots which have driven us to study the photophysics related to these systems in order to gain detailed fundamental understanding.

1.7. Present study

Controlled incorporation of a few impurity atoms/ions, especially transition metal ions into semiconductor quantum dots (QDs) impart many interesting properties that play a major role in making the semiconductor industry more versatile. The effect of doping becomes further pronounced due to the strong quantum confinement effect and high surface-to-volume ratio in QD materials. However, the lack of a few fundamental yet very significant aspects has been the major bottleneck in the development of these materials for practical applications. In this thesis, we studied various singly doped QDs to elucidate the unresolved problems related to their fundamental photo-physics. We also synthetically engineered a few dual-doped QD systems and studied their interesting photo-physics. The thesis is divided into seven chapters:

Chapter 1 The first chapter provides a brief overview of the existing literature including the opportunities and challenges related to transition metal doping in II-VI semiconductor QDs as already discussed in this chapter.

Chapter 2 In this chapter we briefly describe several synthetic methodologies to obtain transition metal-doped semiconductor quantum dots that were used in this thesis. This chapter also discusses the advanced techniques that have been employed to study different QD systems reported in this thesis, like single-particle fluorescence spectroscopy, transient absorption spectroscopy, extended x-ray absorption fine structure followed by a discussion on various characterization techniques used to study the doped QDs.

The rest of the thesis is largely divided into two parts based on the research findings of the work. **Part I** discusses the fundamental emission mechanism of Cu and Mn-doped nanocrystals as well as the excited state carrier dynamics of various singly doped nanocrystals. This part is further divided into three subsequent chapters.

Chapter 3 is divided into 2 parts. **Chapter 3A** first discusses the fundamental quantum mechanical phenomenon explaining the optical properties of the monovalent and divalent Cu dopants acquired from the reported literature, and then describes the lack of unanimity regarding the Cu oxidation state and hence their emission mechanism due to the spatial clutter that arises from the existing ensemble measurements. Following this debate, **Chapter 3B** involves determining the dopant oxidation state by employing a fluorescence microscopic technique specifically probing individual Cu-doped nanocrystals to eliminate the uncertainty arising from ensemble behavior. This chapter provides more conclusive evidence to the long-lasting debate on the dopant emission mechanism even though the system was studied extensively.

Chapter 4 again consists of 2 parts. **Chapter 4A** involves the study of bandgap-dependent energy/charge transfer in Mn-doped II-VI semiconductor nanocrystals and the burial of signature yellow-orange Mn emission when the host bandgap approaches the Mn excitation energy. Based on the optical studies like temperature-dependent as well as gated PL we study the nature of tunable higher energy emission in Mn-doped nanocrystals which in literature was wrongly attributed to the excitonic emission. In **Chapter 4B** we further study the origin of the tunable higher energy emission as well as the broad emission width of Mn in Mn-doped CdZnSe alloy nanocrystals using single-particle fluorescence spectroscopy to have a

comprehensive understanding of the Mn emission mechanism that was elusive for past several decades.

Chapter 5 introduces various transition metal-doped CdS nanocrystals, especially studies the carrier dynamics involving the vibrational states in CdS nanocrystals as well as host-dopant interactions using the ultrafast pump-probe technique. Transient absorption analysis of these doped nanocrystals gives a quantitative measure of the excitation and decay processes that occur within the vibrational levels after non-resonant excitation of such doped systems. In addition to that, the oxidation state of dopants is studied which is further corroborated by EXAFS.

Further, **Section II** talks about dual doping in semiconductor nanocrystals where dual doping can induce synergistic properties those are otherwise negligible or absent in the individually doped systems. Here, we have discussed the challenges associated with dual doping in quantum dots as it has not been very trivial to incorporate two different dopants at the same time in a host lattice with good reproducibility. In the subsequent chapters, we have addressed various synthetic aspects of dual doping followed by their optical and optoelectronic properties. This section is divided into chapters 6 and 7 respectively.

In **Chapter 6** we designed and synthetically engineered Cu, Mn dual-doped II-VI semiconductor quantum dots in search of an efficient single-source white light emitter. In the process, we have discussed various challenges involved in administering multiple dopants within the constraint of one host due to the factors like differential bonding strength, diffusivity, etc and keeping that in mind, in this chapter we adopted two distinct doping strategies, namely nucleation doping, and growth doping to ensure the incorporation of both the dopants within the same host lattice. Dual doping of Cu and Mn in a large bandgap material like ZnSe brings in the blue-green emission related to Cu and yellow-orange emission related to Mn dopants, giving rise to a synergy of bright white light emission in dual-doped nanocrystals. Here, we have engineered the nanocrystals in such a way that their core and surface electronic structures can be manipulated by various factors so that one can customize the type of white light emission from warm white to cool white from the single-source dual-doped emitters.

Chapter 7 focuses on the study of host-dopant as well as dopant-dopant interactions in dual-doped semiconductor nanocrystals. Herein, Mn, Fe dual-doped CdS nanocrystals have been synthesized. Fe is known as an efficient fluorescence quencher due to the presence of acceptor states induced by Fe doping. However, the administration of Fe into Mn-doped CdS behaves

differently without much alteration in photoluminescence perhaps due to the interactions between the electronic states of the host and two dopants. We study these interactions as well as the excited state charge carrier dynamics using the ultrafast pump-probe technique as well as EXAFS.

Bibliography

1. Ye, Qui-yi.; Tsu, R.; Nicollian, E. H., Resonant Tunneling Via Microcrystalline-Silicon Quantum Confinement. *Phys. Rev. B* **1991**, *44*, 1806-1811.

2. Butkus, J.; Vashishtha, P.; Chen, K.; Gallaher, J. K.; Prasad, S. K. K.; Metin, D. Z.; Laufersky, G.; Gaston, N.; Halpert, J. E.; Hodgkiss, J. M., The Evolution of Quantum Confinement in $CsPbBr_3$ Perovskite Nanocrystals. *Chem. Mater.* **2017**, *29*, 3644-3652.

3. Hou, J. G.; Wang, B.; Yang, J.; Wang, K.; Lu, W.; Li, Z.; Wang, H.; Chen, D. M.; Zhu, Q., Disorder and Suppression of Quantum Confinement Effects in Pd Nanoparticles. *Phys. Rev. Lett.* **2003**, *90*, 246803.

4. Tong, X., et al., Optoelectronic Properties in near-Infrared Colloidal Heterostructured Pyramidal "Giant" Core/Shell Quantum Dots. *Adv. Sci.* **2018**, *5*, 1800656.

5. Yanover, D.; Vaxenburg, R.; Tilchin, J.; Rubin-Brusilovski, A.; Zaiats, G.; Čapek, R. K.; Sashchiuk, A.; Lifshitz, E., Significance of Small-Sized PbSe/PbS Core/Shell Colloidal Quantum Dots for Optoelectronic Applications. *J.Phys.Chem. C* **2014**, *118*, 17001-17009.

6. Duan, L.; Hu, L.; Guan, X.; Lin, C.-H.; Chu, D.; Huang, S.; Liu, X.; Yuan, J.; Wu, T., Quantum Dots for Photovoltaics: A Tale of Two Materials. *Adv. Energy Mater.* **2021**, *11*, 2100354.

7. Bang, J., et al., ZnTe/ZnSe (Core/Shell) Type-II Quantum Dots: Their Optical and Photovoltaic Properties. *Chem. Mater.* **2010**, *22*, 233-240.

8. Zhou, S., et al., Towards Scalable Synthesis of High-Quality PbS Colloidal Quantum Dots for Photovoltaic Applications. *J. Mater. Chem. C* **2019**, *7*, 1575-1583.

9. Chistyakov, A. A.; Zvaigzne, M. A.; Nikitenko, V. R.; Tameev, A. R.; Martynov, I. L.; Prezhdo, O. V., Optoelectronic Properties of Semiconductor Quantum Dot Solids for Photovoltaic Applications. *J. Phys. Chem. Lett.* **2017**, *8*, 4129-4139.

10. Zhao, H.; Liu, J.; Vidal, F.; Vomiero, A.; Rosei, F., Tailoring the Interfacial Structure of Colloidal "Giant" Quantum Dots for Optoelectronic Applications. *Nanoscale* **2018**, *10*, 17189-17197.

11. Makkar, M.; Viswanatha, R., Frontier Challenges in Doping Quantum Dots: Synthesis and Characterization. *RSC Adv.* **2018**, *8*, 22103-22112.

12. Norris David, J.; Efros Alexander, L.; Erwin Steven, C., Doped Nanocrystals. *Science* **2008**, *319*, 1776-1779.

13. Li, G.; Huang, J.; Zhu, H.; Li, Y.; Tang, J.-X.; Jiang, Y., Surface Ligand Engineering for near-Unity Quantum Yield Inorganic Halide Perovskite Qds and High-Performance Qleds. *Chem. Mater.* **2018**, *30*, 6099-6107.

14. Wang, X.; Qu, L.; Zhang, J.; Peng, X.; Xiao, M., Surface-Related Emission in Highly Luminescent CdSe Quantum Dots. *Nano Lett.* **2003**, *3*, 1103-1106.

15. Leng, M., et al., Surface Passivation of Bismuth-Based Perovskite Variant Quantum Dots to Achieve Efficient Blue Emission. *Nano Lett.* **2018**, *18*, 6076-6083.

16. Pu, C.; Peng, X., To Battle Surface Traps on CdSe/CdS Core/Shell Nanocrystals: Shell Isolation Versus Surface Treatment. *J. Am. Chem.Soc.* **2016**, *138*, 8134-8142.

17. Subila, K. B.; Kishore Kumar, G.; Shivaprasad, S. M.; George Thomas, K., Luminescence Properties of CdSe Quantum Dots: Role of Crystal Structure and Surface Composition. *J. Phys. Chem. Lett.* **2013**, *4*, 2774-2779.

18. Grandhi, G. K.; M, A.; Viswanatha, R., Understanding the Role of Surface Capping Ligands in Passivating the Quantum Dots Using Copper Dopants as Internal Sensor. *J. Phys. Chem. C* **2016**, *120*, 19785-19795.

19. Stouwdam, J. W.; Janssen, R. A. J., Electroluminescent Cu-Doped CdS Quantum Dots. *Adv. Mater.* **2009**, *21*, 2916-2920.

20. Yuan, X.; Hua, J.; Zeng, R.; Zhu, D.; Ji, W.; Jing, P.; Meng, X.; Zhao, J.; Li, H., Efficient White Light Emitting Diodes Based on Cu-Doped ZnInS/ZnS Core/Shell Quantum Dots. *Nanotechnology* **2014**, *25*, 435202.

21. Dutta, A.; Bera, R.; Ghosh, A.; Patra, A., Ultrafast Carrier Dynamics of Photo-Induced Cu-Doped CdSe Nanocrystals. *J. Phys. Chem. C* **2018**, *122*, 16992-17000.

22. Radovanovic, P. V.; Norberg, N. S.; McNally, K. E.; Gamelin, D. R., Colloidal Transition-Metal-Doped ZnO Quantum Dots. *J. Am. Chem. Soc.* **2002**, *124*, 15192-15193.

23. Ca, N. X.; Hien, N. T.; Loan, P. N.; Tan, P. M.; Thuy, U. T. D.; Phan, T. L.; Nguyen, Q. B., Optical and Ferromagnetic Properties of Ni-Doped CdTeSe Quantum Dots. *J. Electron. Mater.* **2019**, *48*, 2593-2599.

24. Le Gall, C.; Brunetti, A.; Boukari, H.; Besombes, L., Optical Stark Effect and Dressed Exciton States in a Mn-Doped CdTe Quantum Dot. *Phys. Rev. Lett.* **2011**, *107*, 057401.

25. Debnath, T.; Maity, P.; Maiti, S.; Ghosh, H. N., Electron Trap to Electron Storage Center in Specially Aligned Mn-Doped CdSe D-Dot: A Step Forward in the Design of Higher Efficient Quantum-Dot Solar Cell. *J. Phys. Chem. Lett.* **2014**, *5*, 2836-2842.

26. Lee, S. M.; Lim, H.; Lee, Y.; Bang, J., Facile in Situ Synthesis of Ag-Doped CdSe Supra-Quantum Dots and Their Characterization. *ChemPhysChem* **2019**, *20*, 1885-1889.

27. Panda, S. K.; Hickey, S. G.; Demir, H. V.; Eychmüller, A., Bright White-Light Emitting Manganese and Copper Co-Doped ZnSe Quantum Dots. *Angew. Chem. Int. Ed.* **2011**, *50*, 4432-4436.

28. Zhang, J. Z.; Cooper, J. K.; Gul, S., Rational Codoping as a Strategy to Improve Optical Properties of Doped Semiconductor Quantum Dots. *J. Phys. Chem. Lett.* **2014**, *5*, 3694-3700.

29. Sakthivel, P.; Muthukumaran, S., Structural, Photoluminescence and Magnetic Properties of Mn, Cr Dual-Doped ZnS Quantum Dots: Influence of Cr Concentration. *J. Phys. Chem. Solids* **2018**, *120*, 183-189.

30. Makkar, M.; Saha, A.; Khalid, S.; Viswanatha, R., Thermodynamics of Dual Doping in Quantum Dots. *J. Phys. Chem. Lett.* **2019**, *10*, 1992-1998.

31. Ca, N. X.; Vinh, N. D.; Bharti, S.; Tan, P. M.; Hien, N. T.; Hoa, V. X.; Peng, Y.; Do, P. V., Optical Properties of Ce^{3+} and Tb^{3+} Co-Doped ZnS Quantum Dots. *J. Alloys Compd.* **2021**, *883*, 160764.

32. Xin, S. H.; Wang, P. D.; Yin, A.; Kim, C.; Dobrowolska, M.; Merz, J. L.; Furdyna, J. K., Formation of Self-Assembling CdSe Quantum Dots on ZnSe by Molecular Beam Epitaxy. *Appl. Phys. Lett.* **1996**, *69*, 3884-3886.

33. Fafard, S.; Wasilewski, Z.; McCaffrey, J.; Raymond, S.; Charbonneau, S., InAs Self-Assembled Quantum Dots on InP by Molecular Beam Epitaxy. *Appl. Phys. Lett.* **1996**, *68*, 991-993.

34. Joyce, P. B.; Krzyzewski, T. J.; Bell, G. R.; Jones, T. S.; Malik, S.; Childs, D.; Murray, R., Effect of Growth Rate on the Size, Composition, and Optical Properties of InAs/GaAs Quantum Dots Grown by Molecular-Beam Epitaxy. *Phys. Rev. B* **2000**, *62*, 10891-10895.

35. Oshinowo, J.; Nishioka, M.; Ishida, S.; Arakawa, Y., Highly Uniform InGaAs/GaAs Quantum Dots (∼15 Nm) by Metalorganic Chemical Vapor Deposition. *Appl. Phys. Lett.* **1994**, *65*, 1421-1423.

36. Liao, M. C. H.; Chang, Y. H.; Chen, Y. F.; Hsu, J. W.; Lin, J. M.; Chou, W. C., Fabrication of ZnSe Quantum Dots under Volmer–Weber Mode by Metalorganic Chemical Vapor Deposition. *Appl. Phys. Lett.* **1997**, *70*, 2256-2258.

37. Surrente, A.; Carron, R.; Gallo, P.; Rudra, A.; Dwir, B.; Kapon, E., Self-Formation of Hexagonal Nanotemplates for Growth of Pyramidal Quantum Dots by Metalorganic Vapor Phase Epitaxy on Patterned Substrates. *Nano Res.* **2016**, *9*, 3279-3290.

38. Paul, M.; Kettler, J.; Zeuner, K.; Clausen, C.; Jetter, M.; Michler, P., Metal-Organic Vapor-Phase Epitaxy-Grown Ultra-Low Density InGaAs/GaAs Quantum Dots Exhibiting Cascaded Single-Photon Emission at 1.3 Mm. *Appl. Phys. Lett.* **2015**, *106*, 122105.

39. Samokhvalov, P.; Artemyev, M.; Nabiev, I., Basic Principles and Current Trends in Colloidal Synthesis of Highly Luminescent Semiconductor Nanocrystals. *Chem. Eur. J.* **2013**, *19*, 1534-1546.

40. Tessier, M. D.; Dupont, D.; De Nolf, K.; De Roo, J.; Hens, Z., Economic and Size-Tunable Synthesis of InP/ZnE (E = S, Se) Colloidal Quantum Dots. *Chem. Mater.* **2015**, *27*, 4893-4898.

41. Zhuang, Z.; Peng, Q.; Li, Y., Controlled Synthesis of Semiconductor Nanostructures in the Liquid Phase. *Chem. Soc. Rev.* **2011**, *40*, 5492-5513.

42. Murray, C.; Norris, D. J.; Bawendi, M. G., Synthesis and Characterization of Nearly Monodisperse CdE (E= Sulfur, Selenium, Tellurium) Semiconductor Nanocrystallites. *J. Am. Chem. Soc.* **1993**, *115*, 8706-8715.

43. Pradhan, N.; Goorskey, D.; Thessing, J.; Peng, X., An Alternative of CdSe Nanocrystal Emitters: Pure and Tunable Impurity Emissions in ZnSe Nanocrystals. *J. Am. Chem. Soc.* **2005**, *127*, 17586-17587.

44. Li, L. S.; Pradhan, N.; Wang, Y.; Peng, X., High Quality ZnSe and ZnS Nanocrystals Formed by Activating Zinc Carboxylate Precursors. *Nano Lett.* **2004**, *4*, 2261-2264.

45. Yu, W. W.; Peng, X., Formation of High-Quality Cds and Other II–VI Semiconductor Nanocrystals in Noncoordinating Solvents: Tunable Reactivity of Monomers. *Angew. Chem. Int. Ed.* **2002**, *41*, 2368-2371.

46. Pu, Y.; Cai, F.; Wang, D.; Wang, J.-X.; Chen, J.-F., Colloidal Synthesis of Semiconductor Quantum Dots toward Large-Scale Production: A Review. *Ind. Eng. Chem. Res.* **2018**, *57*, 1790-1802.

47. Norris, D. J.; Yao, N.; Charnock, F. T.; Kennedy, T. A., High-Quality Manganese-Doped ZnSe Nanocrystals. *Nano Lett.* **2001**, *1*, 3-7.

48. Grandhi, G. K.; Tomar, R.; Viswanatha, R., Study of Surface and Bulk Electronic Structure of II–VI Semiconductor Nanocrystals Using Cu as a Nanosensor. *ACS Nano* **2012**, *6*, 9751-9763.

49. Bhargava, R. N.; Gallagher, D.; Hong, X.; Nurmikko, A. J., Optical Properties of Manganese-Doped Nanocrystals of ZnS. *Phys. Rev. Lett.* **1994**, *72*, 416.

50. Saha, A.; Makkar, M.; Shetty, A.; Gahlot, K.; Pavan, A. R.; Viswanatha, R., Diffusion Doping in Quantum Dots: Bond Strength and Diffusivity. *Nanoscale* **2017**, *9*, 2806-2813.

51. Schwartz, D. A.; Kittilstved, K. R.; Gamelin, D. R., Above-Room-Temperature Ferromagnetic Ni^{2+}-Doped ZnO Thin Films Prepared from Colloidal Diluted Magnetic Semiconductor Quantum Dots. *Appl. Phys. Lett.* **2004**, *85*, 1395-1397.

52. Hanif, K. M.; Meulenberg, R. W.; Strouse, G. F., Magnetic Ordering in Doped $Cd_{1-x}Co_xSe$ Diluted Magnetic Quantum Dots. *J. Am. Chem. Soc.* **2002**, *124*, 11495-11502.

53. Bonanni, A.; Dietl, T., A Story of High-Temperature Ferromagnetism in Semiconductors. *Chem. Soc. Rev.* **2010**, *39*, 528-539.

54. Grandhi, G. K.; Swathi, K.; Narayan, K. S.; Viswanatha, R., Cu Doping in Ligand Free CdS Nanocrystals: Conductivity and Electronic Structure Study. *J. Phys. Chem. Lett.* **2014**, *5*, 2382-2389.

55. Sahu, A.; Kang, M. S.; Kompch, A.; Notthoff, C.; Wills, A. W.; Deng, D.; Winterer, M.; Frisbie, C. D.; Norris, D. J., Electronic Impurity Doping in CdSe Nanocrystals. *Nano Lett.* **2012**, *12*, 2587-2594.

56. Viswanatha, R.; Pietryga, J. M.; Klimov, V. I.; Crooker, S. A., Spin-Polarized Mn^{2+} Emission from Mn-Doped Colloidal Nanocrystals. *Phys. Rev. Lett.* **2011**, *107*, 067402.

57. Fuhr, A.; Yun, H. J.; Crooker, S. A.; Klimov, V. I., Spectroscopic and Magneto-Optical Signatures of Cu^{1+} and Cu^{2+} Defects in Copper Indium Sulfide Quantum Dots. *ACS Nano* **2020**, *14*, 2212-2223.

58. Chuang, C.-H. M.; Brown, P. R.; Bulović, V.; Bawendi, M. G., Improved Performance and Stability in Quantum Dot Solar Cells through Band Alignment Engineering. *Nat. Mater.* **2014**, *13*, 796-801.

59. Carey, G. H.; Kramer, I. J.; Kanjanaboos, P.; Moreno-Bautista, G.; Voznyy, O.; Rollny, L.; Tang, J. A.; Hoogland, S.; Sargent, E. H., Electronically Active Impurities in Colloidal Quantum Dot Solids. *ACS Nano* **2014**, *8*, 11763-11769.

60. Steckel, J. S.; Snee, P.; Coe-Sullivan, S.; Zimmer, J. P.; Halpert, J. E.; Anikeeva, P.; Kim, L.-A.; Bulovic, V.; Bawendi, M. G., Color-Saturated Green-Emitting QD-LEDs. *Angew. Chem. Int. Ed.* **2006**, *45*, 5796-5799.

61. Park, S.-J.; Song, S.-H.; Kim, S. S.; Song, J.-K., Charge Modulation Layer and Wide-Color Tunability in a QD-LED with Multiemission Layers. *Small* **2021**, *17*, 2007397.

62. Oertel, D. C.; Bawendi, M. G.; Arango, A. C.; Bulović, V., Photodetectors Based on Treated CdSe Quantum-Dot Films. *Appl. Phys. Lett.* **2005**, *87*, 213505.

63. Ren, Z.; Sun, J.; Li, H.; Mao, P.; Wei, Y.; Zhong, X.; Hu, J.; Yang, S.; Wang, J., Bilayer PbS Quantum Dots for High-Performance Photodetectors. *Adv. Mater.* **2017**, *29*, 1702055.

64. Beaulac, R.; Archer, P. I.; Ochsenbein, S. T.; Gamelin, D. R., Mn^{2+}-Doped CdSe Quantum Dots: New Inorganic Materials for Spin-Electronics and Spin-Photonics. *Adv. Funct. Mater.* **2008**, *18*, 3873-3891.

65. Levy, L.; Hochepied, J. F.; Pileni, M. P., Control of the Size and Composition of Three Dimensionally Diluted Magnetic Semiconductor Clusters. *J. Phys. Chem.* **1996**, *100*, 18322-18326.

66. Suyver, J.; Wuister, S.; Kelly, J.; Meijerink, A., Luminescence of Nanocrystalline ZnSe: Mn^{2+}. *Phys. Chem. Chem. Phys.* **2000**, *2*, 5445-5448.

67. Dalpian, G. M.; Chelikowsky, J. R., Self-Purification in Semiconductor Nanocrystals. *Phys. Rev. Lett.* **2006**, *96*, 226802.

68. Erwin, S. C.; Zu, L.; Haftel, M. I.; Efros, A. L.; Kennedy, T. A.; Norris, D. J., Doping Semiconductor Nanocrystals. *Nature* **2005**, *436*, 91-94.

69. Chen, D.; Viswanatha, R.; Ong, G. L.; Xie, R.; Balasubramaninan, M.; Peng, X., Temperature Dependence of "Elementary Processes" in Doping Semiconductor Nanocrystals. *J. Am. Chem. Soc.* **2009**, *131*, 9333-9339.

70. Grandhi, G. K.; Viswanatha, R., Demystifying Complex Quantum Dot Heterostructures Using Photogenerated Charge Carriers. *J. Phys. Chem. Lett.* **2017**, *8*, 2043-2048.

71. Tananaev, P. N.; Dorofeev, S. G.; Vasil'ev, R. B.; Kuznetsova, T. A., Preparation of Copper-Doped CdSe Nanocrystals. *Inorg. Mater.* **2009**, *45*, 347-351.

72. Saha, A.; Shetty, A.; Pavan, A. R.; Chattopadhyay, S.; Shibata, T.; Viswanatha, R., Uniform Doping in Quantum-Dots-Based Dilute Magnetic Semiconductor. *J. Phys. Chem. Lett.* **2016**, *7*, 2420-2428.

73. Viswanatha, R.; Naveh, D.; Chelikowsky, J. R.; Kronik, L.; Sarma, D. D., Magnetic Properties of Fe/Cu Codoped ZnO Nanocrystals. *J. Phys. Chem. Lett.* **2012**, *3*, 2009-2014.

74. Yuan, X.; Ma, R.; Zhang, W.; Hua, J.; Meng, X.; Zhong, X.; Zhang, J.; Zhao, J.; Li, H., Dual Emissive Manganese and Copper Co-Doped Zn–In–S Quantum Dots as a Single Color-Converter for High Color Rendering White-Light-Emitting Diodes. *ACS Appl. Mater. Interfaces* **2015**, *7*, 8659-8666.

75. Cao, S.; Zheng, J.; Zhao, J.; Yang, Z.; Shang, M.; Li, C.; Yang, W.; Fang, X., Robust and Stable Ratiometric Temperature Sensor Based on Zn–In–S Quantum Dots with Intrinsic Dual-Dopant Ion Emissions. *Adv. Funct. Mater.* **2016**, *26*, 7224-7233.

76. Saha, A.; Gahlot, K.; Viswanatha, R., Exciton Dynamics in Mn/Ni Dual-Doped Semiconductor Quantum Dots. *ChemNanoMat* **2022**, *8*, e202100457.

77. Shim, J. H.; Hwang, T.; Lee, S.; Park, J. H.; Han, S.-J.; Jeong, Y. H., Origin of Ferromagnetism in Fe- and Cu-Codoped ZnO. *Appl. Phys. Lett.* **2005**, *86*, 082503.

78. Radovanovic, P. V.; Gamelin, D. R., High-Temperature Ferromagnetism in Ni^{2+}-Doped ZnO Aggregates Prepared from Colloidal Diluted Magnetic Semiconductor Quantum Dots. *Phys. Rev. Lett.* **2003**, *91*, 157202.

79. Nag, A.; Cherian, R.; Mahadevan, P.; Gopal, A. V.; Hazarika, A.; Mohan, A.; Vengurlekar, A. S.; Sarma, D. D., Size-Dependent Tuning of Mn^{2+} d Emission in Mn^{2+}-Doped CdS Nanocrystals: Bulk Vs Surface. *J. Phys. Chem. C* **2010**, *114*, 18323-18329.

80. Beaulac, R.; Archer, P. I.; van Rijssel, J.; Meijerink, A.; Gamelin, D. R., Exciton Storage by Mn^{2+} in Colloidal Mn^{2+}-Doped CdSe Quantum Dots. *Nano Lett.* **2008**, *8*, 2949-2953.

81. Bol, A. A.; Meijerink, A., Long-Lived Mn^{2+} Emission in Nanocrystalline ZnS: Mn^{2+}. *Phys. Rev. B* **1998**, *58*, R15997.

82. Türe, I. E.; Claybourn, M.; Brinkman, A. W.; Woods, J., Copper Centers in CdSe. *J. Appl. Phys.* **1986**, *60*, 1670-1675.

83. Viswanatha, R.; Brovelli, S.; Pandey, A.; Crooker, S. A.; Klimov, V. I., Copper-Doped Inverted Core/Shell Nanocrystals with "Permanent" Optically Active Holes. *Nano Lett.* **2011**, *11*, 4753-4758.

84. Karan, N. S.; Sarma, D. D.; Kadam, R. M.; Pradhan, N., Doping Transition Metal (Mn or Cu) Ions in Semiconductor Nanocrystals. *J. Phys. Chem. Lett.* **2010**, *1*, 2863-2866.

85. Srivastava, B. B.; Jana, S.; Pradhan, N., Doping Cu in Semiconductor Nanocrystals: Some Old and Some New Physical Insights. *J. Am. Chem. Soc.* **2011**, *133*, 1007-1015.

86. Jana, S.; Srivastava, B. B.; Jana, S.; Bose, R.; Pradhan, N., Multifunctional Doped Semiconductor Nanocrystals. *J. Phys. Chem. Lett.* **2012**, *3*, 2535-2540.

87. Jana, S.; Manna, G.; Srivastava, B. B.; Pradhan, N., Tuning the Emission Colors of Semiconductor Nanocrystals Beyond Their Bandgap Tunability: All in the Dope. *Small* **2013**, *9*, 3753-3758.

88. Leslie-Pelecky, D. L.; Rieke, R. D., Magnetic Properties of Nanostructured Materials. *Chem. Mater.* **1996**, *8*, 1770-1783.

89. Wu, L.; Mendoza-Garcia, A.; Li, Q.; Sun, S., Organic Phase Syntheses of Magnetic Nanoparticles and Their Applications. *Chem. Rev.* **2016**, *116*, 10473-10512.

90. Talapin, D. V.; Lee, J.-S.; Kovalenko, M. V.; Shevchenko, E. V., Prospects of Colloidal Nanocrystals for Electronic and Optoelectronic Applications. *Chem. Rev.* **2010**, *110*, 389-458.

91. Fainblat, R.; Barrows, C. J.; Gamelin, D. R., Single Magnetic Impurities in Colloidal Quantum Dots and Magic-Size Clusters. *Chem. Mater.* **2017**, *29*, 8023-8036.

92. Makkar, M.; Viswanatha, R., Recent Advances in Magnetic Ion-Doped Semiconductor Quantum Dots. *Curr. Sci.* **2017**, *112*, 1421-1429.

93. Schwartz, D. A.; Norberg, N. S.; Nguyen, Q. P.; Parker, J. M.; Gamelin, D. R., Magnetic Quantum Dots: Synthesis, Spectroscopy, and Magnetism of Co^{2+}- and Ni^{2+}-Doped ZnO Nanocrystals. *J. Am. Chem. Soc.* **2003**, *125*, 13205-13218.

94. Ohno, H., Making Nonmagnetic Semiconductors Ferromagnetic. *Science* **1998**, *281*, 951-956.

95. Norberg, N. S.; Parks, G. L.; Salley, G. M.; Gamelin, D. R., Giant Excitonic Zeeman Splittings in Colloidal Co^{2+}-Doped ZnSe Quantum Dots. *J. Am. Chem. Soc.* **2006**, *128*, 13195-13203.

96. Panmand, R. P.; Tekale, S. P.; Daware, K. D.; Gosavi, S. W.; Jha, A.; Kale, B. B., Characterisation of Spectroscopic and Magneto-Optical Faraday Rotation in Mn^{2+}- Doped CdS Quantum Dots in a Silicate Glass. *J. Alloys Compd.* **2020**, *817*, 152696.

97. Beaulac, R.; Schneider, L.; Archer, P. I.; Bacher, G.; Gamelin, D. R., Light-Induced Spontaneous Magnetization in Doped Colloidal Quantum Dots. *Science* **2009**, *325*, 973-976.

98. Fainblat, R.; Frohleiks, J.; Muckel, F.; Yu, J. H.; Yang, J.; Hyeon, T.; Bacher, G., Quantum Confinement-Controlled Exchange Coupling in Manganese(II)-Doped CdSe Two-Dimensional Quantum Well Nanoribbons. *Nano Lett.* **2012**, *12*, 5311-5317.

99. Shim, M.; Guyot-Sionnest, P., N-Type Colloidal Semiconductor Nanocrystals. *Nature* **2000**, *407*, 981-983.

100. Talapin Dmitri, V.; Murray Christopher, B., PbSe Nanocrystal Solids for N- and P-Channel Thin Film Field-Effect Transistors. *Science* **2005**, *310*, 86-89.

101. Wang, C.; Shim, M.; Guyot-Sionnest, P., Electrochromic Nanocrystal Quantum Dots. *Science* **2001**, *291*, 2390-2392.

102. Roest, A. L.; Kelly, J. J.; Vanmaekelbergh, D.; Meulenkamp, E. A., Staircase in the Electron Mobility of a ZnO Quantum Dot Assembly Due to Shell Filling. *Phys. Rev. Lett.* **2002**, *89*, 036801.

103. Geyer, S. M.; Allen, P. M.; Chang, L.-Y.; Wong, C. R.; Osedach, T. P.; Zhao, N.; Bulovic, V.; Bawendi, M. G., Control of the Carrier Type in InAs Nanocrystal Films by Predeposition Incorporation of Cd. *ACS Nano* **2010**, *4*, 7373-7378.

104. Freeman, R.; Willner, I., Optical Molecular Sensing with Semiconductor Quantum Dots (QDs). *Chem. Soc. Rev.* **2012**, *41*, 4067-4085.

105. Cherepanov, D.; Kostrov, A.; Gostev, F.; Shelaev, I.; Motyakin, M.; Kochev, S.; Kabachii, Y.; Nadtochenko, V., Ultrafast Quenching of Excitons in the $Zn_xCd_{1-X}S$/ZnS

Quantum Dots Doped with Mn^{2+} through Charge Transfer Intermediates Results in Manganese Luminescence. *Nanomaterials* **2021**, *11*.

106. K. R, P.; Viswanatha, R., Mechanism of Mn Emission: Energy Transfer Vs Charge Transfer Dynamics in Mn-Doped Quantum Dots. *APL Mater.* **2020**, *8*, 020901.

107. Hsia, C.-H.; Wuttig, A.; Yang, H., An Accessible Approach to Preparing Water-Soluble Mn^{2+}-Doped (CdSSe)ZnS (Core)Shell Nanocrystals for Ratiometric Temperature Sensing. *ACS Nano* **2011**, *5*, 9511-9522.

108. Chen, H.-Y.; Chen, T.-Y.; Son, D. H., Measurement of Energy Transfer Time in Colloidal Mn-Doped Semiconductor Nanocrystals. *J. Phys. Chem. C* **2010**, *114*, 4418-4423.

109. Chen, H.-Y.; Maiti, S.; Son, D. H., Doping Location-Dependent Energy Transfer Dynamics in Mn-Doped CdS/ZnS Nanocrystals. *ACS Nano* **2012**, *6*, 583-591.

110. Gahlot, K.; KR, P.; Camellini, A.; Sirigu, G.; Cerullo, G.; Zavelani-Rossi, M.; Singh, A.; Waghmare, U. V.; Viswanatha, R., Transient Species Mediating Energy Transfer to Spin-Forbidden Mn d States in II–VI Semiconductor Quantum Dots. *ACS Energy Lett.* **2019**, *4*, 729-735.

Chapter 2

Methodology

In this chapter, several experimental methods, as well as a few advanced spectroscopic techniques that have been employed to characterize and study various nanocrystal systems, are discussed in detail. For instance, characterization techniques like UV-visible absorption spectroscopy, photoluminescence (PL) spectroscopy, transmission electron microscopy (TEM), X-ray diffraction (XRD), inductively coupled plasma-optical emission spectroscopy (ICP-OES), electron paramagnetic resonance (EPR) spectroscopy and other advanced spectroscopic techniques like extended X-ray absorption fine structure spectroscopy (EXAFS), single-particle fluorescence spectroscopy, transient absorption (TA) spectroscopy have been used in the work described in this thesis.

2.1. UV-visible absorption spectroscopy

UV-visible absorption spectroscopy happens to be a powerful technique to obtain the bandgap of the semiconductor quantum dots (QDs). Absorption of ultraviolet and visible rays promotes the electron from lower energy to a higher energy state, specifically from the valence band to the conduction band in semiconductor QDs, leading to the formation of an electron-hole pair (exciton). The resultant spectrum is dominated by the absorption feature corresponding to the transition across the bandgap of the QDs.

Typically, when a beam of light hits the material, it may undergo absorption, reflection, interference, and scattering before it is measured by the detector. Thus, the intensity of the transmitted light (I_t) will be reduced as compared to the incident light (I_0).

The change in intensity of light is expressed as:

$$\Delta I = I_0 - I_t$$

Now, the transmittance is defined as the fraction of light that passes through the substance. The % transmittance is given by:

$$\%T = 100\ (I_t/I_0)$$

Absorbance is defined as the amount of light absorbed by a substance and is calculated as the negative logarithm of transmittance.

$$A = \log_{10}(I_0/I_t) = \log_{10}(1/T) = -\log_{10}(T) = 2 - \log_{10}(\%T)$$

Here, we have used Beer-Lambert law to determine the concentration of the absorbing species in solution and is expressed by the equation:

$$A = \varepsilon.c.l$$

Where A = absorbance, ε = molar extinction co-efficient, c = concentration of the sample, and l = cell length.

In this thesis, all the nanocrystals that are studied have bandgaps in the UV-visible region of the electromagnetic spectrum and absorption spectroscopy has been used to determine the bandgap and absorption characteristics of different QDs. The nanocrystals were dissolved in hexane and the measurements were carried out in Agilent 8453 UV-visible spectrophotometer. Due to the quantum confinement effect shown by QDs, size-dependent bandgap change is observed which is quantified using UV-visible absorption spectra.

2.2. Photoluminescence (PL) spectroscopy

Photoluminescence is a subsequent process to absorption where a molecule or a fluorophore emits energy in the form of photons. In our study, the fluorophore is semiconductor nanocrystals that generate exciton upon absorption of light, and when the exciton radiatively recombines it gives rise to photoluminescence. The photo-excitation and relaxation processes that are involved in originating photoluminescence are illustrated by a simple electronic band-structure diagram depicted below in Figure 2.1.

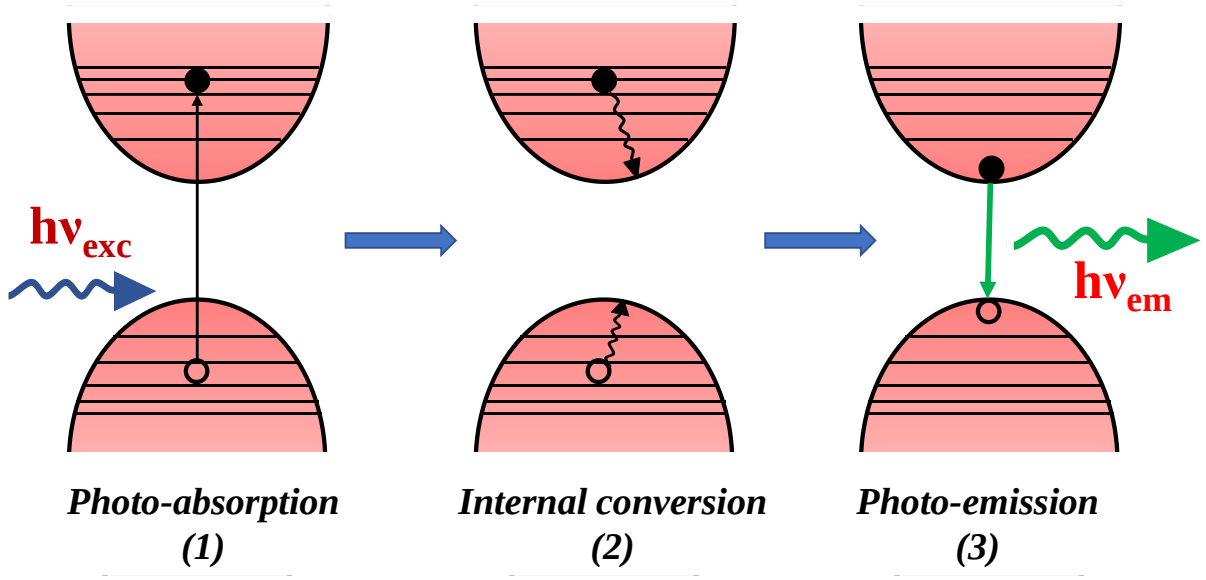

Figure 2.1. *Electronic band-structure diagram illustrating the processes involved in generating an excited electronic state by optical absorption followed by photo-emission through excitonic recombination.*

As is illustrated in the figure, the entire process involves three subsequent steps namely, photo-absorption, internal conversion, and photo-emission. An electron is excited from its ground electronic state (valence band) to its excited electronic state (conduction band) by absorbing a photon of higher energy than the bandgap. The excited electron then relaxes through either non-radiative recombination in the form of heat or vibrationally relaxes to the lowest energy excited state which is assigned to the process named internal conversion. Then the electron at the lowest energy conduction band (CB) state radiatively recombines with the photo-generated hole at the valence band (VB) giving rise to the emission of photons. It is important to note here that the excited electron dissipates some energy in the form of heat during the relaxation through vibrational levels and hence, the energy of the emitted photon ($h\nu_{em}$) is generally lower than that of the absorbing photon ($h\nu_{exc}$). This difference in energy is known as Stokes' shift. To study the nanocrystals, we recorded the PL both as a function of wavelength and time after the excitation.

2.2.1. Steady state PL spectroscopy

Steady state PL involves the measurements of long-term average fluorescence in which the intensity of light emitted by the nanocrystals that are under continuous illumination is detected as a function of the wavelength of the spectrum. Steady state PL spectroscopy is useful in determining the electronic structure and properties of nanocrystals as it gives rise to the peak intensity at a certain wavelength that a material is able to emit. Apart from the excitonic recombination, the charge carriers can also recombine with the defect states/trap states present in the QD systems and this recombination process can either be radiative or non-radiative. Nevertheless, these trap states significantly alter the surface electronic structure of the QDs, and hence, steady state PL can be used to study the QD surfaces as well.

2.2.1.1. Jacobian transformation

Conventionally, in spectroscopic measurements, spectra are recorded as a function of wavelength. In PL spectroscopy, emission intensity and spectral profile are extensively analyzed to explore the bulk and surface electronic structure of the nanocrystal systems. However, simply plotting the intensity versus wavelength is insufficient to extract such information especially when the spectra consist of multiple peaks or the peak is broadened. In contrast to that, the presentation of the data as a function of energy provides more insights into it. However, direct conversion of wavelength to energy using the equation $E = h\frac{c}{\lambda}$ will lead to an inappropriate interpretation of the data. Because of the inverse relationship between the

wavelength and energy, the difference dλ in the wavelength spectrum is not evenly spaced in the energy spectrum. If the collected spectrum in wavelength scale is considered as a function $f(\lambda)$, then from the rule of energy conservation,

$$f(E)dE = f(\lambda)d\lambda$$

$$f(E) = f(\lambda)\frac{d\lambda}{dE} = f(\lambda)\frac{d}{dE}\left(\frac{hc}{E}\right)$$

$$f(E) = -f(\lambda)\left(\frac{hc}{E^2}\right)$$

Thus, in order to avoid this possible intervention of error, the scaling factor hc/E^2 is to be used while converting a plot from wavelength scale to energy scale unit, which is known as the Jacobian transformation.[1] This conversion is very important when the spectra are broad enough to cover a wide range of energies compared to the ones which are having narrow full-width half maximum (fwhm). In the case of QDs with broad dopant emission or trap-state related emission band along with the band edge PL, the transformation significantly alters the spectrum with a slight redshift and intensity change. We have applied this correction to all the PL spectra shown in the thesis.

2.2.2. Time-resolved PL (TrPL)

Time-resolved PL (TrPL) is a powerful experimental technique to investigate the recombination dynamics of the charge carriers as a function of time after the excitation using pulsed light source. The time resolution can be attained in a number of ways which depends on the required sensitivity and time resolution. TCSPC (Time-Correlated Single Photon Counting) is one of them and it is a digital counting technique which counts the photons that are time-correlated in relation to a short excitation light pulse. This technique is used to find radiative and nonradiative lifetimes of exciton pairs in semiconductor QDs. Experimental time-resolved luminescence decays are analyzed by using the following equation:

$$I(t) = \sum_{i=1}^{n} \alpha_i \exp(-t/\tau_i)$$

Here, n is the number of discrete emissive species i.e., no. of decay components, τ_i is the excited-state fluorescence lifetime, and α_i is the amplitude associated with the ith component. For multi-exponential decay (n), the amplitude average lifetime, $\langle\tau\rangle$, is calculated by using the equation:

$$\langle \tau \rangle = \sum_{i=1}^{n} \alpha_i \tau_i^2 / \sum_{i=1}^{n} \alpha_i \tau_i$$

In this thesis, we have extensively used this technique to obtain the average lifetimes of emission in different QDs. We used a 450 W xenon lamp as the source on the FLSP920 spectrometer, Edinburgh instrument, for the excitation of the QDs, while the photoluminescence decay dynamics (Time-resolved PL) measurements were carried out using the EPL-405 ps pulsed diode laser. The micro flash lamp is used to record the long-lived delayed emission lifetime. All the solution-based measurements were performed by dissolving the QDs in hexane collected using a 450 W xenon lamp as the excitation source on the FLSP920 spectrometer, Edinburgh Instruments.

2.2.3. Gated PL spectroscopy

The PL emission decay lifetime depends on many factors like the extent of wavefunction overlap, spin, and orbital selectivity between the states through which transition occurs and hence can vary for different emissions observed in a sample. To differentiate the long-lived delayed PL emissions from the short-lived one(s), a technique integrated into the PL emission spectrometer can be used. Here, the difference in recombination time between short-lived and long-lived components is exploited and the emission spectra are recorded with a time delay of a few microseconds to trace only the long-lived emissions.

2.2.4. Temperature-dependent PL spectroscopy

Herein, the PL spectra and the recombination lifetime are measured as a function of temperature. Since the electron-phonon interaction usually decreases at low temperature, it reduces the non-radiative recombination at low temperature resulting in enhanced PL intensity and average lifetime. Additionally, a few thermally activated decay channels will be inaccessible at lower temperatures in several QD systems. The QDs dispersed in hexane were drop cast on a glass substrate and the solvent was allowed to evaporate leaving behind the QDs forming a thin film. Low-temperature PL emission, TrPL, and gated PLE measurements were performed using Optistat DN2 liquid nitrogen cryostat, Oxford Instrument. Thin films were cooled down to 80 K while starting the measurements and the data were recorded at different intervals of temperature while increasing the temperature to 300 K. Few high-temperature measurements were performed using ARS cryostat, Edinburgh Instruments. Measurements were done at every 10 K interval while increasing the temperature to 350 K. The subsequent chapters will discuss this in detail.

2.2.5. PL quantum yield (PLQY)

The PL QY is defined as the ratio of the number of photons emitted to the number of photons absorbed. It provides information on how the excited charge carriers relax either through radiative or non-radiative processes. If all the excited photons decay radiatively to the ground state, PLQY will be 100%.

$$\text{PLQY} = \frac{\text{Number of emitted photons}}{\text{Number of absorbed photons}}$$

Experimentally, PLQY can be measured by the comparative method or absolute method.[2] The comparative method involves the use of well-characterized standard samples with known QY values and is widely used in weakly absorbing samples in dilute solutions. The solutions of the reference and test samples with identical absorbance at the same excitation wavelength can be assumed to be absorbing the same number of photons. Hence, the ratio of the integrated PL intensities of the two solutions (recorded under the same slit width, dwell time, and other conditions) will yield the ratio of the QY values. Since QY for the reference sample is already known, it is very trivial to calculate the QY for the sample under measurement from the equation given below.

$$\text{QY}_{\text{sample}} = \frac{I_{sample} \times A_{ref} \times \eta_{sample}}{I_{ref} \times A_{sample} \times \eta_{ref}} \times \text{QY}_{\text{ref}}$$

where I= integrated PL Intensity, A= absorbance at an excitation wavelength, and η= refractive index of the solvent.

However, this method strongly depends on the reference sample and there are only a few organic molecules/dyes available as reference samples in visible-NIR wavelengths putting a limit to this method from measuring PLQY in solution phase as the method requires similar optical properties for the standard as well as the sample. These limitations can be overcome by employing an integrating sphere that collects all the emissions from the sample and this method is known as the Absolute method. In the present work, we have used this method to calculate the PLQY of the QD sample. It involves measuring the scattering spectra of solvent and samples along with the emission spectrum of the sample. The intensity of the scattering spectrum of the sample is less than that of solvent as the QDs present in the sample absorbs the incident light. The number of photons absorbed by the sample will be given by the intensity difference in the scattering spectra of solvent and sample. Then with the help of the emission

spectrum which gives the number of photons emitted and the intensity difference in the scattering spectra, the calculation of PLQY of the sample is trivial.

2.3. X-ray diffraction (XRD)

XRD is a non-destructive analytical technique that reveals information about materials and thin films' crystallographic structure, chemical composition, and physical properties.[3] This technique is based on observing the scattered intensity of an X-ray beam hitting a sample due to incident and scattered angle, polarization, and wavelength or energy. The intensity of diffracted X-rays is measured as a function of the diffraction angle 2θ.

For diffraction applications, only short-wavelength X-rays (hard X-rays) in the range of a few angstroms to 0.1 angstroms (1 keV-120 keV) are used. As the X-ray wavelength is comparable to the size of the atoms, they are ideally suited for probing the structural arrangement of atoms and molecules in a wide range of materials. When crystals are irradiated with X-rays, crystal atoms scatter X-ray waves, primarily through the atomic electrons. Also, X-ray striking an electron produces secondary spherical waves emanating from the electron. This phenomenon is known as scattering, and the electron is known as the scatterer. A regular array of scatterers produces a regular array of spherical waves. Although these waves cancel one another out in most directions (destructive interference), they add constructively in a few specific directions, determined by Bragg's law, illustrated in Figure 2.2.

$$2d \sin \theta = n\lambda$$

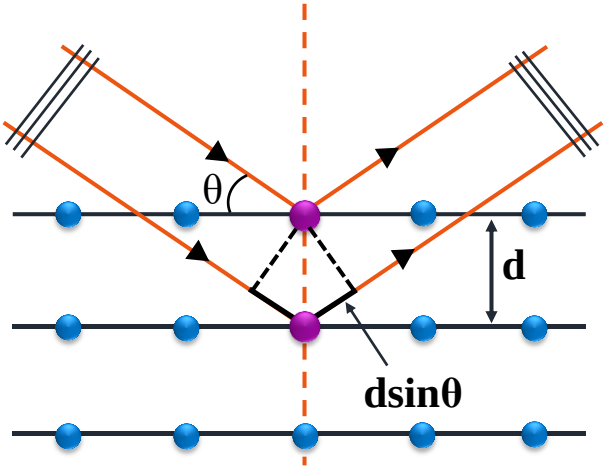

Figure 2.2. *A schematic demonstration of X-ray diffraction.*

where *n* is an integer representing the order of the X-ray, θ is the scattering angle, and λ is the wavelength of the X-ray. These specific directions appear as spots on the diffraction pattern, often called reflections. Thus, x-ray diffraction results from an electromagnetic wave (the X-ray) impinging on a regular array of scatters (the repeating arrangement of atoms within the crystal).

Generally, the broadenings of the diffraction peaks depend upon crystallite size and strain. The crystallite size of the nanoparticles can be obtained from the broadened XRD pattern. The crystallite sizes are calculated using the Scherrer equation:

$$D_{hkl} = K\lambda / \beta_{hkl} \cos \theta$$

where K = 0.89 and related to shape factor, D_{hkl} represents crystallite size (Å), λ is the wavelength of Cu kα radiation, β_{hkl} is the corrected half-width of the diffraction peak, and θ is the Bragg angle.

We have carried out powder X-ray diffraction experiments on the samples using Bruker D8 Advance diffractometer using Cu-Kα radiation having wavelength 1.5406 Å. Powder or precipitates of the sample were placed on a sample holder during measurement. Since the diffraction peak intensity from the QDs is very weak, we have taken scans for sufficient intensity at a slow scan rate to obtain a reasonable signal-to-noise ratio. The bulk XRD patterns were obtained from the inorganic crystal structure database (ICSD) for the crystal structure analysis.

2.4. Transmission electron microscopy (TEM)

One of the efficient microscopic techniques is transmission electron microscopy (TEM). A beam of electrons is transmitted through an ultra-thin specimen, interacting with the sample as it passes through it.[4] The image appears on an imaging screen from the collection of the magnified and focused transmitted electron through the sample. High-resolution TEM (HRTEM) provides the size, shape, and lattice-fringes of the nanocrystals.

The basic working principle of TEM is similar to the optical microscope. However, the wavelength of light limits the use of optical microscope. Thus, in order to get a better resolution which is the basic criteria to study the nanocrystals, TEM uses electrons as a probe source having a much lower wavelength as compared to light. The beam of electrons sourced from the electron gun is focused into a small, thin, coherent beam by the use of electromagnetic condenser lenses. The beam then strikes the sample and parts of it are transmitted depending

upon the thickness and electron transparency of the sample. The transmitted portion is focused by the objective lens into an image on a charge-coupled device camera, to obtain the image of the sample. We have used TEM to study the crystalline quality, shape, size, defects in semiconductors QDs as well as growth of layers in core/shell materials. We have used this technique to study the formation, size, and shape of the QDs. The monodispersity of the formed QDs was examined by calculating the size distribution of a large number of QDs present on the TEM grid.

2.5. Inductively coupled plasma-optical emission spectroscopy

This technique is extensively used for the quantitative detection of the elements present in the given unknown sample or to determine the composition of constituents in a given sample. The instrument consists of a light source unit, plasma generator, spectrometer, detector, and a data processing unit. The elemental components of the material are first excited into higher energy levels by applying plasma (ionized gas) energy having a very high electron density and temperature (up to 8000 K). Sample solutions are then sent into the plasma environment through a capillary. The excited atoms relax to their lower energy states by emitting photons, and the type of element is determined based on the energy of the emitted photons, and the content of each element is determined based on the signal intensity.

We have used ICP-OES mainly for detecting the percentage of dopants in various doped-QDs as well as cation composition in alloy QDs. The samples were prepared by washing the QDs several times to remove excess precursors and then digested in a concentrated HNO_3-HCl mixture followed by dilution with 2% HNO_3-Millipore water to match the matrix with the commercial standards. ICP-OES measurements were then carried out using a Perkin-Elmer Optima 7000 DV instrument.

2.6. Single-particle fluorescence spectroscopy

Currently single-particle fluorescence spectroscopy is one of the most commonly used spectroscopic technique. The basis of single-molecule fluorescence microscopy is the labeling of the molecules of interest with a fluorophore and observing it in an optical microscope. Depending on the experimental system, these fluorophores should be preferably bright and show a desired photophysics. In our study, the nanocrystals are the fluorophores. Here along with tracing the single particles through a fluorescence microscope, we study the photoluminescence properties (such as, PL blinking, steady state and time-resolved PL) of individual nanocrystals. To study the behavior of the NCs at a single-particle level, the

concentration of NCs in solution should be low enough. Purified NCs were dissolved in toluene and diluted using poly(methyl methacrylate) (PMMA) solution. Then, the diluted NC solution was spun cast onto a glass coverslip at 2,500 rpm for 60 s. Specifically, the synthesized NCs are capped with different long-chain organic ligands such as oleic acid, oleylamine, etc[5] and on the other hand, lone pair electrons present on the oxygen atom make PMMA capable of coordination with the active site of NCs. As a result, the surface capping of the NCs might be substituted partially by PMMA.[6] PMMA majorly interacts with the surface of the NCs and the chemical environment in the bulk of the NCs remains intact, which helps in retaining their pristine PL emission under the optimal ratio of the NCs with the PMMA as has been extensively studied in the literature.[6]

Single-particle fluorescence imaging was performed using a confocal inverted microscope Olympus IX73 equipped with an oil immersion objective (Olympus 100X/NA 1.4) and the 404 nm output of a 1 MHz, picosecond pulsed diode laser was used as the excitation source. The laser beam was focused onto the sample substrate by the immersion-oil objective (NA = 1.4). The PL signal of a single NC was collected by the same objective and sent through a 0.5 m spectrometer to an ultrasensitive electron-multiplying charge-coupled-device (EMCCD) camera for the PL spectral measurements. The PL signal of a single NC can be alternatively sent through a nonpolarizing 50/50 beam splitter to two avalanche photodiodes (APDs) in a time-correlated single-photon counting (TCSPC) system. The TCSPC system was operated under the time-tagged, time-resolved (TTTR) mode so that the arrival times of each photon relative to the laboratory time and the laser pulse time could both be obtained. A spectrograph is attached to an exit port of the main optical unit of MicroTime 200, which is SR193i equipped with ixon ultra 897 EMCCD provided by Andor Technology. Single-particle fluorescence spectra have been taken using 300 lines/mm grating and 500 nm blaze. The fluorescence was then focused through a 50 μm pinhole and split with a 50/50 beam-splitter through 565/40 nm band-pass filters (part number D565/40m, Chroma, Rockingham, VT) and focused onto two avalanche photodiode detectors (Tau-SPAD 50, Picoquant, Berlin, Germany).

2.6.1. Standardization of the instrument

Single-particle fluorescence microscope, which is the main instrument we used for the work described here, does have four major optical units. Excitation segment, inverted microscope, main optical unit, and detector extension unit. A spectrograph is attached to an

exit port of the main optical unit of MicroTime 200, which is SR193i equipped with ixon ultra 897 EMCCD provided by Andor Technology. However, the spectrograph is not a commercially bought instrument, but it is set up in-house by integrating different optical elements. A basic schematic of the instrument is shown in Figure 2.3.

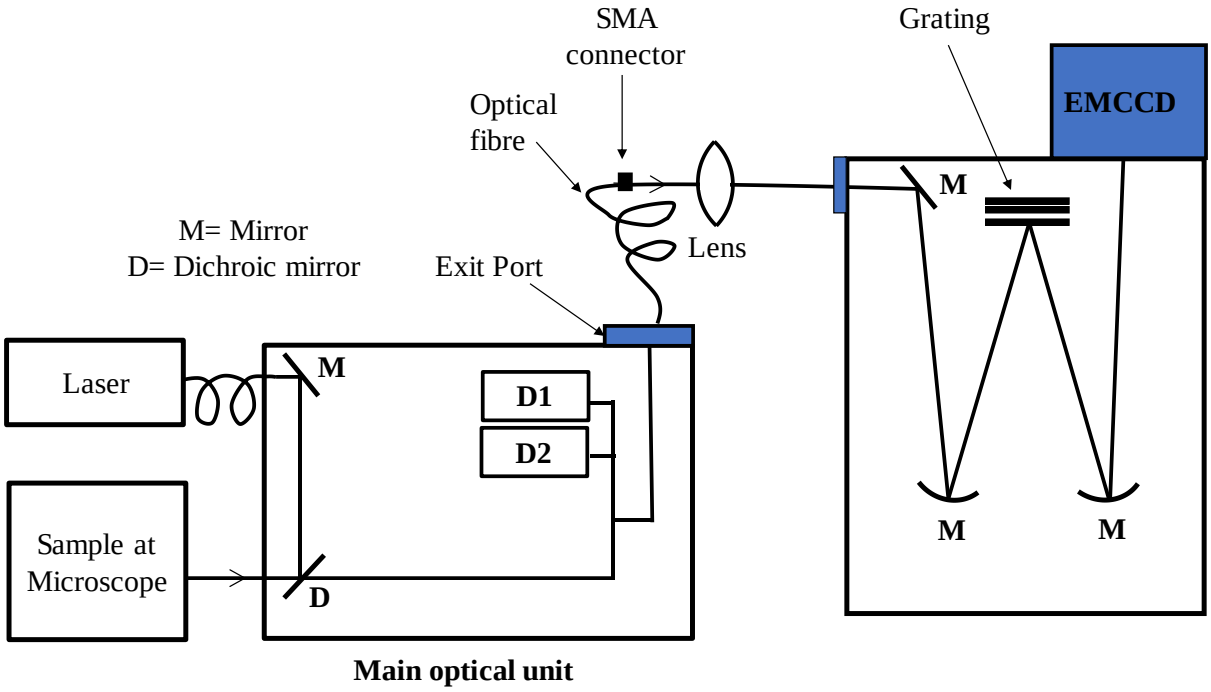

Figure 2.3. *Schematic representation of the fluorescence microscope coupled with a PL spectrometer showing four major optical units namely, (i) laser excitation segment, (ii) inverted confocal microscope, (iii) main optical unit, and (iv) detector extension unit.*

Thus, we needed to standardize the spectrograph by measuring the spectra of individual particles (referred to as single molecules/nanocrystals later on) of different samples. Also, we looked at various factors and optical elements which can influence the characteristics of PL spectra and most of the factors have been taken care of. Here, we will give a brief overview of the entire standardization procedure that we have gone through to obtain proper spectra with any instrumental artefact.

We started with the sample CdSe core overcoated with CdS shell (CdSe/CdS), which is known to have nearly 100 % quantum yield[7] and hence, we considered this sample to be a nearly ideal sample to standardize the spectrometer.

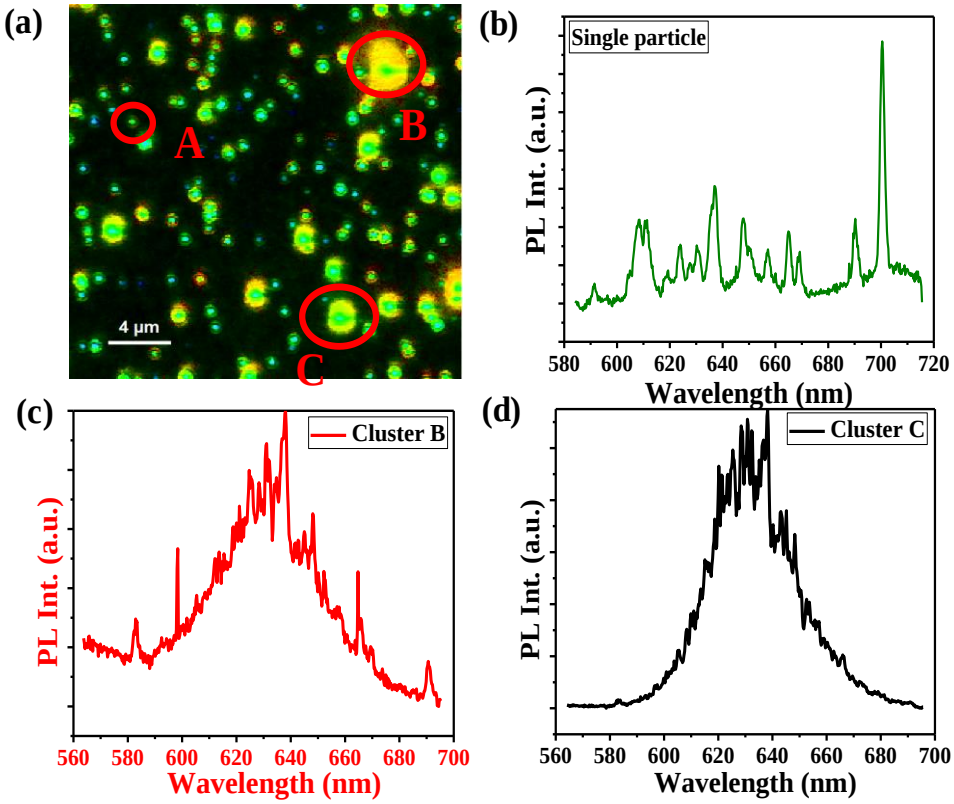

Figure. 2.4. *Fluorescence lifetime imaging of CdSe/CdS core/shell NCs, where 3 particles are spotted with circles. Amongst them "A" is single-particle and "B" and "C" are two clusters or assembly of two or more NCs. Corresponding PL spectra of (b) particle "A" (c) Cluster "B" (d) Cluster "C".*

In the Figure. 2.4, fluorescence lifetime imaging has been shown where two big-sized clusters have been spotted along with a single particle (highlighted with red circle) and the steady state PL spectra have been recorded for each of them. Here we have used a substantially high laser power of 50 arbitrary unit (a.u.) with exposure time/scan of 0.5 s, cycle of accumulation 200 and electron magnifying (EM) gain of 250. However, most of the spectra we obtained were from clusters and the spectra obtained from single particles showed a low signal-to-noise ratio.

Since we did not obtain satisfactory data even from a sample having nearly 100% QY, we decided to realign the spectrograph instrument. Once it has been done, we took the same sample for the measurement.

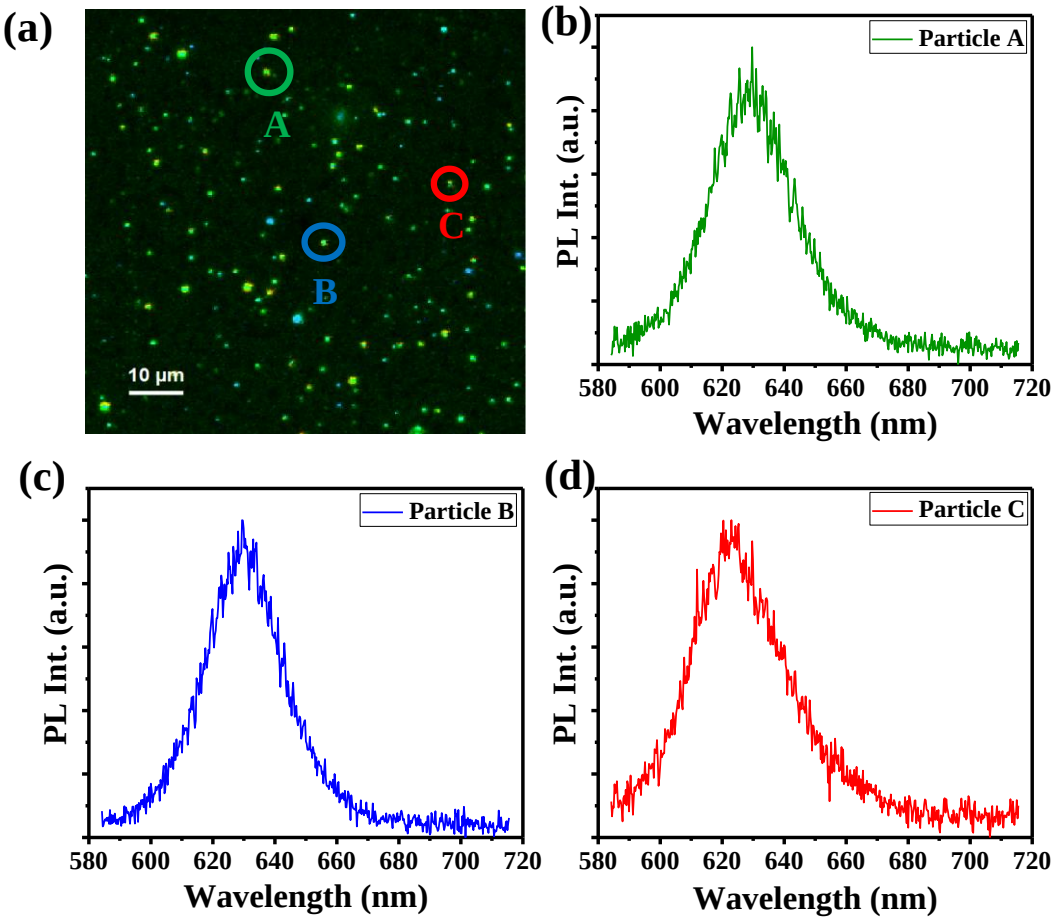

Figure. 2.5. *(a) Fluorescence lifetime imaging of CdSe/CdS core/shell NCs, where 3 single particles are spotted. PL spectra of (b) particle "A" (c) Particle "B" (d) Particle "C".*

After the realignment of the instrument, substantial improvement in the spectral data has been observed. Figure. 2.5(a) represents a typical fluorescence lifetime image obtained from CdSe/CdS NCs and 2.5(b), (c) and (d) are three spectra obtained from three representative single particles. Unlike the previous set of experiment, the present study on single-particles showed a very high signal-to-noise ratio, though we used comparatively very low laser power of 10 a.u. and exposure time/scan is 0.5 s, 100 accumulations and 200 EM gain. When we compared the single-molecule spectra with that of the ensemble, we observed a very good agreement of single-molecule spectra with that of the ensemble, which is shown in the Figure. 2.6.

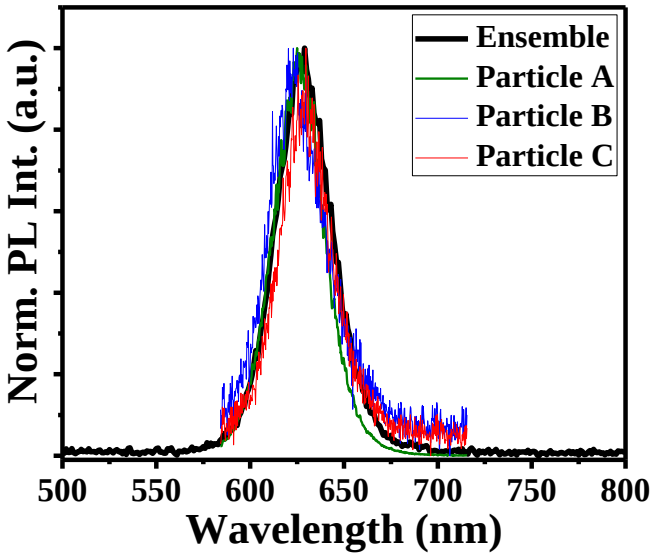

Figure. 2.6. *Comparison between ensemble spectra (black thick line) with single-molecule spectra for three different particles "A" (green line), "B" (blue line), and "C" (red line).*

Once we have been able to get satisfactorily good data from the spectrograph which showed a good agreement with the ensemble spectra, we proceeded with our own research problem and for that we have chosen a system which is Cu-doped CdSe nanocrystals. The detailed study of the same is described in chapter 3.

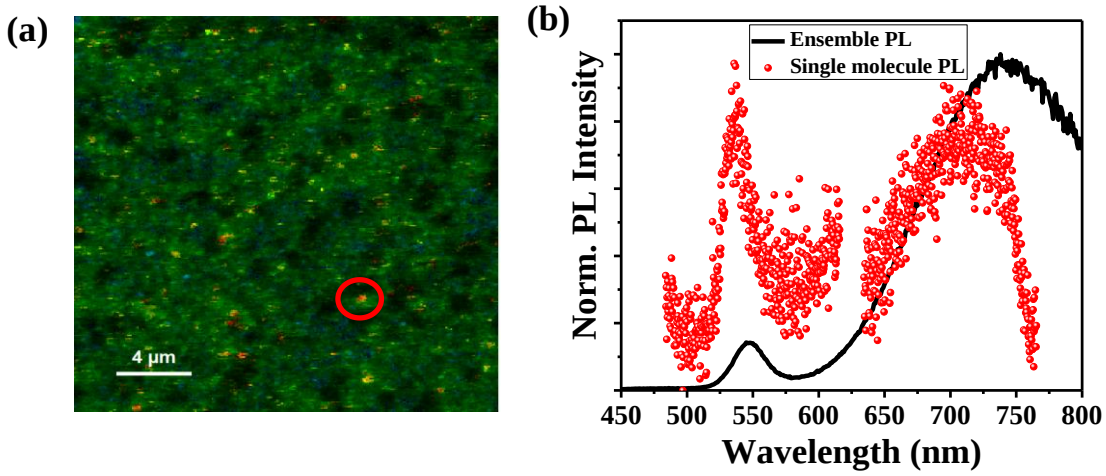

Figure. 2.7. *(a) Fluorescence lifetime imaging (FLIM), and (b) Comparison of single-particle spectra (red scattered line) with ensemble spectra (black line).*

In Figure 2.7(a), a single NC has been spotted in the FLIM circled in red, and Figure. 2.7(b) shows that there is a good agreement between single NC and ensemble spectra in case of band-edge PL feature, but Cu PL of single-NC is not in very good agreement with that of the ensemble. Also, the band-edge to Cu PL intensity ratio does not match which made us think of correcting the spectra with the detector efficiency curve because the Cu PL is broad over a range from 600-800 nm and most of the detector's efficiency is known to be very less beyond 600 nm. Here it is noteworthy that, in the spectrograph, we can only take a scan of maximum 133 nm by setting a center wavelength or start wavelength, or end wavelength. Here, we have set the center wavelength at 540 nm for band-edge and 700 nm for Cu emission and taken the scan separately.

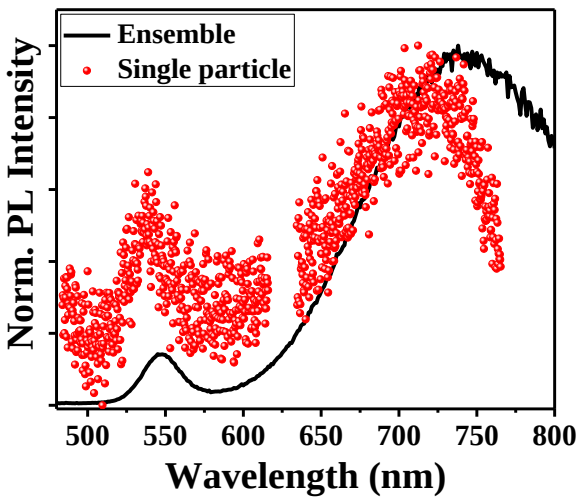

Figure. 2.8. Comparison of single-molecule spectra (red scattered line) with ensemble spectra (black line) after the correction using detector efficiency curve.

After the correction of the spectra using the detector efficiency curve, we observed a betterment in terms of band-edge to Cu PL intensity ratio but here also a sudden decay in intensity beyond 750 nm was observed as shown in Figure 2.8. Thus, we checked whether there exists any instrumental artefact associated with the spectrometer. To do that, we changed the central wavelength for taking both band-edge and Cu PL as shown in Figure 2.9.

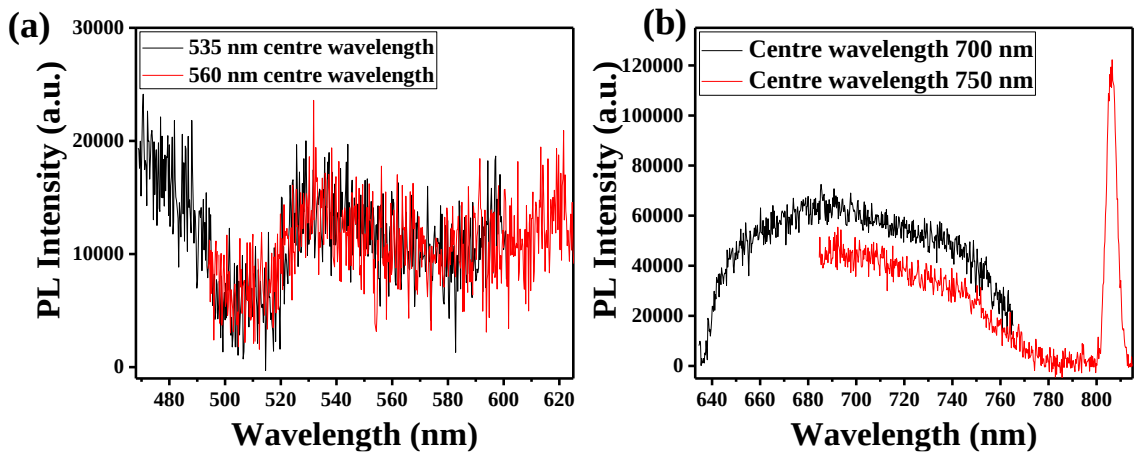

Figure. 2.9. *(a) Band-edge PL using 535 nm centre wavelength (black line) and 560 nm centre wavelength (b) Cu PL using centre wavelength 700 nm (black line) and 750 nm (red line).*

Here, we used two different centre wavelengths for band-edge PL and we observed that in case of both 535 and 560 nm centre wavelengths the PL characteristics are very well matched. Similarly, for Cu PL, both 700 nm and 750 nm give similar spectra, which suggests that the spectra we are getting are not because of any instrumental artefact rather it is originating from the sample itself. Also, in the Figure. 2.9(b) the sharp peak in red spectra due the 2nd harmonic generation as we used the laser excitation is 404 nm.

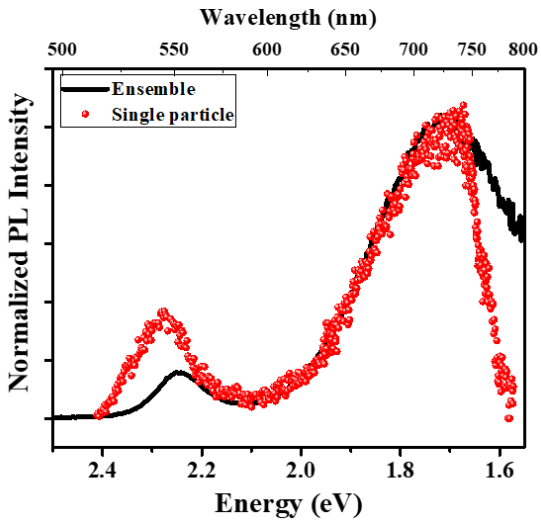

Figure. 2.10. *Comparison of single-molecule spectra (red scattered line) with ensemble spectra (black line).*

Then, we worked on the noises in the spectra obtained from single NCs and found out that external lights can be the probable reason for getting such noises. Then we covered the whole spectrograph with a material that can restrict the external rays to come to the detector and we observed an improvement in signal to noise ratio, shown in Figure 2.10. However, here also we observed a similar kind of sudden decay in intensity beyond 750 nm which we thought is due to the scan getting over within 800 nm. To check the credibility, we collected the spectra till 830 nm. Here we used a 430 nm long-pass filter to avoid the second harmonic peak at around 808 nm (double of excitation wavelength).

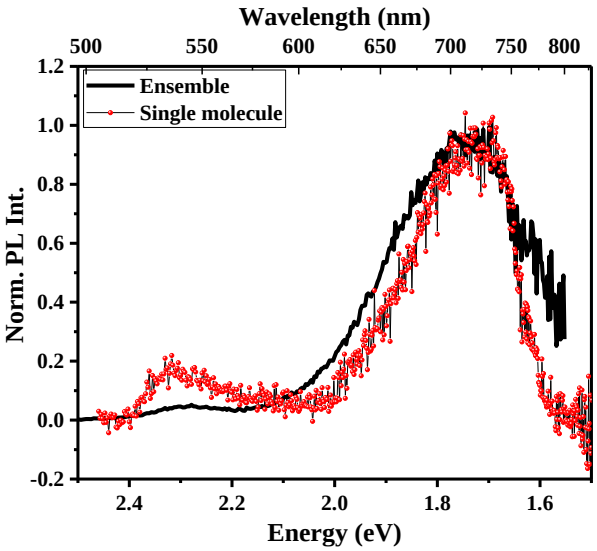

Figure. 2.11. *Comparison of single molecule spectra (red scattered line) with ensemble spectra (black line).*

In Figure. 2.11, the PL spectra show a similar decay trend beyond 750 nm, which suggests that the end wavelength does not have any role in this.

Single-molecule fluorescence spectra have been taken using 300 lines/mm grating and 500 nm blaze. Then we looked at the grating efficiency curve for the detector shown in the Figure. 2.12. Though we observed that the grating efficiency is not dyeing completely at that specific range but 50-60 % efficiency is there. Hence, grating efficiency is also not the reason for that sudden intensity decay.

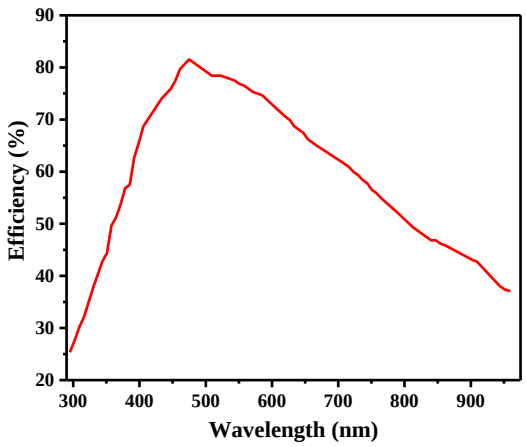

Figure. 2.12. *Grating efficiency curve for the detector.*

Then we took a commercially available dye that does have an emission beyond 800 nm and has a decent QY to check if we get anything beyond that range. We have taken an inorganic dye named IRDC3 which emits within 950-1050 range and have a QY of 5-6%.

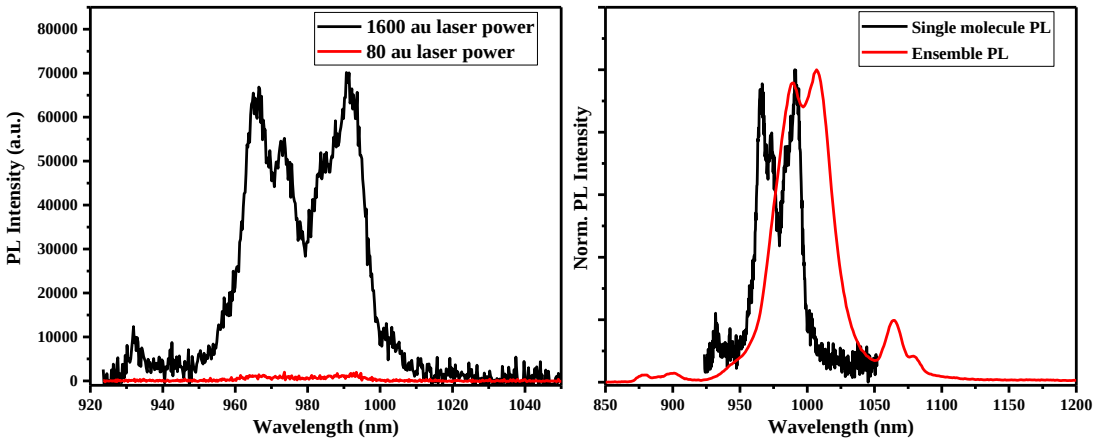

Figure. 2.13. *Comparison between ensemble spectra and spectra obtained from single-molecule spectrograph.*

Though the dye has a substantially high QY, we had used a very high laser power (1600 a.u.) as compared to the laser power we generally use to take the spectra (80 a.u.) for single-NCs in order to get the spectra as shown in Figure 2.13. These observations indicate that some other optical element is responsible for not getting expected spectral data and we found out that there

is an optical lens present on the signal pathway and chromatic aberration of that lens can probably be the reason for having such problems. Later on, re-alignment of the optical components present in the signal pathway resulted in good quality single-particle spectra that are similar to the ensemble spectra.

2.7. Transient absorption spectroscopy

Transient absorption is an essential time-resolved spectroscopic technique applied to study energy and charge transfer processes involving very short time scales. In transient absorption, firstly, the sample is excited by the pump pulse. Afterward, a relatively low intensity (compared to the pump pulse) white-light continuum probe pulse measures the absorption of that excited sample after some delay. The pump pulse is synchronized in such a way that every alternative pump pulse and probe pulse coincide at the sample. Therefore, the difference in the absorbance of the sample with the pump pulse ($A_{pump\ on}$) and absorbance without the pump pulse ($A_{pump\ off}$) is measured at different delay times.

$$\Delta A = A_{pump\ on} - A_{pump\ off}$$

Excitation by the pump pulse followed by absorption of the white light continuum induces different electronic transitions in the sample shown in Figure 2.14. The probe intensity must be kept low enough to inhibit further sample excitation by the probe pulse. Thus, the probe does not significantly alter the excited state population.

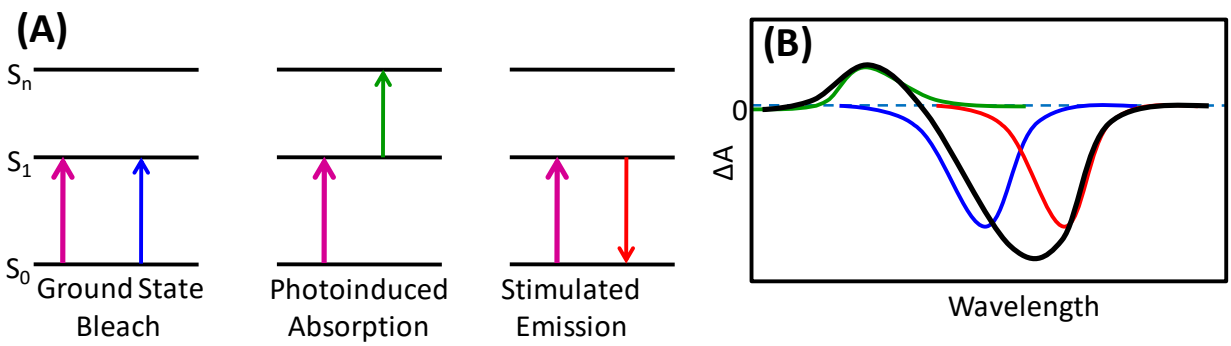

Figure 2.14. *(A) Probable transitions detected by the probe pulse in a typical transient absorption experiment. The thick and thin lines indicate the pump and probe pulses, respectively (B) Contributions to a ΔA spectrum: ground state bleach (blue line), excited-state absorption (green line), stimulated emission (red line), the sum of these contributions (black line).*

The ground state bleach occurs when the probe wavelength becomes resonant with the electronic transition of the sample. Thus, the ground state population reduces as the fractions of the absorbing units of the samples are promoted to the excited state by the pump pulse. Consequently, a negative signal in the ΔA spectrum is observed in the wavelength region of the ground state absorption. Again, absorbing units, which reside in the sample's excited state, may further promote to the higher excited state if the probe's energy is resonant with the transition from the first excited state to a higher energy excited state. This photoinduced absorption leads to a positive signal in transient absorption. It is also noted that the intensity of the probe pulse is so weak that the excited-state population is not affected significantly by the excited-state absorption process. Another transition can be induced by the probe pulse i.e., stimulated emission. In this process, a probe photon returns an excited state molecule to the ground state by emitting an additional photon of equal energy. The probe and emitted photons are identical and therefore share the same direction of propagation. Both photons will be measured by the detector producing a negative transient absorption signal, as there is no stimulated emission and therefore fewer photons detected when the pump is absent. Generally, stimulated emission mirrors the fluorescence profile and thus provides the same information as fluorescence upconversion with greater practical convenience in appropriate samples when using a broadband probe.

In our study, ultrafast transient absorption measurements were performed by an amplified Ti:Sapphire laser (Coherent Libra) generating 100-fs pulses at 800 nm and 2 kHz repetition rate. Pump pulses at 400 nm were generated by frequency doubling the fundamental wavelength by a 2-mm-thick β-barium borate crystal; they were modulated at 1 kHz by a mechanical chopper and focused in a spot of (400x180) μm^2 on samples dispersed in hexane. UV-visible probe pulses were produced by white light supercontinuum generation focusing a part of the fundamental beam in a calcium fluoride plate. Chirp-free differential transmission spectra $\Delta T/T = (T_{on} - T_{off})/ T_{off}$, T_{on} and T_{off} being the transmission of the probe through the perturbed and unperturbed samples were acquired at different pump-probe delays by a fast optical multichannel analyzer operating at the full laser repetition rate. The temporal resolution of the setup is ≈100 fs. All the measurements were carried out at room temperature.

2.8. Extended X-ray absorption fine structure spectroscopy (EXAFS)

X-ray absorption fine structure spectroscopy is an important tool to characterize the local structure of nanocrystals. This technique has been extensively used to probe the evolution of the local structure of various undoped and doped QDs in this thesis. EXAFS gives

information about how X-rays are absorbed by a specific element (atoms) of its near and above the core binding energy through the "photoelectric effect". Usually, the energy range of X-ray used for the EXAFS covers from 500 eV to 50 keV. When high energy X-rays strike the sample (X-ray energy higher than the binding energy), the oscillating electric field of the electromagnetic radiation interacts with bound electrons of the absorbing atom and removes from its quantum level to the continuum. This results in the absorption of X-ray energy and emission of a photoelectron, from the atom. In EXAFS we study the probability of X-ray absorption coefficient (μ) as a function of X-ray energy. X-ray diffraction (XRD), relies on the long-range ordering of atomic planes to probe crystalline structures at a length scale of approximately 50 Å or more. X-ray absorption spectroscopy probes the immediate environment of the selected element, within about 6 Å. The probability for absorption increases sharply when the incident X-ray energy equals the energy required to excite an electron to an unoccupied electron orbital. These steps in the absorption coefficient is termed as absorption edges.

A typical EXAFS spectrum is generally divided into two components (i) X-ray absorption near edge structure (XANES) which extends from just below the edge to about 30 eV and (ii) extended X-ray absorption fine structure spectroscopy (EXAFS) which starts after XANES and continues up to 1000 eV above the edge. As, XANES occurs at lower energy, when the transition happens, it provides information about electronic properties, oxidation states, the density of available states, etc. However, the EXAFS provides information about the neighbors and the local structure around the absorbing atom. Moreover, it also gives information about local defects and can extract site-specific structural information.

2.8.1. EXAFS data processing

The obtained data from the synchrotron beamline represent the variation of μ as a function of energy which can be transformed in a wavevector in k-space by changing energy to photoelectron wavenumber k [$k= (2m(E-E_0)/\hbar^2)^{1/2}$]. This spectrum has more physical consequences than when it represents in terms of radial function (R) i.e., in R-space by applying Fourier transformation on the k-space EXAFS. In this thesis, we processed and deglitched the data using software Athena[8] and fitted using the software Artemis.[9]

Bibliography

1. Mooney, J.; Kambhampati, P., Get the Basics Right: Jacobian Conversion of Wavelength and Energy Scales for Quantitative Analysis of Emission Spectra. *J. Phys. Chem. Lett.* **2013**, *4*, 3316-3318.

2. Porres, L.; Holland, A.; Pålsson, L. O.; Monkman, A. P.; Kemp, C.; Beeby, A., Absolute Measurements of Photoluminescence Quantum Yields of Solutions Using an Integrating Sphere. *J. Fluoresc.* **2006**, *16*, 267-273.

3. Klug, H. P.; Alexander, L. E., *X-Ray Diffraction Procedures: For Polycrystalline and Amorphous Materials*, 1974.

4. Kittel, C.; McEuen, P., Introduction to Solid State Physics, Vol 8 Wiley New York. **1976**.

5. Grandhi, G. K.; Viswanatha, R., Understanding the Role of Surface Capping Ligands in Passivating the Quantum Dots Using Copper Dopants as Internal Sensor. *J. Phys.Chem. C* **2016**, *120*, 19785-19795.

6. Wei, Q.; Zhao, Y.; Di, Q.; Liu, J.; Xu, M.; Liu, J.; Zhang, J., Good Dispersion of Large-Stokes-Shift Heterovalent-Doped CdX Quantum Dots into Bulk PMMA Matrix and Their Optical Properties Characterization. *J. Phys. Chem. C* **2017**, *121*, 6152-6159.

7. Saha, A.; Chellappan, K. V.; Narayan, K. S.; Ghatak, J.; Datta, R.; Viswanatha, R., Near-Unity Quantum Yield in Semiconducting Nanostructures: Structural Understanding Leading to Energy Efficient Applications. *J. Phys. Chem. Lett.* **2013**, *4*, 3544-3549.

8. Newville, M., IFEFFIT: Interactive XAFS Analysis and FEFF Fitting. *J. of Synchrotron Radiat* **2001**, *8*, 322-324.

9. Ravel, B.; Newville, M., Athena, Artemis, Hephaestus: Data Analysis for X-Ray Absorption Spectroscopy Using IFEFFIT. *J. of Synchrotron Radiat.* **2005**, *12*, 537-541.

Part 1

Fundamental Photophysics of Transition Metal-Doped II-VI Semiconductor Quantum Dots

Chapter 3

Mechanism of Cu Emission

The following papers have been published based on the work presented here:

1. Payel Mondal, and Ranjani Viswanatha. "Insights into the Oxidation State of Cu Dopants in II-VI Semiconductor Nanocrystals." J. Phys. Chem. Lett., **2022**, *13*, 1952-1961.

2. Payel Mondal, Saptarshi Chakraborty, G. Krishnamurthy Grandhi, and Ranjani Viswanatha. "Cu Doping in II-VI Semiconductor Nanocrystals: Single-Particle Fluorescence Study." J. Phys. Chem. Lett., **2020**, *11*, 5367-5372.

Chapter 3

Part A

Oxidation State of Cu: Photophysics and the Debate

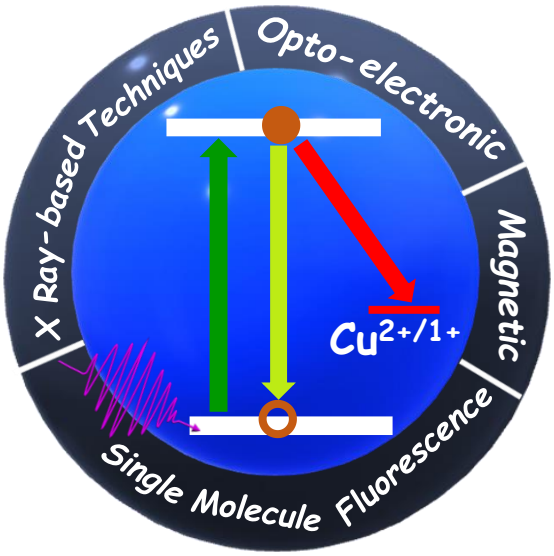

3.1. Abstract

Luminescent Cu-doped semiconductor nanocrystals have played a pivotal role in the emergence of lighting and display applications for a long time. However, consensus regarding the Cu oxidation state and hence their emission mechanism has not been attained. The distinction between seemingly simple optically and magnetically active Cu^{2+} and inactive Cu^{1+} has surprisingly been the subject matter of debate in literature for more than a decade. In this chapter, we first discuss the fundamental quantum mechanical phenomenon explaining the optical properties of the monovalent and divalent Cu dopants. We then focus down on various techniques used to differentiate between these two fundamental mechanisms, their benefits, and their pitfalls majorly arising due to the lack of spatial separation that has been the major bottleneck in understanding the mechanism of Cu emission in II-VI semiconductor nanocrystals.

3.2. Introduction

Controlled incorporation of a few impurity atoms/ions, particularly transition metal ions (Mn, Cu, Ni, Fe, etc.) into intrinsic semiconductor nanocrystal (NC) lattices have shown a number of desirable optical,[1-2] magnetic,[3-4] electronic[5-7] and magneto-optical properties[8-10] making the semiconductor industry more versatile to meet the current demands of various functional materials. One of the most extensively studied dopants other than Mn has been Cu which is known to alter the photo-physics of host NCs. Controlled doping of Cu into II-VI semiconductor NCs imparts interesting functionalities such as new emission bands at midgap energy, longer carrier recombination time through dopant state, unusual magnetic responses, etc. Although Cu intragap luminescence in bulk semiconductors was first reported in the early 1960s,[11-12] Cu doping in various semiconductor NCs has garnered a lot of attention during the last two decades due to their high photoluminescence quantum yield (PLQY) and their versatility.[13-17] The newly evolved dopant emission band is attributed to the recombination of the photoexcited electron at the conduction band edge state to the intra-gap atomic like Cu d-state making the transition lower in energy compared to the host bandgap.[18-20] This results in large Stokes shifted dopant emission, termed as the Cu PL band in the rest of the manuscript, which reduces the chance of self-absorption compared to the undoped NCs[18, 21-22] leading to high PLQY in devices with concentrated thick films. Additionally, doping provides improved photo stability[23-24] along with emission tunability achieved by controlling particle size (quantum-size effect) as well as composition (wave function modulation). For example, Viswanatha et al.[25] showed that Cu-related emission tunability in an 'inverted' core/shell

structure ZnSe/CdSe can be achieved ranging from ~1.3 eV to ~2.7 eV by simply changing the dimension of both the core and/or shell as depicted in Figure 3.1. These very properties make Cu-doped NCs potential candidates for applications like photodetectors,[26-27] light-emitting diodes (LEDs),[17, 22] photovoltaics[28] and recently in luminescent solar concentrators.[29-30]

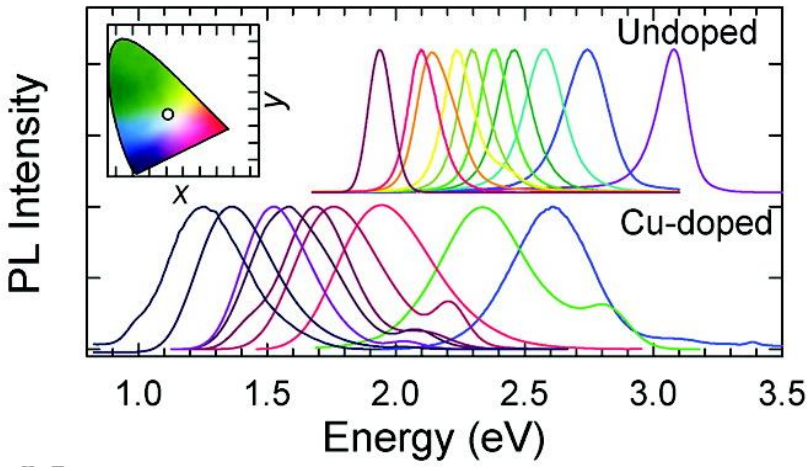

Figure 3.1. *Spectral tunability of undoped (top) and Cu-doped (bottom) ZnSe/CdSe core/shell NCs. Chromaticity diagram coordinates of the PL spectrum of Cu-doped NCs. Adapted with permission from ref 25. Copyright 2011 American Chemical Society.*

However, Cu is known to exist in +1 and +2 oxidation states and a fundamental understanding of the oxidation state is critical to enhance our perception towards the emission mechanism. Although this could play a critical role in our efforts to enhance the PLQY for devices, unfortunately, there is no unanimous consensus amongst the researchers regarding this very fundamental building block, and has been the subject of prolonged debate. It is well accepted that most of the synthetic procedures for doping Cu into NCs involve the use of Cu^{2+} precursors[7, 13, 21, 31-34] and some reports[19, 25, 35-37] suggest the retention of oxidation state while the others indicate towards the reduction of Cu^{2+} to $Cu^{1`+}$ during the reaction in presence of electron rich solvents and ligands, such as amines, phosphines, etc.[31-32, 38-39] Exact determination of the oxidation state is complicated by the presence of fully filled d^{10} electronic configuration in the Cu^{1+} state, thus reducing the effectiveness of any magnetic signatures or the lack thereof. Additionally, with a fully filled 3d band, quantum mechanically, Cu^{1+} would not be able to accept an electron and be optically active. However, the copper ion can non-

radiatively capture the photo-generated hole (PGH) from the valence band (VB) of the host and form a transient Cu^{2+} species. Hence, the use of optical methods to distinguish the oxidation states should involve the study of transient state dynamics.

Thus, to comprehend the oxidation state of Cu in Cu-doped NCs, various experimental techniques have been used and reported in the literature by several groups. In this chapter, we first discuss some of the indirect proof of oxidation state arising from the interpretation of the chemistry and quantum mechanics and the complications thereof. We follow up this with more direct proofs from optical, magnetic, and magneto-optical studies pertaining to the Cu oxidation state in detail while we scrutinize the gap in experimentation that contributed to the debate. Finally, we close the discussion with the suggestion of a useful probe to draw a conclusion to the debate.

3.3. Discussion

3.3.1. Mechanism of Cu emission

A typical PL spectrum of Cu-doped NCs, contains two emission bands, one of which is an intense low energy broad dopant peak while the other is a higher energy excitonic peak (band edge emission or BE emission) as illustrated in Figure 3.2(a) for the case of Cu-doped CdSe. The relative strength of the recombination matrix element is obtained by studying the time-resolved photoluminescence (TrPL). The time-resolved photoluminescence suggests that Cu PL decays in ~500 ns while the band edge PL decay occurs several orders of magnitude faster with a lifetime of a few ns as shown in Figure 3.2(b). In the case of Cu^{1+}, wherein, we have a single photo generated hole (PGH) and photo generated electron (PGE) these two bands can be explained as arising from two different fractions of the NCs, namely the doped fraction and the undoped fraction. However, in the case of +2 oxidation state, the impurity level may be considered to have a permanent hole creating an additional recombination pathway in the emission dynamics as depicted in Figure 3.2(c) and the relative intensity is governed by the recombination matrix element. Since the recombination matrix element of the transition from CB to the Cu PL is weak, ideally, in presence of the PGH in the VB, quantum mechanically, dopant emission should be negligible. These observations and the corresponding analysis in literature pointed towards the formation of Cu^{1+}. With this pre-set bias of possible +1 oxidation state for copper ion, researchers set out to obtain more direct proof for the oxidation state.

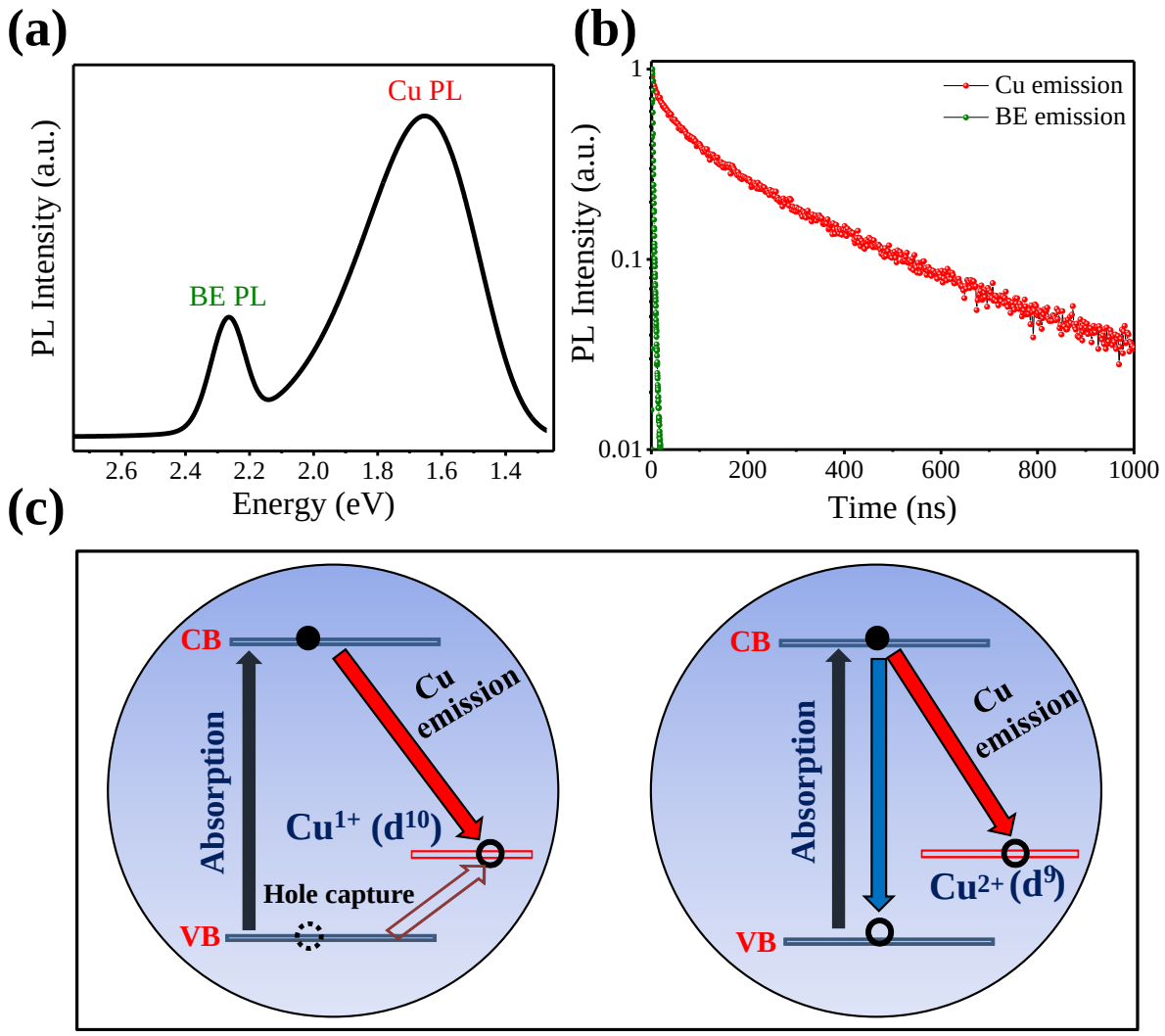

Figure 3.2. *(a) Typical PL spectra of Cu-doped NCs. In particular, Cu-doped CdSe has been taken here (b) Typical time-resolved photoluminescence curves of band edge (green) and Cu-related (red) emission. (c) Schematic illustration of dopant emission mechanism in case of* Cu^{1+} *(left) and* Cu^{2+} *(right).*

3.3.2. Ensemble studies and the debate

One of the simplest, though efficient techniques to probe the oxidation state of Cu-dopants is x-ray-based techniques like x-ray photoelectron spectroscopy (XPS) and more importantly, from a local perspective, x-ray absorption near edge structure (XANES). In most of the reports,[40-42] XPS analysis on Cu-doped NCs shows two major peaks at around 932.5 eV and 952.5 eV respectively which are characteristic peaks of Cu^{1+} ions. In addition to that, observation of weak satellite peak which is the fingerprint of Cu^{2+} in XPS was also reported.[43]

However, these observations cannot solely be used to assign the oxidation state of Cu as XPS is well-known to be a surface phenomenon and reflects the surface composition rather than the nature of internally doped Cu ions. Since Cu^{1+} is a soft metal ion, it binds better to soft donor sites like sulphur or selenium unlike Cu^{2+} (borderline acceptor), which is more stable as compared to Cu^{2+}. Additionally, it has been shown using DFT studies that copper is more stable in its +1 oxidation state when it is adsorbed on the surface of the nanocrystal while it prefers the +2 oxidation state when present in the core of the nanocrystal.[44] Hence, the atoms on the surface would most likely be in Cu^{1+} state while the satellite peaks might not be detected in the XPS spectrum due to their weak/undetectable intensities. On the other hand, x-ray absorption spectroscopy has been used to extract relevant information like valence state and the local environment of the elements present in any metal containing nanomaterials. Strong photoelectron scattering and weak inelastic losses make this technique more powerful tool to determine the same. However, formation of clusters, and inherent size effects impact the oxidation state and hence the XANES signatures.[45] Figure 3.3(a) shows a representative analysis of Cu L_3-edge XANES spectra.[46] It is claimed from the data that the onset of x-ray absorption of the Cu-doped NCs is similar to Cu^{1+} reference rather than Cu^{2+}. However, with a dopant percentage as high as 15%, it is unlikely to arise solely from the internally doped ions. There could be clusters of Cu which can alter the electronic structure and also provide a false oxidation state during doping. It should be noted that in presence of more than one oxidation state, one would expect a linear combination fitting (LCF) of the XANES spectrum to determine the oxidation state and not just the onset of the x-ray absorption of the NCs as has been done in earlier literature.[47] Hence the presence of +2 oxidation state has not been established although we observe some signatures as seen from a typical spectrum in Figure 3.3(a). So, these results are not enough to understand the oxidation state of Cu in the doped NCs where the host electronic structure is expected to be preserved.

Similar analyses were performed on the Cu K-edge of CdSe:Cu_4 shown in Figure 3.3(b). Comparison of Cu K-edges indicates towards the presence of Cu^{1+} before photodarkening and oxidized to Cu^{2+} after the same. However, here again, high Cu doping percentages were employed.[48]

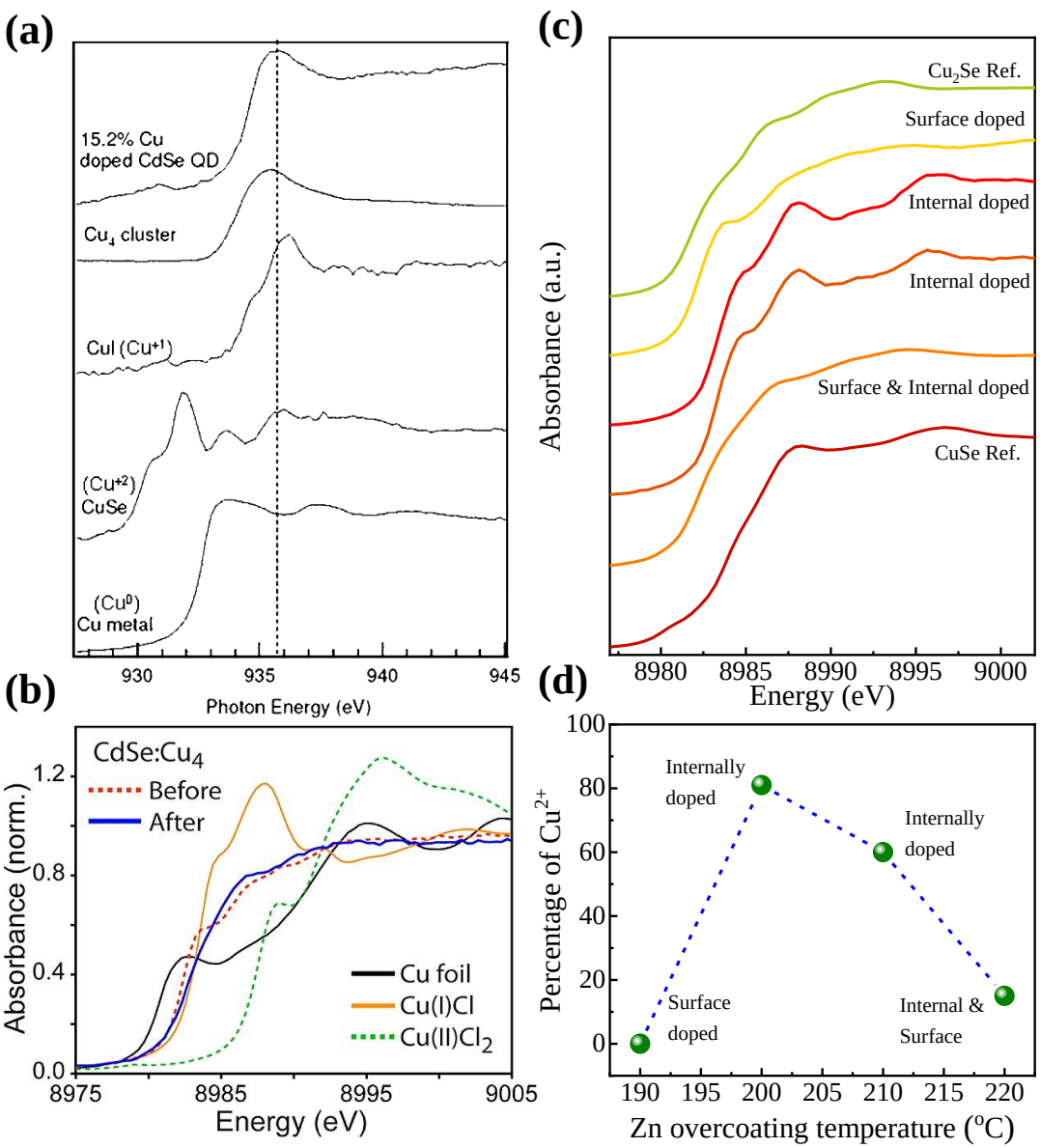

Figure 3.3. *(a) Cu L_3-edge XANES spectra of Cu metal, CuSe, CuI, Cu_4 cluster, and 15.2% Cu-doped CdSe QD (from bottom to top). The spectra are normalized to unity at the L_3 peak maximum. Adapted with permission from ref 46. Copyright 2004 American Chemical Society. (b) Cu K-edge XANES spectra of Cu foil (solid black line), Cu(I)Cl (solid orange line), $Cu(II)Cl_2$ (dashed green line), $CdSe:Cu_4$ QDs before (dashed red line) and after (solid blue line) photodarkening of sample. Adapted with permission from ref 48. Copyright 2013 American Chemical Society. (c) Normalized XANES spectra of Cu_2Se (greenish yellow) and CuSe (dark brown) along with Cu-doped ZnSe NCs overcoated at temperatures starting from 190 °C to 220 °C (top to bottom). The colour contrasts of Cu-doped ZnSe samples are according to the percentage contribution from both the oxidation states. (d) Percentages of Cu^{2+} as a function of ZnSe overcoating temperature.*

To check the credibility of these results we performed a similar study by synthesizing ZnSe NCs uniformly doped with Cu following the literature[21] and subsequent XANES measurements of the same. It is important to note here that doped NCs were synthesized by adding Cu dopant precursor to the already nucleated and purified ZnSe NCs to get the Cu dopants adsorbed onto the surface of the NCs followed by the internal doping arising from the overcoating of ZnSe shells at varying temperatures ranging from 190 ^{o}C to 220 ^{o}C and percentage of dopant incorporated is less than 1% in all the cases obtained from ICP-OES. Cu K-edge XANES spectra of these samples are compared with corresponding selenide references of Cu having oxidation states +1 (Cu_2Se) and +2 (CuSe) in Figure 3.3(c). The absorption onset or the edge of Cu-doped ZnSe NCs overcoated at 190 ^{o}C, wherein most of the Cu is expected to remain on the surface,[21] is very similar to the reference Cu_2Se. However, with the increased overcoating temperature and addition of more Zn precursors to assist the growth of ZnSe and thus internal doping of Cu, the absorption edges clearly shift towards higher energy. Further heating to higher temperatures (220°C) facilitates the migration of Cu to the surface and thus the formation of Cu^{1+} state, and hence, a shift of Cu K-edge XANES to lower energy as observed in the figure. In addition to that, the white line intensity of Cu-ZnSe overcoated at 210 ^{o}C and 220 ^{o}C match with CuSe while the other two match better with Cu_2Se.

To obtain more clarity about the data, linear combination fittings of the spectra have been done using a combination of Cu_2Se (Cu^{1+}) and CuSe (Cu^{2+}) references which could extract the information about the percentages that each component contributes to the overall fit. Figure 3.3(d) shows the percentage of Cu^{2+} present in each of the Cu-doped ZnSe samples that traces the journey of the Cu ion and its oxidation state from surface doping to internal doping and finally surface expulsion. When the overcoating temperature is 190 ^{o}C, Cu^{2+} is negligible which suggests that the dopant ions were loosely adsorbed onto the NC surfaces (surface doped) and reduced to their surface stable state Cu^{1+} consistent with earlier literature.[44] However, when the dopant ions are properly adsorbed and uniformly diffused inside the NC lattice (internally doped) at relatively higher overcoating temperatures (200 ^{o}C and 210 ^{o}C), most of the dopant ions are present in +2 oxidation state. If the overcoating temperature is further raised beyond 210 ^{o}C, the dopant ions are expected to be expelled out of the NCs leading to the formation of Cu_2Se as discussed in earlier literature,[1, 21] although some of the Cu ions remain doped inside the NCs (internal & surface doped).

However, although the XANES analysis traces the journey of the Cu ion and demonstrates the presence of Cu^{2+} and Cu^{1+} ions, it is only circumstantial evidence that binds

the substitutionally doped Cu ion to the 2+ oxidation state. Additionally, it is recently shown that the XANES spectral feature is not just sensitive to the oxidation state of the ion but also depends on a few more parameters such as coordination number and bond length.[49-50] Most of the reference samples used in the XANES studies on Cu-doped NCs have different local environment and coordination numbers to that of the NCs. So, it is not very straight forward to assign the oxidation state of Cu just by looking at the spectral feature. Hence in the quest for irrefutable proof, researchers leaned towards the study of magnetic properties.

Since Cu^{1+} is diamagnetic and Cu^{2+} is paramagnetic, they should easily be distinguishable through different magnetic measurements such as electron paramagnetic resonance (EPR) and magnetic circular dichroism (MCD). EPR spectroscopy can probe the unpaired electrons present in any metal complexes. To date several reports affirmed the absence of Cu^{2+} due to the lack of EPR signal in Cu-doped NCs.[31, 34, 51] Srivastava et al.[34] studied EPR spectroscopy of copper stearate (Cu precursor) as well as Cu-doped $ZnS/Zn_{1-x}Cd_xS$ NCs and no EPR signal was observed in Cu-doped NCs unlike the Cu precursor shown in Figure 3.4(a). This was then speculated that Cu^{2+} precursors, could be reduced to Cu^{1+} by the electron-rich ligands as well as the chalcogen anions employed during the synthesis of Cu-doped NCs.[32] However, EPR signals in semiconductor NCs are generally very weak[52] and marred by strong spin-orbit coupling and Jahn-Teller effects in the Cu-doped NCs. This causes internal strains in the crystal lattice which can make the EPR signal of Cu^{2+} broader and hence undetectable.[53-55] In fact, calculation of the g-factor suggests the presence of two types of Cu^{2+} centres and $g_{\parallel}$ value (2. 1621) is higher than $g_{\perp}$ value (1.85009) suggesting that the Cu^{2+} ions are subjected to tetragonal elongation. This Jahn-Teller distortion induced line broadening[55] could also accommodate the lack of EPR signal, albeit being +2 oxidation state. In addition, recently, several reports also demonstrate the existence of Cu ions in the +2 oxidation state by the same technique.[12, 43, 56-58] Jana et al.[56] performed an EPR spectroscopic study on Cu-doped ZnSe NCs and demonstrate the splitting of EPR spectra suggesting the presence of Cu^{2+} centre as shown in Figure 3.4(b). Therefore, EPR spectroscopy does not provide sufficient evidence to conclude the oxidation state of Cu.

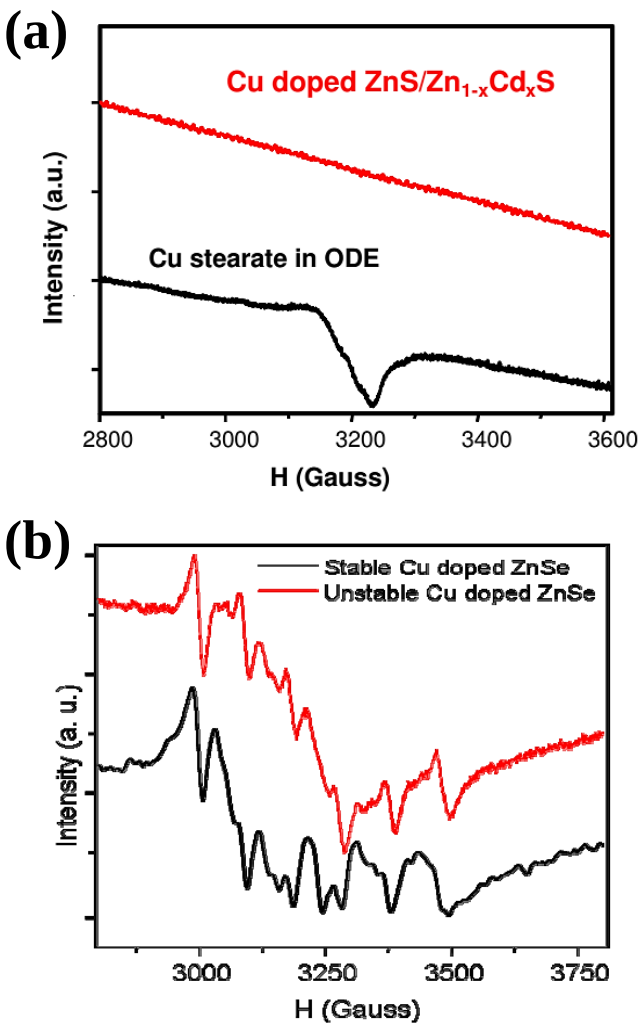

Figure 3.4. *(a) EPR spectra of Cu stearate (black) and Cu-doped ZnS/$Zn_{1-x}Cd_xS$ (red). Adapted with permission from ref 34. Copyright 2011 American Chemical Society. (b) EPR spectra of stable (black) and quenched (red) Cu-doped ZnSe NCs. Adapted with permission from ref 56. Copyright 2010 Royal Society of Chemistry.*

The second technique that could prove the existence of paramagnetic dopants in a material is magnetic circular dichroism (MCD). Cu^{1+} having a fully filled d^{10} configuration is expected to be non-magnetic. In contrast to that, Cu^{2+} (d^9) contains a single unpaired spin -1/2 electron in its 3d shell and is therefore expected to be magnetically active. To judge whether it is magnetically active, MCD studies have been performed on Cu-doped ZnSe/CdSe NCs.[59]

MCD spectra clearly reveal a markedly enhanced Zeeman splitting of nanocrystal's 1S exciton and an effective exciton g-factor in the order of +20 which is approximately 10-fold enhancement as compared to the undoped NCs with a very small Zeeman splitting of 1S exciton and exciton g-factor in the order of +1.5. Also, the high field saturation and very strong

temperature dependence suggest a significant sp-d exchange coupling between paramagnetic Cu^{2+} dopants and the valence band/conduction bands of the host. This result strongly suggests the presence of magnetically active Cu^{2+}.

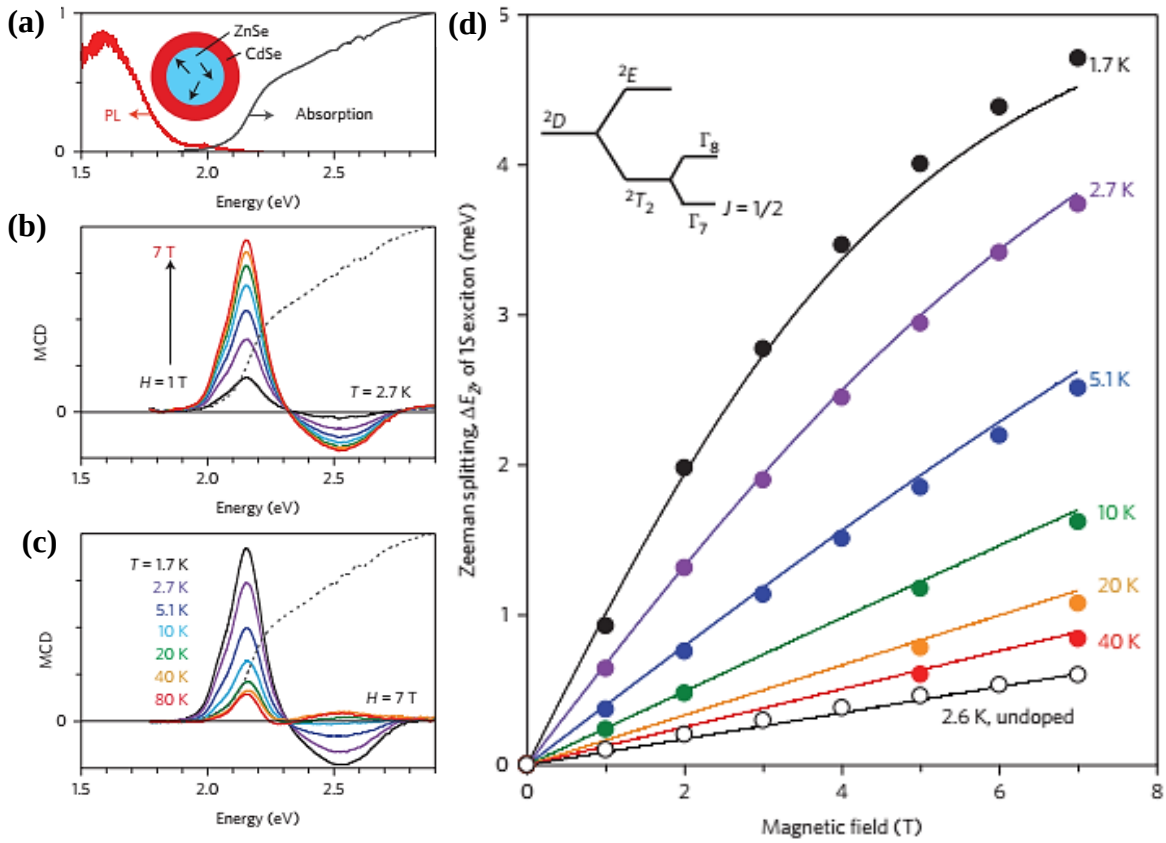

Figure 3.5. *(a) Typical absorbance and PL spectra from a film of ZnSe/CdSe core/shell NCs at 2.7 K (b) MCD spectra at 2.7 K at different magnetic fields from 1 T to 7 T. (c) MCD spectra taken at 7 T and at varying temperatures ranging from 1.7 K to 80 K and (d) Enhanced Zeeman splitting at 1S band edge exciton as a function of magnetic field at different temperature. Energy levels of Cu^{2+} in ZnSe are shown in the inset. Adapted with permission from ref 59. Copyright 2012 Macmillan Publishers Ltd.*

The results obtained from optical and magnetic properties seemed to suggest +2 oxidation state, albeit based on the fundamental properties of an electron in an excited state, it was concluded that the dopant emission cannot be observed due to its long-lived excited state lifetime. However, one possible scenario that was till then not considered is the accessibility

of the PGH in the VB. While it is evident that the dopant emission could not be observed in presence of the PGH in the VB, it is well known in NCs that they contain a large number of surface trap states that could capture the PGH within a few picoseconds, a much faster process as compared to excitonic recombination as shown schematically in Figure 3.6(a). This hypothesis was tested in the literature by titrating against known hole trapping agents, namely dodecanethiol (DDT)[25] in ZnSe/CdSe NCs, and the Cu emission intensity was observed to enhance with increasing surface hole trapping states as shown in the Figure 3.6(b) and quantified in Figure 3.6(c).

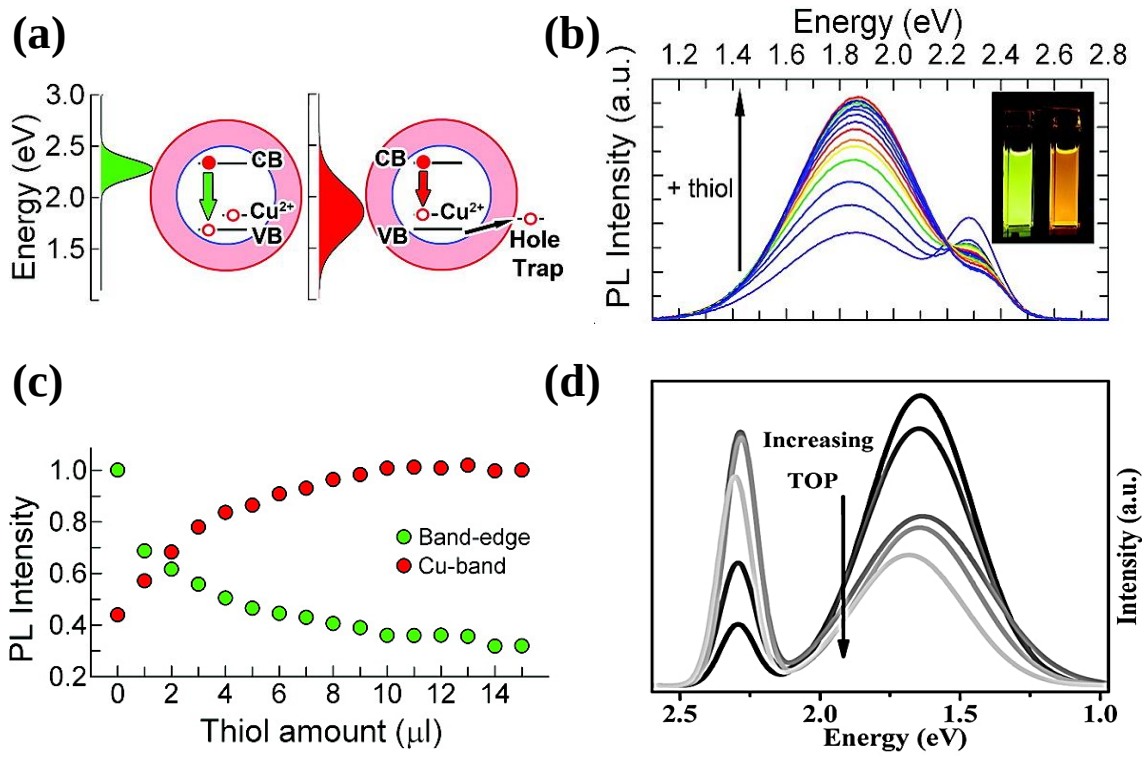

Figure 3.6. *(a) Schematic representation of emission mechanism in Cu-doped NCs. (b) Titration of Cu-doped ZnSe/CdSe NCs with hole trapping agent dodecanethiol (DDT) leads to an increase in Cu PL intensity accompanied by suppression of BE emission intensity. (c) Quantitative change in Cu and BE intensity during the titration process. Adapted with permission from ref 25. Copyright 2011 American Chemical Society. (d) Typical PL spectra of Cu-doped CdSe NCs containing similar Cu content but synthesized with different TOP concentration shows an increase in BE emission intensity with increasing TOP concentration. Adapted with permission from ref 7. Copyright 2012 American Chemical Society.*

Dodecanethiol (DDT)[25] is well known to trap the photogenerated holes efficiently when attached to CdSe NCs surfaces.[60] DDT molecules or ligands quench the PL rapidly in case of undoped NCs. However, when Cu-doped ZnSe/CdSe NCs were titrated using the same DDT, Cu emission gradually enhanced at the expense of band edge emission as shown in Figure 3.6(c). The emission of the NCs also changed gradually during the process of titration from green to orange due to increasing contribution from Cu emission and decreasing contribution from band edge emission. This result suggests that the Cu is in +2 oxidation state, where the holes in Cu d-level and VB compete for the recombination with the same CB PGE and Cu emission occurs only if the VB hole is quickly trapped. In the case of Cu^{1+}, which possesses a single hole capable of recombining with the PGE, we observe a radiative transition only when the PGH is successfully encapsulated within the NC, either in the VB or in the Cu d-band.

Similarly, in another report[7] the NCs were titrated against trioctylphosphine (TOP) which contains a lone pair of electrons that could passivate the hole trap states thus facilitating the recombination through the VB provided its absolute energy level lies above the VB. The concentration of TOP is varied systematically while keeping the Cu to Cd ratio constant. This leads to a systematic decrease in QY of Cu PL while the intensity of BE PL increases as shown in Figure 3.6(d), thus proving that TOP is effective in scavenging the hole trap states. It is important to note here that the BE emission does not arise at the cost of Cu emission but rather occurs independently. This observation further corroborates the theory that the Cu emission can only be seen in presence of surface hole trap states which in turn suggests the presence of Cu^{2+} centre.

This theory was further strengthened by spectro-electrochemical measurements on Cu-doped ZnSe/CdSe core/shell NCs that control the surface defect states leading to the tuning of photoluminescence intensity.[15] Herein, the researchers developed a quantitative model to study the effect of negative and positive electrochemical (EC) potentials on the photoluminescence intensities of the excitonic as well as impurity related bands by modulating the occupancies of surface defect sites. Specifically, upon application of negative EC potential the Fermi level shifts up in energy leading to activation of hole traps thereby facilitating the Cu-related emission accompanied by a suppressed BE emission ($-1 < V_{EC} < -1.5$ V), shown in Figure 3.7(a). Overall PL intensity also increases which is attributed to the passivation of electron traps. Contrary to that, when positive EC potentials were employed, hole traps were passivated, and simultaneously electron traps were activated leading to an increase in the population of NCs emitting through BE channel and a reduction in Cu PL intensity, shown in Figure 3.7(b).

Positive EC potential also affects the occupancy of electron traps, and at V_{EC} of +1.75 V both BE and Cu emission intensity decreases leading to overall dimming of the NCs. While these measurements do not exclude the possibility that some of the NCs might contain +1 copper ions, they strongly suggest the PL is arising primarily due to Cu^{2+}.

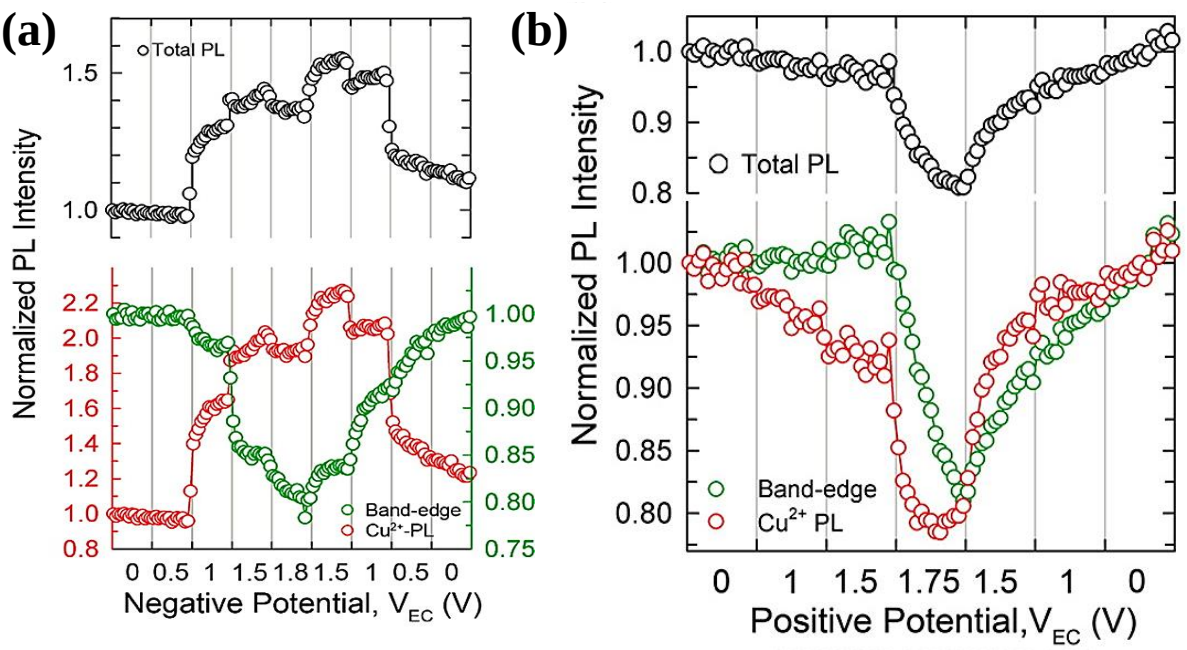

Figure 3.7. *Variation of Cu^{2+} PL (red circles), BE PL (green circles), and overall PL intensities (black circles, topmost panel) with the applied (a) negative potentials and (b) positive potentials. Adapted with permission from ref 15. Copyright 2012 American Chemical Society.*

In contrast to this argument, the role of TOP in another report is interpreted in an entirely different way.[61] Here the authors use an one-pot synthesis of colloidal Cu-doped CdSe (Cu^{1+}: CdSe) NCs were carried out by purposefully injecting Cu^{1+} precursor (CuI) and TOP into pre-formed CdSe NCs. A similar observation of increasing excitonic PL intensity after the addition of TOP was made here as well. However, here the authors suggest that Cu^{1+} is known to bind with TOP ligands due to soft Lewis acid-base interactions, forming Cu^{1+}-TOP complex which is thermodynamically more favourable over Cu^{1+}-doped CdSe. At elevated temperature, addition of TOP during the reaction causes loss of Cu dopants from CdSe hosts. Therefore, it leads to the loss of Cu-based metal-to-ligand (conduction band) charge-transfer ($ML_{CB}CT$) PL, while increasing the population of undoped CdSe NCs and hence recovery of excitonic PL.

This suggests an alternate mechanism for explaining the observed PL behaviour but is only true for copper doped on the surface of the nanocrystal. However, as previously observed, the copper doped in the core of the nanocrystals behave substantially different than that of the surface including the stabilization of the +2 oxidation state.

As is evident, the direct proof of oxidation state through optical and magnetic properties is complicated by the presence of internally doped as well as the surface ions and the lack of signal for the Cu^{1+} ions. The indirect proofs such as ligand chemistry and electrochemistry are the matter of subjective interpretation and hence can be biased. However, most of this subjective interpretation arises due to the experiments being performed on the ensemble of NCs and the observations provide a sum of the various signals leading to the absence of any direct evidence to draw any conclusive remark. In this context, single-molecule fluorescence spectroscopy happens to be uniquely equipped to handle the shortcomings of the other experimental methods. This provides a PL spectrum of a single NC removing the uncertainty arising due to the ensemble averaging.

3.3.3. Summary

In summary, we discuss here the plausible mechanisms of Cu emission and how it depends on the oxidation state of Cu. We then discussed a few important reports based on ensemble of measurements regarding the oxidation state of Cu when it is doped in II-VI semiconductor NCs and the shortcomings of those reports which stir up controversy on the oxidation state of Cu and make the whole topic elusive and single-particle fluorescence spectroscopy could be advantageous over ensemble measurements to find any conclusive evidence which is discussed in the following chapter.

Bibliography

1. Saha, A.; Makkar, M.; Shetty, A.; Gahlot, K.; Pavan, A. R.; Viswanatha, R., Diffusion Doping in Quantum Dots: Bond Strength and Diffusivity. *Nanoscale* **2017**, *9*, 2806-2813.

2. Norris, D. J.; Yao, N.; Charnock, F. T.; Kennedy, T. A., High-Quality Manganese-Doped ZnSe Nanocrystals. *Nano Lett.* **2001**, *1*, 3-7.

3. Viswanatha, R.; Naveh, D.; Chelikowsky, J. R.; Kronik, L.; Sarma, D. D., Magnetic Properties of Fe/Cu Codoped ZnO Nanocrystals. *J. Phys. Chem. Lett.* **2012**, *3*, 2009-2014.

4. Bonanni, A.; Dietl, T., A Story of High-Temperature Ferromagnetism in Semiconductors. *Chem. Soc. Rev.* **2010**, *39*, 528-539.

5. Grandhi, G. K.; Swathi, K.; Narayan, K. S.; Viswanatha, R., Cu Doping in Ligand Free CdS Nanocrystals: Conductivity and Electronic Structure Study. *J. Phys. Chem. Lett.* **2014**, *5*, 2382-2389.

6. Sahu, A.; Kang, M. S.; Kompch, A.; Notthoff, C.; Wills, A. W.; Deng, D.; Winterer, M.; Frisbie, C. D.; Norris, D. J., Electronic Impurity Doping in CdSe Nanocrystals. *Nano Lett.* **2012**, *12*, 2587-2594.

7. Grandhi, G. K.; Tomar, R.; Viswanatha, R., Study of Surface and Bulk Electronic Structure of II–VI Semiconductor Nanocrystals Using Cu as a Nanosensor. *ACS Nano* **2012**, *6*, 9751-9763.

8. Fainblat, R.; Muckel, F.; Barrows, C. J.; Vlaskin, V. A.; Gamelin, D. R.; Bacher, G., Valence-Band Mixing Effects in the Upper-Excited-State Magneto-Optical Responses of Colloidal Mn^{2+}-Doped CdSe Quantum Dots. *ACS Nano* **2014**, *8*, 12669-12675.

9. Viswanatha, R.; Pietryga, J. M.; Klimov, V. I.; Crooker, S. A., Spin-Polarized Mn^{2+} Emission from Mn-Doped Colloidal Nanocrystals. *Phys. Rev. Lett.* **2011**, *107*, 067402.

10. Fuhr, A.; Yun, H. J.; Crooker, S. A.; Klimov, V. I., Spectroscopic and Magneto-Optical Signatures of Cu^{1+} and Cu^{2+} Defects in Copper Indium Sulfide Quantum Dots. *ACS Nano* **2020**, *14*, 2212-2223.

11. Halperin, A.; Arbell, H., Transients in the Blue and Green Luminescence of ZnS: Cu: Cl Crystals. *J. Chem. Phys.* **1961**, *34*, 879-883.

12. Holton, W. C.; De Wit, M.; Watts, R. K.; Estle, T. L.; Schneider, J., Paramagnetic Copper Centers in ZnS. *J. Phys. Chem. Solids* **1969**, *30*, 963-977.

13. Grandhi, G. K.; Viswanatha, R., Demystifying Complex Quantum Dot Heterostructures Using Photogenerated Charge Carriers. *J. Phys. Chem. Lett.* **2017**, *8*, 2043-2048.

14. Zhang, W.; Lou, Q.; Ji, W.; Zhao, J.; Zhong, X., Color-Tunable Highly Bright Photoluminescence of Cadmium-Free Cu-Doped Zn–In–S Nanocrystals and Electroluminescence. *Chem. of Mater.* **2014**, *26*, 1204-1212.

15. Brovelli, S.; Galland, C.; Viswanatha, R.; Klimov, V. I., Tuning Radiative Recombination in Cu-Doped Nanocrystals Via Electrochemical Control of Surface Trapping. *Nano Lett.* **2012**, *12*, 4372-4379.

16. Zhang, W.; Zhou, X.; Zhong, X., One-Pot Noninjection Synthesis of Cu-Doped $Zn_xCd_{1-x}S$ Nanocrystals with Emission Color Tunable over Entire Visible Spectrum. *Inorg. Chem.* **2012**, *51*, 3579-3587.

17. Cao, S.; Ji, W.; Zhao, J.; Yang, W.; Li, C.; Zheng, J., Color-Tunable Photoluminescence of Cu-Doped Zn–In–Se Quantum Dots and Their Electroluminescence Properties. *J. Mater. Chem. C* **2016**, *4*, 581-588.

18. Pradhan, N.; Goorskey, D.; Thessing, J.; Peng, X., An Alternative of CdSe Nanocrystal Emitters: Pure and Tunable Impurity Emissions in ZnSe Nanocrystals. *J. Am. Chem. Soc.* **2005**, *127*, 17586-17587.

19. Suyver, J. F.; Van der Beek, T.; Wuister, S. F.; Kelly, J. J.; Meijerink, A., Luminescence of Nanocrystalline ZnSe: Cu. *Appl. Phys. Lett.* **2001**, *79*, 4222-4224.

20. Nelson, H. D.; Hinterding, S. O. M.; Fainblat, R.; Creutz, S. E.; Li, X.; Gamelin, D. R., Mid-Gap States and Normal Vs Inverted Bonding in Luminescent Cu^+-and Ag^+-Doped CdSe Nanocrystals. *J. Am. Chem. Soc.* **2017**, *139*, 6411-6421.

21. Chen, D.; Viswanatha, R.; Ong, G. L.; Xie, R.; Balasubramaninan, M.; Peng, X., Temperature Dependence of "Elementary Processes" in Doping Semiconductor Nanocrystals. *J. Am. Chem. Soc.* **2009**, *131*, 9333-9339.

22. Zhang, Z.; Luan, S.; Huang, K.; Zhang, Y.; Shi, Z.; Xie, R.; Yang, W., Single-Phase Dual Emissive Cu:CdS–ZnSe Core–Shell Nanocrystals with "Zero Self-Absorption" and Their Application in White Light Emitting Diodes. *J. Mater. Chem. C* **2015**, *3*, 3614-3622.

23. Gopi, C. V. V. M.; Venkata-Haritha, M.; Kim, S. K.; Kim, H. J., A Strategy to Improve the Energy Conversion Efficiency and Stability of Quantum Dot-Sensitized Solar Cells Using Manganese-Doped Cadmium Sulfide Quantum Dots. *Dalton Trans.* **2015**, *44*, 630-638.

24. Pradhan, N.; Battaglia, D. M.; Liu, Y.; Peng, X., Efficient, Stable, Small, and Water-Soluble Doped ZnSe Nanocrystal Emitters as Non-Cadmium Biomedical Labels. *Nano Lett.* **2007**, *7*, 312-317.

25. Viswanatha, R.; Brovelli, S.; Pandey, A.; Crooker, S. A.; Klimov, V. I., Copper-Doped Inverted Core/Shell Nanocrystals with "Permanent" Optically Active Holes. *Nano Lett.* **2011**, *11*, 4753-4758.

26. Kakati, J.; Datta, P., Schottky Junction Uv Photodetector Based on CdS and Visible Photodetector Based on CdS: Cu Quantum Dots. *Optik* **2015**, *126*, 1656-1661.

27. Grandhi, G. K.; Krishna, M.; Mondal, P.; Viswanatha, R., Cation Co-Doping into ZnS Quantum Dots:Towards Visible Light Sensing Applications. *Bull. Mater. Sci.* **2020**, *43*, 1-6.

28. Nguyen, T. P.; Ha, T. T.; Nguyen, T. T.; Ho, N. P.; Huynh, T. D.; Lam, Q. V., Effect of Cu^{2+} Ions Doped on the Photovoltaic Features of CdSe Quantum Dot Sensitized Solar Cells. *Electrochim. Acta* **2018**, *282*, 16-23.

29. Bradshaw, L. R.; Knowles, K. E.; McDowall, S.; Gamelin, D. R., Nanocrystals for Luminescent Solar Concentrators. *Nano Lett.* **2015**, *15*, 1315-1323.

30. Liu, X.; Luo, B.; Liu, J.; Jing, D.; Benetti, D.; Rosei, F., Eco-Friendly Quantum Dots for Liquid Luminescent Solar Concentrators. *J. Mater. Chem. A* **2020**, *8*, 1787-1798.

31. Corrado, C.; Jiang, Y.; Oba, F.; Kozina, M.; Bridges, F.; Zhang, J. Z., Synthesis, Structural, and Optical Properties of Stable ZnS: Cu, Cl Nanocrystals. *J. Phys. Chem. A* **2009**, *113*, 3830-3839.

32. Isarov, A. V.; Chrysochoos, J., Optical and Photochemical Properties of Nonstoichiometric Cadmium Sulfide Nanoparticles: Surface Modification with Copper (II) Ions. *Langmuir* **1997**, *13*, 3142-3149.

33. Grandhi, G. K.; Viswanatha, R., Tunable Infrared Phosphors Using Cu Doping in Semiconductor Nanocrystals: Surface Electronic Structure Evaluation. *J. Phys. Chem. Lett.* **2013**, *4*, 409-415.

34. Srivastava, B. B.; Jana, S.; Pradhan, N., Doping Cu in Semiconductor Nanocrystals: Some Old and Some New Physical Insights. *J. Am. Chem. Soc.* **2011**, *133*, 1007-1015.

35. Bol, A. A.; Ferwerda, J.; Bergwerff, J. A.; Meijerink, A., Luminescence of Nanocrystalline ZnS: Cu^{2+}. *J. Lumin.* **2002**, *99*, 325-334.

36. Wang, M.; Sun, L.; Fu, X.; Liao, C.; Yan, C., Synthesis and Optical Properties of ZnS: Cu (II) Nanoparticles. *Solid State Commun.* **2000**, *115*, 493-496.

37. Yang, P.; Lü, M.; Xu, D.; Yuan, D.; Song, C., Photoluminescence Characteristics of ZnS Nanocrystallites Co-Doped with Cu^{2+} and Cd^{2+}. *J. Phys. Chem. Solids* **2003**, *64*, 155-158.

38. Whitham, P. J.; Knowles, K. E.; Reid, P. J.; Gamelin, D. R., Photoluminescence Blinking and Reversible Electron Trapping in Copper-Doped CdSe Nanocrystals. *Nano Lett.* **2015**, *15*, 4045-4051.

39. Tananaev, P. N.; Dorofeev, S. G.; Vasil'ev, R. B.; Kuznetsova, T. A., Preparation of Copper-Doped CdSe Nanocrystals. *Inorg. Mater.* **2009**, *45*, 347-351.

40. Hao, E.; Zhang, H.; Yang, B.; Ren, H.; Shen, J., Preparation of Luminescent Polyelectrolyte/Cu-Doped ZnSe Nanoparticle Multilayer Composite Films. *J. Colloid Interface Sci.* **2001**, *238*, 285-290.

41. Tang, A.; Yi, L.; Han, W.; Teng, F.; Wang, Y.; Hou, Y.; Gao, M., Synthesis, Optical Properties, and Superlattice Structure of Cu (I)-Doped CdS Nanocrystals. *Appl. Phys. Lett.* **2010**, *97*, 033112.

42. Bear, J. C.; Hollingsworth, N.; McNaughter, P. D.; Mayes, A. G.; Ward, M. B.; Nann, T.; Hogarth, G.; Parkin, I. P., Copper-Doped CdSe/ZnS Quantum Dots: Controllable Photoactivated Copper (I) Cation Storage and Release Vectors for Catalysis. *Angew. Chem. Int. Ed.* **2014**, *53*, 1598-1601.

43. Dutta, A.; Bera, R.; Ghosh, A.; Patra, A., Ultrafast Carrier Dynamics of Photo-Induced Cu-Doped CdSe Nanocrystals. *J. Phys. Chem. C* **2018**, *122*, 16992-17000.

44. Zhao, F.; Hu, S.; Xu, C.; Xiao, H.; Zhou, X.; Zu, X.; Peng, S., Effect of Copper Doping on Electronic Structure and Optical Absorption of $Cd_{33}Se_{33}$ Quantum Dots. *Nanomaterials* **2021**, *11*, 2531.

45. Zandkarimi, B.; Sun, G.; Halder, A.; Seifert, S.; Vajda, S.; Sautet, P.; Alexandrova, A. N., Interpreting the Operando XANES of Surface-Supported Subnanometer Clusters: When Fluxionality, Oxidation State, and Size Effect Fight. *J. Phys. Chem. C* **2020**, *124*, 10057-10066.

46. Meulenberg, R. W.; van Buuren, T.; Hanif, K. M.; Willey, T. M.; Strouse, G. F.; Terminello, L. J., Structure and Composition of Cu-Doped CdSe Nanocrystals Using Soft X-Ray Absorption Spectroscopy. *Nano Lett.* **2004**, *4*, 2277-2285.

47. Gaur, A.; Shrivastava, B. D.; Joshi, S. K. In Copper K-Edge XANES of Cu (I) and Cu (II) Oxide Mixtures, *J. Phys.: Conf. Ser.*, IOP Publishing: 2009; p 012084.

48. Jawaid, A. M.; Chattopadhyay, S.; Wink, D. J.; Page, L. E.; Snee, P. T., Cluster-Seeded Synthesis of Doped CdSe: Cu_4 Quantum Dots. *ACS Nano* **2013**, *7*, 3190-3197.

49. Smolentsev, G.; Soldatov, A. V.; Feiters, M. C., Three-Dimensional Local Structure Refinement Using a Full-Potential XANES Analysis. *Phys. Rev. B* **2007**, *75*, 144106.

50. Zhang, R.; McEwen, J. S., Local Environment Sensitivity of the Cu K-Edge XANES Features in Cu-SSZ-13: Analysis from First-Principles. *J. Phys. Chem. Lett.* **2018**, *9*, 3035-3042.

51. Gul, S.; Cooper, J. K.; Corrado, C.; Vollbrecht, B.; Bridges, F.; Guo, J.; Zhang, J. Z., Synthesis, Optical and Structural Properties, and Charge Carrier Dynamics of Cu-Doped ZnSe Nanocrystals. *J. Phys. Chem. C* **2011**, *115*, 20864-20875.

52. Ke, J.; Li, X.; Zhao, Q.; Shi, Y.; Chen, G., A Novel Approach to Synthesize Ultrasmall Cu Doped Zn–In–Se Nanocrystal Emitters in a Colloidal System. *Nanoscale* **2014**, *6*, 3403-3409.

53. Allmann, R.; Henke, W.; Reinen, D., Presence of a Static Jahn-Teller Distortion in Copper (II) Terpyridine Complexes. 1. Crystal Structure of Diterpyridinecopper (II) Nitrate. *Inorg. Chem.* **1978**, *17*, 378-382.

54. Volnianska, O., Computational Studies of the Electronic Structure of Copper-Doped ZnO Quantum Dots. *J. Chem. Phys.* **2021**, *154*, 124710.

55. Clerjaud, B.; Gelineau, A., Strong Spin-Lattice Coupling of Kramers Doublets. *Phys. Rev. B* **1977**, *16*, 82.

56. Jana, S.; Srivastava, B. B.; Acharya, S.; Santra, P. K.; Jana, N. R.; Sarma, D. D.; Pradhan, N., Prevention of Photooxidation in Blue–Green Emitting Cu Doped ZnSe Nanocrystals. *Chem. Comm.* **2010**, *46*, 2853-2855.

57. Yadav, A. N.; Singh, A. K.; Chauhan, D.; Solanki, P. R.; Kumar, P.; Singh, K., Evaluation of Dopant Energy and Stokes Shift in Cu-Doped CdS Quantum Dots Via Spectro-Electrochemical Probing. *New J. Chem.* **2020**, *44*, 13529-13533.

58. Kumar, P.; Singh, K., Ferromagnetism in Cu-Doped ZnSe Semiconducting Quantum Dots. *J. Nanoparticle Res.* **2011**, *13*, 1613-1620.

59. Pandey, A.; Brovelli, S.; Viswanatha, R.; Li, L.; Pietryga, J. M.; Klimov, V. I.; Crooker, S. A., Long-Lived Photoinduced Magnetization in Copper-Doped ZnSe–CdSe Core–Shell Nanocrystals. *Nat. Nanotech.* **2012**, *7*, 792-797.

60. Wuister, S. F.; de Mello Donega, C.; Meijerink, A., Influence of Thiol Capping on the Exciton Luminescence and Decay Kinetics of CdTe and CdSe Quantum Dots. *J. Phys. Chem. B* **2004**, *108*, 17393-17397.

61. Yang, L.; Knowles, K. E.; Gopalan, A.; Hughes, K. E.; James, M. C.; Gamelin, D. R., One-Pot Synthesis of Monodisperse Colloidal Copper-Doped CdSe Nanocrystals Mediated by Ligand–Copper Interactions. *Chem. Mater.* **2016**, *28*, 7375-7384.

Chapter 3

Part B

Probing Copper Oxidation State Using Single-Particle Fluorescence Spectroscopy

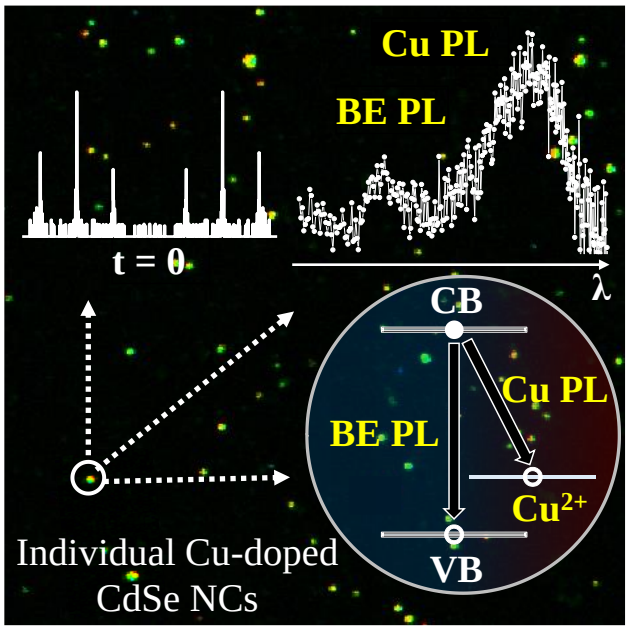

3.4. Previous part

In the previous part, we discussed the fundamental quantum mechanical phenomenon explaining the optical properties related to the monovalent and divalent Cu dopants acquired from the existing literature. We then describe the lack of unanimity regarding the Cu oxidation state and its emission mechanism due to the spatial clutter that arises from the existing ensemble measurements. This disagreement becomes a major bottleneck in the development of this class of doped QDs. Thus, following the debate, in the present chapter, we discuss how single-particle fluorescence spectroscopy declutters the data obtained in the ensemble of measurements.

3.5. Abstract

Copper doping in II-VI semiconductor nanocrystals (NCs) has sparked enormous debate regarding the oxidation state of Cu ions and their hugely differing consequences in optoelectronic applications. The identity of a magnetically active Cu^{2+} ion or a magnetically inactive d^{10} Cu^{+} ion has generally been probed using optical techniques, and confusion arises from the spatial clutter that is part of the technique. One major probe that could declutter the data obtained from ensemble emission is single-particle fluorescence spectroscopy. In this work, using this very technique along with X-ray absorption spectroscopy probing the local environment of dopant ions, we study Cu-doped II-VI semiconductor NCs to find conclusive evidence on the oxidation state of Cu dopants and hence the mechanism of their emission. Detailed analysis of blinking properties has been used to study the single-particle nature of the NCs.

3.6. Introduction

Doping Cu into semiconductors introduces a localized intragap energy state, which undergoes charge carrier exchange with the valence band (VB) and conduction band (CB) through radiative as well as nonradiative pathways[1-5] and gives rise to new photoluminescence (PL) property at the cost of excitonic PL (also known as band-edge PL). This intragap Cu luminescence center has been extensively studied[1, 6-10] and has shed light on various electronic properties of the doped nanocrystals (NCs). While the photogenerated electron (PGE) has been largely accepted to be involved in the Cu-related peak in the PL spectrum,[11-13] the origin of the hole is very controversial and has become a “center table subject” for debate amongst the researchers. This scenario is largely contributed by the ease of formation of two different oxidation states of Cu, namely, +1 and +2 oxidation states.[14-15] Briefly, Cu ions having +1

oxidation state consist of a fully filled $3d^{10}$ shell, and the PL peak arising from Cu is also dictated completely by routine transient state optics.[15-18] In contrast, Cu^{2+} having a d^9 configuration contains one permanent optically active hole that can directly recombine with the PGE, inducing dopant emission and thus partially deviating from the transient state optics for the Cu peak. Additionally, the PGE can also recombine with the photogenerated hole (PGH) in VB and gives rise to band-edge (BE) emission.[19-22] The probability of recombination of PGE with either the PGH or the optically active Cu hole depends on the competition between the radiative and nonradiative pathways of decay of the PGH followed by the lifetime of the two processes. Essentially, in most cases, a divalent copper (Cu^{2+}, $3d^9$) doped NC gives rise to both BE and dopant emission.

Interestingly, several reports have been published in support of both the oxidation states. In particular, X-ray absorption near-edge structure (XANES) of the Cu L-edge for Cu-doped CdSe NCs[23] and the absence of electron paramagnetic resonance (EPR) signal have been claimed as proof for the +1 oxidation state.[16] However, to counter these arguments, EPR signal is shown to appear in Cu-doped ZnSe NCs[24] as well as the significant increase in the Zeeman splitting for 1s exciton (~3.0 meV at 6 T magnetic field) in Cu-doped ZnSe/CdSe core/shell structure[22] have opened the doors for +2 oxidation state. Hence, despite several studies, conclusive evidence on the oxidation state of Cu has not been found and these contradicting reports make the entire topic debatable.

In this context, we note that while optical methods can provide the most convincing evidence, a typical spectrum with multiple peaks is a consequence of spectra averaged from individual NCs, leaving the door open for a discussion regarding a single fluorophore or multiple fluorophores. This flaw can be effectively nullified by studying the single-particle fluorescence of a sample with substantial BE emission as well as the Cu emission in the ensemble PL spectra. Importantly, use of samples with almost an exclusive dopant emission profile in the ensemble PL[25-26] does not show a difference in the two oxidation states, and hence any comment on the oxidation state of the Cu ion even within this method is inconclusive. Here in this work, we used Cu-doped CdSe samples that show both substantial BE and Cu dopant peaks. We then measured and analyzed extended X-ray absorption fine structure (EXAFS) to determine the exact position of Cu dopants within the host NCs. The same set of Cu-doped NCs was studied using single-particle fluorescence spectroscopy. The single particular nature of the sample was studied from antibunching and blinking of the NCs. Blinking statistics were calculated to understand the decay mechanism of the emission pathways. In addition, we

measured the single-particle lifetime of the two peaks using fluorescence lifetime imaging microscopy (FLIM) and compared it with the ensemble PL to reach a conclusion to this long-standing debate.

3.7. Experimental Section

3.7.1. Synthesis and characterization of Cu-doped CdSe

Cu-doped CdSe NCs with varying sizes, synthesized by the hot-injection method following literature. Briefly, copper stearate ($CuSt_2$) was prepared using copper acetate ($CuAc_2$) in methanol with a dropwise addition of TMAH and stearic acid in methanol under continuous stirring. A light blue precipitate of $CuSt_2$ was obtained which was thoroughly washed using methanol and acetone. The typical synthesis of CdSe NCs includes 0.83M cadmium oleate in ODE that was degassed and 0.25 mL of 1M TOPSe being injected at a temperature of 180°C. To this solution, 15 μmol $Cu(St)_2$ solution in ODE was added dropwise and annealed at 140°C to obtain Cu-doped NCs.

Ensemble averaged UV-visible absorption spectra of Cu-doped CdSe NCs dissolved in toluene were obtained using Agilent 8453 UV-visible spectrometer. Steady state PL spectra were collected using the 450 W xenon lamp as the source on the FLSP920 spectrometer, Edinburgh Instruments, while the PL lifetime measurements were carried out in the same instrument using an EPL-405 pulsed diode laser as the excitation source (λ_{ex} = 405 nm).

3.7.2. Preparation of samples for single-particle fluorescence measurements

To study the behaviour of NCs at single particle level, the concentration of NCs in solution should be low enough. Purified NCs were dissolved in toluene and diluted using poly(methyl methacrylate) (PMMA) solution. Then, the diluted NC solution was spun cast onto a glass coverslip. Specifically, the synthesized NCs are capped with different long-chain organic ligands such as oleic acid, oleylamine, etc. and on the other hand, lone pair electrons present on the oxygen atom make PMMA capable of coordinating with the active site of NCs. As a result, the surface capping of the NCs might be substituted partially by PMMA. PMMA majorly interacts with the surface of the NCs and the chemical environment in the bulk of the NCs remains intact, which helps in retaining their pristine PL emission under optimal ratio of the NCs with the PMMA.

3.7.3. Single-particle fluorescence spectroscopy

Single-particle fluorescence imaging was performed using a confocal inverted microscope Olympus IX73 equipped with an oil immersion objective (Olympus 100X/NA 1.4) and the 404 nm output of a 1 MHz, picosecond pulsed diode laser was used as the excitation source. The laser beam was focused onto the sample substrate by the immersion-oil objective (NA = 1.4). The PL signal of a single NC was collected by the same objective and sent through a 0.5 m spectrometer to a charge coupled-device camera for the PL spectral measurements. The PL signal of a single NC can be alternatively sent through a nonpolarizing 50/50 beam splitter to two avalanche photodiodes (APDs) in a time-correlated single photon counting (TCSPC) system. The TCSPC system was operated under the time-tagged, time resolved (TTTR) mode so that the arrival times of each photon relative to the laboratory time and the laser pulse time could both be obtained. A spectrograph is attached to an exit port of the main optical unit of MicroTime 200, which is SR193i equipped with ixon ultra 897 EMCCD provided by Andor Technology. Single-particle fluorescence spectra have been taken using 300 lines/mm grating and 500 nm blaze. The fluorescence was then focused through a 50 μm pinhole and split with a 50/50 beam-splitter through 565/40 nm band-pass filters (part number D565/40m, Chroma, Rockingham, VT) and focused onto two avalanche photodiode detectors (Tau-SPAD 50, Picoquant, Berlin, Germany).

3.7.4. Extended X-ray Absorption Fine Structure spectroscopy

Cd K-edge (26711 eV) and Cu K-edge (8978.9 eV) measurement of the sample was carried out in P64 beamline in DESY Photon Science, Germany. All spectra were collected at fluorescence mode in an ion chamber. Pt mirror was used to eliminate photons of higher energy for Cd edge measurement. Data were processed using the software *Athena* plotting the EXAFS oscillation in momentum (k) space as a function of photoelectron momentum (or, wavenumber) k and then Fourier transforming in position (R) space through a Hanning window for visual representation of the bond-lengths involved in the system, which were analysed with the software *Artemis* to get quantitative information about the local environment of the NCs. Throughout the analysis, the theoretical standards to which the experimental data were fitted, were generated from FEFF6 built into *Artemis.*

3.8. Results and Discussion

Cu-doped CdSe NCs with varying sizes, synthesized by the hot-injection method,[20] were used to study the oxidation state and hence the dopant emission mechanism. Size variation allowed the tunability of Cu emission from 600 to 800 nm. The percentage of dopant concentration incorporated was determined to be ~1% from inductively coupled plasma optical emission spectroscopy. The formation of NCs was characterized by transmission electron microscopy (TEM) images and X-ray diffraction (XRD) patterns as shown for a typical sample in Figure 3.8.

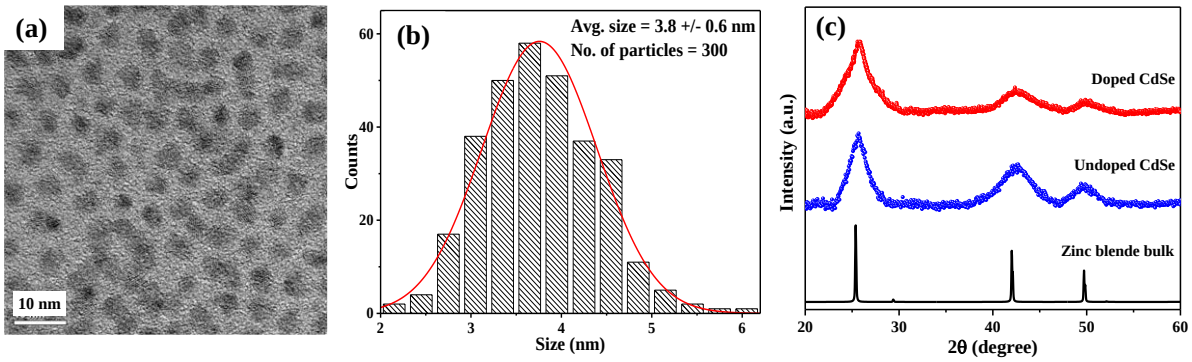

Figure 3.8. *(a) TEM image of Cu-doped NCs shows uniform distribution of spherical particles (b) Corresponding particle size distribution histogram (c) X-ray diffraction pattern of undoped (blue) and doped (red) CdSe nanocrystals along with bulk cubic zinc blende pattern.*

TEM shows a nearly uniform distribution of spherical particles with an average size of 3-4 nm. XRD patterns of the doped and undoped samples reveal the formation of cubic zinc blende phase as obtained by a comparison of the bulk data from the ICSD database. Any lattice constant changes due to doping could not be perceived beyond the experimental error due to the inherent peak broadening arising from the small size of NCs. Though XRD and TEM can ensure the overall formation of NCs with a given size distribution, they are not very sensitive to the incorporation of the dopant ion within the lattice.

We performed X-ray absorption spectroscopy, with emphasis on the EXAFS region, to obtain the local environment around the Cu ion with respect to the Cd environment by studying the Cu K_α state and the Cd K_α state. Our study focuses on the similarities and the differences in the local environment between the Cd and the Cu ion within the first and second shell. The

real space data, $\chi(R)$, of the Cd and Cu K-edge obtained by Fourier transforming the k^2-weighted $\chi(k)$ are shown as black empty circles in panel a and b of Figure 3.9 respectively, while the thick black lines show the fit to the experiment. The fit was obtained by introducing the expected paths. The component paths are shown as dashed lines in the figure, while the detailed parameters as obtained from the fit are tabulated in Table 3.1.

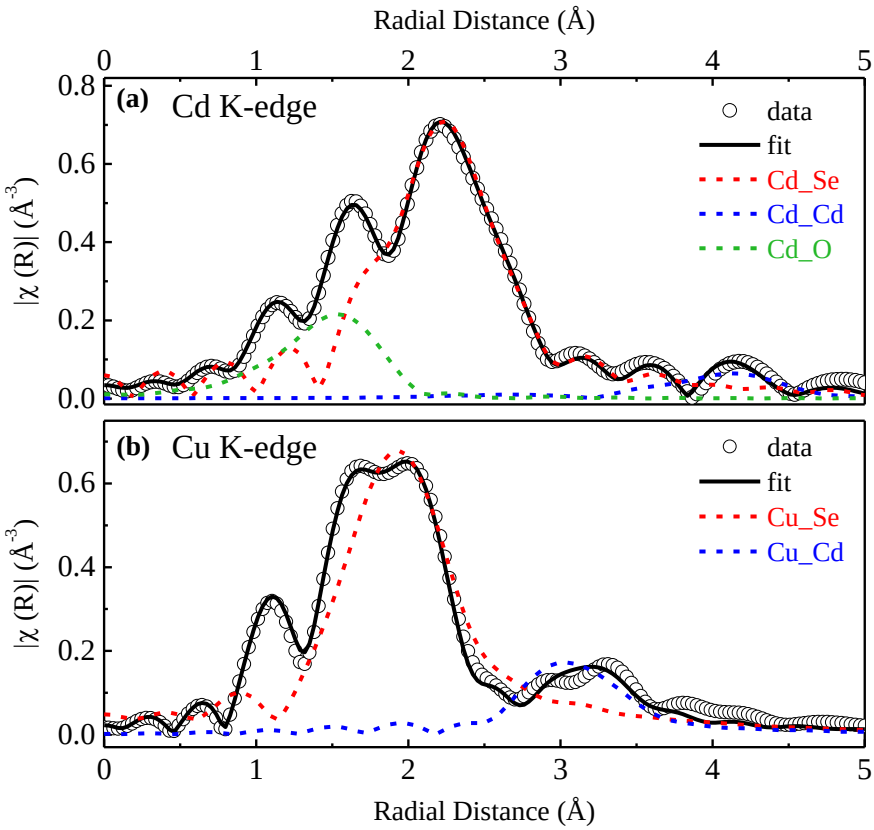

Figure 3.9. *Magnitude of Fourier-transformed (a) Cd K-edge and (b) Cu K-edge EXAFS spectra (black empty circles) and their best fit (black line).*

The obtained bond length of Cd-Se bond (2.63 ± 0.01 Å) is similar to that of bulk CdSe (2.61 Å),[27] suggesting that the NC does not undergo structural changes or distortion upon doping with a small percentage (~1%). However, the Cu-Se bond length is substantially reduced to 2.35 Å, due to the smaller atomic number element like Cu (Z= 29) replacing a higher atomic numbered Cd (Z: 48). Similarly, we observe a substantial decrease in the second nearest neighbour Cu-Cd distance compared to that of the Cd_Cd path, suggesting a substitutional

doping of the Cu ion. To fit the experimentally observed curves better and to account for the substantial surface states, we introduced a Cd_O path representing the interaction of Cd with low-Z elements on the surface. The peak was found to be at 1.63 Å (Figure 3.9(a)) as obtained through a quick-shell fitting in *Artemis* to model the Cd K-edge. Interestingly, the introduction of the same path into the Cu K-edge substantially worsened the fit, suggesting that Cu does not reside on the surface of the NCs. This suggests that not only does the Cu replaces Cd in the lattice sites rather than in an interstitial position but is also buried inside the bulk of the NCs and is not present at the surface of the NCs. This doping in the bulk of the NCs protects the dopants from being oxidized and provides stable and intense emission,[11] a necessary asset for single-particle studies.

Table 3.1. *List of fit parameters (independent points (N_{indp}) and Number of variables (N_{var}) for the fit, Coordination number (CN), Energy shift (ΔE_0), Debye-Waller factor (σ^2), Bond length (R), and R-factor) obtained from modelling the data for Cd-K edge and Cu-K edge.*

edge	shell	CN	ΔE_0 (eV)	σ^2 (Å^2)	R (Å)	R-factor
Cd_K k (1,9) R (1,7.5) N_{indp} =38 N_{var} = 19	Cd-Se Cd-Cd Cd-O	3.92 ± 0.42 6.70 ± 2.72 1.49±0.309	3.91 ± 0.94 3.76 ± 1.37 -1.62±2.18	0.007±0.0006 0.03 ± 0.0083 0.014 ±0.0044	2.63 ±0.0003 4.39 ± 0.091 2.22 ± 0.121	0.003
Cu_K k (0.8,8.85) R (1,5) N_{indp} =25 N_{var} = 15	Cu-Se Cu-Cd	1.65 ± 0.44 1.29 ± 0.98	-14.40±2.63 -7.18 ±2.96	0.004 ± 0.002 0.007 ± 0.007	2.35 ± 0.278 3.48 ± 0.820	0.018

Ensemble optical characterization shown in Figure 3.10(a) revealed similar absorption features for the doped and undoped counterparts at ~2.4 eV. The doped NCs showed two distinct PL emission features at ~2.30 eV (BE emission) and an intense, broad, red-shifted emission at ~1.70 eV. The average PL quantum yield (QY) of the doped NCs is found to be ~15%. In addition, time-resolved photoluminescence (TRPL) studies (empty circles) along with the multi-exponential fits (solid lines) at maxima of BE and Cu PL (Figure 3.10(b)) show

a dominant radiative decay lifetime of ~450 ns for the dopant-based emission as compared to ~30 ns for the BE emission. This long lifetime suggests weak spatial overlap between the localized copper state and the delocalized CB electron wave function. Post-doping annealing showed an intensification of the dopant emission at the cost of BE emission as shown in Figure 3.11., suggesting the diffusion of dopant ions from surface to the core of NCs.

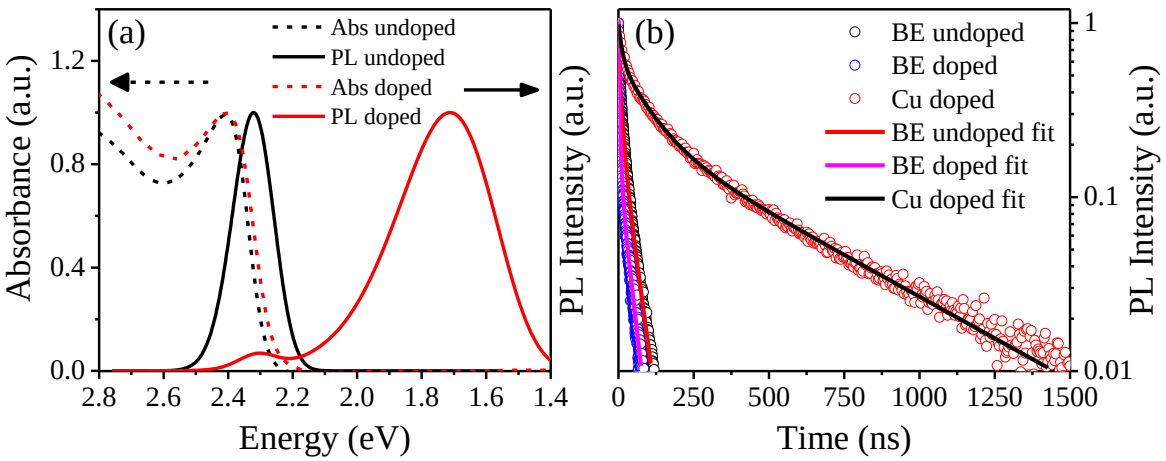

Figure 3.10. *Optical characterization of undoped and Cu-doped nanocrystals (a) Normalized absorption and PL spectra of undoped (black dotted and solid lines, respectively) and Cu-doped CdSe (red dotted and solid lines, respectively) nanocrystals. (b) TRPL spectra of undoped (black circles) and doped NCs measured at excitonic (blue circles) and at dopant (red circles) emission maxima.* λ_{ex} *= 405 nm. Corresponding fits are shown in red, magenta, and black solid lines respectively.*

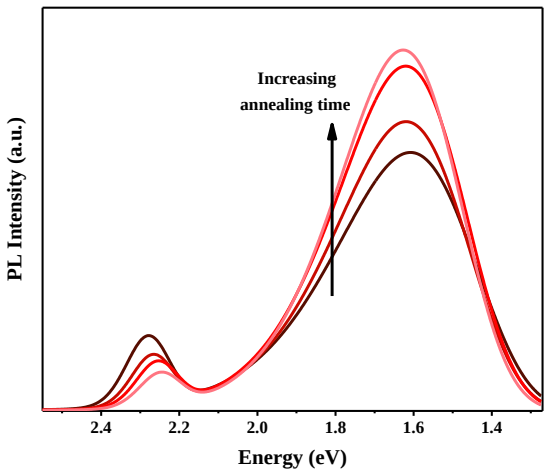

Figure 3.11. *Typical PL spectra of CdSe nanocrystals after adding Cu precursor with increase in the annealing time.*

The fully characterized Cu-doped CdSe NCs were encapsulated in the poly(methyl methacrylate) (PMMA) matrix as discussed in the Supporting Information. Any instrumental artifact arising due to PMMA encapsulation in single-particle spectra has been nullified by checking the tunability of the Cu emission in the steady state PL spectra of single particle of Cu doped CdSe NCs of varying sizes (shown in Figure 3.12(a)) similar to the ensemble measurements, shown in Figure 3.12(b). It reveals that even in the single-particle regime, the mean position of the dopant PL changes as a function of BE emission position, shown in Figure 3.12(c), confirming that the peaks originate from the NCs. However, the wide variation in the peak position obtained for each of the individual particles makes a meaningful quantitative analysis impossible.

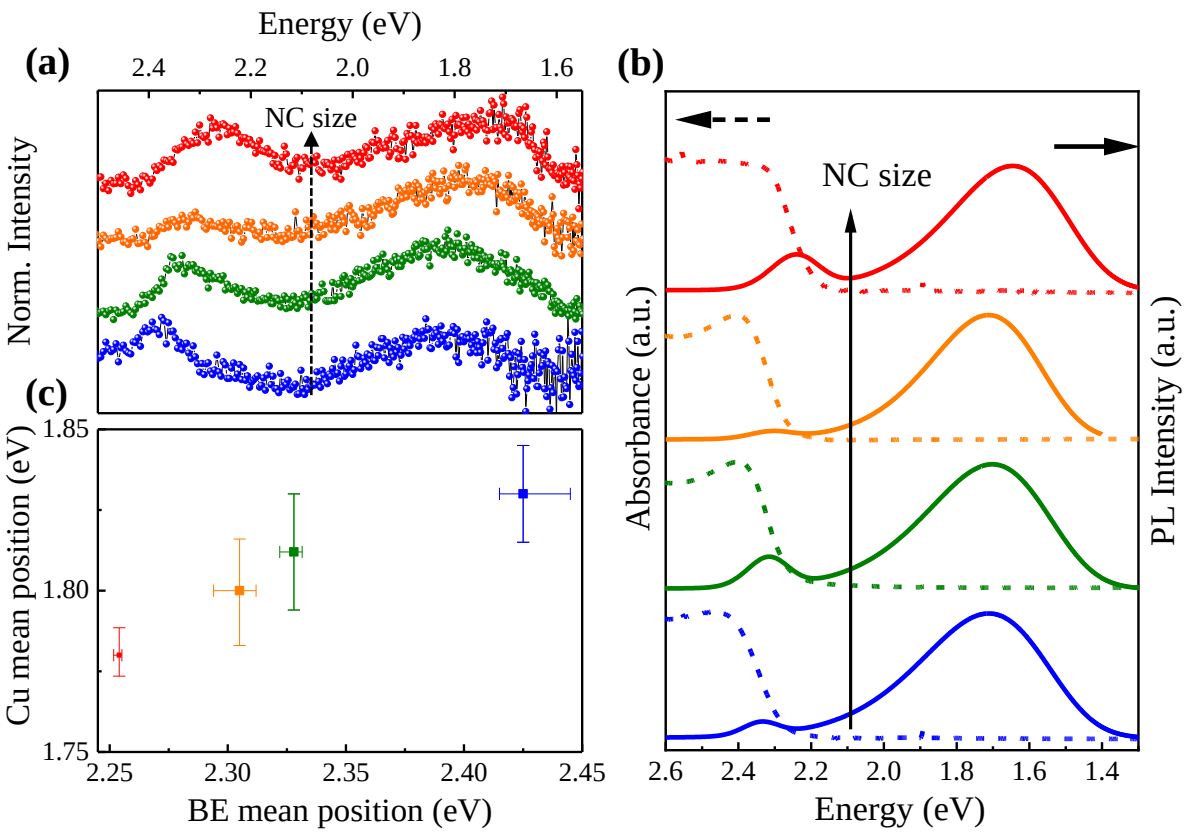

Figure 3.12. *(a) Single-particle PL spectra of NCs of different sizes. (b) Ensemble absorbance and PL spectra of Cu-doped CdSe nanocrystals of various sizes which have been used to study the PL shift in single nanocrystals.* ***(c)*** *Variation of BE and Cu PL position with respect to the mean position.*

Further, we performed fluorescence lifetime imaging (FLIM) on these samples using 404 nm pulsed laser excitation with 1 MHz repetition rate. Representative images of the same are shown in Figure 3.13.

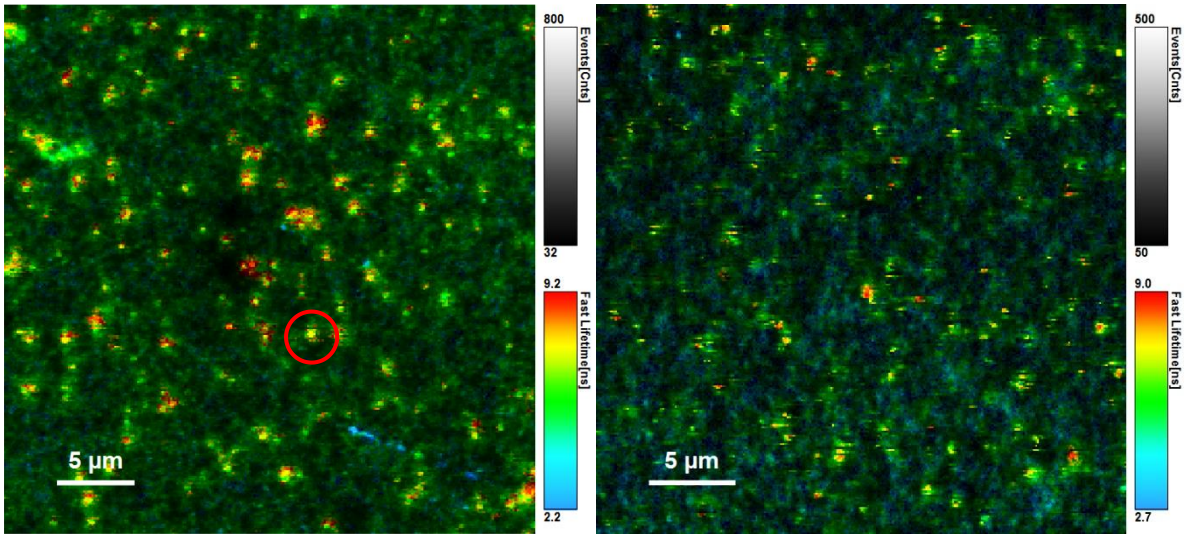

Figure 3.13. *Representative fluorescence lifetime images with false colour representation show single nanoparticle distribution.*

The steady state PL spectra were measured using a spectrograph attached to the exit port of the microscope. Figure 3.14 shows the comparison of a typical steady state PL and the lifetime of a single particle with that of the ensemble. From the figure, the steady state PL spectrum of the single-particle (Figure 3.14(a)) is in reasonable agreement with the ensemble PL spectrum (Figure 3.14(b)) except for a higher ratio of the BE to Cu emission in a single particle. This could be assigned to the well-known surface effect[2, 28] arising from the altered surface due to the PMMA matrix. Additionally, due to the instrument limitations of a maximum of 1 MHz, i.e., 1 µs pulse rate of the laser excitation, longer-lived emission pathways like Cu emission are known to be adversely affected compared to the BE emission with a lifetime of a few ns. Despite this shortcoming, the most important point to note here is that a single NC gives rise to both BE as well as dopant emission. While the spectrum shown here is a representative one, we observed similar data across all the particles measured (~200 particles) without exception, suggesting the presence of Cu^{2+}.

Similarly, the TRPL spectra at the BE and the dopant emission peaks present a very similar decay profile for the single-particle and ensemble-averaged spectra as shown in panel c and d of Figure 3.14 respectively. For a single NC, two different bandpass filters were used, namely 515-565 nm and 705-740 nm, to record the PL decay dynamics at BE (blue circles) and Cu (red circles) emission features respectively. Similar to the steady state PL, the lifetime of dopant emission (~400 ns), though substantially longer than the BE lifetime (~10 ns), is substantially shorter than its ensemble counterpart due to the instrumental limitations. We studied the decay dynamics for ~30 single NCs and all of them exhibited both BE and Cu emissions.

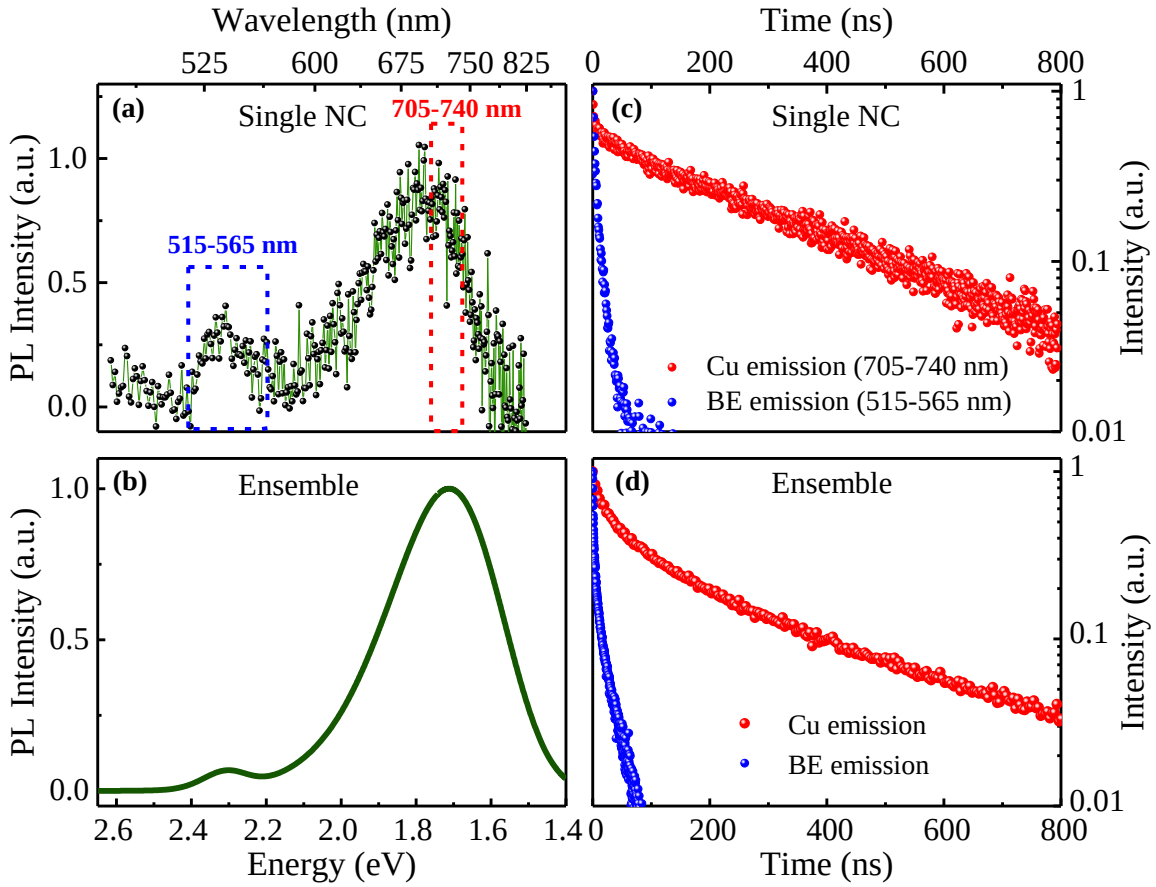

Figure 3.14. *(a) Steady state PL spectra obtained from a single NC. (b) Corresponding ensemble PL (solid line) with substantial BE emission as well as dopant emission. (c) TRPL measured at both optical windows (shown in the single-particle spectra, windows marked as blue and red rectangles)* λ_{em} *= 515-565 nm (blue circles) and* λ_{em} *= 705-740 nm (red circles) corresponds to BE and Cu PL respectively. (d) Ensemble TRPL measured at* λ_{em} *= 540 nm (blue circles) as well as at* λ_{em} *= 720 nm (red circles).*

However, such an overwhelming resemblance with the ensemble behaviour as observed here begs an answer to the question that if it is indeed single particle. In that context, we studied the blinking, an inherent property of the single NC[29] unless specially modified to combat the same,[30] wherein PL intensity goes from bright '*on*' state and dark '*off*' state under continuous excitation, for all particles under study. Though blinking implies serious constraints on a wide range of applications of semiconductor NCs,[31] it is an excellent tool for probing the single-particle nature. The intermittency in the PL intensity of the NC is attributed to illumination-induced charging (on → off) followed by neutralization (off → on) of the NC. In the case of any finite ensemble, PL blinking will be smoothed out and hence undetectable but can be observed in the case of a single NC.[32] Panel (a) and (b) of Figure 3.15 show blinking traces for the 515-565 nm (BE emission) and 705-740 nm (Cu emission) spectral windows, respectively, of a representative NC (circled in red, in Figure 3.13(a)) taken over a period of 120 seconds. In both cases, the black line demonstrates the background intensity measured on PMMA on a glass substrate in the absence of the NCs. As expected, we observe that the time dependence of PL intensity exhibits a sequence of '*on*' and '*off*' periods, suggesting the observed particle to be a single NC. To further confirm a single NC, we studied single-photon emission behaviour by performing photon correlation measurements. Figure 3.15(c) shows the second-order autocorrelation function also known as antibunching peak, collected using pulsed laser excitation with 1 MHz repetition rate. As one can clearly see from the figure, at zero delay time, photon antibunching dip goes down to zero within the background noise, even though a value as high as 0.5 is universally accepted in the literature[31, 33] as a single-particle photon emission.

In addition, as discussed above, Cu^{+} is completely dependent on the transient state optical recombination while Cu^{2+} provides an independent pathway.[20] Hence, the statistical distribution of the PL intermittency for both BE emission and Cu emission would be identical in Cu^{+} as they are both dependent on the charging nature of the PGE/PGH. However, in the case of Cu^{2+}, the presence of an optically active hole that is independent of the NCs charging through the PGH produces non-identical statistics for the dopant and BE emission. Hence, study of the underlying statistical distribution could shed further light on the oxidation state of the dopant ion. Analysis of the photoluminescence intermittency using power law distribution of the '*on*' (all events above the mean background intensity) and '*off*' events have recently been debated.[34] Hence, to compare distributions without assuming a parametric form for the underlying probability distribution functions, we calculate the cumulative distribution function

(CDF) for each data set.[35] The conversion of probability distribution functions to CDFs is described elsewhere.[36] Briefly, the time duration of '*on*' and '*off*' events were calculated followed by CDF calculation using the formula, $CDF(t) = \frac{1}{N}\sum_i t_i$, where N is the total number of on/off events, t_i is the event duration. The complementary CDF (cCDF), defined by cCDF(t) = 1- CDF(t), as a function of time for '*on*' and '*off* ' duration of both BE and Cu blinking are plotted as a logarithmic plot in Figure 3.15(d). From the figure, it is evident that, '*off* ' cCDF for Cu blinking shows a rapid falloff in a shorter time as compared to '*on*' cCDF.

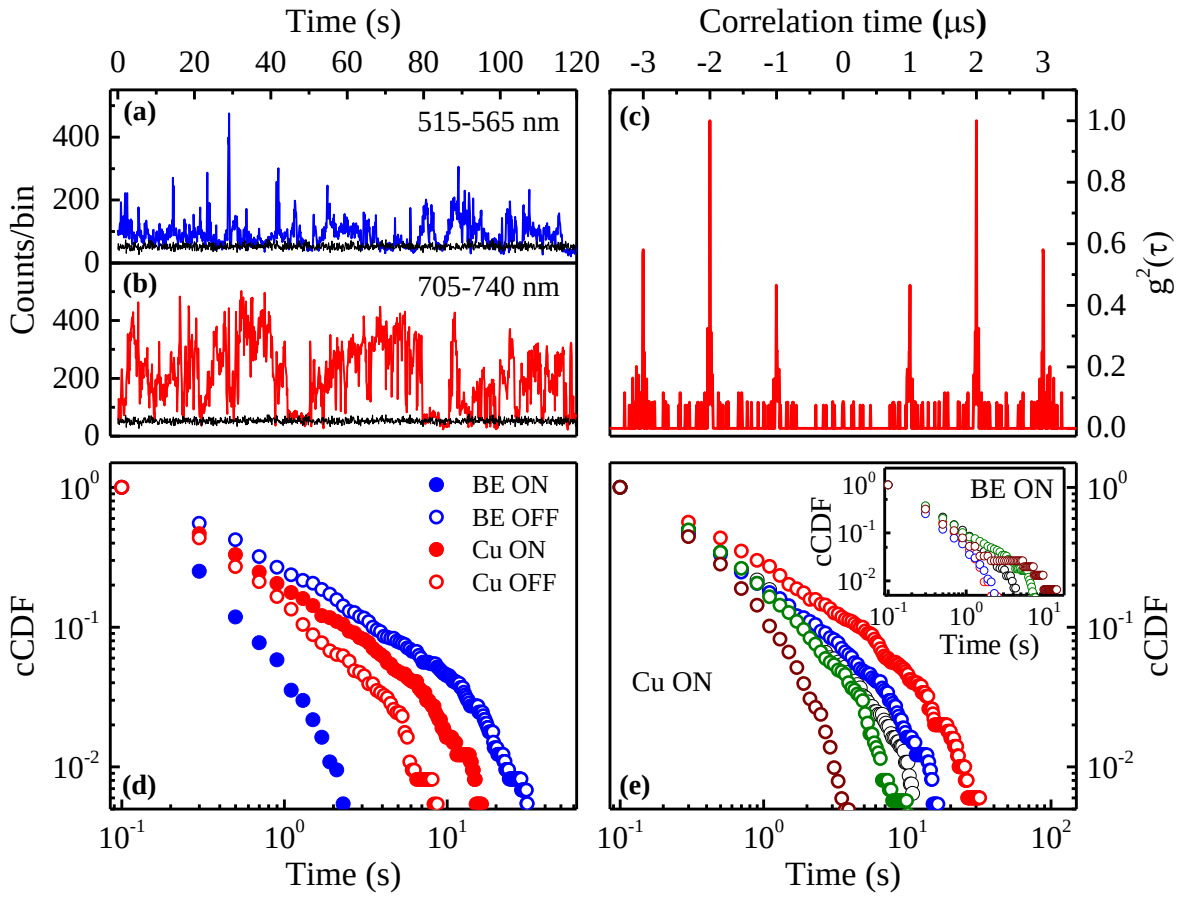

Figure 3.15. *(a) and (b) Blinking dynamics of a single-particle within two optical windows 515-565 nm and 705-740 nm respectively show continuous 'ON' and 'OFF' sequence. (c) Second-order photon autocorrelation measurement of a single NC with a $g^2(\tau)$ value of ~ zero at the zero-time delay. (d) Logarithmic plots of 'ON' (filled circles) and 'OFF'(empty circles) complementary distribution functions (cCDF) of BE (black) and Cu (red) emission. (e) Logarithmic cCDF plots of 'ON' state duration in Cu emission traces for different single NCs and corresponding 'ON' state duration in BE emission traces are shown in the inset.*

However, cCDFs for BE blinking show the exact opposite trend, i.e., the Cu blinking trace does have longer '*on*' state than '*off* ' state, and in contrast to that, the BE blinking trace shows a longer '*off*' state than '*on*' state, suggesting the presence of two different distributions for the dopant emission and the BE emission. In addition, it is well known that unlike the BE emission '*off*' state, BE emission '*on*' state is largely independent of the surface ligands and is largely similar across different sets of particles as shown in the inset to Figure 3.15(e). However, due to the extremely long lifetime of the dopant emission compared to the BE emission, we observe the Cu emission only if the PGH is scavenged by the surface hole traps.[19] Hence, the '*on*' state of the Cu emission is highly dependent on the surface of the NCs. This is also evident in Figure 3.15(e) which shows a widely varying statistical distribution for each of the particles as shown by the logarithmic cCDF plots for Cu '*on*' events of different particles within the same ensemble due to the uncontrollable nature of the surface. This is similar to the behaviour of the '*off*' states for both dopant emission and the BE emission across various sets of particles as shown in Figure 3.16.

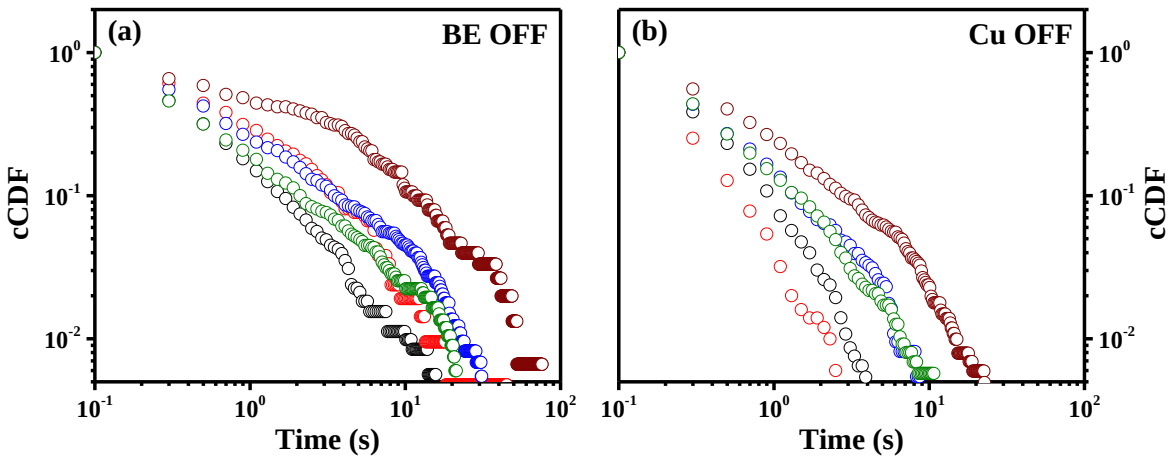

Figure 3.16. *(a) Logarithmic cCDF plots of 'OFF' state duration in BE emission traces for different single NCs and (b) corresponding 'OFF' state duration in Cu emission traces.*

Furthermore, due to the extremely long lifetime of the dopant emission compared to the BE emission, the Cu emission is observed only if the PGH is scavenged by the surface hole traps, as discussed in the earlier chapter. To confirm this, Cu-doped CdSe NCs of almost similar size but different BE to Cu PL intensity ratio by using different TOP concentration were

synthesized. Following that the single-particle fluorescence was measured and the collected spectra of individual doped NCs having different BE to Cu ratio were studied. It was observed to have a similar trend as ensemble measurements as shown in Figure 3.17. Thus, this observation from single doped NC confirms that exclusive Cu emission is only possible when the VB hole is trapped by surface trap states and increased BE emission intensity due to TOP addition is not because of increasing population of undoped NCs but because of less VB hole trapping by trap states. In addition to that significant BE emission intensity along with dopant emission in all the samples is seen which confirms that the Cu ions when doped into NCs are indeed present in 2+ oxidation state.

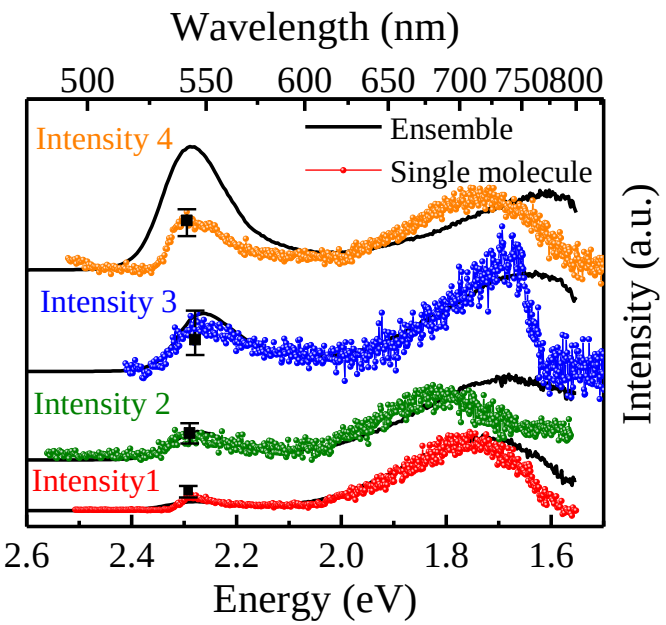

Figure 3.17. *Steady state PL spectra of ensemble (black solid lines) and corresponding single NCs (scattered dots) having increased BE emission (bottom to top) with increasing TOP amount.*

3.9. Conclusion

Thus, in conclusion, after a thorough analysis of blinking dynamics, statistical distribution and identification of a single NC, we propose that the BE emission does not originate from undoped NCs, but rather from BE recombination in the doped NC itself. Finally, with solid proof of the study from single-particle exhibiting both BE emission and dopant

emission, we confirm the presence of Cu ion in +2 oxidation state, providing a conclusion to the prolonged debate. Additionally, the width of Cu PL in both cases (ensemble and single-particle) is almost similar, which suggests that the broad emission width is not caused by the size distribution but is an inherent property of the NC itself. Finally, understanding the oxidation state will help us to know more details of the Cu emission mechanism which in turn would help to improve such useful and tunable light-emitting NCs and broaden their applications in optoelectronic devices.

Bibliography

1. Grandhi, G. K.; Viswanatha, R. Demystifying Complex Quantum Dot Heterostructures Using Photogenerated Charge Carriers. *J. Phys. Chem. Lett.* **2017,** *8*, 2043-2048.

2. Grandhi, G. K.; Viswanatha, R. Tunable Infrared Phosphors Using Cu Doping in Semiconductor Nanocrystals: Surface Electronic Structure Evaluation. *J. Phys. Chem. Lett.* **2013,** *4*, 409-415.

3. Wright, J. T.; Forsythe, K.; Hutchins, J.; Meulenberg, R. W. Implications of Orbital Hybridization on The Electronic Properties of Doped Quantum Dots: The Case of Cu: CdSe. *Nanoscale* **2016,** *8*, 9417-9424.

4. Halperin, A.; Arbell, H. Transients in the Blue and Green Luminescence of ZnS: Cu: Cl Crystals. *J. Chem. Phys.* **1961,** *34*, 879-883.

5. Holton, W. C.; De Wit, M.; Watts, R. K.; Estle, T. L.; Schneider, J. Paramagnetic Copper Centers in ZnS. *J. Phys. Chem. Solids* **1969,** *30*, 963-977.

6. Viswanatha, R.; Chakraborty, S.; Basu, S.; Sarma, D. D. Blue-Emitting Copper-Doped Zinc Oxide Nanocrystals. *J. Phys. Chem. B* **2006,** *110*, 22310-22312.

7. Brovelli, S.; Galland, C.; Viswanatha, R.; Klimov, V. I. Tuning Radiative Recombination in Cu-Doped Nanocrystals Via Electrochemical Control of Surface Trapping. *Nano Lett.* **2012,** *12*, 4372-4379.

8. Grandhi, G. K.; Swathi, K.; Narayan, K. S.; Viswanatha, R. Cu Doping in Ligand Free CdS Nanocrystals: Conductivity and Electronic Structure Study. *J. Phys. Chem. Lett.* **2014,** *5*, 2382-2389.

9. Hughes, K. E.; Ostheller, S. R.; Nelson, H. D.; Gamelin, D. R. Copper's Role in the Photoluminescence of $Ag_{1-x}Cu_xInS_2$ Nanocrystals, from Copper-Doped $AgInS_2$ (x~ 0) to $CuInS_2$ (x= 1). *Nano Lett.* **2018,** *19*, 1318-1325.

10. Xie, R.; Peng, X. Synthesis of Cu-doped InP Nanocrystals (d-dots) with ZnSe Diffusion Barrier as Efficient and Color-Tunable NIR Emitters. *J. Am. Chem. Soc.* **2009,** *131*, 10645-10651.

11. Pradhan, N.; Goorskey, D.; Thessing, J.; Peng, X. An Alternative of CdSe Nanocrystal Emitters: Pure and Tunable Impurity Emissions in ZnSe Nanocrystals. *J. Am. Chem. Soc.* **2005,** *127*, 17586-17587.

12. Suyver, J. F.; Van der Beek, T.; Wuister, S. F.; Kelly, J. J.; Meijerink, A. Luminescence of Nanocrystalline ZnSe: Cu. *Appl. Phys. Lett.* **2001,** *79*, 4222-4224.

13. Nelson, H. D.; Hinterding, S. O. M.; Fainblat, R.; Creutz, S. E.; Li, X.; Gamelin, D. R. Mid-Gap States and Normal vs Inverted Bonding in Luminescent Cu^{+}-and Ag^{+}-Doped CdSe Nanocrystals. *J. Am. Chem. Soc.* **2017,** *139*, 6411-6421.

14. Dutta, A.; Bera, R.; Ghosh, A.; Patra, A. Ultrafast Carrier Dynamics of Photo-Induced Cu-Doped CdSe Nanocrystals. *J. Phys. Chem. C* **2018,** *122*, 16992-17000.

15. Nelson, H. D.; Li, X.; Gamelin, D. R. Computational Studies of the Electronic Structures of Copper-Doped CdSe Nanocrystals: Oxidation States, Jahn–Teller Distortions, Vibronic Bandshapes, and Singlet–Triplet Splittings. *J. Phys. Chem. C* **2016,** *120*, 5714-5723.

16. Srivastava, B. B.; Jana, S.; Pradhan, N. Doping Cu in Semiconductor Nanocrystals: Some Old and Some New Physical Insights. *J. Am. Chem. Soc.* **2011,** *133*, 1007-1015.

17. Corrado, C.; Jiang, Y.; Oba, F.; Kozina, M.; Bridges, F.; Zhang, J. Z. Synthesis, Structural, and Optical Properties of Stable ZnS: Cu, Cl Nanocrystals. *J. Phys. Chem. A* **2009,** *113*, 3830-3839.

18. Hughes, K. E.; Hartstein, K. H.; Gamelin, D. R. Photodoping and Transient Spectroscopies of Copper-Doped CdSe/CdS Nanocrystals. *ACS nano* **2018,** *12*, 718-728.

19. Viswanatha, R.; Brovelli, S.; Pandey, A.; Crooker, S. A.; Klimov, V. I. Copper-Doped Inverted Core/Shell Nanocrystals with "Permanent" Optically Active Holes. *Nano Lett.* **2011,** *11*, 4753-4758.

20. Grandhi, G. K.; Tomar, R.; Viswanatha, R. Study of Surface and Bulk Electronic Structure of II–VI Semiconductor Nanocrystals Using Cu as a Nanosensor. *ACS nano* **2012,** *6*, 9751-9763.

21. Bol, A. A.; Ferwerda, J.; Bergwerff, J. A.; Meijerink, A. Luminescence of Nanocrystalline ZnS: Cu^{2+}. *J. Lumin.* **2002,** *99*, 325-334.

22. Pandey, A.; Brovelli, S.; Viswanatha, R.; Li, L.; Pietryga, J. M.; Klimov, V. I.; Crooker, S. A. Long-Lived Photoinduced Magnetization in Copper-Doped ZnSe–CdSe Core–Shell Nanocrystals. *Nat. Nanotechnol.* **2012,** *7*, 792-797.

23. Meulenberg, R. W.; van Buuren, T.; Hanif, K. M.; Willey, T. M.; Strouse, G. F.; Terminello, L. J. Structure and Composition of Cu-Doped CdSe Nanocrystals Using Soft X-ray Absorption Spectroscopy. *Nano Lett.* **2004,** *4*, 2277-2285.

24. Jana, S.; Srivastava, B. B.; Acharya, S.; Santra, P. K.; Jana, N. R.; Sarma, D. D.; Pradhan, N. Prevention of Photooxidation in Blue–Green Emitting Cu Doped ZnSe Nanocrystals. *Chem. Commun.* **2010,** *46*, 2853-2855.

25. Marchioro, A.; Whitham, P. J.; Knowles, K. E.; Kilburn, T. B.; Reid, P. J.; Gamelin, D. R. Tunneling in the Delayed Luminescence of Colloidal CdSe, Cu^+-Doped CdSe, and $CuInS_2$ Semiconductor Nanocrystals and Relationship to Blinking. *J. Phys. Chem. C* **2016,** *120*, 27040-27049.

26. Whitham, P. J.; Knowles, K. E.; Reid, P. J.; Gamelin, D. R. Photoluminescence Blinking and Reversible Electron Trapping in Copper-Doped CdSe Nanocrystals. *Nano Lett.* **2015,** *15*, 4045-4051.

27. Galicia-Hernandez, J. M.; Sanchez-Castillo, A.; De La Garza, L. M.; Cocoletzi, G. H. Two-Dimensional Cadmium Selenide Electronic and Optical Properties: First Principles Studies. *Bull. Mater. Sci.* **2017,** *40*, 1111-1119.

28. Grandhi, G. K.; A., M.; Viswanatha, R. Understanding the Role of Surface Capping Ligands in Passivating the Quantum Dots Using Copper Dopants as Internal Sensor. *J. Phys. Chem. C* **2016,** *120*, 19785-19795.

29. Efros, A. L.; Nesbitt, D. J. Origin and Control of Blinking in Quantum Dots. *Nat. Nanotechnol.* **2016,** *11*, 661-671.

30. Saha, A.; Chellappan, K. V.; Narayan, K. S.; Ghatak, J.; Datta, R.; Viswanatha, R. Near-Unity Quantum Yield in Semiconducting Nanostructures: Structural Understanding Leading to Energy Efficient Applications. *J. Phys. Chem. Lett.* **2013,** *4*, 3544-3549.

31. Li, Z.; Chen, F.; Wang, L.; Shen, H.; Guo, L.; Kuang, Y.; Wang, H.; Li, N.; Li, L. S. Synthesis and Evaluation of Ideal Core/Shell Quantum Dots with Precisely Controlled Shell Growth: Nonblinking, Single Photoluminescence Decay Channel, and Suppressed FRET. *Chem. Mater.* **2018,** *30*, 3668-3676.

32. Nirmal, M.; Dabbousi, B. O.; Bawendi, M. G.; Macklin, J. J.; Trautman, J. K.; Harris, T. D.; Brus, L. E. Fluorescence Intermittency in Single Cadmium Selenide Nanocrystals. *Nature* **1996,** *383*, 802-804.

33. Lv, B.; Zhang, H.; Wang, L.; Zhang, C.; Wang, X.; Zhang, J.; Xiao, M. Photon Antibunching in a Cluster of Giant CdSe/CdS Nanocrystals. *Nature commun.* **2018,** *9*, 1-7.

34. Amecke, N.; Heber, A.; Cichos, F. Distortion of Power Law Blinking With Binning and Thresholding. *J. Chem. Phys.* **2014,** *140*, 114306.

35. Hess, C. M.; Riley, E. A.; Reid, P. J. Dielectric Dependence of Single-Molecule Photoluminescence Intermittency: Nile Red in Poly (vinylidene fluoride). *J. Phys. Chem. B* **2014,** *118*, 8905-8913.

36. Riley, E. A.; Hess, C. M.; Whitham, P. J.; Reid, P. J. Beyond Power Laws: A New Approach for Analyzing Single Molecule Photoluminescence Intermittency. *J. Chem. Phys.* **2012,** *136*, 184508.

Chapter 4

Photophysics of Mn Emission

The following paper have been published based on the work presented here:

1. Payel Mondal, Sowmeya Sathiyamani, Kushagra Gahlot, and Ranjani Viswanatha. "Is the Lack of Orange Emission Infallible Proof of Unsuccessful Doping of Mn in Quantum Dots?" J. Phys. Chem. C, **2021**, *125*, 11007-11013.

Chapter 4

Part A

Study of Mn-Doped II-VI Semiconductor Quantum Dots as a Function of Bandgap and Composition

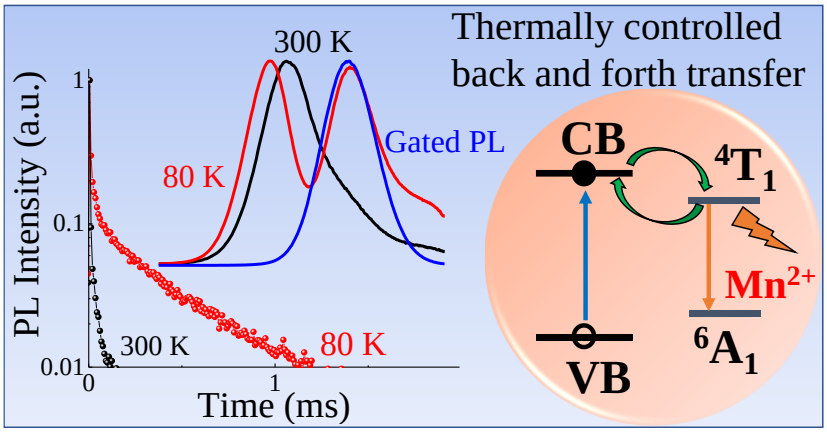

4.1. Abstract

Manganese (Mn) is one of the most studied transition metal dopants to alter the optical properties of host nanocrystals (NCs). In most cases, the doped NCs are characterized by an invariant broad photoluminescence (PL) spectrum at 2.12 eV. The nature of this emission, although thought to be atomic-like, has revealed several dependencies on the host NCs in recent literature that facilitates the energy/charge transfer to a spin and orbital forbidden channel. In this work, we study this transfer as a function of the host bandgap and spin-orbit coupling. We demonstrate that while the energy/charge transfer is facilitated by the energy difference between the bandgap and Mn excitation energy, the high spin-orbit coupling allows transfer and back transfer of energy/charge, thus giving rise to a tunable higher energy transition even in successful doping of Mn. We use low-temperature PL and gated PL to demonstrate this phenomenon.

4.2. Introduction

Deliberate insertion of impurities functionalizes the semiconductor nanocrystals (NCs) yielding numerous interesting properties like optical,[1-4] magnetic,[5-7] electronic,[8-9] magneto-optical[10-12] properties which are otherwise absent or not very prominent in their undoped counterparts. One of the most hugely explored properties is the intense orange photoluminescence (PL) of Mn-doped NCs.[13-15] Upon doping into semiconductor NCs with a sufficiently wide bandgap, Mn^{2+} ion is known to introduce two atomic-like energy states in the mid-gap region[16-17] giving rise to a manganese luminescence centre arising from the radiative transition of $^4T_1$ electrons to the $^6A_1$ level. This transition has so far been treated as an ultimate proof of Mn substitution into the NCs.[18-19] The important characteristics of this spin-forbidden $^4T_1 \rightarrow {}^6A_1$ transition include a substantially longer PL decay lifetime (~ms),[20] at an energy of ~2.12 eV (~585 nm) that is so far been claimed to be independent of any external factors like size and composition of host NCs due to its atomic-like nature. However, there have been extensive studies in literature discussing the various anomalous observations regarding the nature of Mn emission.[10, 15, 21-23] Despite 25 years of research,[24-28] the enigma surrounding the mechanism of Mn emission still exists, and several properties are yet to be explained. For example, although the lack of emission tunability has been demonstrated by a series of NCs with different composition in literature,[29-32] recent work[33-34] on Mn-doped ZnSe/CdSe/ZnSe core/shell NCs has shown the tunability of Mn emission as a function of lattice strain generated at the interfaces of core and shell covering almost the entire visible range. Additionally, there exist few other NC systems which do not exhibit the characteristic Mn emission peak at 2.12

eV including free standing as well as ligand capped wide band gap ZnO NCs and narrow band gap CdSe NCs.[35-39] These reports led us to revisit the problem to study the nature of Mn emission and to determine whether the absence of the signature 2.12 eV peak implies the absence of successful Mn doping. Specifically, many reports[40-41] have observed a tunable higher energy second peak in addition to the 2.12 eV peak in narrow band gap semiconductors. However, due to its tunability, it has been wrongly attributed to excitonic emission from undoped fraction of QDs. Recently, it was shown that the energy of this second peak is far smaller than the excitonic emission obtained in undoped QDs of similar composition and band gap and that the Mn emission is responsible for the peak arising at 2.5 eV (~500 nm).[42] However, tunability of this peak, arising at 500 nm but being tuned to lower energies with decreasing band gap has not been explained.

Hence in this work, we choose hosts such that they have different band gaps that is slightly higher than 2.12 eV emission energy. These hosts were obtained by varying the composition of Cd doped ZnSe NCs. A series of NC systems with varying cadmium content, from x = 0 to x = 0.2 (from S1 to S12, mentioned in Table 4.1) doped $Cd_xZn_{1-x}Se$ NCs with Mn doping were synthesized by alloying Cd through cation exchange. Cd alloying not only brings the band gap closer to 2.12 eV Mn^{2+} transition but also buries the Mn level deeper in the conduction band due to spin-orbit coupling. Study of $Cd_xZn_{1-x}Se$ alloy NCs using gated as well as temperature dependent PL paves way to understand the nature of the transient species during the excitation of the spin forbidden excitation. Clearly, we observe an interaction between the excited state of the dopant and the conduction band (CB) of the semiconductor host as a function of host bandgap.

4.3. Experimental Methods

4.3.1. Materials

Cadmium oxide CdO, zinc stearate $ZnSt_2$, elemental selenium, trioctyl phosphine (TOP, 90%), octadecene (ODE, 90%), oleylamine (technical grade, 70%), oleic acid (technical grade, 90%) were purchased from Sigma Aldrich. Manganous chloride AR ($MnCl_2$), stearic acid LR, were purchased from SD Fine chemicals. Tetramethyl ammonium hydroxide pentahydrate (TMAH, 98%) was purchased from Spectrochem. Methanol, acetone and hexane were purchased from Merck. All purchased chemicals were used without further purification.

4.3.2. Synthesis of precursors

Manganese stearate ($MnSt_2$) was synthesized by the method mentioned in literature.[15] Briefly, stearic acid (20mmol) was dissolved in methanol and added to TMAH solution of similar concentration and stirred for 20 min. Meanwhile, 10 mmol manganous chloride was dissolved separately in methanol and added dropwise to the above-mentioned mixture with constant stirring. The appearance of white precipitate shows the formation of $MnSt_2$. The solution was washed repeatedly with methanol followed by acetone. The white precipitate of $MnSt_2$ obtained was then dried in vacuum and used for further synthesis.

Cadmium oleate ($CdOl_2$) was prepared by heating a mixture of 0.32 g of cadmium oxide, 7 mL oleic acid and 9 mL of ODE to a higher temperature until the solution appeared colorless (~220-240 ^oC) under Ar atmosphere. 1.5 (M) TOPSe was prepared by dissolving 1.18 g Se pellets into 10 mL of TOP in inert atmosphere.

4.3.3. Synthesis of Mn-doped NCs

Synthesis of Mn-doped $Cd_xZn_{1-x}Se$ NCs

Mn-doped ZnSe NCs were synthesized following modified literature method.[15] Briefly, a mixture of 0.03 mmol $MnSt_2$ and ODE was degassed. The reaction temperature was then increased to 280 ^oC under Ar atmosphere and 0.5 mL of TOPSe was injected leading to formation of MnSe nanoclusters. 0.6 mL $ZnSt_2$ precursor (0.5 mmol $ZnSt_2$ in 1.2 mL ODE) was added to grow ZnSe shell over MnSe core. The orange-red fluorescence confirms the formation of Mn-ZnSe NCs. To increase the PL efficiency 0.6 mL OlAm+ODE (1:1) solution was added. The reaction temperature was then reduced to 140 ^oC to add Cd. Cd precursor was added dropwise using a syringe pump to maintain a constant addition rate. Aliquots were taken at different time interval and all the samples were thoroughly washed for further measurements.

Synthesis of Mn-doped CdSe NCs

Mn-doped CdSe NCs were synthesized following nucleation doping method almost similar to Mn-doped $Cd_xZn_{1-x}Se$. Briefly, $MnSt_2$ and ODE were taken in a three necked flask and degassed. The temperature was then increased to 300 ^oC under Ar atmosphere followed by natural cooling to 140 ^oC. Once the temperature reduced to 260 ^oC, TOPSe was added followed by the addition of $CdOl_2$ at 140 ^oC to obtain Mn-doped CdSe NCs.

4.3.4. Characterization

The structure of the as-synthesized nanoparticles was determined using x-ray diffraction (XRD) technique and transmission electron microscopy (TEM). TEM images were recorded using Tecnai F30 UHR version electron microscope, using a Field Emission Gun at an accelerating voltage of 300 kV. XRD was recorded on Bruker D8 advance diffractometer using Cu-Kα radiation. To get a high signal-to-noise ratio all patterns were recorded at a slow scan rate. Inductively coupled plasma optical emission spectroscopy (ICP-OES) was performed using PerkinElmer Optima 7000 DV instrument. Samples were prepared by washing the NCs to remove the excess precursors. Washed NCs were then digested in concentrated HNO_3 and diluted with Millipore water.

UV-Visible absorption spectra of various aliquots dissolved in hexane was obtained using Agilent 8453 UV-Visible spectrometer. Steady state PL spectra were collected using the 450 W Xenon lamp as the source on the FLSP920 spectrometer, Edinburgh Instruments while the lifetime and gated PL measurements were carried out using microflash lamp. Typical overall quantum yield of the PL emission at room temperature for all samples was found to be in the range of 30-50% as obtained from the integrating sphere measurements.

Low temperature measurements were performed using the cryostat Optistat DN2, Oxford Instruments. Low temperature measurements were done on thin films which were cooled down to 80K while starting the measurements and the data were recorded at different interval of temperature while increasing the temperature to 300K.

4.4. Results and discussion

Mn-doped ZnSe NCs were synthesized using nucleation doping strategy first devised successfully by Pradhan *et al.*[43] followed by Cd alloying through cation exchange to form Mn-doped $Cd_xZn_{1-x}Se$ NCs. Percentage of incorporated Mn along with Cd and Zn was quantified using ICP-OES and the Mn percentage was found to be ~1%. The value of x in $Cd_xZn_{1-x}Se$ host NCs for different samples is tabulated in Table 4.1. XRD, shown in Figure 4.1, demonstrate the formation of zinc blende structure upon comparing the pattern of Mn-doped $Cd_xZn_{1-x}Se$ NCs with that of bulk ZnSe and CdSe obtained from ICSD database. XRD pattern shows a shift from ZnSe zinc blende to CdSe zinc blende with increase in Cd percentage indicating Cd alloying into Mn-doped ZnSe NCs. Broadening of XRD peaks reveal the formation of small sized NCs which is consistent with TEM images shown in Figure 4.2. From the images it is evident that the NCs are largely spherical in shape and size analysis shows that

the average size of NCs is found to be ~5 nm irrespective of the Cd percentage suggesting that the cation exchange does not affect the size of the NCs.

Table 4.1. *The amount of incorporated Cd (x) in $Cd_xZn_{1-x}Se$ host NCs for different samples obtained from ICP-OES analysis.*

Sample	X value
S1	0.00
S2	0.0001
S3	0.001
S4	0.003
S5	0.004
S6	0.005
S7	0.006
S8	0.02
S9	0.05
S10	0.07
S11	0.15
S12	0.20

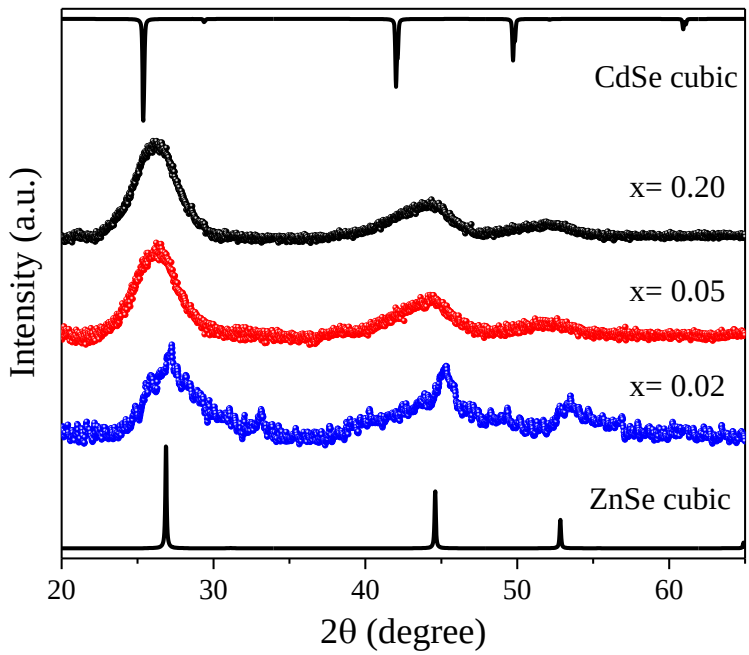

Figure 4.1. *(a) X-ray diffraction pattern of Mn-doped $Cd_xZn_{1-x}Se$ NCs with cadmium content x= 0.02 (blue), x= 0.05 (red) and x= 0.20 (black circles) along with ZnSe and CdSe bulk XRD pattern.*

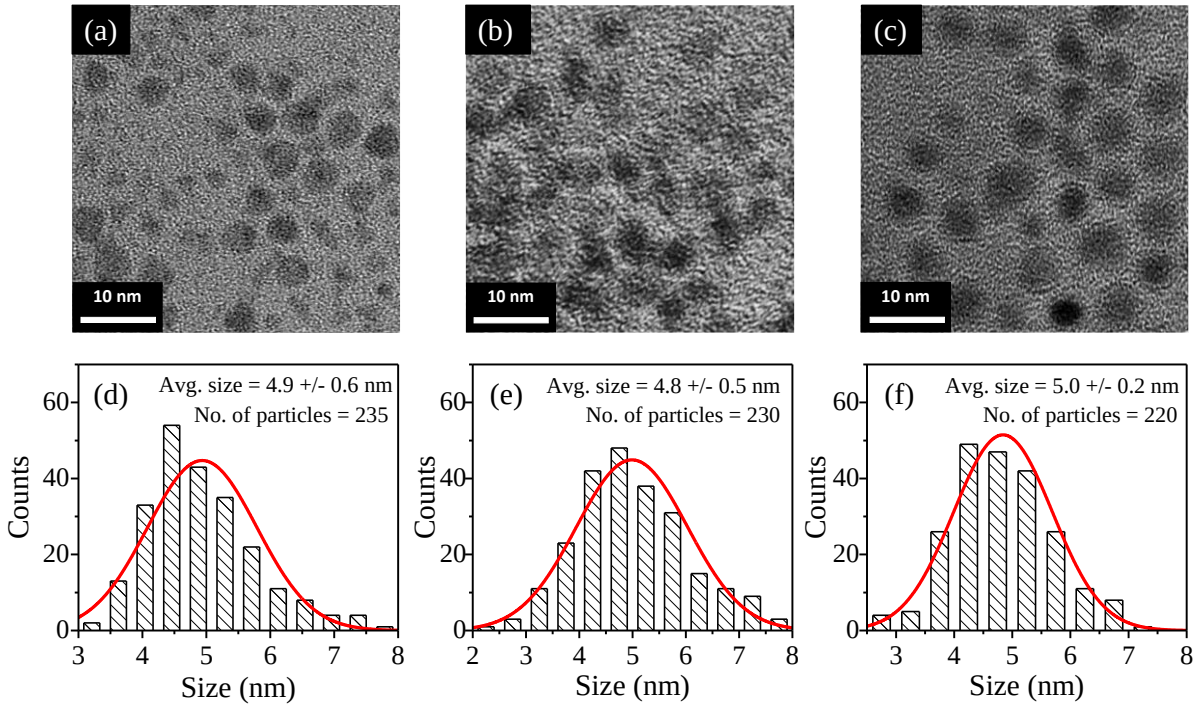

Figure 4.2. *TEM images of Mn-doped $Cd_xZn_{1-x}Se$ nanocrystals containing (a) 0.6% (x=0.006) (b) 2.0% (x=0.02) and (c) 20% (x=0.20) Cd and their corresponding particle size distribution histogram are shown in (d), (e) and (f) respectively.*

These NCs, synthesized by mild cation exchange were characterized spectroscopically using UV-visible and photoluminescence spectroscopy to observe the expression of the Mn emission peak. UV-visible absorption spectra of Mn-doped $Cd_xZn_{1-x}Se$ show a systematic red-shift in 1S absorbance peak with increase in Cd percentage suggesting the decrease in band gap shown in Figure 4.3(a). However, unlike pure Mn-doped ZnSe, with increasing amount of Cd doping, we observe an evolution in the corresponding PL spectra as shown in Figure 4.3(b), where an additional peak along with the characteristic Mn peak starts rising at about 500 nm (~2.50 eV). With the host band gap approaching Mn energy, this peak at 2.50 eV red shifts, becomes more and more dominant while the emission at 2.12 eV is suppressed. These results, at first glance, may be interpreted as the diffusion of Mn out of the sample and the emergence of the band edge emission from undoped NC as mentioned in literature.[1] In fact, many reports[40-41] have observed similar tunable higher energy second peak in addition to the 2.12 eV peak in narrow band gap semiconductors. Due to its tunability, it has been attributed to excitonic emission from undoped fraction of NCs. However, comparison of the energy position from similar composition and size of the undoped NCs shows that the band edge emission is expected at much higher energy as shown in Figure 4.4 as observed in recent literature.[42]

Moreover, the process of Cd exchange is done at 140 °C and Mn^{2+} ions are not expected to diffuse out of the NCs at this temperature. Nevertheless, tunability of this peak, initially arising at 500 nm and eventually being tuned to lower energies with decreasing band gap has not been explained. Further, the decay dynamics, shown in Figure 4.3(c), demonstrate a consistent decrease in the lifetime of the emission at 2.12 eV with increase in Cd concentration, eventually becoming smaller than the instrument response function (IRF). Hence it is necessary to probe the NC systems closely. This decrease in the lifetime could be due to an increase in the contribution from the transient state as shown in Figure 4.5(a) – 4.5(c) with increasing Cd percentage. However, it is important to note the electronic contribution to the Mn d-d transition as well to understand this decreasing lifetime.

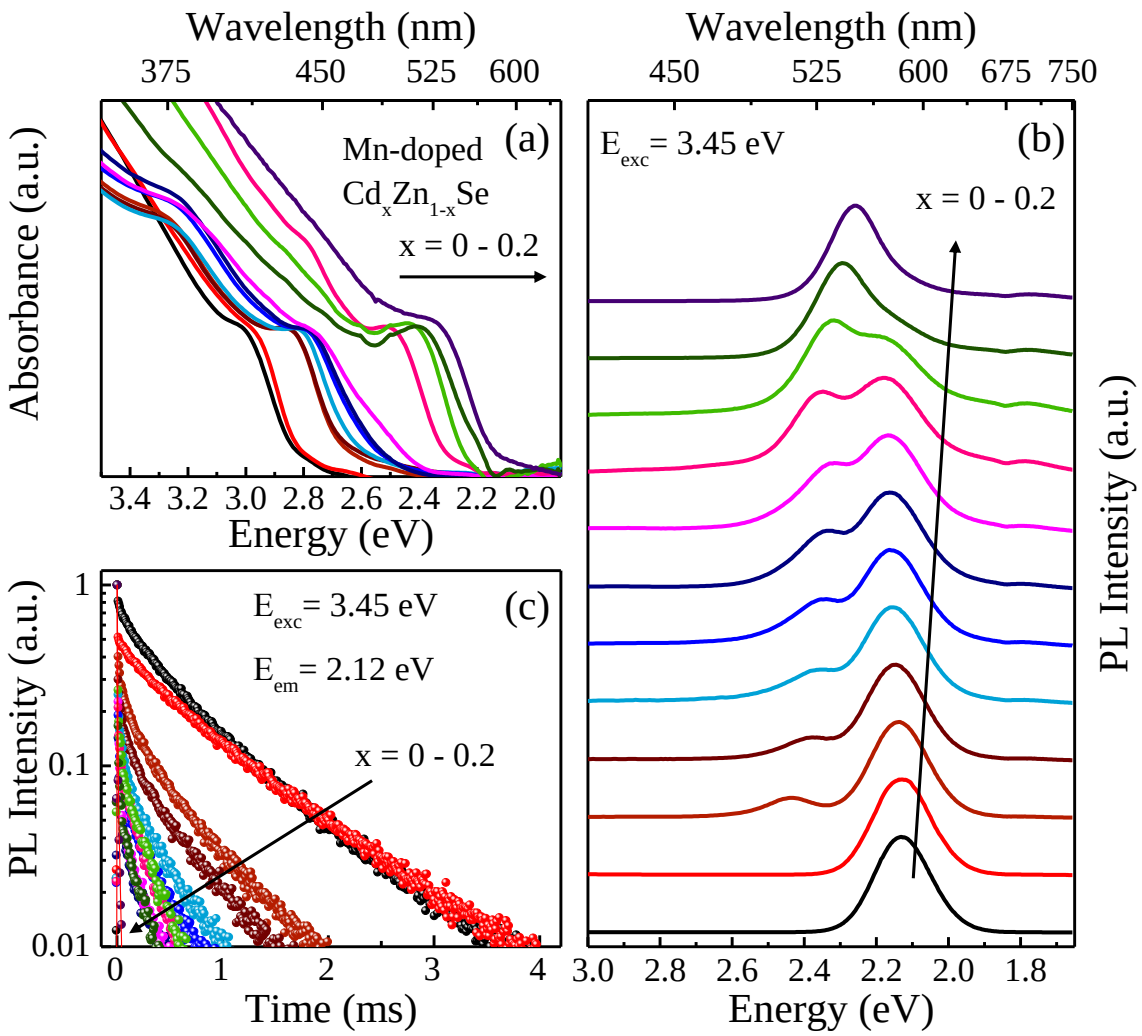

Figure 4.3. *Characterization of Mn-doped NCs (a) Absorption spectra of doped NCs containing different amount of Cd. (b) Evolution of steady state PL spectra and (c) Decay dynamics of 2.12 eV emission with increasing Cd content.*

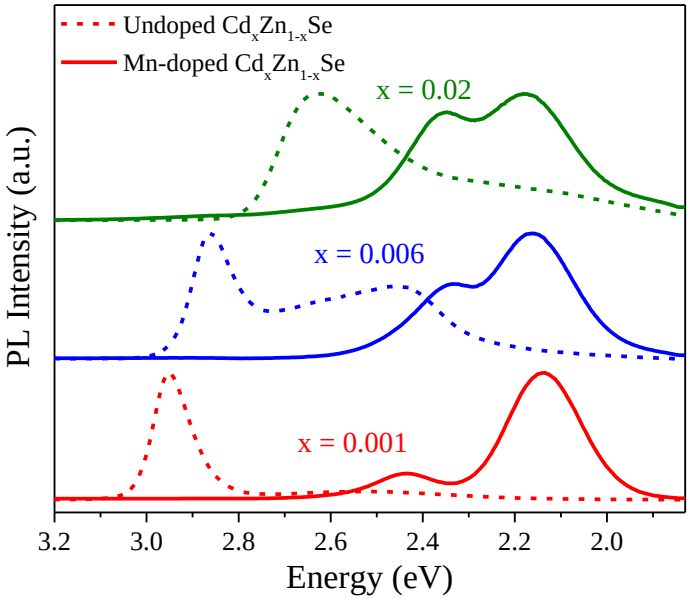

Figure 4.4. *Steady state PL comparison of undoped (dotted lines) and Mn-doped (solid lines) $Cd_xZn_{1-x}Se$ NCs of similar composition.*

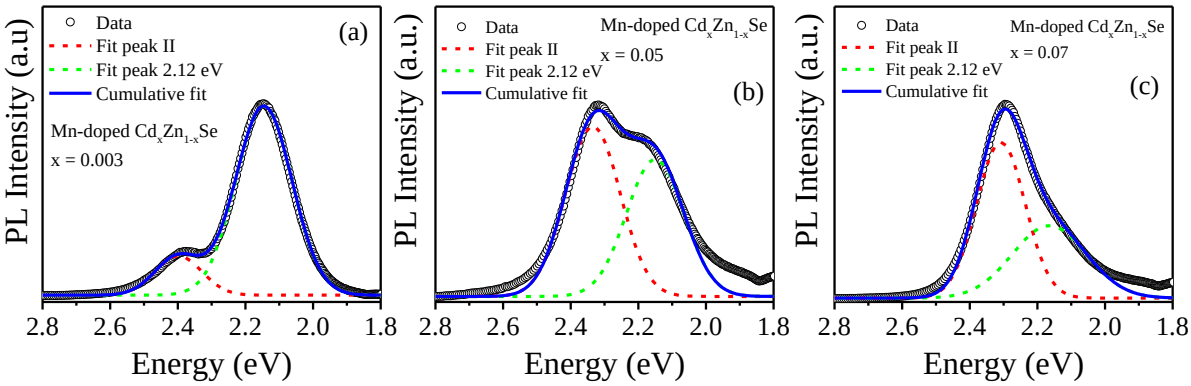

Figure 4.5. *Deconvolution of steady state PL spectra of Mn-doped $Cd_xZn_{1-x}Se$ NCs containing (a) 0.3% (x = 0.003), (b) 5% (x= 0.05), and (c) 7% Cd (x = 0.07).*

To review the nature of the emission peaks better, we take advantage of the large difference in the lifetime of the emission arising from the dopant as well as the recombination from the band edge centers. To locate the origin of the obtained emission at 2.12 eV, we record the emission after 150 μs of excitation, also known as gated PL, thus ignoring all the low lifetime components. The gated PL spectra exhibit the characteristic Mn peak at 2.12 eV irrespective of the band gap of NCs in addition to a small feature at 2.50 eV for lower band gap

materials as shown in Figure 4.6, suggesting the presence of Mn^{2+} ions at the interior of the NCs.

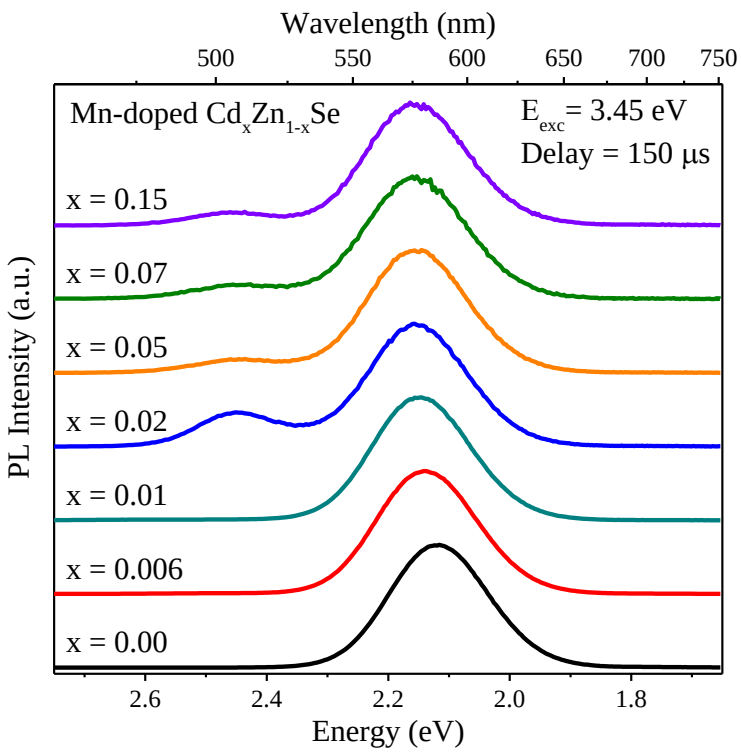

Figure 4.6. *Gated PL of Mn-doped $Cd_xZn_{1-x}Se$ NCs having different Cd content.*

Analysis of temperature-dependent steady state PL spectra, in addition to an increase in the absolute intensity due to reduced lattice vibration with decreasing temperature also gives us an understanding of the thermally allowed transfer and back transfers. We note here that when the energy / charge transfer process occurs from host to the transient species, we refer to it as a 'transfer' while the process of transfer from Mn to the transient species is referred to as 'back-transfer'. Normalized low temperature emission studies are shown in Figure 4.7. From the Figure 4.7(a), it is evident that while the peak at 2.12 eV is dominant for high band gap materials, the low band gap materials with larger Cd percentage is dominated by the presence of a single peak at ~2.25 eV (~550 nm) at room temperature that splits into two peaks as a function of temperature suggests the presence of several thermal energy activated intermediate states in these materials. Although temperature-dependent dual emission in Mn-doped NCs

have been studied earlier,[40-41, 44-46] the origin of the peaks has been wrongly attributed to band edge emission. Excitonic PL peak in undoped NCs of similar composition and band gap arises at much higher energy than the newly evolved low temperature peak suggesting that the latter is indeed not purely an excitonic peak as mentioned in earlier literature.

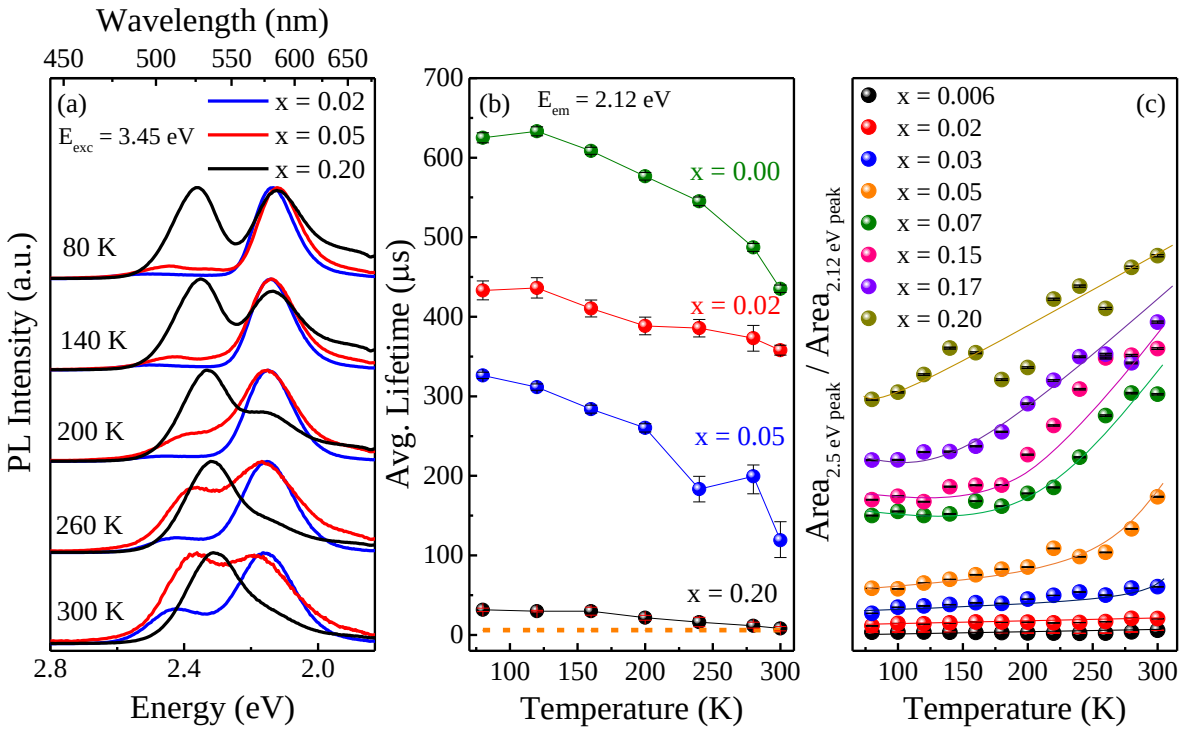

Figure 4.7. *(a) Temperature dependent PL evolution of Mn-doped $Cd_xZn_{1-x}Se$ NCs having wide band gap (blue), intermediate band gap (red) and low band gap (black). (b) Amplitude-weighted average lifetime along with error bar as a function of temperature collected at 2.12 eV for Mn-doped NCs with Cd content 0% (x = 0.00) (green), 2% (x = 0.02) (red), 5% (x = 0.05) (blue), and 20% (x = 0.2) (black). Orange colored dashed line represents the IRF (c) Evolution of relative ratio of area under 2.50 eV peak to 2.12 peak as a function of temperature. The solid lines represent the guide to the eyes. Error limit is found to be smaller than the size of the symbols and is shown in the figure as black bars.*

This peak is quite broad and intense and upon deconvolution as shown in Figure 4.5(a) – 4.5(c), we observe substantial contribution at 2.12 eV. It is known from electronic structure DFT calculation in earlier literature[42] that spin-orbit coupling pulls the conduction band deeper

into the band gap and thus burying the atomic-like Mn states within the conduction band states. Here, Cd incorporation into the host lattice increases the extent of spin-orbit coupling which shows that this single peak arising from a narrow bandgap material, not only has contribution from the atomic-like lines of Mn ions but also from the conduction band of the host. With contributions from two or more factors, one can expect a large competition from the thermal factors as well as back-transfer kinetics (kinetics of charge/energy transfer from Mn to transient state) as a function of temperature that is clearly evident as observed in Figure 4.7(b) and Figure 4.7(c).

Figure 4.7(b) shows the study of lifetime as a function of temperature. This study shows a decrease in amplitude-weighted average lifetime of the 2.12 eV emission with increasing temperature in these materials, calculated following the formula $<\tau> = \frac{\sum_i \alpha_i \tau_i^2}{\sum_i \alpha_i \tau_i}$, where $<\tau>$ is the average lifetime, α = amplitude of lifetime components, τ = lifetime of each component. The decrease in $<\tau>$ is attributed to the increase in thermal energy facilitating the decay process as observed in any typical case in literature, as well as electron exchange from the excitonic excitation to Mn excitation and vice versa mediated by the transient species. The temperature dependence of back transfer process, as quantified by the ratio of the area under the 2.50 eV to the area under 2.12 eV peak, is different for NCs having different band gap as shown in Figure 4.7(c). The solid lines in Figure 4.7(c) represent the guide to the eye, specifically demonstrating a rather flat line up to a particular temperature. From the figure, we observe that for higher band gap materials, the relative intensity ratio of the two peaks is almost constant with temperature. However, in case of lower band gap materials, the intensity ratio increases with increase in temperature. This figure demonstrates a critical temperature, T_c, above which back-transfer of charge/energy from Mn to transient state occurs extensively and this critical temperature T_c increases with increasing band gap and reaches room temperature for materials with band gap of ~2.50 eV (500 nm) or larger.

This suggests that as the band gap decreases, there is an interaction of the host with the forbidden states of Mn mediated by the transient state. As mentioned earlier, although contributions from the transient species lead to a decrease in the lifetime of the Mn emission at 2.12 eV as shown in Figure 4.3(c), it is important to ascertain the contributions due to the increased spin-orbit coupling and hence the nature of Mn emission at 2.12 eV. Increased spin-orbit coupling leads to more allowed transitions and could hence facilitate the electron exchange process. Hence, the decrease in dopant lifetime with more and more Cd incorporation

(Figure 4.3(c)) can also be attributed to this strong spin-orbit coupling making the Mn emission a more allowed transition and hence a lower lifetime. To verify if these changes in Mn emission is independent of host NCs, but only dependent on the band gap of the material, we synthesized different sizes of Mn-doped $Cd_xZn_{1-x}Se$ NCs to have different band gaps with similar percentages of Cd metal and study the evolution of Mn emission.

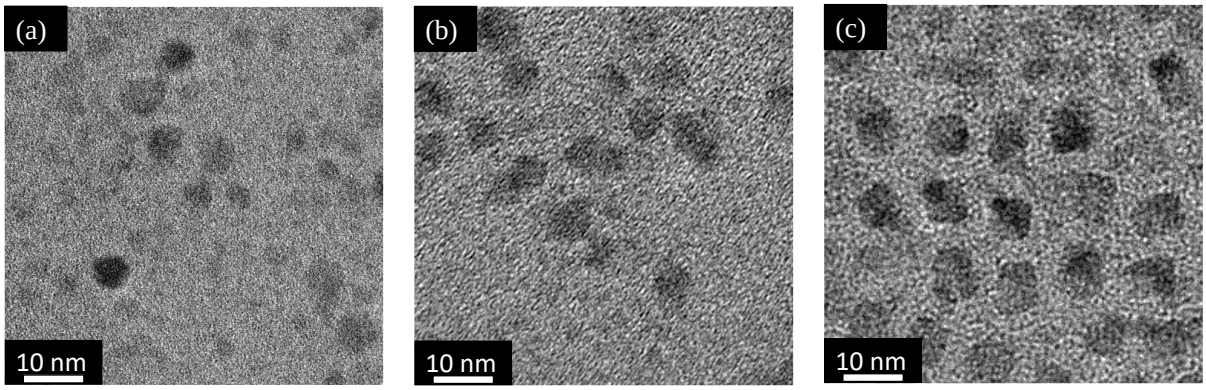

Figure 4.8. *TEM images of (a) small (4.9 +/- 0.4 nm), (b) medium (5.5 +/- 0.6 nm) and (c) big (7.9 +/- 0.3) sized Mn-doped $Cd_xZn_{1-x}Se$ NCs.*

To obtain different sizes, NCs were kept at high temperature to allow the growth. Once a particular size is attained, the synthesis temperature has been reduced and the Cd precursor has been added. The size variation has been confirmed by UV-visible spectra with a red shift in the band gap as well as from TEM. TEM images of NCs of all three sizes are provided in Figure 4.8. Figure 4.9(a) shows the UV-visible absorption and corresponding steady state PL spectra of three different sizes of Mn-doped $Cd_xZn_{1-x}Se$ NCs with about 0.5% Cd (x= 0.005) doping in all the samples. We observe that although the ratio of the PL emission from the transient species to that of Mn emission at 2.12 eV is slightly different, the emission spectra are largely similar, in spite of varying band gaps of the QDs. However, to critically evaluate the role of Cd percentages, we compare materials with similar band gap, but differing Cd percentages as shown in Figure 4.9(b). From the figure it is evident that although the band gap plays an important role in the electron transfer, a fundamentally forbidden transition is better facilitated by a material with higher spin-orbit coupling as shown by an increase in the intensity of higher energy peak (2.50 eV) for higher Cd percentage despite similar band gaps.

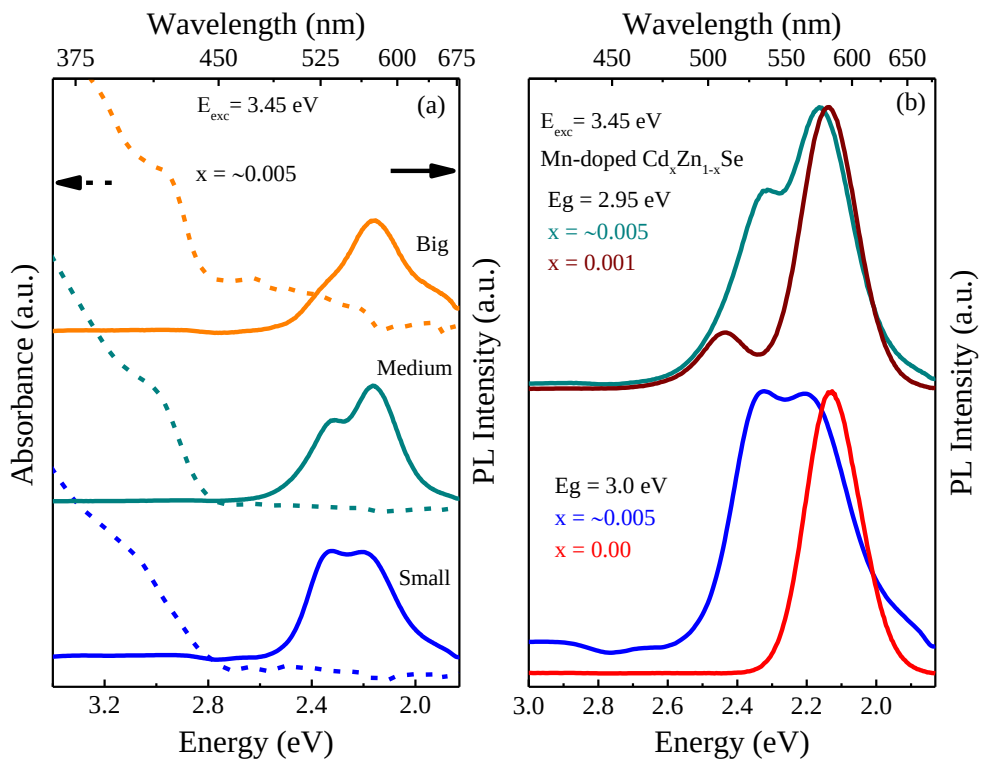

Figure 4.9. *(a) UV-visible (dotted lines) and steady state PL spectra (solid lines) of Mn-doped $Cd_xZn_{1-x}Se$ NCs of different sizes. (b) Comparison of PL spectra having similar band gap but with different Cd percentage.*

The role of spin-orbit coupling can be further strengthened by the study of Mn-doped CdSe, wherein the system is replaced by 100 % Cd. However, Mn-doped CdSe in literature shows no signature of long lifetime and has been considered as a failure to dope Mn^{2+} in CdSe NC host. In this work, we prepared Mn-doped CdSe using the nucleation doping technique to obtain CdSe of various sizes. The steady state and lifetime PL spectroscopy studies of Mn-doped CdSe in comparison to that of Mn-doped ZnSe are shown in Figure 4.10(a) and 4.10(b), respectively.

As expected, we observe a single asymmetric peak with a very short lifetime for Mn-doped CdSe at room temperature. However, based on our earlier results with alloyed samples, we explore the PL steady state spectra and lifetime of each of these samples as a function of temperature. We observe that in the smallest CdSe QDs, with a size of ~3 nm (obtained from TEM images shown in Figure 4.11), we observe surprisingly a dominant signature dopant peak at ~2.12 eV as shown in Figure 4.10(c). The lifetime also increases substantially to the order of few hundred microseconds at lower temperature (shown in Figure 4.10(d)) confirming our

hypothesis that the 100% Cd is indeed further facilitating the electron transfer through spin-orbit coupling.

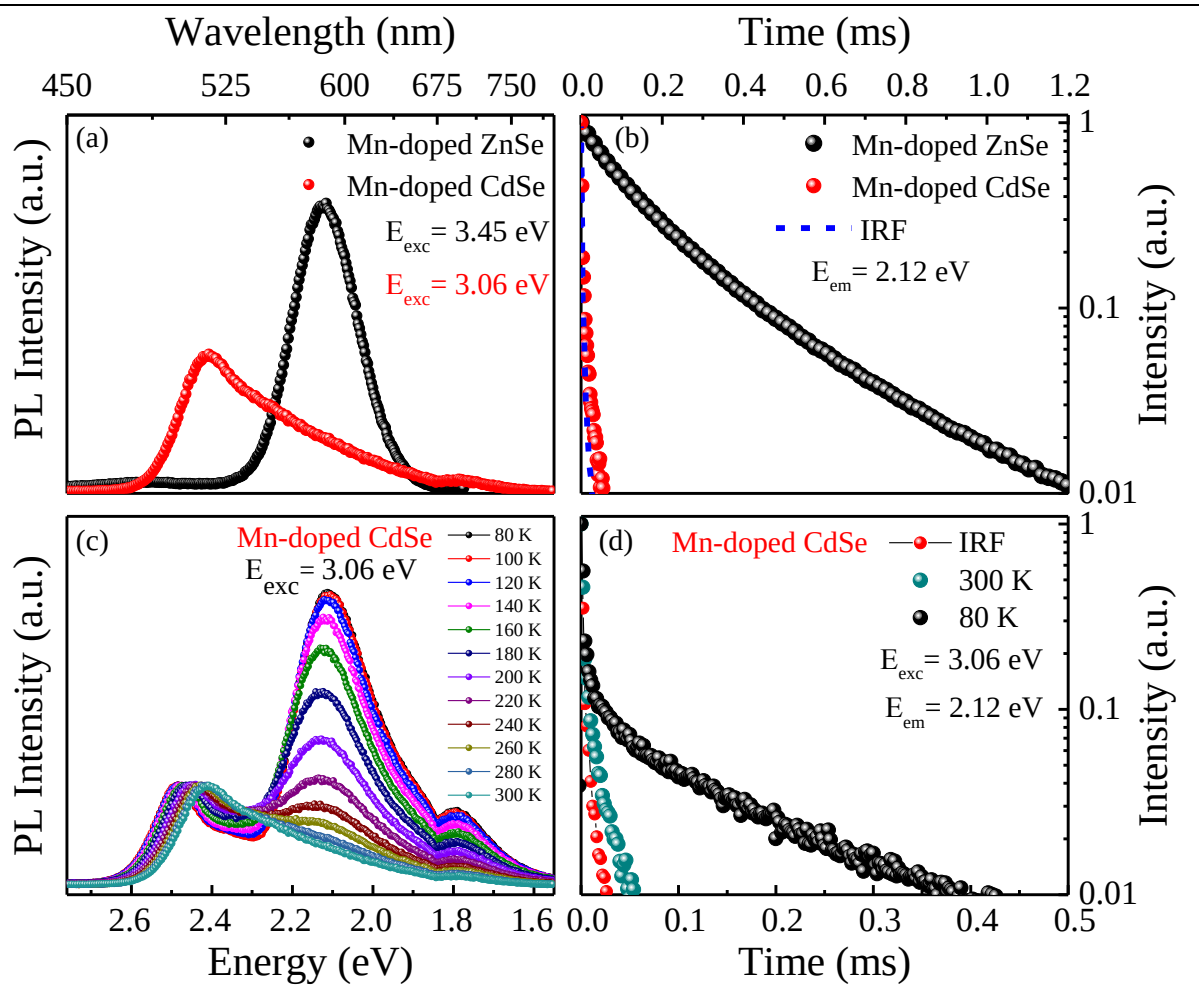

Figure 4.10. *Room temperature (a) steady state and (b) time-resolved PL spectra of Mn-doped ZnSe (black circles) and Mn-doped CdSe NCs (red circles). (c) Temperature map of the PL spectra of Mn-doped CdSe NCs ranging from 80K to 300K. (d) Lifetime at 2.12 eV for Mn-doped CdSe NCs at room temperature (cyan circles) and at 80K (black circles). The data in red circles shows the IRF of lamp.*

Thus, due to facilitated back-transfer at room temperature, one observes a single asymmetric peak that arises from the atomic-like Mn levels interacting strongly with the host leading to a single peak that separates into two peaks at lower temperature when the thermal energy is limited. Thus, it can be concluded that Mn^{2+} is indeed doped and present in the NCs. However, the "signature peak" at 2.12 eV (585 nm) is not the only evidence for a successful

doping of Mn. In fact, this emission could be suppressed at room temperature due to thermal transfer of charge carriers in materials with large spin-orbit coupling.

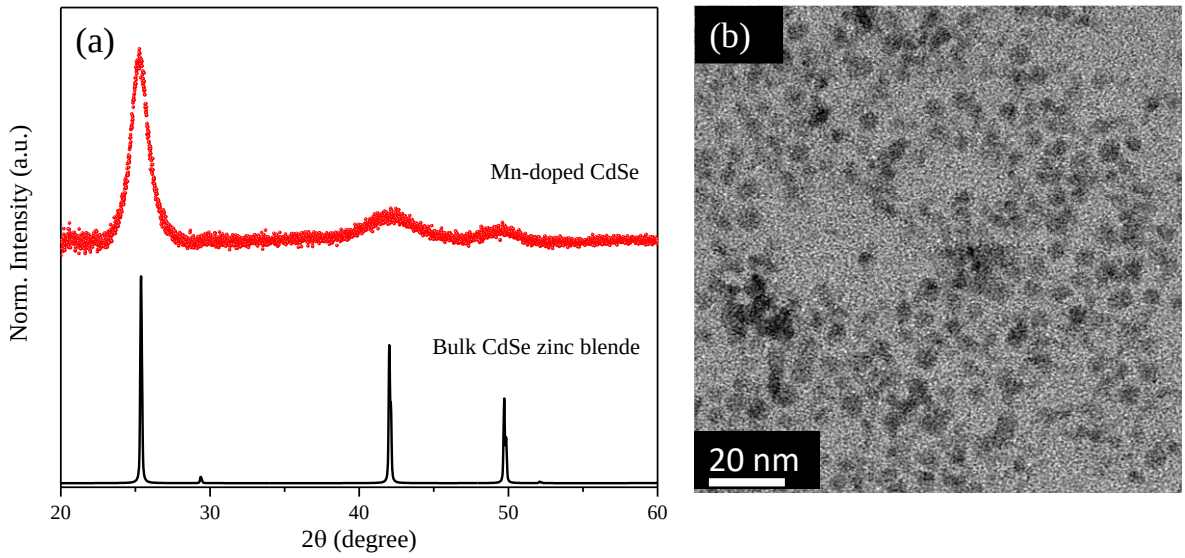

Figure 4.11. *(a) X-ray diffraction pattern of Mn-doped (red) $Cd_xZn_{1-x}Se$ nanocrystals along with bulk cubic zinc blende pattern (b) TEM image show formation of spherical Mn-doped nanocrystals.*

4.5. Conclusion

In conclusion, we have observed that with incorporation of Cd, the band gap comes in the proximity of the atomic-like Mn levels leading to the electron exchange process and hence causing the burial of the "signature" Mn emission peak overshadowed by the emergence of faster decay component. This exchange process is further facilitated by strong spin-orbit coupling and hence becomes more facile for increasing percentage of Cd doping. However, upon lowering the temperature, or by gating the PL spectra to long time scales, it is possible to observe the presence of signature dopant emission peak as well as longer lifetime suggesting that both band gap and composition influence the nature of Mn emission. It is also concluded from these studies that not always yellow-orange emission is observed even though the Mn is doped and present at the interior of the NCs. Our work not only discusses the yellow-orange emission but also studies the nature of the second peak that has so far in literature, due to its tunability, been wrongly attributed to band edge emission. Also, we show for the first time,

the contribution of the host to the transient species in addition to the contribution from the atomic-like lines of Mn ions.

Bibliography

1. Norris, D. J.; Yao, N.; Charnock, F. T.; Kennedy, T. A., High-Quality Manganese-Doped ZnSe Nanocrystals. *Nano Lett.* **2001**, *1*, 3-7.

2. Grandhi, G. K.; Tomar, R.; Viswanatha, R., Study of Surface and Bulk Electronic Structure of II–VI Semiconductor Nanocrystals Using Cu as a Nanosensor. *ACS Nano* **2012**, *6*, 9751-9763.

3. Bhargava, R. N.; Gallagher, D.; Hong, X.; Nurmikko, A., Optical Properties of Manganese-Doped Nanocrystals of ZnS. *Phys. Rev. Lett.* **1994**, *72*, 416-419.

4. Saha, A.; Makkar, M.; Shetty, A.; Gahlot, K.; Pavan, A. R.; Viswanatha, R., Diffusion Doping in Quantum Dots: Bond Strength and Diffusivity. *Nanoscale* **2017**, *9*, 2806-2813.

5. Schwartz, D. A.; Kittilstved, K. R.; Gamelin, D. R., Above-Room-Temperature Ferromagnetic Ni^{2+}-Doped ZnO Thin Films Prepared from Colloidal Diluted Magnetic Semiconductor Quantum Dots. *Appl. Phys. Lett.* **2004**, *85*, 1395-1397.

6. Hanif, K. M.; Meulenberg, R. W.; Strouse, G. F., Magnetic Ordering in Doped $Cd_{1-x}Co_xSe$ Diluted Magnetic Quantum Dots. *J. Am. Chem. Soc.* **2002**, *124*, 11495-11502.

7. Bonanni, A.; Dietl, T., A Story of High-Temperature Ferromagnetism in Semiconductors. *Chem. Soc. Rev.* **2010**, *39*, 528-539.

8. Grandhi, G. K.; Swathi, K.; Narayan, K. S.; Viswanatha, R., Cu Doping in Ligand Free CdS Nanocrystals: Conductivity and Electronic Structure Study. *J. Phys. Chem. Lett.* **2014**, *5*, 2382-2389.

9. Sahu, A.; Kang, M. S.; Kompch, A.; Notthoff, C.; Wills, A. W.; Deng, D.; Winterer, M.; Frisbie, C. D.; Norris, D. J., Electronic Impurity Doping in CdSe Nanocrystals. *Nano Lett.* **2012**, *12*, 2587-2594.

10. Viswanatha, R.; Pietryga, J. M.; Klimov, V. I.; Crooker, S. A., Spin-Polarized Mn^{2+} Emission from Mn-Doped Colloidal Nanocrystals. *Phys. Rev. Lett.* **2011**, *107*, 067402.

11. Fuhr, A.; Yun, H. J.; Crooker, S. A.; Klimov, V. I., Spectroscopic and Magneto-Optical Signatures of Cu^{1+} and Cu^{2+} Defects in Copper Indium Sulfide Quantum Dots. *ACS Nano* **2020**, *14*, 2212-2223.

12. Fainblat, R.; Muckel, F.; Barrows, C. J.; Vlaskin, V. A.; Gamelin, D. R.; Bacher, G., Valence-Band Mixing Effects in the Upper-Excited-State Magneto-Optical Responses of Colloidal Mn^{2+}-Doped CdSe Quantum Dots. *ACS Nano* **2014**, *8*, 12669-12675.

13. Zhang, W.; Li, Y.; Zhang, H.; Zhou, X.; Zhong, X., Facile Synthesis of Highly Luminescent Mn-Doped ZnS Nanocrystals. *Inorg. Chem.* **2011**, *50*, 10432-10438.

14. Zeng, R.; Rutherford, M.; Xie, R.; Zou, B.; Peng, X., Synthesis of Highly Emissive Mn-Doped ZnSe Nanocrystals without Pyrophoric Reagents. *Chem. Mater.* **2010**, *22*, 2107-2113.

15. Pradhan, N.; Peng, X., Efficient and Color-Tunable Mn-Doped ZnSe Nanocrystal Emitters: Control of Optical Performance Via Greener Synthetic Chemistry. *J. Am. Chem. Soc.* **2007**, *129*, 3339-3347.

16. Yang, Y.; Chen, O.; Angerhofer, A.; Cao, Y. C., Radial-Position-Controlled Doping in CdS/ZnS Core/Shell Nanocrystals. *J. Am. Chem. Soc.* **2006**, *128*, 12428-12429.

17. Behboudnia, M.; Sen, P., Systematics in the Nanoparticle Band Gap of ZnS and $Zn_{1-x}M_xS$ (M= Mn, Fe, Ni) for Various Dopant Concentrations. *Phys. Rev. B* **2001**, *63*, 035316.

18. Ithurria, S.; Guyot-Sionnest, P.; Mahler, B.; Dubertret, B., Mn^{2+} as a Radial Pressure Gauge in Colloidal Core/Shell Nanocrystals. *Phys. Rev. Lett.* **2007**, *99*, 265501.

19. Nag, A.; Cherian, R.; Mahadevan, P.; Gopal, A. V.; Hazarika, A.; Mohan, A.; Vengurlekar, A. S.; Sarma, D. D., Size-Dependent Tuning of Mn^{2+} d Emission in Mn^{2+}-Doped CdS Nanocrystals: Bulk Vs Surface. *J. Phys. Chem. C* **2010**, *114*, 18323-18329.

20. Bol, A. A.; Meijerink, A., Long-Lived Mn^{2+} Emission in Nanocrystalline ZnS: Mn^{2+}. *Phys. Rev. B* **1998**, *58*, R15997.

21. Bacher, G.; Schneider, L.; Beaulac, R.; Archer, P. I.; Gamelin, D. R., Magnetic Polaron Formation Dynamics in Mn^{2+}-Doped Colloidal Nanocrystals up to Room Temperature. *J. Korean Phys. Soc.* **2011**, *58*, 1261-1266.

22. Beaulac, R.; Schneider, L.; Archer, P. I.; Bacher, G.; Gamelin, D. R., Light-Induced Spontaneous Magnetization in Doped Colloidal Quantum Dots. *Science* **2009**, *325*, 973-976.

23. Rice, W. D.; Liu, W.; Pinchetti, V.; Yakovlev, D. R.; Klimov, V. I.; Crooker, S. A., Direct Measurements of Magnetic Polarons in $Cd_{1-X}Mn_xSe$ Nanocrystals from Resonant Photoluminescence. *Nano Lett.* **2017**, *17*, 3068-3075.

24. Chen, H. Y.; Chen, T. Y.; Son, D. H., Measurement of Energy Transfer Time in Colloidal Mn-Doped Semiconductor Nanocrystals. *J. Phys. Chem. C* **2010**, *114*, 4418-4423.

25. Debnath, T.; Ghosh, H. N., Recent Progress of Electron Storage Mn Center in Doped Nanocrystals. *J. Phys. Chem. C* **2019**, *123*, 10703-10719.

26. Maiti, S.; Chen, H. Y.; Park, Y.; Son, D. H., Evidence for the Ligand-Assisted Energy Transfer from Trapped Exciton to Dopant in Mn-Doped CdS/ZnS Semiconductor Nanocrystals. *J. Phys. Chem. C* **2014**, *118*, 18226-18232.

27. Bindra, J. K.; Singh, K.; Van Tol, J.; Dalal, N. S.; Strouse, G. F., Spin Dynamics in Mn: ZnSe Quantum Dots: A Pulsed High-Frequency Epr Study. *J. Phys. Chem. C* **2020**, *124*, 19348-19354.

28. Yost, A. J.; Ekanayaka, T. K.; Gurung, G.; Rimal, G.; Horoz, S.; Tang, J.; Paudel, T.; Chien, T., Influence of the Cation on the Surface Electronic Band Structure and Magnetic Properties of Mn: ZnS and Mn: CdS Quantum Dot Thin Films. *J. Phys. Chem. C* **2019**, *123*, 24890-24898.

29. Pradhan, N.; Sarma, D. D., Advances in Light-Emitting Doped Semiconductor Nanocrystals. *J. Phys. Chem. Lett.* **2011**, *2*, 2818-2826.

30. Levy, L.; Ingert, D.; Feltin, N.; Pileni, M. P., Effect of Aging on Luminescence from Isolated Mn^{2+} Confined in $Cd_{0.95}Mn_{0.05}S$ Clusters. *Adv. Mater.* **1998**, *10*, 53-57.

31. Zu, L.; Norris, D. J.; Kennedy, T. A.; Erwin, S. C.; Efros, A. L., Impact of Ripening on Manganese-Doped ZnSe Nanocrystals. *Nano Lett.* **2006**, *6*, 334-340.

32. Karan, N. S.; Sarma, D. D.; Kadam, R. M.; Pradhan, N., Doping Transition Metal (Mn or Cu) Ions in Semiconductor Nanocrystals. *J. Phys. Chem. Lett.* **2010**, *1*, 2863-2866.

33. Hazarika, A.; Pandey, A.; Sarma, D. D., Rainbow Emission from an Atomic Transition in Doped Quantum Dots. *J. Phys. Chem. Lett.* **2014**, *5*, 2208-2213.

34. Hazarika, A.; Layek, A.; De, S.; Nag, A.; Debnath, S.; Mahadevan, P.; Chowdhury, A.; Sarma, D. D., Ultranarrow and Widely Tunable Mn^{2+}-Induced Photoluminescence from Single Mn-Doped Nanocrystals of ZnS-CdS Alloys. *Phys. Rev. Lett.* **2013**, *110*, 267401.

35. Viswanatha, R.; Sapra, S.; Sen Gupta, S.; Satpati, B.; Satyam, P. V.; Dev, B. N.; Sarma, D. D., Synthesis and Characterization of Mn-Doped ZnO Nanocrystals. *J. Phys. Chem. B* **2004**, *108*, 6303-6310.

36. Mikulec, F. V.; Kuno, M.; Bennati, M.; Hall, D. A.; Griffin, R. G.; Bawendi, M. G., Organometallic Synthesis and Spectroscopic Characterization of Manganese-Doped CdSe Nanocrystals. *J. Am. Chem. Soc.* **2000**, *122*, 2532-2540.

37. Erwin, S. C.; Zu, L.; Haftel, M. I.; Efros, A. L.; Kennedy, T. A.; Norris, D. J., Doping Semiconductor Nanocrystals. *Nature* **2005**, *436*, 91-94.

38. Norris, D. J.; Efros, A. L.; Erwin, S. C., Doped Nanocrystals. *Science* **2008**, *319*, 1776-1779.

39. Wang, Y. S.; Thomas, P. J.; O'Brien, P., Optical Properties of Zno Nanocrystals Doped with Cd, Mg, Mn, and Fe Ions. *J. Phys. Chem. B* **2006**, *110*, 21412-21415.

40. Vlaskin, V. A.; Janssen, N.; van Rijssel, J.; Beaulac, R.; Gamelin, D. R., Tunable Dual Emission in Doped Semiconductor Nanocrystals. *Nano Lett.* **2010**, *10*, 3670-3674.

41. McLaurin, E. J.; Vlaskin, V. A.; Gamelin, D. R., Water-Soluble Dual-Emitting Nanocrystals for Ratiometric Optical Thermometry. *J. Am. Chem. Soc.* **2011**, *133*, 14978-14980.

42. Gahlot, K.; KR, P.; Camellini, A.; Sirigu, G.; Cerullo, G.; Zavelani-Rossi, M.; Singh, A.; Waghmare, U. V.; Viswanatha, R., Transient Species Mediating Energy Transfer to Spin-Forbidden Mn d States in II–VI Semiconductor Quantum Dots. *ACS Energy Lett.* **2019**, *4*, 729-735.

43. Pradhan, N.; Goorskey, D.; Thessing, J.; Peng, X., An Alternative of CdSe Nanocrystal Emitters: Pure and Tunable Impurity Emissions in ZnSe Nanocrystals. *J. Am. Chem. Soc.* **2005**, *127*, 17586-17587.

44. Leinen, D., Excitonic Energy Transfer to the 3d Electrons of Mn^{2+} in $Cd_{1-X}Mn_xTe$. *Phys. Rev. B* **1997**, *55*, 6975-6980.

45. Beaulac, R.; Archer, P. I.; van Rijssel, J.; Meijerink, A.; Gamelin, D. R., Exciton Storage by Mn^{2+} in Colloidal Mn^{2+}-Doped CdSe Quantum Dots. *Nano Lett.* **2008**, *8*, 2949-2953.

46. McLaurin, E. J.; Bradshaw, L. R.; Gamelin, D. R., Dual-Emitting Nanoscale Temperature Sensors. *Chem. Mater.* **2013**, *25*, 1283-1292.

Chapter 4

Part B

Study of the Origin of Tunable Higher Energy Emission in Mn-Doped II-VI Semiconductor Quantum Dots

4.6. Introduction

In the previous part of the chapter, we discussed the nature of Mn-related emission as a function of the host bandgap as well as the host composition, especially, the spin-orbit coupling caused by the variation in composition. We observed that the introduction of Cd into the ZnSe QDs reduces the host bandgap, and the excitonic levels come in the proximity of Mn energy states. An evolution in the PL spectra was also observed, where an additional peak along with the characteristic Mn peak starts rising at about 500 nm (~2.50 eV). With the host band gap approaching Mn energy, this peak at 2.50 eV red shifts, and becomes more dominant while the emission at 2.12 eV is suppressed and due to the tunable nature of the higher energy peak it has been attributed to excitonic emission from undoped fraction of NCs in earlier literature.[1-2] While the excitonic emission at much higher energy arising from undoped QDs of similar composition ruled out the possibility of the higher energy peak being excitonic PL in doped QDs, we gave a plausible explanation of the same. The close proximity of the excitonic and Mn energy levels facilitates the back transfer of charge/energy from Mn excited states to the transient states which is further fuelled by strong spin-orbit coupling introduced by heavy atom Cd leading to the evolution of tunable higher energy peak. However, this explanation is largely based on the circumstantial evidences obtained from DFT study, performed on similar system in earlier literature[3] and the optical studies done in the work discussed in the previous part of the chapter. To gain more insight into the origin of the higher energy peak, we employed single-particle fluorescence spectroscopy where PL properties of individual NCs were studied in order to declutter the data obtained from ensemble averaging.

It is largely accepted in the literature that Mn doping in wide bandgap materials is characterized by a broad invariant peak at ~2.15 eV inspite of its atomic-like origin.[4-9] In contrast, a different observation was made in one of the reports,[10] where Mn-doped ZnS-CdS alloy NCs were subjected to single-particle fluorescence study and the emission from individual NCs showed the tunability varying over a wide range with substantially lower emission width as compared to the ensemble PL. However, this result has never been reproduced in other Mn-doped semiconductor QDs and hence, the universality of the same has not been established. Here, in this work, we intend to study an independent Mn-doped NC system in single-particle level to study the spectral resolution of Mn emission. We have taken the same host Mn-doped $Cd_xZn_{1-x}Se$, synthesized by alloying Cd in Mn-doped ZnSe through cation exchange as discussed in the earlier part of the chapter. We observe that the spectra obtained from Mn-doped single NCs consist of two peaks confirming that the higher energy

PL peak observed in doped system is not from the undoped fraction of the NCs. Also, the spectra obtained from single NCs are much narrower in width as compared to ensemble PL spectra similar to earlier literature.

4.7. Experimental methods

Mn-doped $Cd_xZn_{1-x}Se$ QDs were synthesized following the similar method described in chapter 4, part A.[11] The NCs were then characterized optically using UV-visible and PL spectroscopy. UV-Visible absorption spectra of various aliquots dissolved in hexane was obtained using Agilent 8453 UV-Visible spectrometer. Steady state PL spectra were collected using the 450 W Xenon lamp as the source on the FLSP920 spectrometer, Edinburgh Instruments while the lifetime and gated PL measurements were carried out using microflash lamp.

4.7.1. Single-particle fluorescence spectroscopy

Spatially resolved single-particle PL imaging and spectroscopic data were collected using our home build wide-field epifluorescence microscopic setup, further details can be found elsewhere.[12] In brief, the optimized concentration of NCs in toluene was spin-casted on a freshly cleaned glass coverslip and excited using a 405 nm laser (LaserGlow, LRD-0405PFR) via an oil immersive objective lens (Nikon TIRF 1.49NA 60X oil). The emission from samples was collected using the same objective lens, passed through appropriate dichroic and band-pass filters, and imaged using an sCMOS camera (Hamamatsu Orca flash4 V3). For single-particle PL spectroscopy, the emitted light was passed through a slit and a transmission grating (70 g/mm) in the emission path before the sCMOS detector, which allowed us to obtain spectrally resolve single-particle spectra.

4.8. Results and discussion

The NCs, synthesized by mild cation exchange were characterized spectroscopically using UV-visible and photoluminescence spectroscopy to observe the expression of the Mn emission peak. We doped Cd into Mn-doped ZnSe in such a way that both Mn emission peak and the higher energy emission peak have substantial intensity and also the host bandgap is lower than our excitation energy source. Percentage of incorporated Mn and Cd were found to be ~1% and 5%, respectively from inductively coupled plasma-optical emission spectroscopy (ICP-OES) measurement.

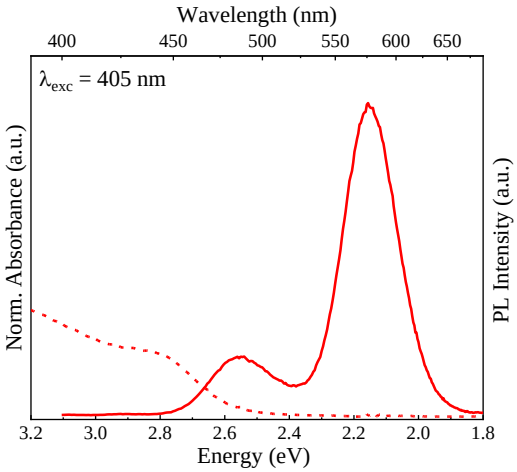

Figure 4.12. *UV-vis absorption (dashed line) and steady state PL (solid line) spectra of ensemble Mn-doped* $Cd_xZn_{1-x}Se$ *NCs.*

UV-visible spectra of the QDs show absorption onset at its bandgap energy ~2.8 eV as shown in Figure 4.12. The steady-state PL measurements show a two peak structure where a higher energy peak at ~2.5 eV along with characteristic yellow-orange Mn emission at 2.15 eV as is observed in the earlier work.

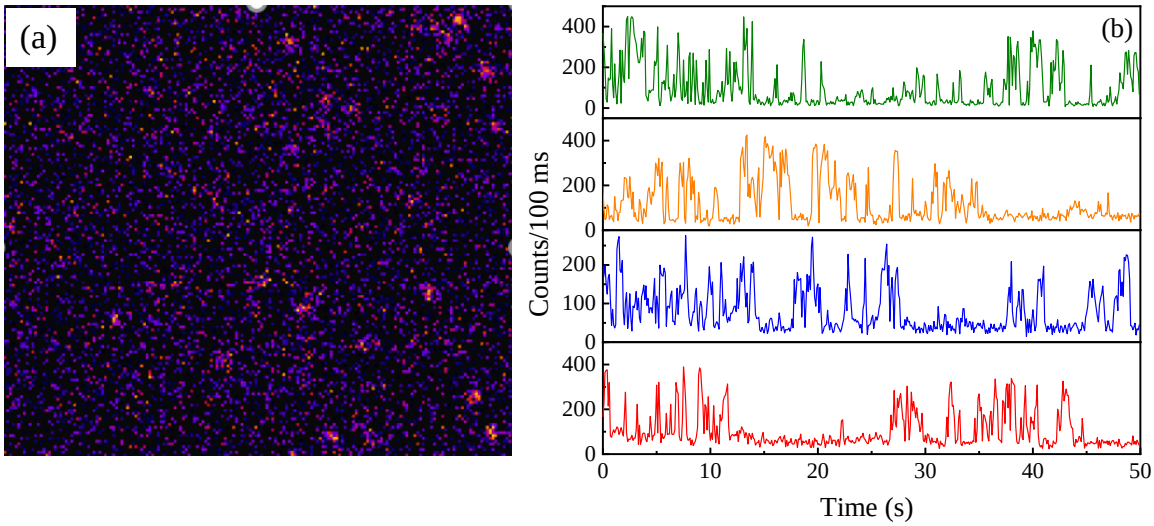

Figure 4.13. (a) *Representative fluorescence lifetime images with false colour representation show single nanoparticle distribution. (b) blinking dynamics of a single-particles show continuous 'ON' and 'OFF' sequence in their intensity.*

In this context, we note that a typical ensemble PL spectrum with multiple peaks could be a consequence of averaged spectra obtained from individual fluorophores. Thus, study of individual NCs would nullify the problem, especially when we intend to find the origin of any emission peak appeared in ensemble PL spectra. To explore the emission nature of NCs in single-particle regime, we diluted the NCs and recorded the fluorescence lifetime images (FLIM) using a fluorescence microscope shown in Figure 4.13(a) where diffraction limited NCs were spotted. To identify the NCs to be single NCs, we studied the blinking, a behaviour essentially shown by the single NC,[13] wherein PL intensity fluctuates from bright '*on*' state and dark '*off*' state under continuous excitation, for all particles under study. Though blinking implies serious restrictions on a wide range of applications of semiconductor NCs,[14-15] it is a very useful technique to distinguish between single-particles and clusters of particles. The intermittency in the PL intensity of the NC is due to the illumination-induced charging (on → off) followed by neutralization (off → on) of the NC.[16] In the case of any finite ensemble, PL blinking will be smoothed out and hence undetectable but can be observed in the case of a single NC.[17] Blinking traces for a few representative particles are shown in Figure 4.13(b) which reveals a clear PL intermittency between '*on*' and '*off*' states suggesting that the particles under study are indeed single particles.

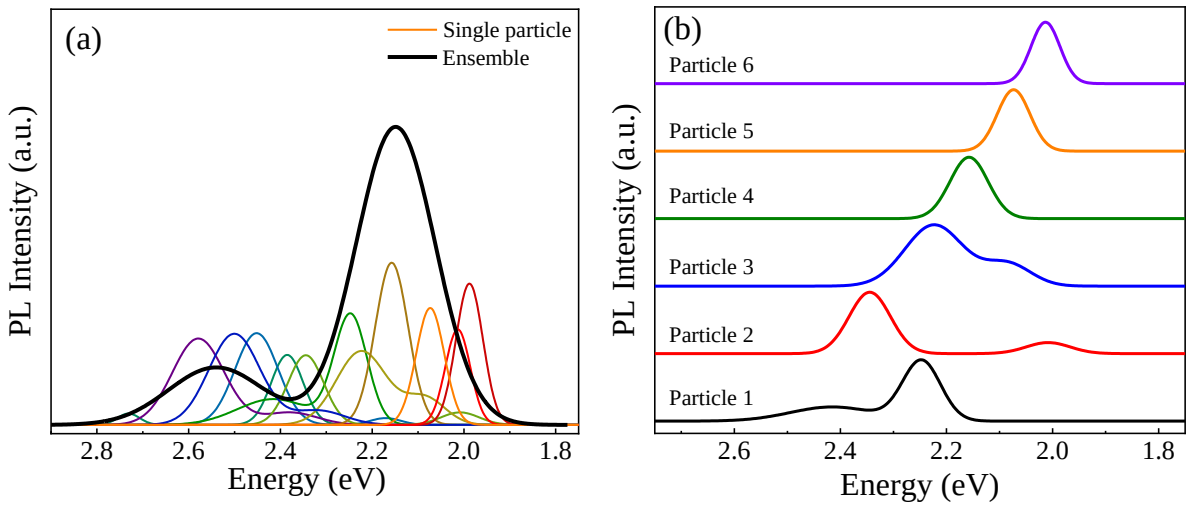

Figure 4.14. *(a) Comparison of steady state PL spectra of single NCs with that of the ensemble (b) Few representative single particle spectra showing both dual emission and single emission nature.*

The steady state PL spectra were then measured using a spectrograph instrument attached to the microscope. Figure 4.14(a) shows the comparison of steady state PL spectra of a number of single particles with that of the ensemble. From the figure, it is evident that the steady state PL spectra from single particles cover the entire band width of the emission obtained from ensemble measurement ranging from green to red. It is very important to note here that, almost 50% of the single particles exhibit dual emission nature while the other 50% show only Mn emission as shown in Figure 4.14(b), suggesting a statistical probability of charge carrier recombination through two competing pathways, either through $^4T_1 \rightarrow {}^6A_1$ energy levels of Mn^{2+} or the transient states created by the contribution from both excitonic and dopant states or through both. The relative intensity of the two peaks decides the probability of the transitions. Importantly, the higher energy emission peak is arising from a single NC along with the characteristic Mn emission peak confirms that the same is not from the undoped fraction of the NCs, rather due to the efficient back transfer of charge/energy from Mn excited states to the transient state corroborating our previous claim.

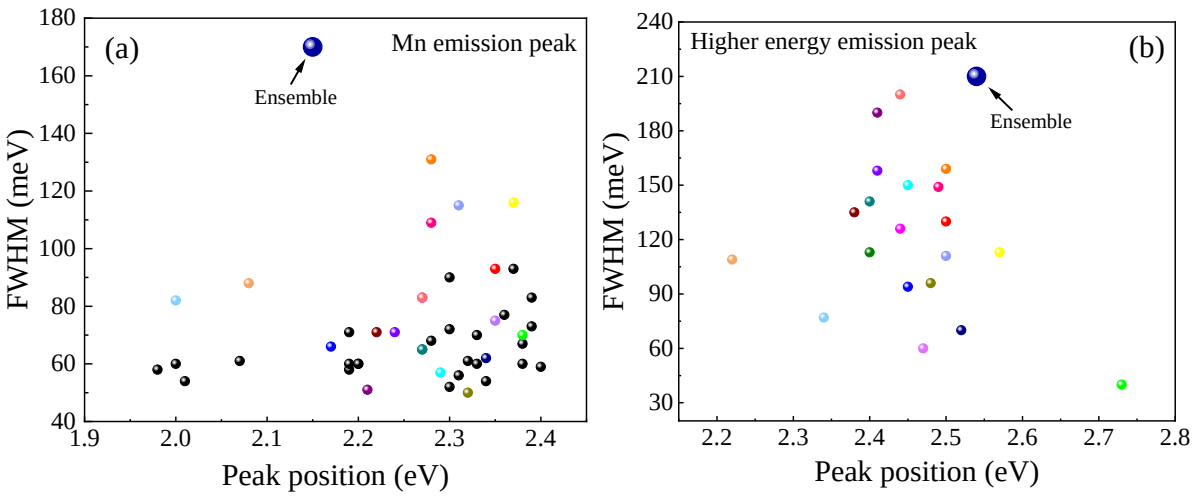

Figure 4.15. *Spectral width (FWHM) of (a) Mn-related emission and (b) higher energy emission feature arising from ensemble (big blue dot) as well as individual NC (small dots). Note that, the black dots represent the particles having only Mn-related emission and the colored dots are particles having dual emission nature.*

The spectral width of Mn emission from individual NCs are strikingly different from the one obtained from the ensemble measurement. It is evident from the Figure 4.14(a) that the

spectral widths in single-particle PL are significantly narrower as compared to that of the ensemble-averaged PL. We analyzed and compared the emission spectral features of each single NC as well as the ensemble by calculating the full width half maxima (FWHM) and plotted against the peak position as shown in figure 4.15(a) and (b). In case of Mn emission, while the spectral widths of individual NCs are distributed between 50 meV to 130 meV, the FWHM of ensemble PL is 170 meV. Similar observation is made in case of higher energy peak as well. This study suggests that the overlap of multiple PL contributions with different emission energies obtained from individual NCs is the reason for the large experimental width obtained in ensemble measurement, an observation very similar to earlier report.[10]

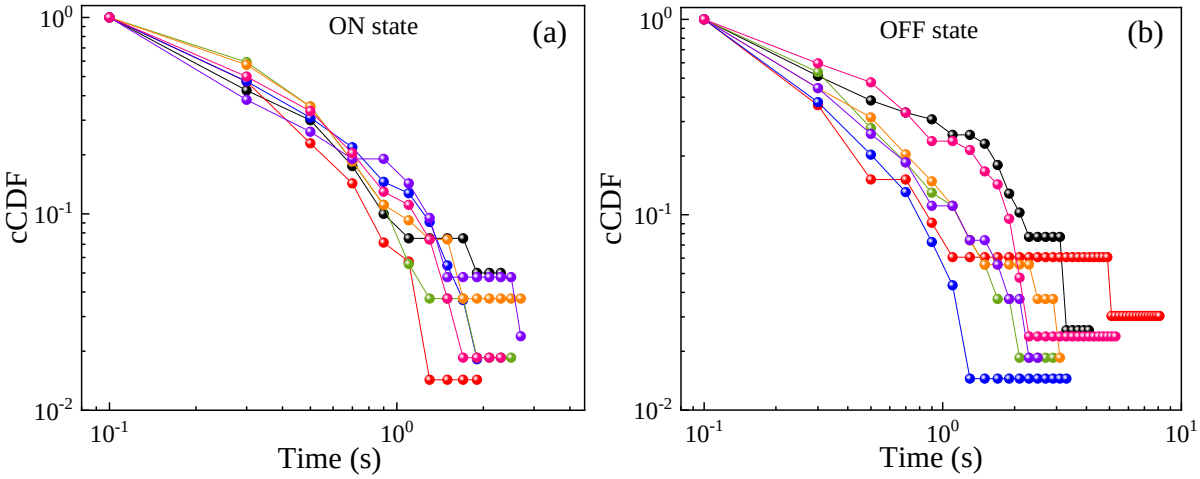

Figure 4.16. *Logarithmic plots of (a) 'ON' and (b) 'OFF' complementary distribution functions (cCDF) of Mn emission traces in individual nanocrystals.*

Since the transitions occur through two competitive channels as observed from the single-particle PL spectra, it very important to understand the probability of recombination in individual nanocrystals. Contextually, PL blinking is an outcome of charging (carrier trapping) and neutralization (recombination) of nanocrystals. Thus, we analyzed the photoluminescence intermittency of the '*on*' (all events above the mean background intensity) and '*off*' events for a set of individual NCs. We calculated the cumulative distribution function (CDF)[18] for each data set to compare the distributions without assuming a parametric form for the underlying probability distribution functions. The conversion of probability distribution functions to CDFs is described elsewhere.[19] Briefly, the time durations of '*on*' and '*off*' events were calculated

followed by the calculation of CDF using the formula, $CDF(t) = \frac{1}{N}\sum_i t_i$, where N is the total number of on/off events, t_i is the event duration. We plotted the logarithmic complementary CDF (cCDF), defined by cCDF(t) = 1- CDF(t), as a function of time for '*on*' and '*off*' duration of a set of individual NCs in Figure 4.16(a) and (b), respectively. From the figure 4.16(a), it is evident that, cCDF of the '*on*' cCDF of all the single NCs under scrutiny are nearly identical. In contrast, the '*off*' cCDF show a significant variation from particle to particle as shown in Figure 4.16(b). Even though the transitions involve different pathways as well as different energies in single NCs, the nearly identical '*on*' states in all cases imply that the recombination processes are independent of any external factors associated with the semiconductor NCs like surface states etc. On the other hand, 'off' states are observed due to the capturing of charge carriers by the trap states. Since it is very difficult to have control over the trap states, the nature of the trap states is non-uniform across the nanocrystals which results in a significant variation in the '*off*' state distribution.

4.9. Conclusion

Thus, in conclusion, after identification of single NCs and a thorough analysis of the spectral behaviour, blinking dynamics, statistical distribution, we confirm that the higher energy emission feature does not originate from undoped fraction of the NCs, but rather due to a back transfer of charge/energy from Mn excited state to a transient state in doped NC itself. In addition, we observed a spectral resolution in case of both the emission features observed in Mn-doped $Cd_xZn_{1-x}Se$ alloy NCs where the individual NCs show a much narrower spectral width as compared to the ensemble-averaged one. The blinking analysis suggests that even though the transitions involve different pathways and energies, the probability of radiative recombination is unaltered across the NCs. The nonuniformity in the surface nature results in a different surface trapping probability in individual NCs.

Bibliography

1. Vlaskin, V. A.; Janssen, N.; van Rijssel, J.; Beaulac, R.; Gamelin, D. R., Tunable Dual Emission in Doped Semiconductor Nanocrystals. *Nano Lett.* **2010**, *10*, 3670-3674.

2. McLaurin, E. J.; Vlaskin, V. A.; Gamelin, D. R., Water-Soluble Dual-Emitting Nanocrystals for Ratiometric Optical Thermometry. *J. Am. Chem. Soc.* **2011**, *133*, 14978-14980.

3. Gahlot, K.; KR, P.; Camellini, A.; Sirigu, G.; Cerullo, G.; Zavelani-Rossi, M.; Singh, A.; Waghmare, U. V.; Viswanatha, R., Transient Species Mediating Energy Transfer to Spin-Forbidden Mn d States in II–VI Semiconductor Quantum Dots. *ACS Energy Lett.* **2019**, *4*, 729-735.

4. Behboudnia, M.; Sen, P., Systematics in the Nanoparticle Band Gap of Zns and $Zn_{1-x}M_xS$ (M= Mn, Fe, Ni) for Various Dopant Concentrations. *Phys. Rev. B* **2001**, *63*, 035316.

5. Yang, Y.; Chen, O.; Angerhofer, A.; Cao, Y. C., Radial-Position-Controlled Doping in CdS/ZnS Core/Shell Nanocrystals. *J. Am. Chem. Soc.* **2006**, *128*, 12428-12429.

6. Nag, A.; Cherian, R.; Mahadevan, P.; Gopal, A. V.; Hazarika, A.; Mohan, A.; Vengurlekar, A. S.; Sarma, D. D., Size-Dependent Tuning of Mn^{2+} d Emission in Mn^{2+}-Doped CdS Nanocrystals: Bulk Vs Surface. *J. Phys. Chem. C* **2010**, *114*, 18323-18329.

7. Ithurria, S.; Guyot-Sionnest, P.; Mahler, B.; Dubertret, B., Mn^{2+} as a Radial Pressure Gauge in Colloidal Core/Shell Nanocrystals. *Phys. Rev. Lett.* **2007**, *99*, 265501.

8. Bol, A. A.; Meijerink, A., Long-Lived Mn^{2+} Emission in Nanocrystalline ZnS: Mn^{2+}. *Phys. Rev. B* **1998**, *58*, R15997.

9. Bhargava, R. N.; Gallagher, D.; Hong, X.; Nurmikko, A., Optical Properties of Manganese-Doped Nanocrystals of ZnS. *Phys. Rev. Lett.* **1994**, *72*, 416-419.

10. Hazarika, A.; Layek, A.; De, S.; Nag, A.; Debnath, S.; Mahadevan, P.; Chowdhury, A.; Sarma, D. D., Ultranarrow and Widely Tunable Mn^{2+}-Induced Photoluminescence from Single Mn-Doped Nanocrystals of ZnS-CdS Alloys. *Phys. Rev. Lett.* **2013**, *110*, 267401.

11. Pradhan, N.; Peng, X., Efficient and Color-Tunable Mn-Doped ZnSe Nanocrystal Emitters: Control of Optical Performance Via Greener Synthetic Chemistry. *J. Am. Chem. Soc.* **2007**, *129*, 3339-3347.

12. Sharma, D. K.; Chowdhury, A., Spectrally Resolved Optical Microscopy Using a Transmission Grating Spectrograph: Importance of Spatial Selection. *Analyst* **2014**, *139*, 473-481.

13. Efros, A. L.; Nesbitt, D. J., Origin and Control of Blinking in Quantum Dots. *Nat. Nanotechnol.* **2016**, *11*, 661-671.

14. Li, Z.; Chen, F.; Wang, L.; Shen, H.; Guo, L.; Kuang, Y.; Wang, H.; Li, N.; Li, L. S., Synthesis and Evaluation of Ideal Core/Shell Quantum Dots with Precisely Controlled Shell Growth: Nonblinking, Single Photoluminescence Decay Channel, and Suppressed Fret. *Chem. Mater.* **2018**, *30*, 3668-3676.

15. Zhang, A.; Dong, C.; Liu, H.; Ren, J., Blinking Behavior of CdSe/CdS Quantum Dots Controlled by Alkylthiols as Surface Trap Modifiers. *J.Phys. Chem. C* **2013**, *117*, 24592-24600.

16. Yuan, G.; Gómez, D. E.; Kirkwood, N.; Boldt, K.; Mulvaney, P., Two Mechanisms Determine Quantum Dot Blinking. *ACS Nano* **2018**, *12*, 3397-3405.

17. Nirmal, M.; Dabbousi, B. O.; Bawendi, M. G.; Macklin, J. J.; Trautman, J. K.; Harris, T. D.; Brus, L. E., Fluorescence Intermittency in Single Cadmium Selenide Nanocrystals. *Nature* **1996**, *383*, 802-804.

18. Hess, C. M.; Riley, E. A.; Reid, P. J., Dielectric Dependence of Single-Molecule Photoluminescence Intermittency: Nile Red in Poly(Vinylidene Fluoride). *J. Phys. Chem. B* **2014**, *118*, 8905-8913.

19. Riley, E. A.; Hess, C. M.; Whitham, P. J.; Reid, P. J., Beyond Power Laws: A New Approach for Analyzing Single Molecule Photoluminescence Intermittency. *J. Chem. Phys.* **2012**, *136*, 184508.

Chapter 5

Ultrafast Carrier Dynamics in Transition Metal-Doped CdS Quantum Dots

5.1. Abstract

Functionality of colloidal semiconductor quantum dots (QDs) as the source of charge carriers and photons for photonic and photovoltaic applications attracted a lot of attention in the scientific community and created a vast field of research focusing on the manipulation of charge carrier dynamics. Doping impurity ions into host quantum dots further alters the characteristics of photons and charge carriers in terms of their relaxation processes. While a number of reports investigated the mechanistic understanding of the underlying processes, a comprehensive study of ultrafast carrier dynamics across the dopants in the same host is not done so far. In addition to the modification in synthesis enabling the fine control of the structure of doped QDs, our work focuses on gaining microscopic details of excited state exciton dynamics across a series of transition metal-doped CdS QDs. We show a possible carrier trapping by dopant states leading to the switching between multiple oxidation states involving a transient time scale, which is further corroborated by EXAFS analysis.

5.2. Introduction

Doping transition metal (TM) ions into colloidal semiconductor quantum dots (QDs) efficiently imparts new optoelectronic properties arising due to exciton-dopant interaction.[1, 2] For example, the most widely explored TM dopants (Mn^{2+}, Cu^{2+}, Co^{2+}, Ni^{2+}) are known to introduce mid-gap states in the host II-VI QDs[3] that control the carrier dynamics of the pristine host which, in turn, can give rise to new dopant-related emission.[4-6] These optoelectronic properties and the relevant applications rely on the photo-induced charge carriers and their relaxation dynamics. Therefore, extensive effort has been put into the research to improve the generation of photons and charge carriers and modulate the relaxation dynamics. For instance, isoelectronic Mn^{2+} ions substitute the divalent host cations in binary or ternary QDs, which results in the sensitization of Mn levels followed by intense photoluminescence (PL) arising due to ligand field transition in Mn^{2+}.[7-11] Although spectroscopically well-observed, the mechanism of sensitization of Mn levels has been debated in literature whether it is through energy or charge transfer from the host.[12] Due to the intense photoluminescence and relative insensitivity of Mn emission on the external perturbation, it is widely accepted in the community that the Mn excitation occurs through energy transfer.[13, 14] Additionally, a strong spin-exchange interaction between the host and Mn levels further supports the argument for an efficient energy transfer.[15] However, the measurement of the rate of exciton-dopant energy transfer by time-resolved pump-probe transient absorption (TA) spectroscopy revealed a

substantially higher timescale than a typical energy transfer rate.[16, 17] In addition, the timescale involved in the nonradiative hole trapping process (50-100 ps) suggested a possible charge transfer. Though the charge transfer from host to Mn^{2+} was thought to be energetically unfavorable, recently it was shown that the transient Mn excited state (Mn^{3+}) is formed by a charge transfer from the host to dopant.[11] However, direct experimental evidence of a transient Mn excited state is lacking. Another widely explored TM dopant Cu fueled a disagreement because of the proposition of two different emission mechanisms based on dopant oxidation states Cu^{1+} and Cu^{2+}.[18-22] and so the carrier dynamics. For example, an increase in hot carrier relaxation times in Cu doped CdSe QDs as compared to undoped ones is attributed to the suppression of Auger processes through ultrafast hole trapping and a nonadiabatic transition leading to the decoupling of carriers and enabling a phonon bottleneck for electrons supporting the presence of Cu^{1+}. In contrast, ground state bleach (GSB) recovery in 100 ps and 8970 ps timescale represents the exciton-Cu^{2+} energy transfer and the exciton relaxation in the subpopulation of the host in Cu-doped ZnInS/ZnS QDs, respectively.[23] Thus, despite several studies on a number of TM-doped QDs,[24-27] a cohesive study that tries to harmonize the carrier dynamics involving the vibrational levels across a series of different TM dopants is still lacking.

In this work, we have used a simple system of CdS QDs doped with various TM dopants, namely, Mn, Fe, Co, Ni, and Cu to probe the carrier relaxation pathways with the help of femtosecond (fs) TA spectroscopy. As suggested from our earlier study,[11] we find evidence that some dopants (Mn and Co) can transiently switch between multiple oxidation states, which is further correlated with the data obtained from EXAFS spectroscopy.

5.3. Experimental methods

5.3.1. Synthesis of TM-doped and undoped QDs

Undoped, and all the TM-doped CdS (except Cu-doped CdS) were synthesized using diffusion doping technique following the literature.[4] Briefly, metal sulfide (M-S) cores are formed at high temperature by injecting S-precursor into solution containing metal precursors followed by CdS shell growth using successive ionic layer adsorption and reaction (SILAR) technique. 0.2 M cadmium oleate and 0.2 M sulfur dissolved in 1-Octadecene (ODE) were used as precursors to overcoat the CdS matrix over the TM sulfide core QDs at a high annealing temperature of 140 °C (250 °C for Fe-CdS). Cd precursors followed by S precursors were injected into the reaction mixture, where each monolayer (ML) took 30 minutes to form. This

cycle continued till all the samples achieved sufficient CdS shell thickness (>13 MLs) to ensure the dopants are properly diffused throughout the host and the overall dopant amount is less than 5% of Cd. Undoped CdS was synthesized under similar experimental conditions without using any metal sulfide core. CdS was nucleated first at 240 °C followed by overcoating at 140 °C as stated above. Cu-doped CdS was synthesized following growth doping method[5] by first forming the CdS QDs, followed by the addition of 10 μmoles of $Cu(St)_2$ solution in 1 ml of ODE at 180 °C and annealing for 2 hours.

5.3.2. Characterization

The samples were characterized using x-ray diffraction, transmission electron microscopy (TEM), and optical measurements. Powder XRD patterns for the QDs were recorded on a Bruker D8 Advance diffractometer using Cu-Kα radiation (1.5418 Å). TEM was performed on a Tecnai F30 UHR version electron microscope, using a field emission gun (FEG) operating at an accelerating voltage of 200 kV in bright field mode using Cu coated holey carbon TEM grids. Absorption spectra of samples were recorded using an Agilent 8453 UV visible spectrometer. Steady-state PL spectra were collected using the 450 W xenon lamp as the source on the FLSP920 spectrometer, Edinburgh Instruments, while the PL lifetime measurements were carried out in the same instrument using EPL-405 pulsed diode laser as the excitation source (λ_{ex} = 405 nm).

Ultrafast transient absorption measurements were performed by an amplified Ti:Sapphire laser (Coherent Libra) generating 100-fs pulses at 800 nm and 2 kHz repetition rate. Pump pulses at 400 nm were generated by frequency doubling the fundamental wavelength by a 2-mm-thick β-barium borate crystal; they were modulated at 1 kHz by a mechanical chopper and focused in a spot of (400x180) μm^2 on samples dispersed in hexane. UV-visible probe pulses were produced by white light supercontinuum generation focusing a part of the fundamental beam in a calcium fluoride plate. Chirp-free differential transmission spectra $\Delta T/T = (T_{on} - T_{off})/ T_{off}$, T_{on} and T_{off} being the transmission of the probe through the perturbed and unperturbed samples were acquired at different pump-probe delays by a fast optical multichannel analyzer operating at the full laser repetition rate. The temporal resolution of the setup is ~100 fs. All the measurements were carried out at room temperature.

5.4. Results & discussion

All the samples except Cu-doped CdS were synthesized using colloidal method via Successive Ion Layer Adsorption and Reaction (SILAR) technique following the literature

report. The details of the synthesis and structural characterization is mentioned elsewhere.[4, 5] Formation of the QDs was characterized by X-ray diffraction pattern (XRD) and transmission electron microscopy (TEM) as shown in Figure 5.1(a). XRD patterns demonstrate the formation of hexagonal ($P6_3mc$) structure (Materials Project ID: mp-672) upon comparing the doped QDs with that of the bulk CdS without any impurity. Broadening of XRD peaks reveal the formation of small-sized particle, consistent with the TEM images shown in Figures 5.1(b), (c), (d), and (e).

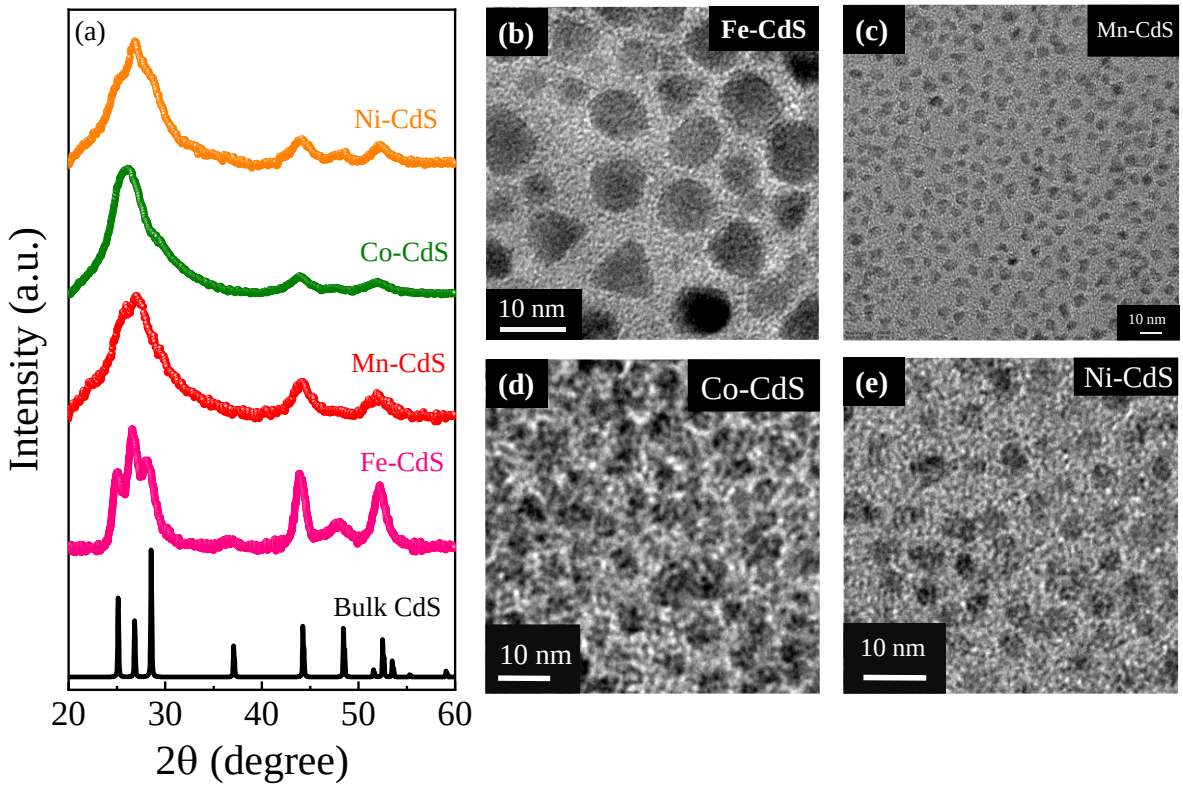

Figure 5.1. *(a) X-ray diffraction patterns of Mn, Fe, Co, Ni-doped CdS along with the CdS bulk hexagonal pattern. TEM images of (b) Fe-doped, (c) Mn-doped, (d) Co-doped, and (e) Ni-doped CdS QDs.*

The optical properties of QDs were characterized using UV-visible and steady-state PL spectroscopy. UV-visible spectra show absorption onset at their respective bandgap energy, the steady-state as shown in Figure 5.2, which confirms the formation of nanocrystals.

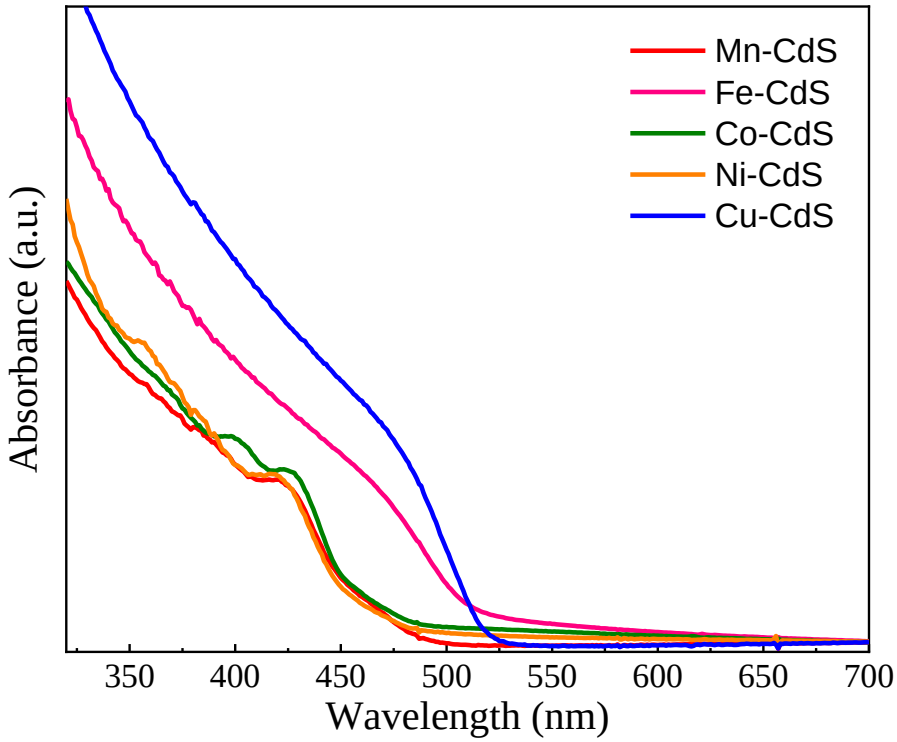

Figure 5.2. *UV-visible absorption spectra of TM-doped CdS QDs shows absorption onset at the respective bandgap energy of the doped QDs.*

The doped nanocrystals are further characterized using extended X-ray absorption fine structure (EXAFS) spectroscopy. Analysis of Cd-K edge in undoped (bulk data obtained from database) and all the TM-doped QDs reveals minimal or almost no perturbation at the Cd site due to doping. No involvement of the Cd_O path in the Cd-K edge fit confirms the formation of high-quality defect-free QDs as is expected in case of dilute level of doping. Details of the EXAFS analysis is part of another thesis and therefore not discussed here. In this thesis we have taken the necessary data in order to explain our work.

The M-S (M = TM dopants, Mn, Fe, Co, Ni and Cu here) bond-lengths obtained from EXAFS analysis of dopant-K edge, were plotted as a function of the dopants' ionic radii, shown in Figure 5.3. We used two very crucial information that both Fe and Cu are conclusively known to have a +2 state from the literature as well as our previous studies discussed in chapter 3,[28] where the synthesis strategy was same. We have drawn a line joining the two data points corresponding to Fe^{2+} and Cu^{2+} and plotted the rest of the dopants' ionic radii in both +2 and +3 states in a tetrahedral configuration. $^{+}$. Following this method, we find that the oxidation state of Ni in +2 nearly overlapping with that line. Interestingly, Mn and Co's two oxidation states lie opposite to the line, which suggests that both of them have intermediate M-S (M: Mn,

Co) bond-lengths. This suggests that there is a possibility for the switching between two different oxidation states in case of Mn and Co due to various triggers like photoinduction. In fact, XANES analysis Mn-K edge shows an average oxidation state to be +2.43.

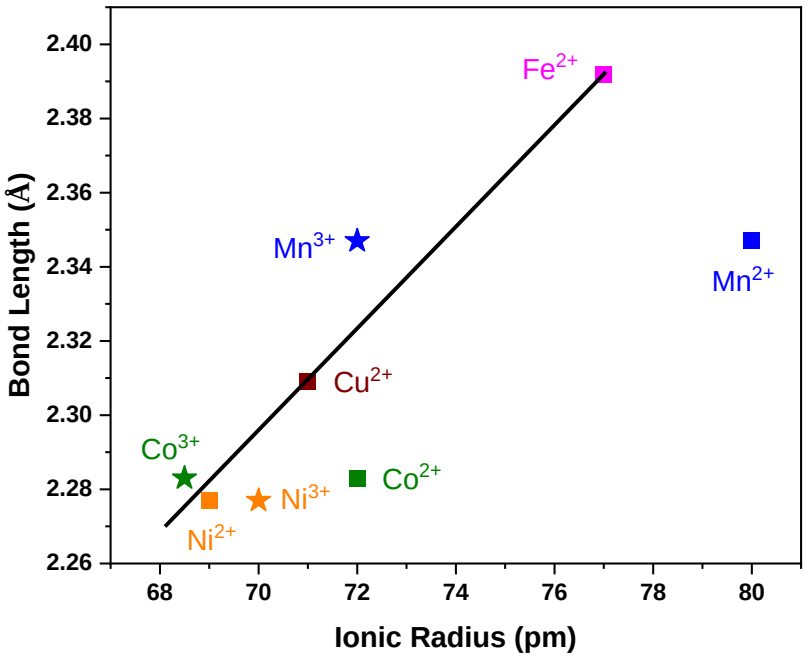

Figure 5.3. *The dopants can be arranged in a systematic way when M-S bond-lengths are plotted as a function of the ionic radii. Note that both Mn and Co lie opposite to the central line, suggesting the presence of multiple oxidation states.* *This figure is adapted with permission from the dissertation by Mr. Saptarshi Chakraborty.*

Signatures of photoinduced switching of the oxidation state of Mn have already been observed in earlier literature.[11] However, to exclusively understand the role of the dopants in modulating the exciton dynamics we studied the carrier relaxation processes using femtosecond TA spectroscopy. We did a comparative study of the ground state bleach (GSB) growth and recovery dynamics in undoped and doped CdS using a pump fluence of 24 μJ/cm^2 under the non-resonant excitation condition where the photoexcitation energy (3.1 eV) is higher than the bandgap of the QDs. Figure 5.4 represents the differential transmission dynamics ΔT/T for undoped and all the doped CdS QDs probed at their respective band edges. The positive ΔT/T signal is assigned to the photo-bleaching of the excitonic transition. We observe a fast rise in

the signal followed by an exponential decay which holds the information about the depopulation and population dynamics of the ground state respectively.

From the fitting of undoped CdS kinetics, we obtain a finite build-up time of 560 ± 7 fs. This was studied in earlier literature using undoped CdS QDs synthesized in a similar method,[29] where it was observed that the gradual population of the charge carriers at the band edges arises from the relaxation of the carriers from the higher vibrational energy levels to the band edges without any intervention from the trap states. Similar to earlier findings, we observe a single exponential recovery of the charge carriers in undoped CdS with a time constant of 692 ± 48 ps without any fast component suggesting that the QDs are devoid of trap states. Since the EXAFS data did not show any trap states in the QDs, we do not include any trap states in our analysis.

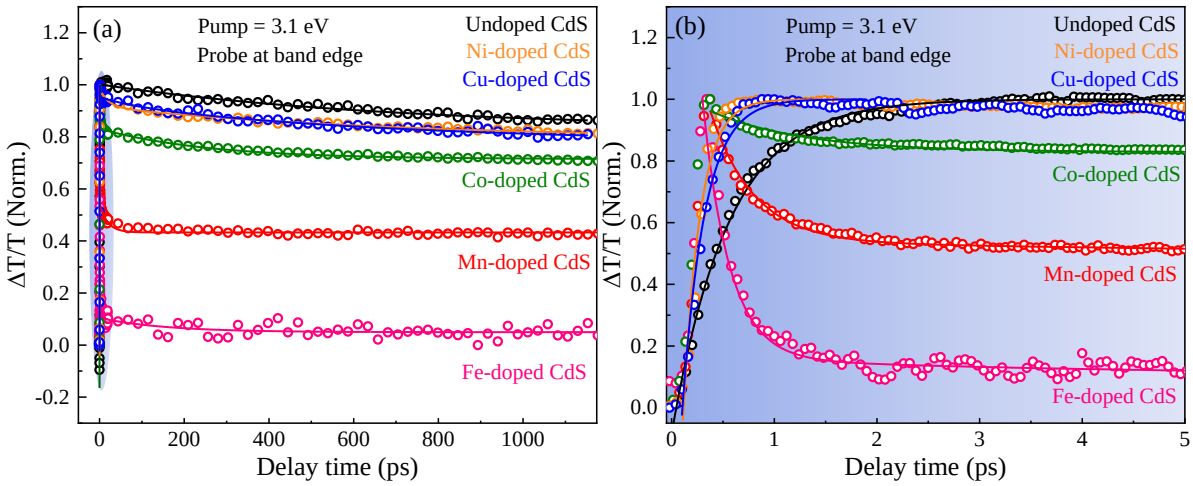

Figure 5.4. *(a) Differential transmission dynamics ΔT/T as a function of pump-probe delay for undoped and all the doped CdS QDs upon 3.1 eV laser excitation with a pump fluence of 24 μJ/Cm^2 (b) Zoom-in of the transmission dynamics up to 5 ps probe delay showing the GSB growth.*

As expected, the GSB growth dynamics of TM-doped CdS is quite different than that of the undoped CdS as shown in Figure 5.4. While the kinetics of the undoped CdS require a single exponential build-up and a single exponential recovery, the kinetics of all the TM-doped CdS require an additional recovery pathway. GSB growth of TM-doped CdS is faster compared to the undoped CdS. GSB growth of Fe, Mn, and Co-doped CdS is instantaneous or IRF

limited, whereas Ni (164 ± 10) and Cu (218 ± 10) show relatively slower growth but are still faster than that of the pristine CdS. The faster growth in doped CdS can be attributed to the presence of alternative depletion channel introduced by doping. It is interesting to note here that the rate of growth at the band edge energy is directly proportional to the number of states introduced by the dopants and hence the efficiency of the dopants in funneling the charge carriers. For example, while the Ni and Cu are known to have one mid gap state,[30-32] Mn and Co are known to have two mid-gap states[33-35] and Fe, with its extensive hybridization with the host have a large number of mid-gap states with substantial Fe contribution.[36] The growth rate of the GSB is found to be proportional to the increase in the number of mid-gap states.

The analysis of the recovery kinetics by a global fitting is shown in Table 5.1. It is interesting to note that this global fitting, assuming the excitonic decay pathways as one of the decay paths, fits only Cu and Ni doped CdS in addition to the undoped CdS as shown in Table 5.1. The charge carriers in Cu and Ni-doped CdS recover through two pathways, namely one with lifetime of CdS excitonic path and the other with a faster decay, possibly to the mid-gap states in the NCs, revealing that a fraction of charge carriers is captured by the dopant energy levels. The exact efficiency of the decay through the dopant levels is dependent on several factors including the band alignment with the host. The possibility of Auger or trap state recombination is discarded because of the non-availability of surface traps.

Table 5.1. *Fitting summary of the GSB recovery kinetics of undoped, and TM-doped CdS QDs*

Sample Name	y_0	A_1	t_1 (ps)	A_2	t_2 (ps)
CdS	0.83 ± 0.006	-	-	0.17 ± 0.006	692 ± 48
Mn-CdS	0.43 ± 0.001	1.00 ± 0.03	0.42 ± 0.01	0.10 ± 0.002	20 ± 1
Fe-CdS	0.05 ± 0.003	1.40 ± 0.04	0.28 ± 0.008	0.10 ± 0.004	24 ± 3
Co-CdS	0.72 ± 0.002	0.20 ± 0.008	0.90 ± 0.04	0.11 ± 0.002	256 ± 17
Ni-CdS	0.80 ± 0.004	0.06 ± 0.002	21 ± 2.2	0.12 ± 0.005	692 ± 48
Cu-CdS	0.78 ± 0.005	0.02 ± 0.005	83 ± 36	0.15 ± 0.007	692 ± 48

As mentioned earlier, Mn and Co are known to provide two mid-gap states, one near the CB and the other near the VB. Based on our EXAFS analysis, the intermediate M-S bond-lengths indicate towards the feasibility of a transient change in the oxidation state in case of Mn and Co-doped CdS. This suggests that both the dopant induced states are efficient in abstracting the photoexcited charge carriers from the excitonic states. Mn, due to coherence of lot of parameters including the band alignment is quite efficient in withdrawing the charge carriers as also discussed in several of the earlier literature papers.[16, 17, 34, 37, 38] Consistent with the above data, the GSB recovery kinetics also demonstrate two lifetimes, substantially different and faster than the undoped CdS recombination kinetics. This fast biexponential recovery indicates towards the ultrafast capture of charge carriers by the dopant states and hence a possibility of switching between multiple oxidation states in coherence with our EXAFS analysis. It is important to note that an earlier study on Mn-doped CdZnSe alloy QDs revealed the presence of a transient Mn^{3+} excited state created by ultrafast capturing of a photogenerated hole from the host valence band which too suggested the presence of multiple oxidation states.[11] Similar GSB recovery processes occur in Co-CdS except for the fact that the recovery times are slower as compared to that in the Mn-CdS. This is because of the energy states introduced by Co is energetically distant (ligand field transition (LFT) energy in Co^{2+}-doped CdS is at ~728 nm) from the band-edges unlike Mn (LFT energy in Mn^{2+}-doped CdS is at ~585 nm).[39-42]

In the case of Fe-CdS, we notice a nearly instantaneous GSB recovery compared to the rest of the timescales involved (Figure 5.4), similar to our earlier findings.[36] The GSB signal recovers within a few picoseconds (280 ± 8 fs, and 24 ± 3 ps) as shown in Table 5.1 which is much faster as compared to the undoped CdS having a recovery time constant 692 ± 48 ps. This drastic difference is due to the presence of multiple acceptor states induced by Fe^{2+} doping.[36] This instantaneous decay is even faster than the growth time of undoped CdS (560 ± 7 fs), which explains the capture of charge carriers by the dopant induced acceptor states even before they relax down to host band edges confirming the absence of excitonic PL in Fe-doped CdS.

A generalized schematic representation of underlying processes in undoped and TM-doped QDs is depicted in Figure 5.5.

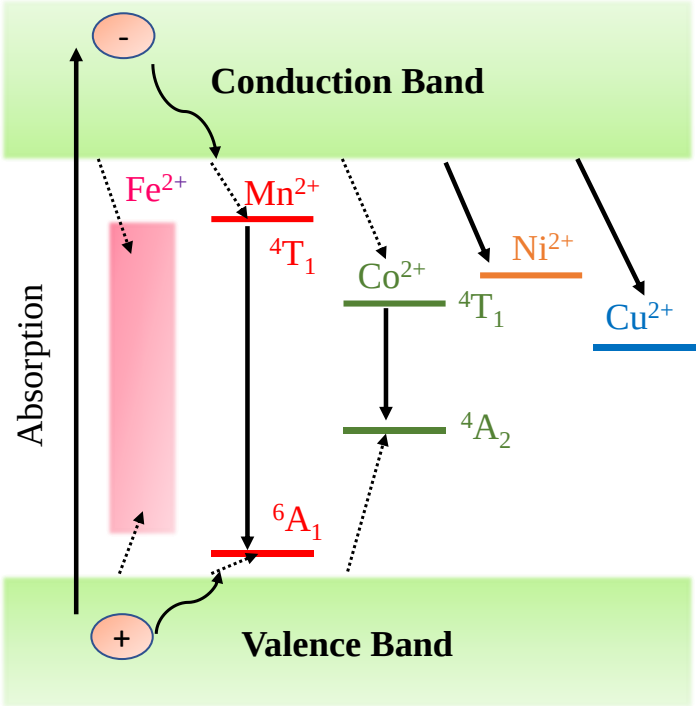

Figure 5.5. *Illustration of various modes of relaxation of charge carriers produced on photoexcitation of the TM-doped QDs.*

5.5. Conclusion

In summary, we have studied the carrier dynamics in various TM doped CdS QDs by employing ultrafast TA spectroscopy. We find that no structural perturbation in the Cd sites caused by doping. The carrier dynamics of undoped CdS is found to be greatly influenced by the dopants, where an ultrafast carrier trapping occurs via dopant states, which in turn, suggest a possibility of photoinduced switching between multiple oxidation states.

Bibliography

1. Fainblat, R.; Barrows, C. J.; Gamelin, D. R., Single Magnetic Impurities in Colloidal Quantum Dots and Magic-Size Clusters. *Chem. Mater.* **2017,** *29* (19), 8023-8036.

2. Pradhan, N.; Das Adhikari, S.; Nag, A.; Sarma, D. D., Luminescence, Plasmonic, and Magnetic Properties of Doped Semiconductor Nanocrystals. *Angew. Chem. Int. Ed.* **2017,** *56* (25), 7038-7054.

3. Umebayashi, T.; Yamaki, T.; Itoh, H.; Asai, K., Analysis of electronic structures of 3d transition metal-doped TiO_2 based on band calculations. *J Phys Chem Solids* **2002,** *63* (10), 1909-1920.

4. Saha, A.; Makkar, M.; Shetty, A.; Gahlot, K.; A. R, P.; Viswanatha, R., Diffusion doping in quantum dots: bond strength and diffusivity. *Nanoscale* **2017,** *9* (8), 2806-2813.

5. Grandhi, G. K.; Tomar, R.; Viswanatha, R., Study of Surface and Bulk Electronic Structure of II–VI Semiconductor Nanocrystals Using Cu as a Nanosensor. *ACS Nano* **2012,** *6* (11), 9751-9763.

6. Pradhan, N.; Goorskey, D.; Thessing, J.; Peng, X., An Alternative of CdSe Nanocrystal Emitters: Pure and Tunable Impurity Emissions in ZnSe Nanocrystals. *J. Am. Chem. Soc.* **2005,** *127* (50), 17586-17587.

7. Nag, A.; Cherian, R.; Mahadevan, P.; Gopal, A. V.; Hazarika, A.; Mohan, A.; Vengurlekar, A. S.; Sarma, D. D., Size-Dependent Tuning of Mn^{2+} d Emission in Mn^{2+}-Doped CdS Nanocrystals: Bulk vs Surface. *J. Phys. Chem. C* **2010,** *114* (43), 18323-18329.

8. Bhargava, R. N.; Gallagher, D.; Hong, X.; Nurmikko, A. J., Optical Properties of Manganese-Doped Nanocrystals of ZnS. *Phys. Rev. Lett.* **1994,** *72* (3), 416.

9. Beaulac, R.; Archer, P. I.; van Rijssel, J.; Meijerink, A.; Gamelin, D. R., Exciton Storage by Mn^{2+} in Colloidal Mn^{2+}-Doped CdSe Quantum Dots. *Nano Lett.* **2008,** *8* (9), 2949-2953.

10. Bol, A. A.; Meijerink, A., Long-Lived Mn^{2+} Emission in Nanocrystalline ZnS: Mn^{2+}. *Phys. Rev. B* **1998,** *58* (24), R15997.

11. Gahlot, K.; KR, P.; Camellini, A.; Sirigu, G.; Cerullo, G.; Zavelani-Rossi, M.; Singh, A.; Waghmare, U. V.; Viswanatha, R., Transient Species Mediating Energy Transfer to Spin-Forbidden Mn d States in II–VI Semiconductor Quantum Dots. *ACS Energy Lett.* **2019,** *4* (3), 729-735.

12. Cherepanov, D.; Kostrov, A.; Gostev, F.; Shelaev, I.; Motyakin, M.; Kochev, S.; Kabachii, Y.; Nadtochenko, V., Ultrafast Quenching of Excitons in the $Zn_xCd_{1-x}S$/ZnS

Quantum Dots Doped with Mn^{2+} through Charge Transfer Intermediates Results in Manganese Luminescence. *Nanomaterials* **2021,** *11* (11), 3007.

13. Chen, H. Y.; Son, D. H. J. I. J. o. C., Energy and Charge Transfer Dynamics in Doped Semiconductor Nanocrystals. *Isr. J. Chem.* **2012,** *52* (11-12), 1016-1026.

14. Hsia, C.-H.; Wuttig, A.; Yang, H., An Accessible Approach to Preparing Water-Soluble Mn^{2+}-Doped (CdSSe) ZnS (Core) Shell Nanocrystals for Ratiometric Temperature Sensing. *ACS nano* **2011,** *5* (12), 9511-9522.

15. Singh, R.; Liu, W.; Lim, J.; Robel, I.; Klimov, V. I., Hot-Electron Dynamics in Quantum Dots Manipulated by Spin-Exchange Auger Interactions. *Nat. Nanotechnol.* **2019,** *14* (11), 1035-1041.

16. Chen, H.-Y.; Chen, T.-Y.; Son, D. H., Measurement of Energy Transfer Time in Colloidal Mn-Doped Semiconductor Nanocrystals. *J. Phys.Chem. C* **2010,** *114* (10), 4418-4423.

17. Chen, H.-Y.; Maiti, S.; Son, D. H., Doping Location-Dependent Energy Transfer Dynamics in Mn-Doped CdS/ZnS Nanocrystals. *ACS Nano* **2012,** *6* (1), 583-591.

18. Suyver, J.; Van der Beek, T.; Wuister, S.; Kelly, J.; Meijerink, A., Luminescence of nanocrystalline ZnSe: Cu. *Appl. Phys. Lett.* **2001,** *79* (25), 4222-4224.

19. Viswanatha, R.; Brovelli, S.; Pandey, A.; Crooker, S. A.; Klimov, V. I., Copper-doped inverted core/shell nanocrystals with “permanent” optically active holes. *Nano Lett.* **2011,** *11* (11), 4753-4758.

20. Corrado, C.; Jiang, Y.; Oba, F.; Kozina, M.; Bridges, F.; Zhang, J. Z., Synthesis, structural, and optical properties of stable ZnS: Cu, Cl nanocrystals. *J. Phys. Chem. A* **2009,** *113* (16), 3830-3839.

21. Isarov, A. V.; Chrysochoos, J., Optical and photochemical properties of nonstoichiometric cadmium sulfide nanoparticles: surface modification with copper (II) ions. *Langmuir* **1997,** *13* (12), 3142-3149.

22. Tananaev, P.; Dorofeev, S.; Vasil’ev, R.; Kuznetsova, T., Preparation of copper-doped CdSe nanocrystals. *Inorg. Mater.* **2009,** *45* (4), 347-351.

23. Gao, Y.; Liu, H.; Li, J.; Xiao, S.; Guo, Z.; Pan, R.; Lin, X.; He, T., Efficient multiphoton absorption of near-infrared emitting Cu-doped ZnInS/ZnS nanocrystals. *J. Phys. D: Appl. Phys.* **2020,** *53* (25), 255103.

24. Wang, L.; Chen, Z.; Liang, G.; Li, Y.; Lai, R.; Ding, T.; Wu, K., Observation of a Phonon Bottleneck in Copper-Doped Colloidal Quantum Dots. *Nat. Commun* **2019,** *10* (1), 1-8.

25. Gao, Y.; Liu, H.; Li, J.; Xiao, S.; Guo, Z.; Pan, R.; Lin, X.; He, T., Efficient Multiphoton Absorption of Near-Infrared Emitting Cu-Doped ZnInS/ZnS Nanocrystals. *J. Phys. D: Appl. Phys.* **2020,** *53* (25), 255103.

26. Ye, Y.; Wang, X.; Ye, S.; Xu, Y.; Feng, Z.; Li, C., Charge-Transfer Dynamics Promoted by Hole Trap States in CdSe Quantum Dots–Ni^{2+} Photocatalytic System. *J. Phys. Chem. C* **2017,** *121* (32), 17112-17120.

27. Maiti, S.; Dana, J.; Jadhav, Y.; Debnath, T.; Haram, S. K.; Ghosh, H. N., Electrochemical Evaluation of Dopant Energetics and the Modulation of Ultrafast Carrier Dynamics in Cu-doped CdSe Nanocrystals. *J. Phys. Chem. C* **2017,** *121* (48), 27233-27240.

28. Saha, A.; Shetty, A.; Pavan, A. R.; Chattopadhyay, S.; Shibata, T.; Viswanatha, R., Uniform Doping in Quantum-Dots-Based Dilute Magnetic Semiconductor. *J. Phys. Chem. Lett.* **2016,** *7* (13), 2420-2428.

29. Makkar, M.; Moretti, L.; Maiuri, M.; Cerullo, G.; Viswanatha, R., Ultrafast Electron–Hole Relaxation Dynamics in CdS Nanocrystals. *J. Phys.: Mater.* **2021,** *4* (3), 034005.

30. Nelson, H. D.; Hinterding, S. O.; Fainblat, R.; Creutz, S. E.; Li, X.; Gamelin, D. R., Mid-gap States and Normal vs Inverted Bonding in Luminescent Cu^{+}-and Ag^{+}-doped CdSe Nanocrystals. *J. Am. Chem. Soc.* **2017,** *139* (18), 6411-6421.

31. Srivastava, B. B.; Jana, S.; Pradhan, N., Doping Cu in Semiconductor Nanocrystals: Some Old and Some New Physical Insights. *J. Am. Chem. Soc.* **2011,** *133* (4), 1007-1015.

32. Jana, S.; Srivastava, B. B.; Jana, S.; Bose, R.; Pradhan, N., Multifunctional doped semiconductor nanocrystals. *J. Phys. Chem. Lett.* **2012,** *3* (18), 2535-2540.

33. May, J. W.; Ma, J.; Badaeva, E.; Li, X. J. T. J. o. P. C. C., Effect of Excited-State Structural Relaxation on Midgap Excitations in Co^{2+}-Doped ZnO Quantum Dots. *J Phys. Chem. C* **2014,** *118* (24), 13152-13156.

34. Santra, P. K.; Kamat, P. V., Mn-Doped Quantum Dot Sensitized Solar Cells: A Strategy to Boost Efficiency over 5%. *J. Am. Chem. Soc.* **2012,** *134* (5), 2508-2511.

35. Norris, D. J.; Yao, N.; Charnock, F. T.; Kennedy, T. A., High-quality manganese-doped ZnSe nanocrystals. *Nano Lett.* **2001,** *1* (1), 3-7.

36. Makkar, M.; Dheer, L.; Singh, A.; Moretti, L.; Maiuri, M.; Ghosh, S.; Cerullo, G.; Waghmare, U. V.; Viswanatha, R., Magneto-Optical Stark Effect in Fe-Doped CdS Nanocrystals. *Nano Lett.* **2021,** *21* (9), 3798-3804.

37. Debnath, T.; Maity, P.; Maiti, S.; Ghosh, H. N., Electron Trap to Electron Storage Center in Specially Aligned Mn-Doped CdSe d-Dot: A Step Forward in the Design of Higher Efficient Quantum-Dot Solar Cell. *J. Phys. Chem. Lett.* **2014,** *5* (16), 2836-2842.

38. Pradhan, N.; Sarma, D., Advances in Light-Emitting Doped Semiconductor Nanocrystals. *J. Phys. Chem. Lett.* **2011,** *2* (21), 2818-2826.

39. Yang, Y.; Chen, O.; Angerhofer, A.; Cao, Y. C., Radial-Position-Controlled Doping in CdS/ZnS Core/Shell Nanocrystals. *J. Am. Chem. Soc.* **2006,** *128* (38), 12428-12429.

40. Zeng, R.; Rutherford, M.; Xie, R.; Zou, B.; Peng, X., Synthesis of Highly Emissive Mn-Doped ZnSe Nanocrystals Without Pyrophoric Reagents. *Chem. Mater.* **2010,** *22* (6), 2107-2113.

41. Zhang, W.; Li, Y.; Zhang, H.; Zhou, X.; Zhong, X., Facile Synthesis of Highly Luminescent Mn-Doped ZnS Nanocrystals. *Inorg. Chem.* **2011,** *50* (20), 10432-10438.

42. Norberg, N. S.; Dalpian, G. M.; Chelikowsky, J. R.; Gamelin, D. R., Energetic Pinning of Magnetic Impurity Levels in Quantum-Confined Semiconductors. *Nano Lett.* **2006,** *6* (12), 2887-2892.

Part 2

Study of Opto-electronic Properties of Dual-Doped II-VI Semiconductor Quantum Dots

Chapter 6

Electronic Structure Study of Dual Doped II-VI Semiconductor Quantum Dots Towards Single-Source White Light Emission

6.1. Abstract

Single-source white light emission (WLE) from colloidal semiconductor quantum dots (QDs) is one of the most exciting and promising high-quality solid-state light sources to meet the current global demand for sustainable resources. While most of the previous methods involve dual (green-red) emissive nanostructures coated on blue LEDs to achieve white light, we came up with the idea of having a single-source to produce the same. Herein, we developed a facile synthetic method for intense white light-emitting Cu, Mn co-doped ZnSe QDs. We engineered the QDs in such a way that their electronic structures get altered by varying the extent of doping and concentration of ligands which then customize the type of white light emission from warm white to cool white. Further, we studied the composition-driven change in the electronic structure of the host QDs to achieve the emission tunability expanded over the entire visible range.

6.2. Introduction

Global electricity consumption has continued to go up at a very fast rate along with the concern of global warming and climate change and the existing renewable sources can fulfill only half of the increasing demand. Thus, it turned out to be very important to find promising light sources from a materials perspective that can replace the conventional lighting systems. Colloidal semiconductor nanocrystals, most commonly known as quantum dots (QDs), have shown enormous potential as new-generation nanophosphors, due to their high photoluminescence quantum yield (PLQY), highly controllable bandgap and bandgap-dependent emission tunability, low-cost synthesis, etc.[1-4] Years of effort have focused on obtaining white light-emitting (WLE) materials been made to reproducibly improve various optoelectronic properties of QDs including high color rendering white-light-emitting materials and devices that are tunable from warm to cool white and robust.[5] Conventionally, white light was achieved using either by mixing the individual QD materials emitting three primary colors blue, green, and red, or by coating a combination of green and red phosphors onto commercially available blue or ultraviolet LEDs. For example, blue, green, and red-emitting CdZnS alloy, ZnSe/CdSe/ZnS, and CdSe/ZnS core/shell QDs respectively,[6] or different compositions of CdSe/ZnS core/shell QDs were blended together to fabricate white light-emitting device (WLED).[7-8] Similarly, green and red-emitting $CuInS_2$ based QDs,[9] Cu : ZnInS core/shell QDs,[10] CdSe/CdS/ZnS/CdSZnS multishell QDs[11] were coated onto blue emitting chips that led to good quality WLEDs. However, simply mixing these QDs of different bandgaps showed undesired energy transfers (ET), reabsorption of the emitted photons, unexpected temporal shift

in the color coordinates due to non-uniform stability of QDs leading to reduced luminous efficacy. Hence, single-source emitters with broad emission were preferred over multi-component systems.

As single source emitters, two different options, specifically, the use of trap states to tune the emission to a white light and the use of dopant mid-gap states to obtain robust reproducible emission were explored in literature. However, as the nature of the interplay of core and surface PL leading to white light emission is poorly understood, white light achieved using ill-defined surface states is not robust. For example, white light from trap-rich CdS QDs and onion-like CdSe/ZnS/CdSe/ZnS,[12] $Zn_{0.93}Cd_{0.07}Se$ alloy QDs,[13] Mn^{2+}-doped metal chalcogenides[14-15] involved sensitive manipulation of trap states, and depended heavily on the reaction parameters and external environmental conditions such as, temperature, moisture, oxygen etc. To overcome this uncertainty and to find suitable alternatives, attempts have been made to synthesize dual-doped QDs to achieve white light emission. Cu, Mn co-doped Zn-In-S/ZnS core/shell QDs was reported as a white light emitter with color rendering index (CRI) as high as 95.[16] However, it still remains a challenge to incorporate two dopants simultaneously into the QDs and reliably tune the emission that is both robust and does not decay upon continuous excitation and higher operating temperatures.[17] Herein, we devised a new synthetic strategy that overcomes all the problems of previously reported materials.

In this work, we use the robustness of the dopant mid-gap states and the tunability afforded by the use of trap states to obtain single source, tunable, robust, dual doped white light emitters. The Cu, Mn dual-doped QDs were synthesized using versatile hot-injection colloidal method. We use diffusion doping,[18] to ensure that the two dopants are incorporated within the same nanocrystal. Diffusion doping emphasizes the need to obtain small clusters that are then diffused into the lattice at high temperature. However, the two dopants, namely Mn and Cu, are best incorporated into the host QDs in two distinct steps during the host formation and growth such that the characteristic emission from both the dopants are present covering the entire visible range. Since, Mn is best doped following nucleation-doping strategy,[19] the first step involves the nucleation of MnSe nanoclusters at high temperature followed by zinc overcoating to obtain Mn-doped ZnSe QDs. Once the Mn-doped QDs are formed, 2nd step involves the doping of Cu following the growth-doping method[20] leading to the formation of Cu, Mn dual-doped ZnSe QDs. The chromaticity of the white light emission was tuned by altering host electronic structure either by surface modification or by wavefunction modulation achieved by varying the extent of doping as well as changing the composition of host. It is

well known that the intensity of the Cu emission to the band edge states are controlled by the number of surface hole states.[21-22] We study the effect of Cu to Mn states in the dual-doped dots and we obtain a scientific rationale to tune the CIE coordinates to the required number by modulating the dopant emission with high PL quantum yield. We also study the stability and robustness of the emission intensity and color as a function of temperature and exposure to UV excitation light. We then changed the host bandgap by alloying Cd into ZnSe and studied the white light-based emission tunability from bluish white to orangish white that can show possible application in fabricating colorful LEDs.

6.3. Experimental Section

6.3.1. Materials

Copper chloride ($CuCl_2$, 97%), elemental selenium, zinc stearate ($ZnSt_2$), zinc undecylenate ($ZnUt_2$), cadmium oxide (CdO), octadecylamine (ODA, 95%), Oleylamine (technical grade, 70%), 1-octadecene (ODE, 90%), tributylphosphine (TBP), trioctylphosphine (TOP, 90%) were purchased from Sigma-Aldrich. Manganous chloride AR ($MnCl_2$), stearic acid LR were purchased from SD Fine chemicals, tetramethylammonium hydroxide pentahydrate (TMAH, 98%) was purchased from Spectrochem. Acetone, methanol, hexane and toluene were purchased from Merck. All the chemicals and solvents were used as purchased without any further purification.

6.3.2. Synthesis of precursors

Manganese stearate ($MnSt_2$) was synthesized by the method mentioned in literature.[19] Briefly, stearic acid (20mmol) was dissolved in methanol and added to TMAH solution of similar concentration and stirred for 20 min. Meanwhile, 10 mmol manganous chloride was dissolved separately in methanol and added dropwise to the above-mentioned mixture with constant stirring. The appearance of white precipitate shows the formation of $MnSt_2$. The solution was washed repeatedly with methanol followed by acetone. The white precipitate of $MnSt_2$ obtained was then dried in vacuum and used for further synthesis.

Copper stearate ($CuSt_2$) was prepared following literature method.[23] Briefly, 10 mmol of stearic acid (SA) was dissolved in methanol and heated at 50 ^{o}C to get a clear solution. 10 mmol of TMAH was also dissolved in methanol separately and dropwise added to the SA-methanol solution. Meanwhile 5 mmol of $CuCl_2$ was dissolved in methanol and slowly

dropwise added to the above-mentioned solution under vigorous stirring. Sky blue precipitate of $CuSt_2$ was obtained and washed thoroughly followed by drying under vacuum.

Cadmium oleate ($CdOl_2$) was prepared by heating a mixture of 0.32 g of cadmium oxide, 7 mL oleic acid and 9 mL of ODE to a higher temperature until the solution appeared colorless (~220-240 ^{o}C) under Ar atmosphere.

6.3.3. Synthesis of the singly-doped and dual-doped NCs

Synthesis of Mn-doped ZnSe QDs

Mn-doped ZnSe NCs were synthesized following nucleation doping method. Briefly, selenium powder (23.7 mg) and oleyl amine (0.05 g) in ODE (5 mL) was loaded into three-neck flask and degassed for 1 hour followed by bubbling with argon. The temperature was then raised to 280 °C. The manganese precursor solution (0.015 mmol $MnSt_2$ in 1 mL ODE) was then rapidly injected into the reaction flask at 280 °C. The reaction mixture was then allowed to cool to 260 °C for zinc overcoating with the injection of 0.5 mL of Zinc precursor solution (0.15 mmol of $ZnSt_2$ in 0.7 mL ODE), followed by injection of oleyl amine to activate the zinc carboxylate. Temperature was further lowered to 240 °C and another 0.5 mL of zinc precursor (0.25 mmol of $ZnUt_2$ and 60 mg undecylenic acid in 1.4 mL ODE) was injected after 10 min. The reaction flask was maintained at 240 °C for 10 min which was followed by injection of a designated amount of TOP. Finally, the reaction was allowed to cool down to room temperature, and the nanocrystals were washed using hexane and ethanol for further study.

Synthesis of Cu-doped ZnSe QDs

Cu-doped ZnSe NCs were synthesized following growth doping method.[24] 0.1 mmol $ZnSt_2$ was taken in 5 mL ODE and the contents were degassed for an hour followed by purging with Argon. The temperature was then increased to 270 °C wherein Se precursor (1 mL TBP-Se in 0.5 g of ODA) was injected rapidly into the reaction mixture. The temperature was then set at 170 °C where Cu precursor was added. The reaction mixture was then annealed for 20-30 min at 190 °C followed by addition of $ZnUt_2$ solution (0.12 g $ZnUt_2$ in 2 mL ODE). The reaction temperature was then increased to 210 °C for 10 min and finally reaction was allowed to cool down and purified using hexane and methanol.

Synthesis of Cu, Mn dual-doped ZnSe QDs

Mn-doped ZnSe NCs were synthesized following nucleation doping method already discussed before in this paper. Once the Mn-doped ZnSe QDs are formed the reaction temperature was lowered to 180 °C and a designated amount of Cu precursor was added. In order for Cu ions to get adsorbed onto the surface of QDs, the reaction temperature was raised to 210 °C and kept for 5 min and further reduced down to 180 °C followed by annealing for 30-45 minutes. This allows the Cu^{2+} ions to migrate inside from the surface results in the formation of Cu, Mn dual-doped ZnSe QDs.

Further, Cd alloying is done after reducing the reaction temperature further to 140 °C and gradual addition of $CdOl_2$ results in the formation of Cu, Mn dual-doped $Cd_xZn_{1-x}Se$ QDs. All the QDs were purified using hexane and methanol and used further for different studies.

6.3.4. Characterization

The structure of the as synthesized nanoparticles was determined using X-ray diffraction (XRD) technique on Rigaku Smartlab using Cu-Kα radiation and to get a high signal-to-noise ratio all patterns were recorded at a slow scan rate. Transmission electron microscopic (TEM) images were recorded using JEOL JEM-3010 transmission electron microscope with an accelerating voltage of 200 kV. Inductively coupled plasma optical emission spectroscopy (ICP-OES) was performed using PerkinElmer Optima 7000 DV instrument. Samples were prepared by washing the NCs to remove the excess precursors. Washed NCs were then digested in concentrated HNO_3 and diluted with Millipore water.

UV-Visible absorption spectra of various aliquots dissolved in hexane was obtained using Agilent 8453 UV-Visible spectrometer. Steady state PL spectra were collected using the 450 W Xenon lamp as the source on the FLSP920 spectrometer, Edinburgh Instruments while the lifetime of Cu PL was measured using an EPL-405 pulsed laser, Edinburgh Instrument and lifetime Mn PL as well as gated PL measurements were carried out using microflash lamp.

High temperature measurements were done using ARS cryostat NCs films were heated up to 350 K and measurements were done at every 10 K interval while reducing the temperature to 295 K.

6.4. Results and discussion

Detailed synthetic procedure is discussed in the experimental methods section and a simple schematic of the synthesis procedure is shown below. Formation of MnSe nanoclusters is the most crucial step towards achieving Mn emission with high PLQY. The previously reported methods involved tributylphosphine-selenium compound as selenium precursor that not only restricts the reactivity of Se but also introduces toxicity due to the presence of unreacted tribuylphosphine. Herein, instead of organo-phosphine we used elemental selenium as Se precursor with greatly controlled reactivity using appropriate amount of oleyl amine that results in a very fast and efficient formation of MnSe. This is followed by overcoating with zinc precursor and then addition of Cu and finally cation exchange to synthesize dual-doped $Cd_xZn_{1-x}Se$ QDs. A general synthesis scheme is shown in Figure 6.1. where nucleation and growth doping methods are decoupled in order to efficiently incorporate both Mn and Cu at two different stages of the reaction.

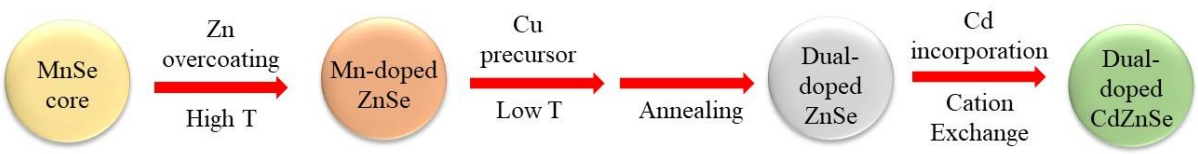

Figure. 6.1. *Synthesis scheme involving nucleation and growth doping method for incorporation of Mn, and Cu into ZnSe lattice.*

Figure 6.2. shows the basic characterization of purified dual-doped QDs. Structural characterization has been carried out by X-ray diffraction pattern (XRD) and transmission electron microscopy (TEM). XRD pattern shown in Figure 6.2(a) demonstrate the formation of cubic zinc blende structure upon comparing the XRD patterns of Cu, Mn dual-doped ZnSe and $Cd_xZn_{1-x}Se$ QDs with that of bulk ZnSe and CdSe cubic structure as obtained from ICSD database. XRD patterns show a shift from ZnSe bulk to CdSe bulk with increase in Cd concentration indicating the alloying of Cd into Mn, Cu dual-doped ZnSe QDs. Broadening of XRD peaks reveal the formation of very small sized particle which is very consistent with the TEM images shown in Figure 6.2(b) and 6.2(c).

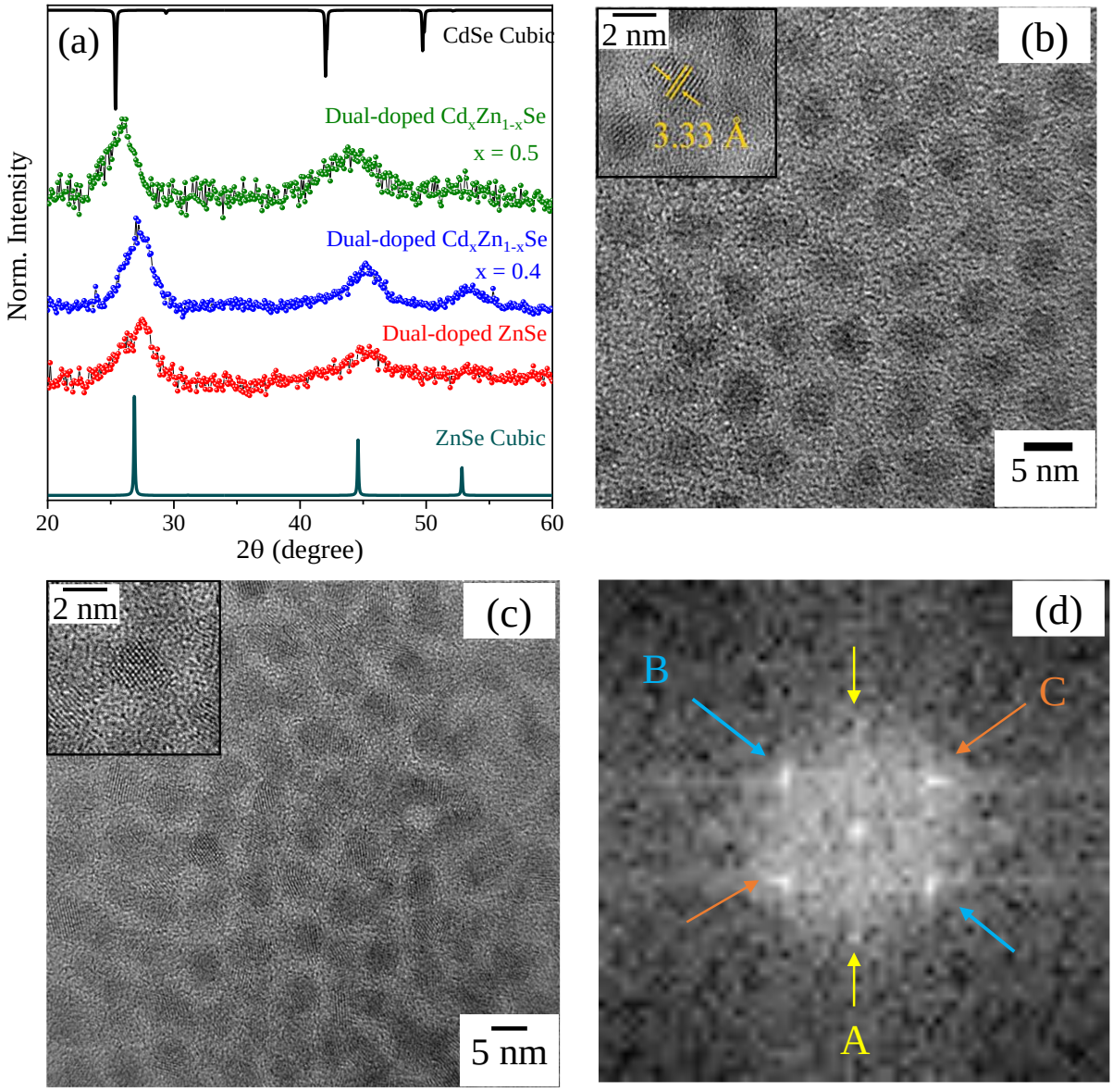

Figure 6.2. *(a) X-ray diffraction patterns of Cu, Mn dual-doped ZnSe (red) and $Cd_xZn_{1-x}Se$ QDs with increasing Cd content (blue and green) along with the ZnSe and CdSe bulk cubic patterns. TEM images of (b) dual-doped ZnSe and (c) dual-doped $Cd_xZn_{1-x}Se$ QDs. Corresponding HR-TEM images are shown in the inset to (b) and (c) respectively. (d) Fourier transform of dual-doped $Cd_xZn_{1-x}Se$ shows three distinct planes namely, $d(111)_{CdSe}$, $d(111)_{ZnSe}$ and $d(200)_{CdSe}$, marked as 'A', 'B', and 'C' respectively.*

TEM images of dual-doped ZnSe and $Cd_xZn_{1-x}Se$ QDs shown in Figure 6.2(b) and (c), respectively reveal the formation of uniformly distributed spherical particles with average size is about 5 nm. The size analysis is shown in Figure 6.3(a) and (b), respectively. Further analysis

of HRTEM images of doped ZnSe QDs, shown in inset to Figure 6.2(b), tells us that the interplanar spacing is about 3.33 Å which corresponds to 111 plane of cubic ZnSe. Similarly, HRTEM image of doped $Cd_xZn_{1-x}Se$ QDs (shown in inset to Figure 6.2(c)) and its analysis suggests that the $Cd_xZn_{1-x}Se$ QDs contain three major planes with d-spacing 3.58 Å, 3.38 Å and 3.05 Å marked as 'A', 'B', and 'C' shown in the corresponding Fourier transform in Figure 6.2(d). The first two nearly match with 111 plane of cubic CdSe and ZnSe respectively and the third plane corresponds to 200 plane of cubic CdSe. This analysis further suggests Cd alloying into the ZnSe crystal lattice.

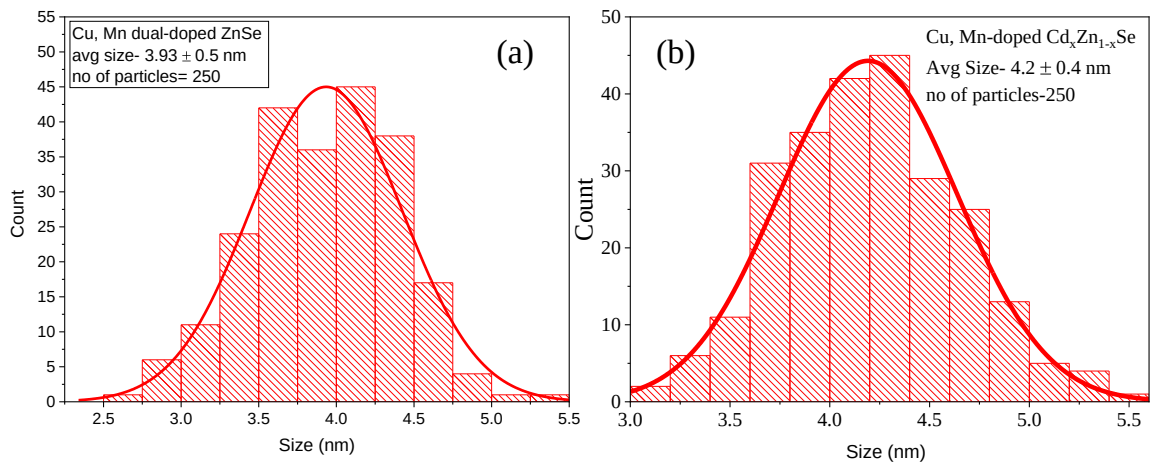

Figure 6.3. *Particle size distribution histogram of (a) Cu, Mn dual-doped ZnSe, and (b) Cu, Mn dual-doped CdxZn1-xSe QDs showing the average size of the QDs are 3.93 ± 0.5 nm, and 4.2 ± 0.4 nm respectively.*

Table 6.1. *The amount of incorporated Cd (x) in $Cd_xZn_{1-x}Se$ host NCs for different samples obtained from ICP-OES analysis*

Sample name	x value (fraction of Cd)
S1	0.10
S2	0.175
S3	0.31
S4	0.42
S5	0.44
S6	0.51

Percentages of incorporated dopants as well as the host cations were quantified using ICP-OES measurement. While, Mn percentage was found to be ~1-2 %, percentage of Cu appeared to be less than 1%. Percentage of host cations ranged from 0.1 % to 51 % of Cd and are tabulated in Table 6.1.

Further, the dual-doped ZnSe QDs were characterized spectroscopically using UV-visible and photoluminescence (PL) spectroscopy and a basic comparative study has been done between QDs doped with individual dopants and dual-doped QDs. Figure 6.4(a) shows the comparison plot of UV-visible spectra of singly-doped and dual-doped QDs. Cu-doped ZnSe shows 1s absorption peak at ~3.27 eV while the Mn-doped ZnSe and the dual-doped ZnSe two show the same at ~3.0 eV. This is probably due to the different nucleation temperature of ZnSe in case of Cu-doped ZnSe and MnSe in case of both Mn-doped ZnSe as well as dual-doped ZnSe QDs. In Figure 6.4(b), PL spectra of Mn-doped ZnSe consist of purely a characteristic orange emission at 2.12 eV arising from the $^4T_1 \rightarrow {}^6A_1$ transition of Mn^{2+} states. On the other hand, Cu-doped ZnSe shows a characteristic broad Cu emission peak at ~2.6 eV with blue-green emission along with the excitonic peak. When we incorporate these two dopants together into the same ZnSe host, we observe a broad three-peak emission feature covering the entire visible spectrum. In order to obtain the color of the emission, we input the spectrum to obtain a bright white light emission with Commission International d'Eclairage (CIE) coordinates (0.31, 0.35) as shown in the chromaticity diagram in Figure 6.4(c).

The decay profiles of Mn and Cu-related emission are presented in Figure 6.4(d), and (e) respectively. Decay dynamics of Mn emission in Mn-doped ZnSe QDs appears to be single exponential. However, addition of Cu increases the lifetime of Mn emission drastically with a very negligible initial fast component. While the calculated amplitude-average lifetime of spin forbidden Mn emission in Mn-doped ZnSe is ~245 μs, Mn emission in dual-doped ZnSe appears to be ~600 μs. Similarly, if we take a look at the Cu-related emission, an increase in Cu lifetime in dual-doped QDs (τ_{avg} = 52 ns) is observed as compared to Cu-doped ZnSe (τ_{avg} = 35 ns). These results suggest that the incorporation of two dopants creates two competitive decay channels. It is by now well observed that the Mn emission occurs due to the ultrafast excitation of the Mn d-states from its ground state to the excited state.[25-26] While the exact mechanism of excitation has been debated and probed in several earlier reports,[27] here we acknowledge the need to have both the photogenerated hole (PGH) and the photogenerated electron (PGE) to excite the Mn d-states. However, on the other hand, Cu emission is driven by the host absorption and requires the presence of only a PGE to obtain a radiative emission.

Hence it is imperative that the efficiency of the hole traps in capturing the PGH determines the overall shape of the spectrum. However, the fact that the lifetime of the Mn emission and the Cu emission increases on dual doping suggests the presence of interaction between the two dopants.

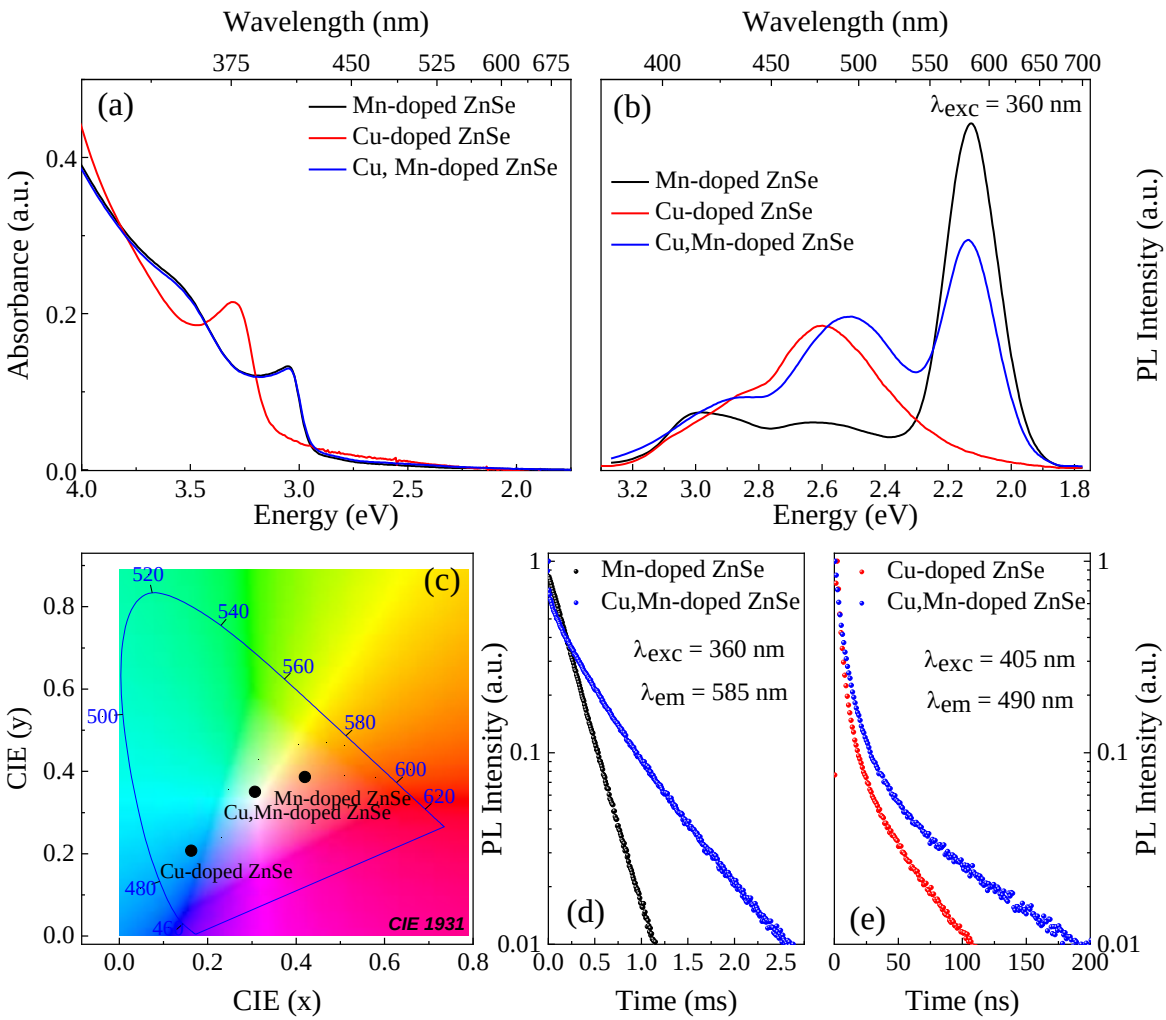

Figure 6.4. *Optical characterization of doped ZnSe QDs. (a) UV-visible, and (b) PL spectra of Mn-doped ZnSe (black), Cu-doped ZnSe (red), and Cu, Mn dual-doped ZnSe. (c) Chromaticity diagram showing the CIE co-ordinates for individually doped ZnSe as well as dual-doped ZnSe QDs. Comparative decay profile of (d) Mn emission and (e) Cu emission.*

To further confirm that both the dopants are incorporated in a single QD and that it is not a mixture of two individually doped QDs we investigate the same with several characterization techniques.

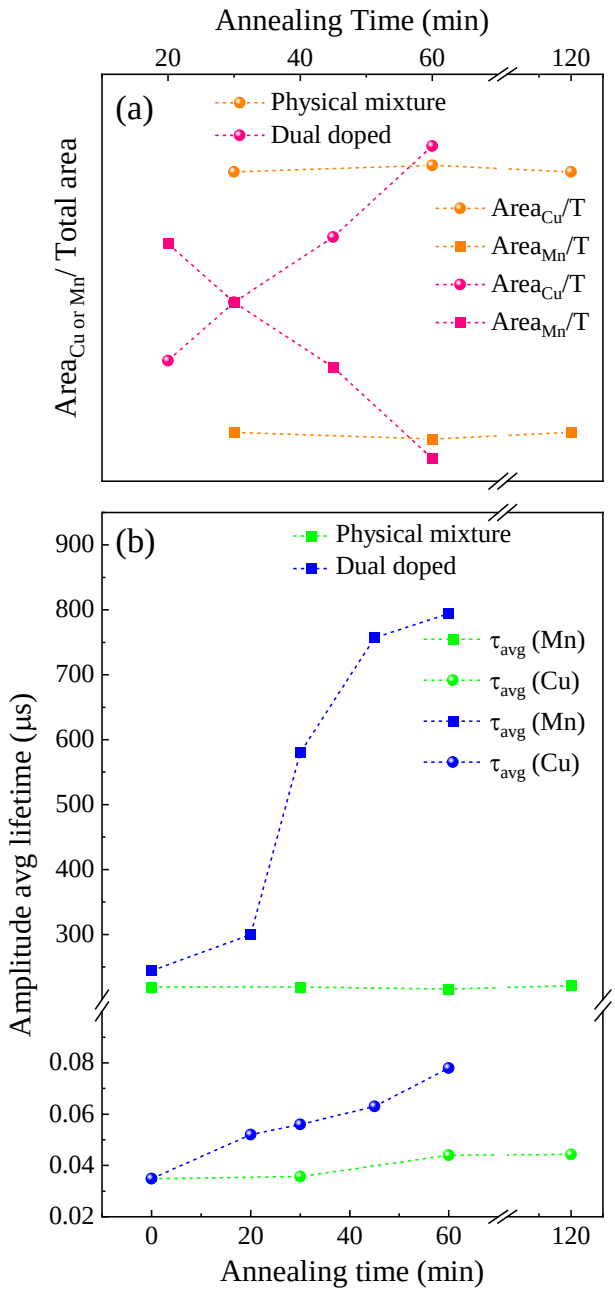

Figure 6.5. *(a) Relative ratio of area under dopant emission peaks (Cu in filled circles and Mn in filled squares) to the total area which actually quantifies the relative intensity ratio of dopant emission in case of both physical mixture of individually doped QDs (orange) and dual-doped QDs (pink). (b) amplitude-average lifetime of Cu (filled circles) and Mn (filled squares) emission of physical mixture of individually doped QDs (green) and dual-doped QDs (blue).*

First, we took the most conventional path by synthesizing Mn-doped ZnSe and Cu-doped ZnSe QDs individually followed by mixing them together. We then annealed the mixture

for a period of 2 hours at temperature as high as 180 °C. We chose the annealing temperature to be 180 °C because Cu is known to be expelled out of the QDs at higher temperature and we judiciously avoided the loss of any dopant ions to retain the electronic structure intact during the annealing process. Few aliquots were collected at different time interval during the annealing and their optical properties were measured.

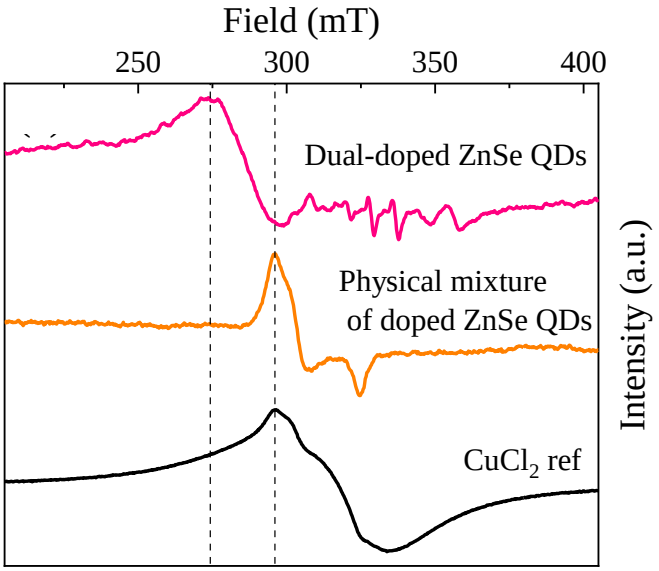

Figure 6.6. *EPR spectra of physical mixture of individually doped QDs (orange) and dual-doped QDs (pink) along with reference Cu salt.*

Steady state PL data were analyzed to track any changes during the process of annealing. The relative are ratio of two dopant emission peaks to the total area represents the relative probability of transition through the dopant channel and the same as a function of annealing time is shown in Figure 6.5(a). We compared the dual doped QDs with that of the physical mixture containing two dopants and observed the probability transition variation over a period of several minutes of annealing for both the cases. The relative intensity of Cu and Mn emission remains same in case of physical mixture of doped QDs for as long as 120 minutes. In contrast to that, Cu emission intensity is seen to be increasing at the cost of Mn emission just within 15-30 min of annealing in case of dual-doped QDs. In addition to that, time-resolved photoluminescence (TRPL) data shown in Figure 6.5(b) reveals that the average

lifetime of Cu and Mn emission show almost no change in annealed physical mixture, while in the dual-doped QDs both the dopant emission lifetime increase drastically, confirming the inclusion of both the dopants in a single dot and not just merely mixed.

Similarly, electron paramagnetic resonance (EPR) spectroscopic measurements were performed for both physical mixture of individual doped QDs as well as dual doped QDs, shown in Figure 6.6. Comparison of the EPR spectra suggests that there is no shift observed in Cu EPR line in case of mixed singly doped QDs as compared to $CuCl_2$ reference. However, a distinct Cu EPR line shift is observed in case of dual-doped QDs suggesting an interaction between dopant ions in dual-doped QDs especially when two dopants are present in a single QD.[28]

Once we confirm that the QDs are indeed dual-doped and the emission arises from a single source, we turn our attention to tuning of the color rendering. It is important to understand the electronic structure of the bulk and surface of the nanocrystal and its effect on the transition dynamics of the different emission bands to modulate the different bands and produce the white light to our demand. Hence in the subsequent sections, we discuss the effects of relative concentration of the dopants as well as the other ligands to modulate the dopant emission.

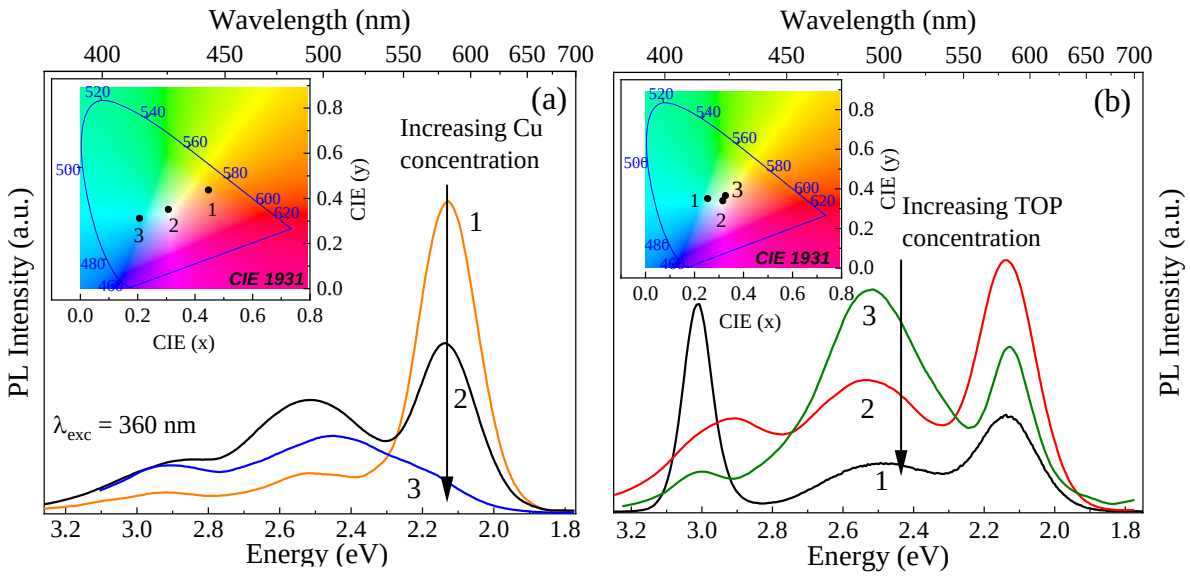

Figure 6.7. *PL spectra of Cu, Mn dual-doped ZnSe QDs as a function of (a) Cu concentration, and (b) TOP concentration. Corresponding chromaticity diagrams are in the inset to the figures showing the variation in white light emission.*

Cu, when doped into the intrinsic QDs, is known to introduce atomic like mid gap state in between valence band (VB) and conduction band (CB) that alters the whole decay dynamics of the QD system. Herein, we introduced Cu precursor in different stoichiometric ratio in the Mn doped QDs, as shown in Figure 6.7(a). Inclusion of Cu in Mn-doped ZnSe QDs results in appearance of a new blue-green emission band at around 2.50 eV (~495 nm) and with increase in the amount of Cu precursor we observe a steady increase of Cu emission intensity along with suppression of characteristic orange emission of Mn and the same is represented in the corresponding chromaticity diagram shown in the inset to Figure 6.7(a). The ICP-OES measurements reveal that the concentration of incorporated Cu remains almost constant, although we increase the stoichiometric percentage of the Cu precursor as shown in Table 6.2. However, quantum yield results show that although the overall quantum yield is initially maintained, upon excess of Cu precursor, we observe a decrease in the quantum yield as shown in Table 6.2. These result points towards the fact that initially more QDs are doped with Cu. When almost the entire fraction of QDs get doped with Cu increase in Cu precursor, some of the Cu^{2+} ions will be present at the surface (shallow trap states) which act as electron trap states and causes an overall reduction in the PL QY.

Table 6.2. *The stoichiometric percentages of Cu precursor, percentages of Cu ions incorporated into ZnSe host lattice for different samples and their quantum yield.*

Sample name	Stoichiometric Cu percentages	Cu percentages from ICP	Quantum yield (%)
Cu_1	1.5 %	1 %	20 %
Cu_2	3.0 %	1 %	22 %
Cu_3	4.5 %	1 %	9.5 %

Trioctylphosphine (TOP) is proven to be a very good solvent for selenium as well as good surface passivator of QDs, especially a good hole trap passivator in CdSe QDs. However, in addition to being a hole trap passivator, it is also known to create electron traps as observed from studying the Cu doped nanocrystals.[22, 29] This suggests the need to use TOP in moderation to increase the overall quantum yield. However, within the range of suitable concentrations

one can use different concentrations to amplify the required dopant emission in the case of dual-doped QDs. Figure 6.7(b) shows the PL spectra of QDs treated with different amount of TOP while their respective QYs are given in Table 6.3. When the highest amount of TOP is employed, we see more intense excitonic as well as Mn emission as compared to the Cu emission. However, due to new electron traps, the overall QY decreases. Upon varying the TOP amount, the emissions dynamics of these three emission peaks changes. The intensity of Cu emission gradually starts increasing while the other two reduces with respect to Cu with decrease in TOP concentration. These results suggest that TOP passivates hole traps present at the QD surfaces by getting attached to the uncoordinated selenium sites similar to the situation observed in Cu doped nanocrystals.[29] Thus, in the QDs with TOP concentrations in the range 0.25 mL to 0.5 mL retain high QY as well as assist in tuning the color of the white light emission as shown in the inset to Figure 6.7(b). CIE coordinates reveal that by varying the TOP concentration one can tune the electronic structure in such a way that different type of white light emission could be achieved.

Table 6.3. *Quantum yield of the dual-doped NCs with varying the TOP concentration*

Sample name	TOP amount (mL)	Quantum yield (%)
TOP_1	1.00 mL	18 %
TOP_2	0.50 mL	35 %
TOP_3	0.25 mL	32 %

Role of oleylamine is known to vary from system to system. For example, it passivates hole traps in CdSe QDs while it creates hole traps in CdS.[29] To examine the role of this amine further, we treated our dual-doped QDs with varying amount of oleylamine and the resulting PL spectra are shown in Figure 6.8(a). From the figure, we observe that while the relative intensities of the Cu to Mn is very similar to that of TOP, overall QY remains largely constant with increasing oleylamine concentration in the reaction. This suggests that oleylamine acts as a hole trap for ZnSe QDs. Due to additional hole traps, PL QY of the band edge emission and Mn emission decreases. However, since the electron traps are relatively unaffected, the overall QY is retained (shown in Table 6.4) changing only the chromaticity of the emission.

Corresponding chromaticity diagram ranging from neutral white to cool white by changing the oleylamine concentration is shown in the inset to Figure 6.8(a).

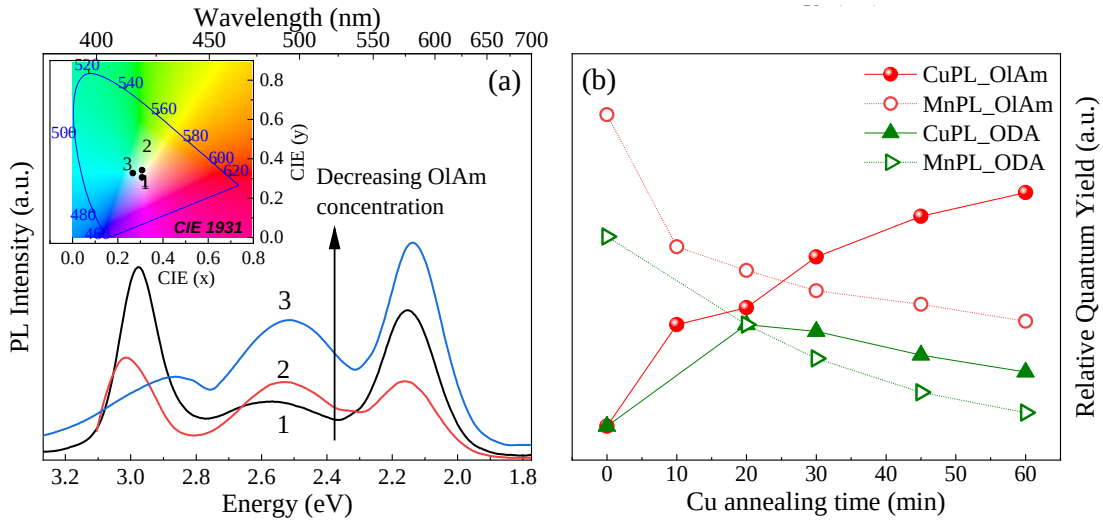

Figure 6.8. *(a) PL spectra of Cu, Mn dual-doped ZnSe QDs as a function of oleylamine concentration. Corresponding chromaticity diagrams are in the inset to the figures showing the variation in white light emission. (b) Relative quantum yield of Cu (filled shapes) and Mn-related (empty shapes) emission as a function of Cu annealing time when the dual-doped QDs were treated with oleylamine (red) and octadecylamine (green).*

Table 6.4. *Quantum yield of the dual-doped NCs with varying the oleylamine (OlAm) concentration*

Sample name	OlAm amount (mL)	Quantum yield (%)
OlAm_1	0.2 mL	26.0 %
OlAm_2	0.3 mL	26.5 %
OlAm_3	0.5 mL	28.0 %

However, the role of amines is complicated and cannot be easily extrapolated to other amines as well as to other hosts. For example, we saw that the oleylamine creates hole traps but largely does not affect the electron traps, we observe very different behavior with the

octadecylamine (ODA). We introduced the Cu dopant and annealed the sample for long time and collected the samples at different intervals of time. However, we observe a substantial change in the relative quantum yield (QY) of the dual-doped samples as shown in Figure 6.8(b). Unlike oleylamine, in the case of ODA, the Cu emission grows at the cost of Mn emission only for the first 15 minutes of annealing. Subsequently, it is evident that the overall QY of the sample is decreasing. Since oleylamine does not affect the electron traps the overall QY remains constant and as more Cu gets incorporated with increasing annealing time, we observe an intensification of Cu emission. However, in case of ODA treatment, there is a drop in overall PLQY suggesting that ODA also creates electron traps along with creating hole traps.

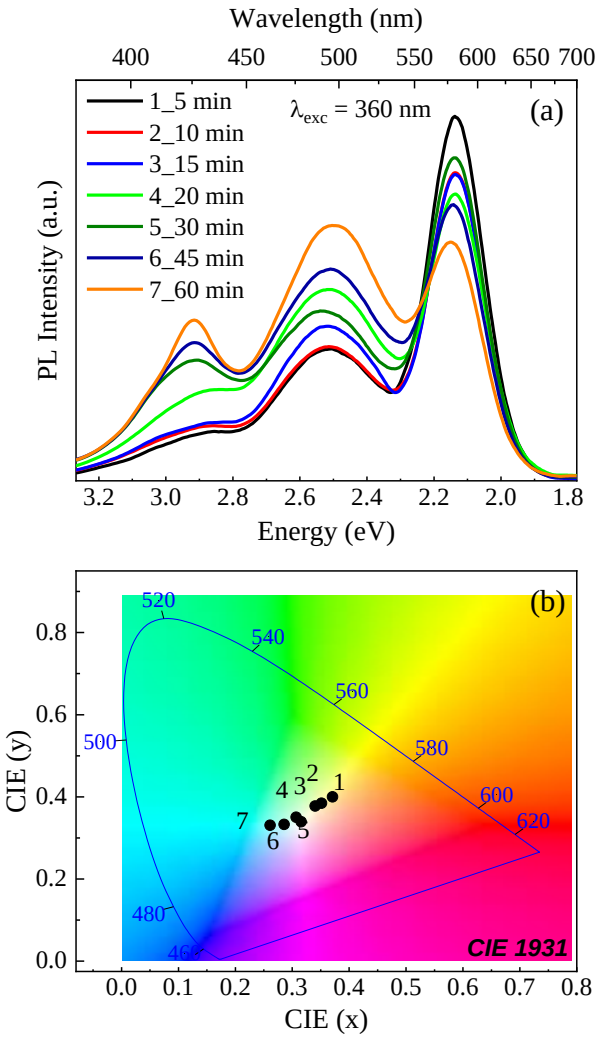

Figure 6.9. *(a) PL spectra of Cu, Mn dual-doped ZnSe QDs as a function Cu annealing time and, (b) corresponding chromaticity diagram shows the gradual shift in CIE coordinates from warm white to neutral white to cool white.*

Having optimized the ligand concentration, we study the effect of annealing time on the QY as well as the chromaticity of the nanocrystals. Figure 6.9(a) shows the contrast of Cu and Mn emission intensity which suggests that initially when concentration of Cu dopants is less, Mn emission dominates and emits warm white light shown in corresponding chromaticity diagram in Figure 6.9(b).

However, when large extent of Cu is incorporated, Cu emission starts dominating over yellow-orange Mn emission and nature of white light shifts from warm to neutral to cool white, marked from 1 to 7, as shown in Figure 6.9(b). Additionally, it was also observed that the overall QY changed very minimally after about 15 minutes of annealing (shown in Table 6.5) providing a path to tune the chromaticity of the white light emission. Further two important parameters that play an important role for the effectiveness of the LED is its stability as a function of temperature and excitation light. Hence, we perform these two studies and the resulting PL spectra and relative quantum yields are shown in Figure 6.10 and 6.11 respectively. From the figure, it is evident that the relative quantum yield of the white light emitting dual-doped QDs does not show any significant reduction with increasing temperature up to 350 K. Similarly, the QDs are significantly robust under continuous excitation and the quantum yield is unaltered in the time frame of our study (up to 50 minutes) as shown in figure 6.10.

Table 6.5. *Quantum yield of the dual-doped ZnSe QDs as a function of annealing time.*

Sample name with annealing time	Quantum yield (%)
1_5 min	19.5 %
2_10 min	19 %
3_15 min	18 %
4_20 min	22 %
5_30 min	23 %
6_45 min	24 %
7_60 min	26 %

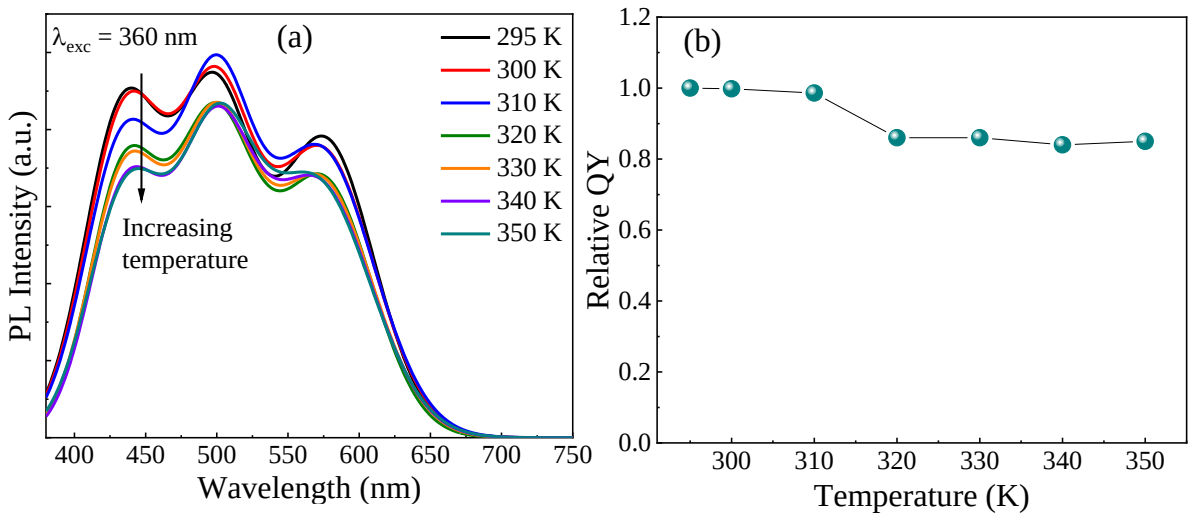

Figure 6.10. *(a) PL spectra of Cu, Mn dual-doped ZnSe QDs as a function of temperature higher than room temperature, and (b) their relative quantum yields.*

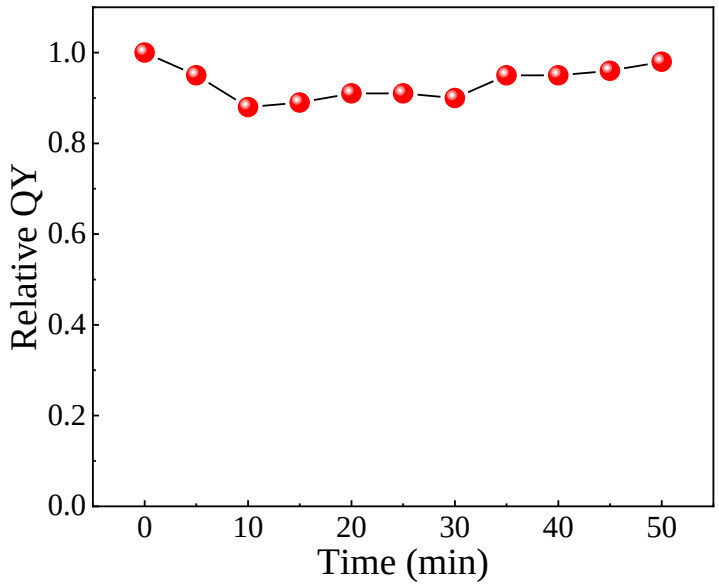

Figure 6.11. *Relative quantum yield of Cu, Mn dual-doped ZnSe QDs as a function of the time duration of continuous excitation.*

Further we altered the host electronic structure by varying the composition of the host to achieve the variation of chromaticity with optimal QY. Since we have observed emission due to Cu dopants to be the dominating one in the optimal case, variation of composition will provide us further emission tunability starting from cool white to blue and up to orange. After the formation of white light emitting Cu, Mn dual-doped ZnSe QDs, we further incorporated Cd into the host to synthesize dual-doped alloyed $Cd_xZn_{1-x}Se$ QDs. The PL spectra of dual

doped $Cd_xZn_{1-x}Se$ QDs with increasing Cd concentration are represented in Figure 6.12(a) and with increase in the Cd concentration, we observe that the three peak structure appears to be a single broad peak covering the entire visible spectrum. Corresponding digital images are shown in Figure 6.12(b). The top panel shows (from left to right) the yellow-orange emission of Mn-ZnSe followed by warm white to cool white emission of dual-doped ZnSe and further tunable color ranging from blue to orange arising out of Cd alloying into dual-doped ZnSe. The bottom panel shows the digital image of orange emitting Mn-doped ZnSe (extreme left), blue-green emitting Cu-doped ZnSe (extreme right) and pure white light emitting Cu, Mn dual-doped ZnSe (middle) QDs demonstrating the variation in chromaticity with good QY for the material.

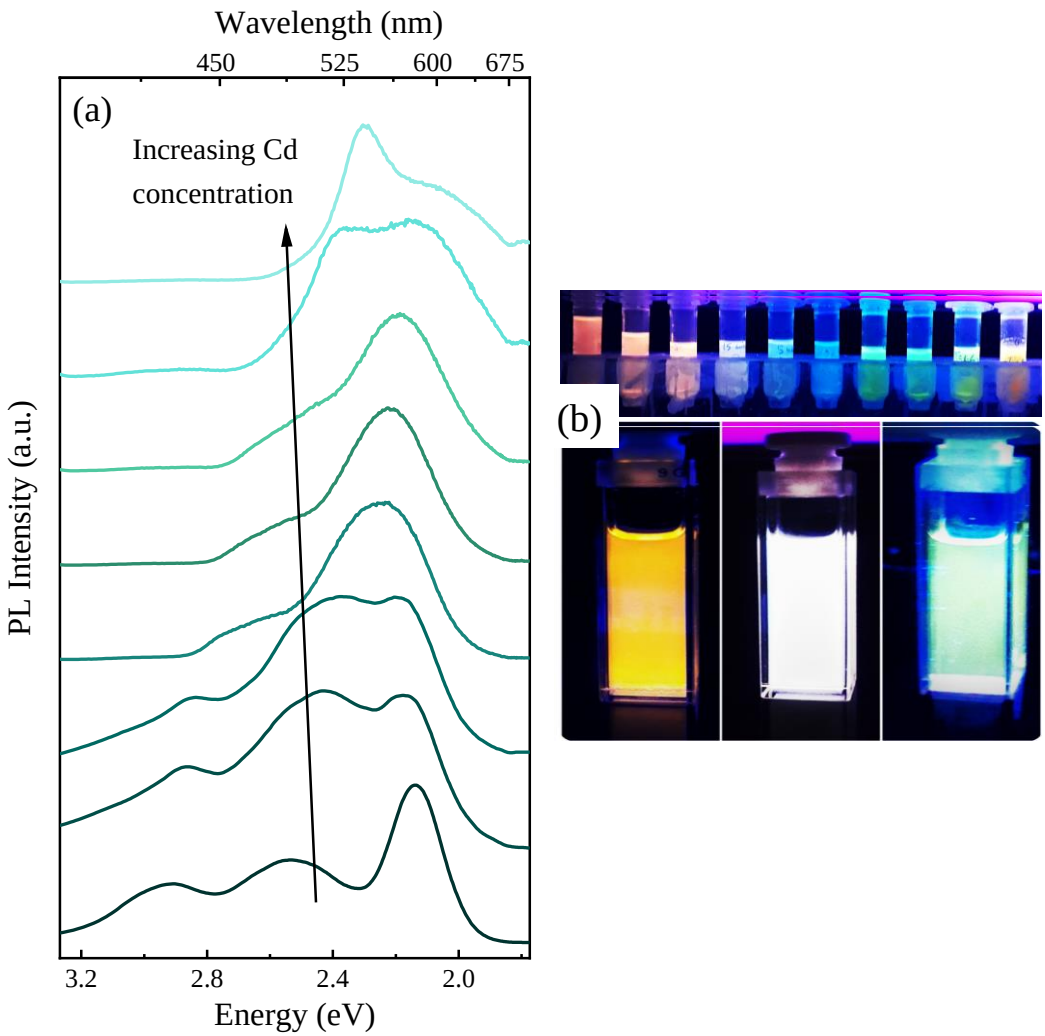

Figure 6.12. *(a) Evolution of steady state PL spectra with increasing Cd content and, (b) digital photographs of dual-doped QDs showing tunable emission including white light.*

6.5. Conclusion

In conclusion, we proposed a facile and robust synthetic method for preparing white light emitting Cu, Mn dual-doped ZnSe QDs and synthesized the same and proved that the QDs are indeed doped with both the dopants simultaneously from the perspective of both ensemble as well as single-particle study. We further explored the host electronic structure and role of surface passivating ligands in altering the electronic structure in details in order to attain very high reproducibility of the white light emitting materials to meet the global demand of solid-state light sources. Further, we altered the host electronic structure by incorporating another host component to attain tunable emission. Thus, we have synthesized a series of QDs with different types of white light emission as well as QDs with tunable emission ranging from blue to orange. These materials will be of great interest in the field of lighting applications especially in light emitting devices.

Bibliography

1. Rogach, A. L.; Gaponik, N.; Lupton, J. M.; Bertoni, C.; Gallardo, D. E.; Dunn, S.; Li Pira, N.; Paderi, M.; Repetto, P.; Romanov, S. G., Light-Emitting Diodes with Semiconductor Nanocrystals. *Angew. Chem. Int. Ed.* **2008**, *47*, 6538-6549.

2. Demir, H. V.; Nizamoglu, S.; Erdem, T.; Mutlugun, E.; Gaponik, N.; Eychmüller, A., Quantum Dot Integrated Leds Using Photonic and Excitonic Color Conversion. *Nano Today* **2011**, *6*, 632-647.

3. Alivisatos, A. P., Semiconductor Clusters, Nanocrystals, and Quantum Dots. **1996**, *271*, 933-937.

4. Resch-Genger, U.; Grabolle, M.; Cavaliere-Jaricot, S.; Nitschke, R.; Nann, T., Quantum Dots Versus Organic Dyes as Fluorescent Labels. *Nature methods* **2008**, *5*, 763-775.

5. Kim, J. Y.; Voznyy, O.; Zhitomirsky, D.; Sargent, E. H., 25th Anniversary Article: Colloidal Quantum Dot Materials and Devices: A Quarter-Century of Advances. *Adv. Mater.* **2013**, *25*, 4986-5010.

6. Anikeeva, P. O.; Halpert, J. E.; Bawendi, M. G.; Bulović, V., Electroluminescence from a Mixed Red− Green− Blue Colloidal Quantum Dot Monolayer. *Nano Lett.* **2007**, *7*, 2196-2200.

7. Li, Y. Q.; Rizzo, A.; Cingolani, R.; Gigli, G., Bright White-Light-Emitting Device from Ternary Nanocrystal Composites. *Adv. Mater.* **2006**, *18*, 2545-2548.

8. Rizzo, A.; Mazzeo, M.; Biasiucci, M.; Cingolani, R.; Gigli, G., White Electroluminescence from a Microcontact-Printing-Deposited CdSe/ZnS Colloidal Quantum-Dot Monolayer. *Small* **2008**, *4*, 2143-2147.

9. Chen, B.; Zhong, H.; Wang, M.; Liu, R.; Zou, B. J. N., Integration of $CuInS_2$-Based Nanocrystals for High Efficiency and High Colour Rendering White Light-Emitting Diodes. *Nanoscale* **2013**, *5*, 3514-3519.

10. Yuan, X.; Hua, J.; Zeng, R.; Zhu, D.; Ji, W.; Jing, P.; Meng, X.; Zhao, J.; Li, H., Efficient White Light Emitting Diodes Based on Cu-Doped ZnInS/ZnS Core/Shell Quantum Dots. *Nanotechnology* **2014**, *25*, 435202.

11. Jang, E.; Jun, S.; Jang, H.; Lim, J.; Kim, B.; Kim, Y., White-Light-Emitting Diodes with Quantum Dot Color Converters for Display Backlights. *Adv. Mater.* **2010**, *22*, 3076-3080.

12. Sapra, S.; Mayilo, S.; Klar, T. A.; Rogach, A. L.; Feldmann, J., Bright White-Light Emission from Semiconductor Nanocrystals: By Chance and by Design. *Adv. Mater.* **2007**, *19*, 569-572.

13. Shen, C. C.; Tseng, W. L., One-Step Synthesis of White-Light-Emitting Quantum Dots at Low Temperature. *Inorg. Chem.* **2009**, *48*, 8689-8694.

14. Nag, A.; Sarma, D. D., White Light from Mn^{2+}-Doped Cds Nanocrystals: A New Approach. *J. Phys. Chem. C* **2007**, *111*, 13641-13644.

15. Sharma, V. K.; Guzelturk, B.; Erdem, T.; Kelestemur, Y.; Demir, H. V.; Interfaces, Tunable White-Light-Emitting Mn-Doped ZnSe Nanocrystals. *ACS Appl. Mater. Interfaces* **2014**, *6*, 3654-3660.

16. Yuan, X.; Ma, R.; Zhang, W.; Hua, J.; Meng, X.; Zhong, X.; Zhang, J.; Zhao, J.; Li, H. J.; Interfaces, Dual Emissive Manganese and Copper Co-Doped Zn–In–S Quantum Dots as a Single Color-Converter for High Color Rendering White-Light-Emitting Diodes. *ACS Appl. Mater. Interfaces* **2015**, *7*, 8659-8666.

17. Nurmikko, A., What Future for Quantum Dot-Based Light Emitters? *Nat. Nanotechnol* **2015**, *10*, 1001-1004.

18. Saha, A.; Makkar, M.; Shetty, A.; Gahlot, K.; A. R, P.; Viswanatha, R., Diffusion Doping in Quantum Dots: Bond Strength and Diffusivity. *Nanoscale* **2017**, *9*, 2806-2813.

19. Pradhan, N.; Peng, X., Efficient and Color-Tunable Mn-Doped ZnSe Nanocrystal Emitters: Control of Optical Performance Via Greener Synthetic Chemistry. *J. Am. Chem. Soc.* **2007**, *129*, 3339-3347.

20. Pradhan, N.; Goorskey, D.; Thessing, J.; Peng, X., An Alternative of CdSe Nanocrystal Emitters: Pure and Tunable Impurity Emissions in ZnSe Nanocrystals. *J. Am. Chem. Soc.* **2005**, *127*, 17586-17587.

21. Viswanatha, R.; Brovelli, S.; Pandey, A.; Crooker, S. A.; Klimov, V. I., Copper-Doped Inverted Core/Shell Nanocrystals with "Permanent" Optically Active Holes. *Nano Lett.* **2011**, *11*, 4753-4758.

22. Grandhi, G. K.; Tomar, R.; Viswanatha, R., Study of Surface and Bulk Electronic Structure of II–VI Semiconductor Nanocrystals Using Cu as a Nanosensor. *ACS Nano* **2012**, *6*, 9751-9763.

23. Sarkar, S.; Guria, A. K.; Patra, B. K.; Pradhan, N., Synthesis and Photo-Darkening/Photo-Brightening of Blue Emitting Doped Semiconductor Nanocrystals. *Nanoscale* **2014**, *6*, 3786-3790.

24. Chen, D.; Viswanatha, R.; Ong, G. L.; Xie, R.; Balasubramaninan, M.; Peng, X., Temperature Dependence of "Elementary Processes" in Doping Semiconductor Nanocrystals. *J. Am. Chem. Soc.* **2009**, *131*, 9333-9339.

25. Gahlot, K.; K.R, P.; Camellini, A.; Sirigu, G.; Cerullo, G.; Zavelani-Rossi, M.; Singh, A.; Waghmare, U. V.; Viswanatha, R., Transient Species Mediating Energy Transfer to Spin-Forbidden Mn d States in II–VI Semiconductor Quantum Dots. *ACS Energy Lett.* **2019**, *4*, 729-735.

26. Chen, H.-Y.; Maiti, S.; Son, D. H., Doping Location-Dependent Energy Transfer Dynamics in Mn-Doped CdS/ZnS Nanocrystals. *ACS Nano* **2012**, *6*, 583-591.

27. KR, P.; Viswanatha, R., Mechanism of Mn Emission: Energy Transfer Vs Charge Transfer Dynamics in Mn-Doped Quantum Dots. *APL Mater.* **2020**, *8*, 020901.

28. Bales, B. L.; Meyer, M.; Smith, S.; Peric, M., Epr Line Shifts and Line Shape Changes Due to Spin Exchange of Nitroxide Free Radicals in Liquids: 6. Separating Line Broadening Due to Spin Exchange and Dipolar Interactions. *J. Phys. Chem. A* **2009**, *113*, 4930-4940.

29. Grandhi, G. K.; Viswanatha, R., Understanding the Role of Surface Capping Ligands in Passivating the Quantum Dots Using Copper Dopants as Internal Sensor. *J. Phys. Chem. C* **2016**, *120*, 19785-19795.

Chapter 7

Synthesis and Study of Ultrafast Carrier Dynamics in Mn, Fe Dual-Doped CdS Quantum Dots

7.1. Abstract

Manganese is one of the optically active transition metal dopants whose emission properties and mechanisms are widely studied in the literature. However, the modulation of Mn-related emission in presence of other impurity remains largely unexplored due to the lack of proper host-dopant modeling and stable dual-doped nanostructures. Here, in this work, we modeled a nanocrystal (NC) system namely Mn, Fe dual-doped CdS where Fe^{2+} ions were introduced into the already nucleated Mn-doped CdS NCs. Analysis of extended x-ray absorption fine structure (EXAFS) data confirms the successful incorporation of both the dopants into the CdS matrix. Photoluminescence (PL) measurements show a significant decrease in Mn-related emission intensity including the decay lifetime even when a very small amount of Fe^{2+} is incorporated. To gain fundamental insights into this optical perturbation, we study the excited-state charge carrier dynamics using femtosecond (fs) transient absorption (TA) spectroscopy. Our findings reveal that the trapping of charge carriers by Fe^{2+} levels in presence of Mn^{2+} is not as efficient as in the case of Fe-doped CdS leading to partial quenching of Mn emission in Mn, Fe dual-doped CdS.

7.2. Introduction

Doping impurities into semiconductor quantum dots (QDs) is the principal strategy to impart and modulate new photophysical properties toward their potential optoelectronic applications.[1-3] Especially, doping Mn^{2+} into the wide bandgap semiconductors has garnered enormous attention due to their distinctive PL behavior such as large stokes shifted intense PL, substantially longer lifetime of Mn-related emission in the order of a few milliseconds (ms) arising due to the spin-forbidden $^4T_1 \rightarrow {}^6A_1$ transition.[4-6] These extraordinary PL features potentially enable many applications in the field of photovoltaics, sensors, luminescent solar concentrators, etc.[7-12] Although Mn^{2+}-doped metal chalcogenide semiconductor quantum dots (QDs) have been extensively studied to understand the fundamental photophysics of Mn emission, less effort has been made in understanding the influence of other impurity ions on Mn emission. To date, there are a few reports on doping impurity ions like Cu^{2+}, Ni^{2+}, Ag^{+} into Mn^{2+}-doped QDs in the literature,[13-15] and among the various impurities, Fe^{2+} has been effectively employed in a few cases to modify the intrinsic behavior of the host NCs.[16-17] For instance, the incorporation of Fe^{2+} into CdS QDs caused a complete quenching of intrinsic PL of the host.[16] Thus, it would be interesting to study the co-existence of Fe^{2+} and Mn^{2+} in the same host, influencing each other. Although Fe^{2+} has been reported to be co-doped with Mn^{2+} in metal chalcogenide semiconductors like ZnSe nanowires and nanobelts,[18-19] the reports

majorly focused on their magnetic behaviors. While studying optical properties, Kim et al. reported that Fe, Mn dual-doping in a ZnS nanostructure resulted in a distinct Fe^{2+}-induced emission along with the characteristic yellow-orange Mn emission.[19] Contrary to that, Fe^{2+} was found to lower the Mn emission intensity in another report[20] without any distinct Fe^{2+}-emission feature. Thus, the influence of Fe^{2+} impurities on the Mn emission behavior is still elusive and a detailed understanding of the same is essential, especially, in the exciton dynamics and efficiency of dopant emission.

In our study, we chose a very simple metal-chalcogenide host CdS and co-doped it with Mn^{2+} and Fe^{2+}impurities. Analysis of extended x-ray absorption fine structure (EXAFS) data confirms the successful incorporation of both the dopants into the host matrix. With the help of femtosecond (fs) TA spectroscopy, we probe the carrier relaxation pathways involving the vibrational energy levels. This excited state carrier dynamics and EXAFS analysis provide a detailed insight into the emission behavior of dual-doped QDs. Our study reveals that Fe^{2+}, a PL quencher in the case of undoped CdS, can only partially quench Mn PL due to inefficient carrier trapping in presence of Mn^{2+}.

7.3. Experimental methods

7.3.1. Materials

Cadmium oxide (CdO), iron acetylacetonate ($Fe(acac)_2$), 1-octadecene (ODE, 90%), oleylamine (technical grade, 70%), oleic acid (technical grade, 90%), and sulfur powder (S, 99.5%) were purchased from Sigma Aldrich. Manganous chloride AR ($MnCl_2$), and stearic acid LR were purchased from SD Fine chemicals. Tetramethylammonium hydroxide pentahydrate (TMAH, 98%) was purchased from Spectrochem. Methanol, acetone, and hexane were purchased from Merck. All purchased chemicals were used without further purification.

7.3.2. Synthesis of the precursors

Cadmium oleate, a precursor for the synthesis of CdS host NCs was synthesized using cadmium oxide salt. Oleic acid and 1-octadecene were used as coordinating solvents. To synthesize 0.2 M cadmium oleate, a mixture of 0.3204 g of cadmium oxide, 9 mL of 1-ODE, and 7 mL of oleic acid was degassed at 80 ^{o}C and then heated to 200-240 ^{o}C under continuous argon flow until all the precursors were completely dissolved and a transparent colorless solution was obtained. It was then cooled down to room temperature.

Iron oleate was used as iron precursor for doping iron into the CdS host. 0.2 M iron oleate was synthesized following the method similar to cadmium oleate, where a mixture of 0.378 mg of iron acetylacetonate, 9 mL of 1-ODE, and 7 mL of oleic acid was degassed at 80 ^{o}C followed by heating the same to 250 ^{o}C until the solution appeared transparent brown under argon atmosphere.

Manganese stearate ($MnSt_2$) was synthesized by the method mentioned in the literature.[21] Briefly, stearic acid (20 mmol) was dissolved in methanol and added to a TMAH-methanol solution of similar concentration, and stirred for 20 min. Meanwhile, 10 mmol manganous chloride was dissolved separately in methanol and added dropwise to the above-mentioned mixture with constant stirring. The appearance of white precipitate shows the formation of $MnSt_2$. The solution was washed repeatedly with methanol followed by acetone to remove excess precursors and then dried in a vacuum.

S-ODE, which is used as sulfur precursor for the synthesis of CdS host, was synthesized using powder of elemental sulfur and 1-ODE as solvent.[22] To synthesize 0.2 M S-ODE, 65 mg of sulfur powder and 10 mL of 1-octadecene (ODE) were taken in a vial. Then the mixture was degassed at room temperature for 15-20 minutes followed by sonication/heating under argon atmosphere for the complete dissolution of sulfur and to obtain a clear solution.

7.3.3. Synthesis of the doped and undoped NCs

Synthesis of Mn, Fe dual-doped CdS

Mn, Fe dual-doping in the CdS matrix was performed following two steps. First, Mn-doped CdS NCs were synthesized using the diffusion doping method[22] described in chapter 5 followed by the incorporation of Fe^{2+} into already grown Mn-doped CdS NCs. 0.03 g of $MnSt_2$ was taken in a three-necked flask with 8 ml of ODE and degassed at 80 °C. Meanwhile, 0.5 ml of 0.2 M S/ODE solution was mixed with 0.2 g of ODA and further diluted with 1 ml of ODE in a vial. The temperature was then raised to 240 °C under the Ar-atmosphere, and the precursor solution S/ODA/ODE was quickly injected followed by quenching of the reaction to 140 °C forming the manganous-sulfide (MnS) core.

Next, 0.2 M cadmium oleate and 0.2 M S-ODE were used as precursors to grow the CdS monolayers over these transition metal sulfide cores. The successive ionic layer adsorption reaction (SILAR) technique[23] was for the same at an annealing temperature of 140 °C. The cycle of Cd followed by S precursor addition was continued until Mn is uniformly diffused into the CdS matrix. After a few monolayers were grown, iron oleate diluted in ODE was added

dropwise and annealed while the further growth of CdS monolayers was continued. This is to make sure that Fe is also doped into the CdS lattice uniformly leading to the formation of Mn, Fe dual-doped CdS NCs.

Undoped CdS NCs were synthesized under similar experimental conditions without using any metal sulfide core. CdS was nucleated first at 240 °C followed by the growth of CdS monolayers at 140 °C using the SILAR technique as discussed above.

7.3.4. Characterization

The NCs were characterized using x-ray diffraction (XRD), transmission electron microscopy (TEM), and optical measurements. Powder XRD patterns of doped NCs were recorded on a Bruker D8 Advance diffractometer using Cu-Kα radiation (1.5418 Å). TEM was performed on a JEOL JEM-3010 electron microscope, using a field emission gun (FEG) operating at an accelerating voltage of 200 kV in bright field mode using Cu-coated holey carbon TEM grids. Absorption spectra of samples were recorded using an Agilent 8453 UV visible spectrometer. Steady-state PL spectra were collected using the 450 W xenon lamp as the source on the FLSP920 spectrometer, Edinburgh Instruments, while the PL lifetime measurements were carried out in the same instrument using EPL-405 pulsed diode laser as the excitation source (λ_{ex} = 405 nm).

Ultrafast transient absorption measurements were performed by an amplified Ti:Sapphire laser (Coherent Libra) generating 100-fs pulses at 800 nm and 2 kHz repetition rate. Pump pulses at 400 nm were generated by frequency doubling the fundamental wavelength by a 2-mm-thick β-barium borate crystal; they were modulated at 1 kHz by a mechanical chopper and focused in a spot of (400x180) μm^2 on samples dispersed in hexane. UV-visible probe pulses were produced by white light supercontinuum generation focusing a part of the fundamental beam in a calcium fluoride plate. Chirp-free differential transmission spectra $\Delta T/T = (T_{on} - T_{off})/ T_{off}$, T_{on} and T_{off} being the transmission of the probe through the perturbed and unperturbed samples were acquired at different pump-probe delays by a fast optical multichannel analyzer operating at the full laser repetition rate. The temporal resolution of the setup is ~100 fs. All the measurements were carried out at room temperature.

EXAFS measurements were carried out in P64 beamline in DESY Photon Science, Germany. All spectra were collected at fluorescence mode in an ion chamber. Pt mirror was used to eliminate photons of higher energy for Cd edge measurement.

Data were processed using the software *Athena*[24] plotting the EXAFS oscillation in momentum (k) space as a function of photoelectron momentum (or, wavenumber) k and then Fourier transforming in position (R) space through a Hanning window for visual representation of the bond-lengths involved in the system, which were analyzed with the software *Artemis*[25] to get quantitative information about the local environment of the NCs. Throughout the analysis, the theoretical standards to which the experimental data were fitted, were generated from FEFF6[26] built into *Artemis*.

7.4. Results and discussion

Mn, Fe dual-doped CdS NCs were synthesized using the colloidal method via successive ion layer adsorption and reaction (SILAR) technique. The details of the synthesis and structural characterization are mentioned above in the methods section.

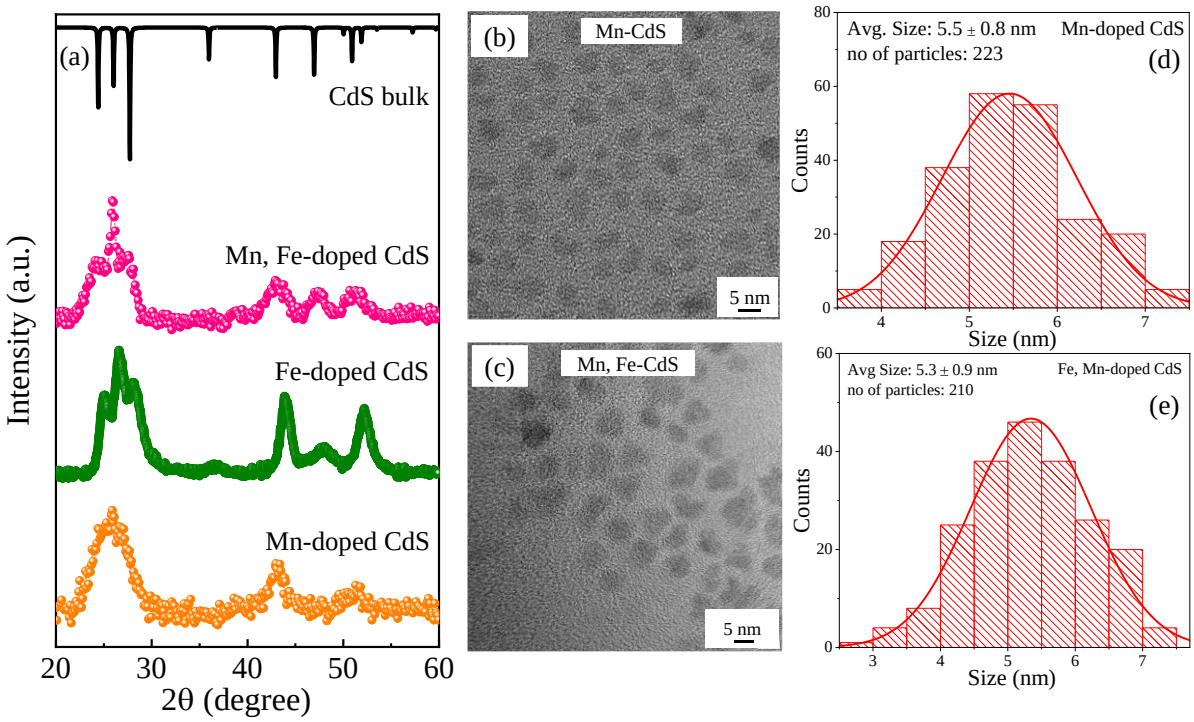

Figure 7.1. *(a) X-ray diffraction pattern of individual Mn-doped (orange), Fe-doped (green), and Mn, Fe dual-doped (pink) CdS nanocrystals along with bulk hexagonal pattern (Black). TEM images of (b) Mn-doped, (c) Mn, Fe dual-doped NCs show uniform distribution of spherical particles and their corresponding particle size distribution histogram (d) and (e), respectively.*

The formation of the QDs was characterized by X-ray diffraction pattern (XRD) and transmission electron microscopy (TEM) as shown in Figure 7.1(a). XRD patterns demonstrate the formation of hexagonal ($P6_3mc$) structure without any impurity upon comparing the doped QDs with that of the bulk CdS pattern obtained from the inorganic crystal structure database (ICSD). Broadening of XRD peaks reveal the formation of small-sized particle, consistent with the TEM image shown in Figures 7.1(b), and the respective histogram in Figure 7.1(c). A comparison of dual-doped CdS with that of individual Mn-doped CdS shows that the incorporation of Fe into Mn-doped CdS lattice does not alter the crystal structure and size of the QDs (TEM image and the corresponding histogram of Mn-doped CdS is shown in Figure 7.1(d), and 7.1(e) respectively).

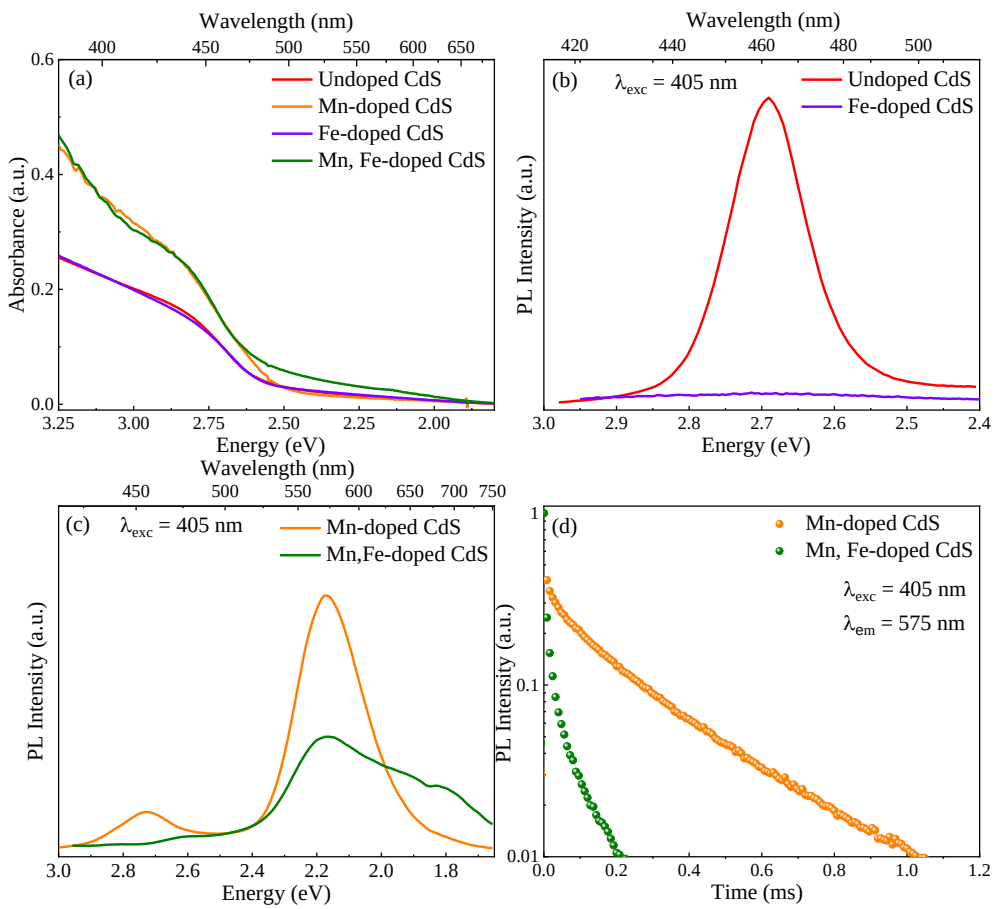

Figure 7.2. *(a) UV-vis absorption spectra of undoped (red), Mn-doped (orange), Fe-doped (violet), and Mn, Fe dual-doped (green) CdS QDs showing their respective bandgaps. (b) PL comparison of undoped and Fe-doped CdS shows a complete emission quenching upon the addition of Fe. Reduction in (c) PL intensity and (d) PL lifetime of Mn-related emission in Mn, Fe dual-doped CdS QDs.*

The optical properties of QDs were studied using UV-visible and steady-state PL spectroscopy. UV-visible spectra of the QDs show absorption onset at their respective bandgap energies as shown in Figure 7.2(a). The steady-state PL measurements show that the introduction of Fe^{2+} into undoped CdS causes a complete quenching of intrinsic PL as shown in Figure 7.2(b), similar to earlier literature.[16] When the same Fe^{2+} is introduced to Mn-doped CdS, it reduces the Mn emission intensity by a few folds causing a reduction in the photoluminescence quantum yield (PLQY). However, interestingly, complete quenching of PL does not occur in this case, unlike undoped CdS as shown in Figure 7.2(c). Also, we observe a decrease in the average lifetime of Mn-related emission upon the addition of Fe^{2+} as shown in Figure 7.2(d). The PLQY is found to be lowering from 47% in Mn-doped CdS to 13% in dual-doped CdS.

Since doping of Fe^{2+} does not evolve any new emission feature, simple optical characterization cannot precisely confirm the incorporation of Fe^{2+} into the host lattice. Thus, we performed X-ray absorption spectroscopic analysis, with emphasis on the EXAFS region, to obtain the local environment around the Fe and Mn ions with respect to the Cd environment by studying the Fe K_α state and the Mn K_α state. Our study focuses on studying the local environment around the Fe and the Mn ions within the first coordination shell. The real space data, $\chi(R)$, of the Fe and Mn K-edge obtained by Fourier transforming the k^3-weighted $\chi(k)$ are shown as black empty circles in Figure 7.3(a) and 7.3(b), respectively, while the thick black lines show the fit to the experiment. The fit was obtained by introducing the expected paths. The component paths are shown as dotted lines in the figure, while the detailed fitting parameters obtained from the fit are tabulated in Table 7.1. As shown in the fitting summary in Table 7.1, the first nearest neighbor of metal dopants (S) is coordinated to nearly 4 in both cases suggests that the doping is substitutional where metal dopants substitute the Cd atoms and sit at the Cd sites of the lattice. The dopant_K edge spectra are dominated by a single peak around 1.6-1.8 Å. The data suggests that the first coordination sphere contains majorly M-S interaction; however, to obtain reasonable fits, each data set required the introduction of an M-X path via *quick shell fit*, wherein the X is an element with a lower atomic number like oxygen or nitrogen accounting for the fact that some of the dopant atoms are near the surface and hence coordinated with ligands.

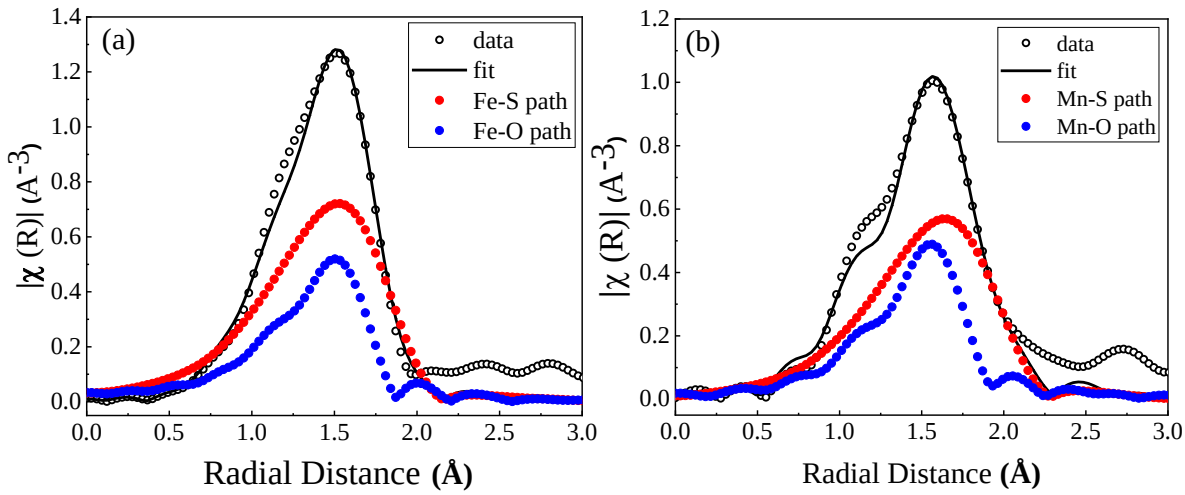

Figure 7.3. *The magnitude of Fourier-transformed (a) Fe K-edge and (b) Mn K-edge EXAFS spectra (black empty circles) and their best fit (black line).*

Table 7.1. *List of fit parameters (independent points (N_{indp}) and Number of variables (N_{var}) for the fit, Coordination number (CN), Energy shift (ΔE_0), Debye-Waller factor (σ^2), Bond length (R), and R-factor) obtained from modelling the data for Fe_K edge and Mn_K edge.*

edge	shell	CN	ΔE_0 (eV)	σ^2 (Å^2)	R (Å)	R-factor
Fe_K k (0,12) R (1,5) N_{indp} =38 N_{var} = 17	Fe_S Fe_O	4.20 ± 0.42 1.00±0.309	-15.0 ± 0.94 -3.95±2.18	0.021±0.0006 0.002 ±0.0044	2.24 ±0.0003 2.01 ± 0.121	0.025
Mn_K k (1.2,11.2) R (1,3.4) N_{indp} =21 N_{var} = 15	Mn_S Mn_O	4.00 ± 0.44 1.00 ± 0.98	-12.65±2.63 -6.01 ±2.96	0.024 ± 0.002 0.001 ± 0.007	2.37 ± 0.278 2.07 ± 0.820	0.035

Additionally, the X-ray absorption near edge structure (XANES) analysis through linear combination fitting (LCF) of the dopant K edges with appropriate standards provides the

average oxidation states as shown in Figures 7.4(a) and (b). From the LCF analysis, the average oxidation state of Fe is found to be increasing to +2.87 in dual-doped CdS from +2.27 in single Fe-doped CdS (shown in Figure 7.5). The actual oxidation state of Fe in individual Fe-doped CdS has been reported to be +2[27] and a different result from XANES is due to the contribution from the undissolved Fe_7S_8 core. On the other hand, the average oxidation state of Mn in dual-doped CdS (+2.49) is found to be largely unaltered from singly-doped Mn-CdS (+2.43), discussed in chapter 5. However, XANES measurement is not site-selective and hence, it would be impossible to separate the contributions from the core (M-S) and surface (M-O) coordination, especially when a substantial surface contribution is present in both the dopant K edges as shown in the EXAFS analysis. Thus, XANES analysis cannot precisely comment on the change in dopant oxidation states present at the core.

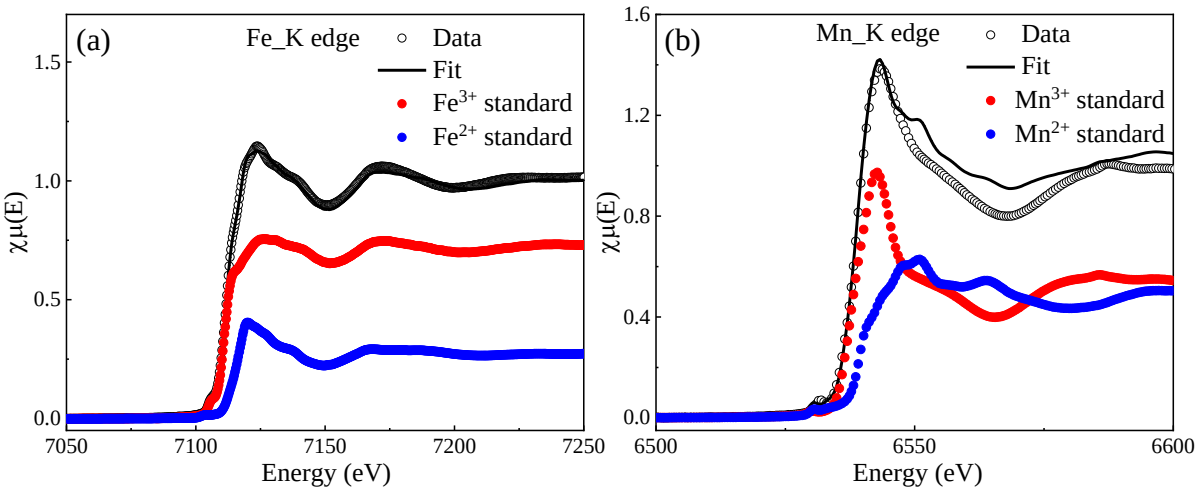

Figure 7.4. *Linear Combination Fitting (LCF) of XANES of (a) Fe_K edge, and (b) Mn_K edge in Mn, Fe dual-doped CdS QDs showing an average oxidation state of Fe and Mn to be +2.87 and +2.49, respectively.*

To find solutions, we take a look at the EXAFS dopant K edge fits and observe that the obtained bond length of the Fe_S bond is substantially reduced to 2.24 Å in Mn, Fe dual-doped CdS from 2.39 Å in singly doped Fe-CdS which further complements the increase in Fe oxidation state to nearly +3. Whereas the Mn-S bond length is found to be similar in both dual-doped (2.37 Å) and individual Mn-doped CdS (2.35 Å).

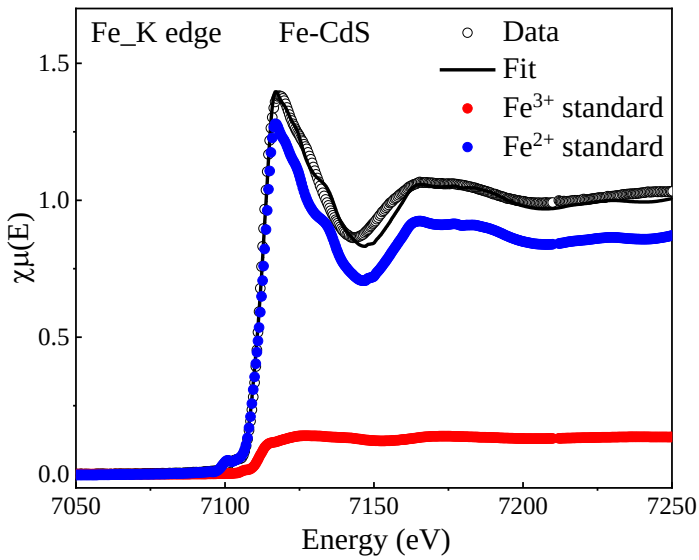

Figure 7.5. *Linear Combination Fitting (LCF) of XANES of Fe_K edge in Fe-doped CdS QDs showing an average oxidation state of Fe to be +2.27.*

To gain insights into these optical and structural perturbations discussed above, we studied the modulation in exciton dynamics of Mn-doped CdS in presence of another impurity (Fe) using femtosecond TA spectroscopy. We performed a comparative study of the charge carrier dynamics in undoped and singly-doped, and dual-doped CdS using a pump fluence of 24 μJ/cm^2 under the non-resonant excitation condition with the photoexcitation energy of 3.1 eV which is higher than the bandgap of the QD systems. Figure 7.6(a) depicts the differential transmission dynamics ΔT/T for undoped, all the singly-doped, and dual-doped CdS QDs probed at their respective band edges. We observe a fast rise in the ΔT/T signal followed by an exponential decay which holds the information about the depopulation and population dynamics of the ground state respectively and are termed as ground state bleach (GSB) growth and recovery. Upon focusing on the initial time scale, we observe that the doped CdS follow different GSB growth dynamics than the undoped as shown in Figure 7.6(b). The GSB growth and recovery kinetics are fitted to study the relaxation dynamics of the charge carriers. While the kinetics of the undoped CdS require a single exponential build-up and a single exponential recovery, the kinetics of singly-doped and dual-doped CdS are biexponential and triexponential, respectively.

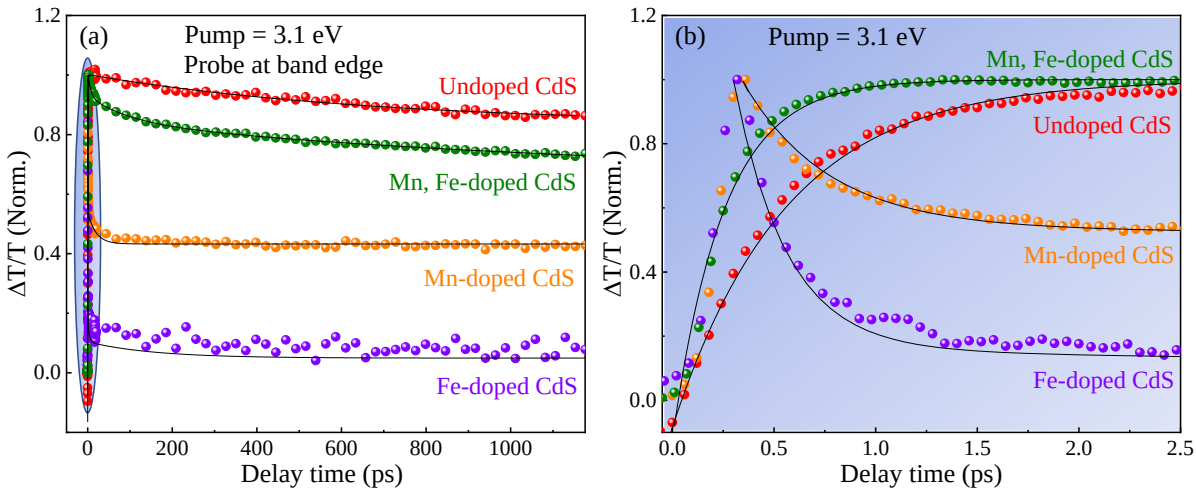

Figure 7.6. *(a) Differential transmission dynamics ΔT/T as a function of pump-probe delay for undoped and doped CdS QDs upon 3.1 eV laser excitation with a pump fluence of 24 μJ/cm2 (b) zoom-in of ΔT/T up to 2.5 ps.*

From the fitting of undoped CdS kinetics, we obtain a finite build-up time of 560 ± 7 fs which is due to the gradual population of the charge carriers at the band edges arising from the relaxation of charge carriers from the higher vibrational energy levels to the band edges.[28] Additionally, we obtained a single exponential recovery of the charge carriers with a time constant of 710 ± 58 ps without any fast component suggesting that the QDs are devoid of trap states similar to earlier report on undoped CdS synthesized in identical method.[28] GSB growth of individual Fe and Mn-doped CdS is instantaneous or IRF limited, whereas the dual-doped CdS show relatively slower growth with a time component of 250 ± 8 fs, which is still faster than that of the pristine CdS. The faster growth in doped CdS is due to the presence of alternative depletion channel introduced by doping.

In the case of individual Mn and Fe-doped CdS, we notice a nearly instantaneous GSB recovery which is due to the ultrafast capture of charge carriers by the dopant states. However, doping of two dopants into the same CdS lattice causes a slower recovery as compared to the singly doped CdS with an extra relaxation pathway. Most importantly, the recovery pathways in dual-doped QDs are distinctly different and slower from the ones present in singly doped QDs as shown in Table 7.2. This slower recovery with time constants 6.5 ± 0.56 ps and 95 ± 17 ps could be attributed to the interaction between two dopants[18] which causes a restriction in the charge carrier relaxation and a new relaxation dynamic is observed in the case of dual doping. Fe being a non-radiative decay center quickly captures the excited state carriers from

the host levels as reported in earlier literature.[16] Hence, we assume that the reduction in Mn-related emission intensity could possibly be correlated with the ultrafast capture of carriers by the Fe levels from the host partially restricting the charge transfer from the host to Mn levels.

Table 7.2. *A fitting summary of the GSB recovery kinetics of undoped, and doped CdS QDs.*

Sample Name	y_0	A_1	t_1 (ps)	A_2	t_2 (ps)	A_3	t_3 (ps)
CdS	0.83 ± 0.007	-	-	-	-	0.17 ± 0.007	710 ± 58
Fe-CdS	0.05 ± 0.003	-	-	1.40 ± 0.04	0.28 ± 0.008	0.10 ± 0.004	24 ± 3
Mn-CdS	0.43 ± 0.001	-	-	1.00 ± 0.03	0.42 ± 0.01	0.10 ± 0.002	20 ± 1
Fe, Mn-CdS	0.65 ± 0.04	0.08 ± 0.002	6.5 ± 0.56	0.08 ± 0.009	95 ± 17	0.19 ± 0.03	1265 ± 110

However, so far, no information could be extracted about the charge/energy transfer between the two dopant states. From the TA analysis, we know that the Mn states get sensitized within a few femtoseconds[29-31] and the emission through spin forbidden d-d transition occurs in a millisecond timescale.[32] Thus, the measured decay lifetime of Mn-related emission largely reflects the carrier population in Mn excited state. The decrease in Mn PL lifetime indicates toward the population reduction in the Mn excited state due to the carrier capturing by Fe impurities from the Mn excited states having a time constant of 1265 ± 110 ps. In fact, when we look at the XANES and EXAFS analysis we observe a substantial decrease in Fe-S bond length (2.24 Å from 2.39 Å) and so an increase in the Fe oxidation state (+2.87) in dual-doped QDs, which further confirms the trapping of charge carriers by the Fe levels from both excitonic as well as Mn excited states leading to a partial quenching in Mn PL intensity along with a reduction in the decay lifetime.

7.5. Conclusion

In this work, we have investigated the Mn-related emission modulation in presence of another impurity ion Fe^{2+} in CdS host QDs. The host-dopant model ensures the incorporation

of both the dopants in the dilute regime. EXAFS analysis confirms the successful incorporation of the dopants into the CdS matrix. The incorporation of Fe^{2+} ions results in a partial quenching of Mn-related emission by capturing the excited charge carriers from both excitonic and Mn levels observed from femtosecond TA spectroscopic analysis. Carrier trapping by Fe levels from the Mn levels is confirmed by the change in Fe-S bond length and Fe oxidation state obtained from EXAFS and XANES analysis. This study establishes the possibility of designing new dual-doped host-dopant models to unfold many fundamental properties like magneto-optics as well as new potential functionalities.

Bibliography

1. Kim, J. Y.; Voznyy, O.; Zhitomirsky, D.; Sargent, E. H., 25th Anniversary Article: Colloidal Quantum Dot Materials and Devices: A Quarter-Century of Advances. *Adv. Mater.* **2013**, *25*, 4986-5010.

2. Talapin, D. V.; Lee, J.-S.; Kovalenko, M. V.; Shevchenko, E. V., Prospects of Colloidal Nanocrystals for Electronic and Optoelectronic Applications. *Chem. Rev.* **2010**, *110*, 389-458.

3. Kagan Cherie, R.; Lifshitz, E.; Sargent Edward, H.; Talapin Dmitri, V., Building Devices from Colloidal Quantum Dots. *Science* **2016**, *353*, aac5523.

4. Bhargava, R. N.; Gallagher, D.; Hong, X.; Nurmikko, A. J., Optical Properties of Manganese-Doped Nanocrystals of Zns. *Phys. Rev. Lett.* **1994**, *72*, 416.

5. Bol, A. A.; Meijerink, A., Long-Lived Mn^{2+} Emission in Nanocrystalline ZnS: Mn^{2+}. *Phys. Rev. B* **1998**, *58*, R15997.

6. Zeng, R.; Rutherford, M.; Xie, R.; Zou, B.; Peng, X., Synthesis of Highly Emissive Mn-Doped ZnSe Nanocrystals without Pyrophoric Reagents. *Chem. Mater.* **2010**, *22*, 2107-2113.

7. Santra, P. K.; Kamat, P. V., Mn-Doped Quantum Dot Sensitized Solar Cells: A Strategy to Boost Efficiency over 5%. *J. Am. Chem. Soc.* **2012**, *134*, 2508-2511.

8. Wu, P.; Yan, X.-P., Doped Quantum Dots for Chemo/Biosensing and Bioimaging. *Chem. Soc. Rev.* **2013**, *42*, 5489-5521.

9. Kim, A.; Hosseinmardi, A.; Annamalai, P. K.; Kumar, P.; Patel, R., Review on Colloidal Quantum Dots Luminescent Solar Concentrators. *ChemistrySelect* **2021**, *6*, 4948-4967.

10. Zhou, Y.; Zhao, H.; Ma, D.; Rosei, F., Harnessing the Properties of Colloidal Quantum Dots in Luminescent Solar Concentrators. *Chem.Soc. Rev.* **2018**, *47*, 5866-5890.

11. Grandhi, G. K.; Tomar, R.; Viswanatha, R., Study of Surface and Bulk Electronic Structure of II–VI Semiconductor Nanocrystals Using Cu as a Nanosensor. *ACS Nano* **2012**, *6*, 9751-9763.

12. Beaulac, R.; Archer, P. I.; Ochsenbein, S. T.; Gamelin, D. R., Mn^{2+}-Doped CdSe Quantum Dots: New Inorganic Materials for Spin-Electronics and Spin-Photonics. *Adv. Funct. Mater.* **2008**, *18*, 3873-3891.

13. Lee, W.; Oh, J.; Kwon, W.; Lee, S. H.; Kim, D.; Kim, S., Synthesis of Ag/Mn Co-Doped CdS/ZnS (Core/Shell) Nanocrystals with Controlled Dopant Concentration and Spatial

Distribution and the Dynamics of Excitons and Energy Transfer between Co-Dopants. *Nano Lett.* **2019**, *19*, 308-317.

14. Panda, S. K.; Hickey, S. G.; Demir, H. V.; Eychmüller, A., Bright White-Light Emitting Manganese and Copper Co-Doped ZnSe Quantum Dots. *Angew. Chem. Int. Ed.* **2011**, *50*, 4432-4436.

15. Saha, A.; Gahlot, K.; Viswanatha, R., Exciton Dynamics in Mn/Ni Dual-Doped Semiconductor Quantum Dots. *ChemNanoMat* **2022**, *8*, e202100457.

16. Makkar, M.; Dheer, L.; Singh, A.; Moretti, L.; Maiuri, M.; Ghosh, S.; Cerullo, G.; Waghmare, U. V.; Viswanatha, R., Magneto-Optical Stark Effect in Fe-Doped CdS Nanocrystals. *Nano Lett.* **2021**, *21*, 3798-3804.

17. Li, Q., et al., Enhanced Valley Zeeman Splitting in Fe-Doped Monolayer Mos_2. *ACS Nano* **2020**, *14*, 4636-4645.

18. Chen, H.; Chen, C., Comparative Studies on Magnetic Properties of Mn/Fe Codoped ZnS Nanowires. *J. Magn. Magn. Mater.* **2013**, *330*, 66-71.

19. Kang, T.; Sung, J.; Shim, W.; Moon, H.; Cho, J.; Jo, Y.; Lee, W.; Kim, B., Synthesis and Magnetic Properties of Single-Crystalline Mn/Fe-Doped and Co-Doped ZnS Nanowires and Nanobelts. *J. Phys. Chem. C* **2009**, *113*, 5352-5357.

20. Wang, Z.; Liu, Y.; Zhang, J.; Wang, X.; Wu, Z.; Wu, J.; Chen, N.; Li, D.-S.; Wu, T., Unveiling the Impurity-Modulated Photoluminescence from Mn^{2+}-Containing Metal Chalcogenide Semiconductors Via Fe^{2+} Doping. *J. Mater. Chem. C* **2021**, *9*, 13680-13686.

21. Pradhan, N.; Peng, X., Efficient and Color-Tunable Mn-Doped ZnSe Nanocrystal Emitters: Control of Optical Performance Via Greener Synthetic Chemistry. *J. Am.Chem. Soc.* **2007**, *129*, 3339-3347.

22. Saha, A.; Makkar, M.; Shetty, A.; Gahlot, K.; A. R, P.; Viswanatha, R., Diffusion Doping in Quantum Dots: Bond Strength and Diffusivity. *Nanoscale* **2017**, *9*, 2806-2813.

23. Li, J. J.; Wang, Y. A.; Guo, W.; Keay, J. C.; Mishima, T. D.; Johnson, M. B.; Peng, X., Large-Scale Synthesis of Nearly Monodisperse CdSe/CdS Core/Shell Nanocrystals Using Air-Stable Reagents Via Successive Ion Layer Adsorption and Reaction. *J. Am. Chem. Soc.* **2003**, *125*, 12567-12575.

24. Newville, M., Ifeffit : Interactive XAFS Analysis and Feff Fitting. *J. Synchrotron Rad.* **2001**, *8*, 322-324.

25. Ravel, B.; Newville, M., Athena, Artemis, Hephaestus: Data Analysis for X-Ray Absorption Spectroscopy Using IFEFFIT. *J. Synchrotron Rad.* **2005**, *12*, 537-541.

26. Rehr, J. J.; Albers, R. C., Theoretical Approaches to X-Ray Absorption Fine Structure. *Rev. Mod. Phys.* **2000**, *72*, 621-654.

27. Saha, A.; Chattopadhyay, S.; Shibata, T.; Viswanatha, R., Core–Shell to Doped Quantum Dots: Evolution of the Local Environment Using XAFS. *J. Phys. Chem. C* **2016**, *120*, 18945-18951.

28. Makkar, M.; Moretti, L.; Maiuri, M.; Cerullo, G.; Viswanatha, R., Ultrafast Electron–Hole Relaxation Dynamics in CdS Nanocrystals. *J. Phys.: Mater.* **2021**, *4*, 034005.

29. Gahlot, K.; KR, P.; Camellini, A.; Sirigu, G.; Cerullo, G.; Zavelani-Rossi, M.; Singh, A.; Waghmare, U. V.; Viswanatha, R., Transient Species Mediating Energy Transfer to Spin-Forbidden Mn d States in Ii–Vi Semiconductor Quantum Dots. *ACS Energy Lett.* **2019**, *4*, 729-735.

30. Cherepanov, D.; Kostrov, A.; Gostev, F.; Shelaev, I.; Motyakin, M.; Kochev, S.; Kabachii, Y.; Nadtochenko, V., Ultrafast Quenching of Excitons in the $Zn_xCd_{1-X}S/ZnS$ Quantum Dots Doped with Mn^{2+} through Charge Transfer Intermediates Results in Manganese Luminescence. *Nanomaterials* **2021**, *11*, 3007.

31. Chen, H. Y.; Son, D. H., Energy and Charge Transfer Dynamics in Doped Semiconductor Nanocrystals. *Isr. J. Chem.* **2012**, *52*, 1016-1026.

32. Nag, A.; Cherian, R.; Mahadevan, P.; Gopal, A. V.; Hazarika, A.; Mohan, A.; Vengurlekar, A. S.; Sarma, D. D., Size-Dependent Tuning of Mn^{2+} d Emission in Mn^{2+}-Doped CdS Nanocrystals: Bulk Vs Surface. *J. Phys. Chem. C* **2010**, *114*, 18323-18329.

Future outlook of my thesis

In my thesis, I majorly focused on the transition metal doped colloidal II-VI semiconductor QDs and their fundamental photophysics. I also designed and successfully synthesized a few dual-doped II-VI QDs which are largely unexplored due to the lack of proper host-dopant modelling and their stability. Here, we have applied high-temperature colloidal method for doping and this approach has a great prospect undoubtedly from the synthetic point of view which can be further extended to doping of several other dopants into II−VI QDs. In fact, further synthetic developments are needed to improve the PL quantum yields of transition metal doped semiconductor nanocrystals while maintaining the optimum concentrations of dopant ions. Such improvements in PL QY would not only improve the performance of luminescent doped semiconductor NCs in various applications ranging from bioimaging to solar concentration but would also enable further fundamental investigations into the physical and photophysical properties of this important class of luminescent nanomaterials. In particular, additional spectroscopic and physical characterization of Cu-doped semiconductor nanocrystals will yield new fundamental insights into their luminescence mechanisms and redox or photo redox properties and ultimately their applicability in future advanced technologies. The other area where such materials are likely to prove technologically useful is in photovoltaic applications. Since dopants can significantly alter the recombination time of the photogenerated charge carriers, these materials could be explored for photovoltaic applications, enhancing their efficiencies. It has already been reported that doping heterovalent ions modifies the charge transport properties, and careful selection of dopant and host can provide nano p-n junctions within the nanocrystals. Clearly, this helps in charge separation, beneficial to photovoltaic and other applications.

There is also a recent trend of attributing multi-functionality to a given kind of nanocrystals through interesting synthetic strategies. For example, quantum confined charge carriers in Mn-doped CdSe based nanocrystals result into giant Zeeman splitting, providing interesting magneto-optic properties. Similarly, Nanocrystals co-doped with magnetic ions and free carriers (plasmonic) might exhibit interesting magneto-plasmonic and magneto-electric properties. However, in most such cases, the future challenge will remain to be in discovery of new doped systems, with better properties and higher efficiencies, but without any toxic material, such as Pb and Cd; this is indeed an essential

step in developing environmentally benign nanocrystals and will play increasingly crucial role in the future.

List of publications

1. "Insights into the Oxidation State of Cu Dopants in II-VI Semiconductor Nanocrystals." **Payel Mondal**, and Ranjani Viswanatha. J. Phys. Chem. Lett., **2022**, *13*, 1952-1961.

2. "Is the Lack of Orange Emission Infallible Proof of Unsuccessful Doping of Mn in Quantum Dots?" **Payel Mondal**, Sowmeya Sathiyamani, Kushagra Gahlot, and Ranjani Viswanatha J. Phys. Chem. C, **2021**, *125*, 11007-11013.

3. "Cu Doping in II-VI Semiconductor Nanocrystals: Single-Particle Fluorescence Study." **Payel Mondal**, , G. Krishnamurthy Grandhi, and Ranjani Viswanatha. J. Phys. Chem. Lett., **2020**, *11*, 5367-5372.

4. "Cation co-doping into ZnS quantum dots: towards visible light sensing applications." G. Krishnamurthy Grandhi, Mahesh Krishna, **Payel Mondal**, and Ranjani Viswanatha. J. Bull. Mater. Sci., **2020**, *43*, 301.

5. "Electronic Structure Study of Dual Doped II-VI Semiconductor Quantum Dots Towards Single-Source White Light Emission" **Payel Mondal**, Sowmeya Sathiyamani, Subham Das, and Ranjani Viswanatha (communicated)

6. "Transition Metal Dopant Induced Perturbation in CdS Quantum Dots: Diffusivity, Magnetism, and Ultrafast Charge Carrier Dynamics" Saptarshi Chakraborty, **Payel Mondal**, Mahima Makkar, Luca Moretti, Giulio Cerullo, and Ranjani Viswanatha. (manuscript under preparation).

7. "Study of Spectral Resolution and Photophysics in Mn-Doped Semiconductor Quantum Dots Using Single-Particle Fluorescence Spectroscopy" **Payel Mondal**, Deepshikha Arora, Somnath Kashid, Arindam Chowdhury, and Ranjani Viswanatha. (manuscript under preparation).

8. “Study of Optical Perturbation in Mn-Doped Semiconductor Quantum Dots in Presence of Other Impurity” **Payel Mondal**, Saptarshi Chakraborty, Mahima Makkar, Luca Moretti, Giulio Cerullo, and Ranjani Viswanatha. (manuscript under preparation).